Final Report

Turbulent Flame Speeds and NOx Kinetics of HHC Fuels with Contaminants and High Dilution Levels

Project Duration:
October 1, 2010 – September 30, 2013

Principal Authors:
Eric Petersen, Michael Krejci, Olivier Mathieu, Andrew Vissotski, Sankar Ravi, Drew Plichta, Travis Sikes, Anthony Levacque, Alejandro Camou, and Christopher Aul

Principal Investigator:
Eric L. Petersen
Department of Mechanical Engineering
Texas A&M University
3123 TAMU
College Station, TX 77843
407-823-6123

Issue Date: January 24, 2014

DOE Award No. DE-FE0004679
TEES Project 32525-B1730

Prepared for:
U. S. Department of Energy/NETL
626 Cochrans Mill Road
P.O. Box 10940
Pittsburgh, PA 15236-0940

DISCLAIMER

ABSTRACT

This final report documents the technical results of the 3-year project entitled, "Turbulent Flame Speeds and NOx Kinetics of HHC Fuels with Contaminants and High Dilution Levels," funded under the NETL of DOE. The research was conducted under six main tasks: 1) program management and planning; 2) turbulent flame speed measurements of syngas mixtures; 3) laminar flame speed measurements with diluents; 4) NOx mechanism validation experiments; 5) fundamental NOx kinetics; and 6) the effect of impurities on NOx kinetics. Experiments were performed using primary constant-volume vessels for laminar and turbulent flame speeds and shock tubes for ignition delay times and species concentrations. In addition to the existing shock-tube and flame speed facilities, a new capability in measuring turbulent flame speeds was developed under this grant. Other highlights include an improved NOx kinetics mechanism; a database on syngas blends for real fuel mixtures with and without impurities; an improved hydrogen sulfide mechanism; an improved ammonia kintics mechanism; laminar flame speed data at high pressures with water addition; and the development of an inexpensive absorption spectroscopy diagnostic for shock-tube measurements of OH time histories.

The Project Results for this work can be divided into 13 major sections, which form the basis of this report. These 13 topics are divided into the five areas: 1) laminar flame speeds; 2) Nitrogen Oxide and Ammonia chemical kinetics; 3) syngas impurities chemical kinetics; 4) turbulent flame speeds; and 5) OH absorption measurements for chemical kinetics.

TABLE OF CONTENTS

LIST OF GRAPHICAL MATERIALS

TABLES

FIGURES

EXECUTIVE SUMMARY

This report presents a new set of correlations for the laminar flame speeds of hydrogen-oxygen mixtures with nitrogen (air) and helium as diluents, using a recently updated chemical kinetics mechanism. A wide excursion of equivalence ratios (ϕ = 0.5-5.0), pressures (1-30 atm) and temperatures (270-620 K) was performed. Flame speed correlations were developed at five pressures, namely 1, 5, 10, 20, and 30 atm for the pure-hydrogen case. The disparities between the kinetic model predictions and the correlation estimates, commonly associated with existing correlations, were significantly reduced, and the correlation estimates are within ± 13 cm/s of the model predictions. Also, a correlation for lean and high-hydrogen-content (HHC) syngas blends of H_2+CO+H_2O was developed from the pure-hydrogen correlations. A wide range of pressures (1-30 atm), initial temperatures (323-550 K), steam contaminant levels (5-15%), and hydrogen content in the fuel blend (15%-100%) were simulated. A design of experiments approach was adopted to determine the critical mixtures necessary to develop the correlation. The developed HHC correlation agrees within ±12% of the model predictions.

Two constant-volume cylindrical vessels were used to visualize the spherical growth of the flame through the use of a schlieren optical setup to measure the laminar flame speed of the mixture. Hydrogen experiments were performed at initial pressures up to 10 atm and initial temperatures up to 443 K. A syngas composition of 50/50 was chosen to demonstrate the effect of carbon monoxide on H_2-O_2 chemical kinetics at standard temperature and pressures up to 10 atm. All atmospheric mixtures were diluted with standard air, while all elevated-pressure experiments were diluted with a He:O_2 of 7:1 to minimize hydrodynamic instabilities. The laminar flame speed measurements of hydrogen and syngas are compared to available literature data over a wide range of equivalence ratios where good agreement can be seen with several data sets.

The presence of steam in syngas blends is of particular interest from a thermo-chemical perspective as there is limited information available in the literature. This project investigated the effect of moisture content (0 – 15% by volume), temperature (323 – 423 K), and pressure (1 – 10 atm) on syngas mixtures by measuring the laminar flame speed in a recently developed constant-volume, heated experimental facility. A design-of-experiments methodology was applied to these conditions to cover the widest range of conditions that are relevant to the gas turbine industry. The experimental flame speed data are compared to a recent chemical kinetics model showing good overall agreement, but there are areas that need improvement, particularly around the peak flame speed. A performance sensitivity analysis showed that the syngas composition is the most important factor affecting the laminar flame speed, but there is inconclusive evidence of a dominant factor that affects the mass burning rate and the Markstein length. Generally, mixtures with high levels of carbon monoxide stabilize the flame structure of thermal-diffusive instability. The increase of steam dilution has only a small effect on the laminar flame speed of high carbon monoxide mixtures, while more hydrogen-dominated mixtures demonstrate a much larger and negative effect on the laminar flame speed at low pressures.

Ignition delay times of H_2/O_2 mixtures highly diluted with Ar and doped with various amounts of N_2O (100, 400, 1600, 3200 ppm) were measured in a shock tube behind reflected shock waves over a wide range of temperatures (940-1675 K). The pressure range investigated during this work (around 1.6, 13, and 30 atm) allows studying the effect of N_2O on hydrogen ignition at pressure conditions that have never been heretofore investigated. Ignition delay times were

decreased when N_2O was added to the mixture only for the higher nitrous oxide concentrations, and some changes in the activation energy were also observed at 1.5 and 30 atm. When it occurred, the decrease in the ignition delay time was proportional to the amount of N_2O added and depended on pressure and temperature conditions. A detailed chemical kinetics model was developed using kinetic mechanisms from the literature. This model predicts well the experimental data obtained during this study and from the literature. The chemical analysis using this model showed that the decrease in the ignition delay time was mainly due to the reaction $N_2O + M \rightleftarrows N_2 + O + M$ which provides O atoms to strengthen the channel $O + H_2 \rightleftarrows OH + H$.

Ignition delay time measurements of $H_2/O_2/NO_2$ mixtures diluted in Ar have been measured in a shock tube behind reflected shock waves. Three different NO_2 concentrations have been studied (100, 400 and 1600 ppm) at three pressure conditions (around 1.5, 13 and 30 atm) and for various H_2-O_2 equivalence ratios for the 100-ppm NO_2 case. Results were compared to some recent ignition delay time measurements of H_2/O_2 mixtures. A strong dependence of the ignition delay time on the pressure and the NO_2 concentration was observed. A mechanism combining recent H_2/O_2 chemistry and a recent, high-pressure NOx sub-mechanism with an updated reaction rate for $H_2 + NO_2 \rightleftarrows HONO + H$ was found to represent correctly the experimental trends over the entire range of conditions. A chemical analysis was conducted to interpret the experimental results. Ignition delay time data with NO_2 and other NOx species as additives or impurities are rare, and the present study provides such data over a relatively wide pressure range.

Ammonia is a common impurity that can be found in many gas turbine-type fuels derived from coal or biomass and can also be used directly as a fuel in internal combustion engines. Past research showed that ammonia can be the source of "fuel NOx" during its combustion but can also be used in NOx reduction strategies in industrials processes. It is therefore important to understand the details of the high-temperature oxidation of ammonia. Unfortunately, a strong disagreement was observed amongst detailed kinetics mechanisms from the literature for predictions under conditions of practical interest. Ignition delay time measurements for ammonia have been performed several decades ago and conditions are not well reported into the literature. To have well characterized data and to assess the validity of the models, new measurements have been performed in diluted conditions (98 and 99% Ar) and for large pressure (around 1.4, 11.0, and 30 atm), temperature (1560-2490 K), and equivalence ratio ranges (0.5, 1.0, and 2.0). Only one mechanism from the literature was capable of modeling these data with good accuracy. On the other hand, comparison with $H_2/O_2/NOx$ literature data shows that this model requires improvements.

Hydrogen sulfide is a common impurity that can greatly change the combustion properties of fuels, even when present in small concentrations. However, the combustion chemistry of H_2S is still poorly understood, and this lack of understanding subsequently leads to difficulties in the design of emission-control and energy-production processes. During this study, ignition delay times were measured behind reflected shock waves for mixtures of 1 % H_2 / 1% O_2 diluted in Ar and doped with various concentration of H_2S (100, 400, and 1600 ppm) over large pressure (around 1.6, 13, and 33 atm) and temperature (1045-1860 K) ranges. Results typically showed a significant increase in the ignition delay time due to the addition of H_2S, in some cases by a factor of 4 or more over the baseline mixtures with no H_2S. The magnitude of the increase is

highly dependent on the temperature and pressure. A detailed chemical kinetics model was developed using recent, up-to-date detailed-kinetics mechanisms from the literature and by changing a few reaction rates within their reported error factor. This updated model predicts well the experimental data obtained during this study and from the shock-tube literature. However, flow reactor data from the literature were poorly predicted when H_2S was a reactant. This study highlights the need for a better estimation of several reaction rates to better predict H_2S oxidation chemistry and its effect on fuel combustion. Using the kinetics model for sensitivity analyses, it was determined that the decrease in reactivity in the presence of H_2S is because H_2S initially reacts before the H_2 fuel does, mainly through the reaction $H_2S + H \rightleftarrows SH + H_2$, thus taking H atoms away from the main branching reaction $H + O_2 \rightleftarrows OH + O$ and inhibiting the ignition process.

Ignition delay times have been measured behind reflected shock waves at 1.5, 12 and 30 atm for a mixture representative of a syngas produced from biomass (0.29659% CO / 0.29659% H_2 / 0.15748% CO_2 / 0.08924% CH_4 / 0.20997% H_2O / 0.95013% O_2 in 98% Ar (mol.%)) and for the same biomass-derived syngas mixture doped with 200 ppm of NH_3. The importance of the various constituents on the ignition delay time was investigated by comparing the results with data from various baseline mixtures (H_2/O_2/Ar, H_2/CO/O_2/Ar and H_2/CO/O_2/Ar with one of the other constituent of the syngas (*i.e.* CO_2, H_2O, CH_4 or NH_3)). The equivalence ratio was set to 0.5 during this study. Several recent detailed kinetics mechanisms from the literature were computed against these data, with fair agreement. Results showed that the mixture composition can have an important effect on the ignition delay time, with most of the effect being due to CH_4 addition through the reaction $CH_4+OH \rightleftarrows CH_3+H_2O$. The ammonia impurity had very little effect on the ignition delay time over the range of conditions studied.

Ignition delay times have been measured behind reflected shock waves for a syngas determined by averaging 40 coal syngas compositions from the literature. The average mixture (0.4554% CO/0.3297% H_2/0.1032% CO_2/0.0172% CH_4/0.2407% H_2O/0.8538% O_2 in 98% Ar (mol. %)) was investigated at an equivalence ratio of 0.5 and at around 1.7, 13, and 32 atm. The same mixture was also investigated with impurities (200 ppm of NH_3 and 50 ppm of H_2S) whereas the effect of the various constituents was studied by comparing results from a baseline mixture (H_2/CO/O_2/Ar) and results with this baseline mixture with only one of the other constituents. Direct measurements of the water vapor mole fractions were performed using a tunable diode laser absorption diagnostic near 1.38 µm. Results showed that extending the mixture composition to include realistic concentrations of species beyond just the CO and H_2 does not have a very large effect on the ignition delay time under the conditions from this study. However, a comparison of this coal-derived syngas with a syngas derived from biomass, tested in an earlier study, exhibited larger differences due to the difference in the CH_4 concentration. Experimental data were compared with recent detailed kinetics mechanisms from the literature.

Depending on the feedstock and the production method, the composition of syngas can include (in addition to H_2 and CO) small hydrocarbons, diluents (CO_2, water, and N_2), and impurities (H_2S, NH_3, NOx, etc.). Despite this fact, most of the studies on syngas combustion do not include hydrocarbons or impurities and in some cases not even diluents in the fuel mixture composition. Hence, studies with realistic syngas composition are necessary to help designing gas turbines. The aim of this work was to investigate numerically the effect of the variation in the

syngas composition on some fundamental combustion properties of premixed systems such as laminar flame speed and ignition delay time at realistic engine operating conditions. Several pressures, temperatures, and equivalence ratios were investigated. To perform this parametric study, a state-of-the-art C0-C5 detailed kinetics mechanism was used. Results of this study showed that the addition of hydrocarbons generally reduces the reactivity of the mixture (longer ignition delay time, slower flame speed) due to chemical kinetic effects. The amplitude of this effect is however dependent on the nature and concentration of the hydrocarbon as well as the initial condition (pressure, temperature, and equivalence ratio).

A new turbulent flame speed capability was designed, and characterization of the new turbulent flame speed vessel design was completed. Turbulence statistics of three impellers with different geometric features were measured using particle image velocimetry inside a Plexiglas model (~1:1 scale) of a cylindrical flame speed vessel (30.5 cm ID × 35.6 cm L). With four impellers arranged in a central-symmetric configuration, turbulence intensities between 1.2 and 1.7 m/s with negligible mean flow (0.1u′) were attained at the lowest fan speeds. Acceptable ranges for homogeneity and isotropy ratios of the velocity fields were set within a narrow bandwidth near unity (0.9-1.1). Homogeneity ratios were unaffected by changes to the impeller geometry, and the prototype with the higher number of blades caused the flow to become anisotropic. The integral length scale of the flow fields varied between 27 and 20 mm, which correlates well with those typically observed inside a gas turbine combustor. The mechanism to independently vary the intensity level and the integral length scale was established, where turbulence intensity level was dependent on the rotational speed of the fan, and the integral length scale decreased with increasing blade pitch angle.

Global displacement speeds were measured in a recently developed fan-stirred, cylindrical flame speed vessel using high-speed schlieren imaging. Measurements were conducted in homogeneous and isotropic turbulent conditions at an average RMS turbulent intensity of 1.5 m/s and at an integral length scale of 27 mm. Methane and a representative synthetic gas or syngas blend containing 50:50 by volume of hydrogen and carbon monoxide, all diluted in air, were studied. A wide range of equivalence ratios was covered, and the flame speeds were estimated when the flame radius was equal to the integral length scale. Turbulent flame speeds were computed using four widely used numerical models: (1) Zimont turbulent burning velocity model (1988); (2) Kerstein pair-exchange model (1988); (3) the coherent flame speed model (1993); and, (4) the distributed reaction zone model (1995). The Kerstein model and the Zimont model agreed well with the experimental measurements. Also, S_T/S_L was higher for syngas than methane for the same u'/S_L, which is indicative of the preferential diffusion effect of hydrogen in increasing the flame surface area by distorting it.

UV absorption spectroscopy was used to measure OH concentration in well-studied H_2/O_2 experiments to calibrate the diagnostic using mechanism predictions of the peak OH mole fraction. More work is needed to derive a correlation for the absorption coefficient for OH, but the work thus far looks promising for the use of a lamp-absorption technique for measuring ground state OH in a high-pressure shock tube. This diagnostic gives accurate measurement of OH and at a cost which is an order of magnitude less than its laser-based counterpart. The spectrometer setup is largely robust with little change in lamp intensity over time, thereby allowing the experimenter to record data quickly and with a high degree of repeatability.

APPROACH

The basic approach is best summarized by the six main tasks, as follows.

Task 1 – Project Management and Program Planning
Project management includes the submission of regular and required reports to DOE, in addition to routine management of the TAMU project by the PI. This task also includes the specific interaction with the industry consultants. Feedback from GE, Siemens, Rolls-Royce, and Alstom will be obtained at the beginning of the program through face-to-face meetings, followed by periodic contact throughout the project.

Task 2 – Turbulent Flame Speed Measurements of Syngas Mixtures
The original flame speed vessel at Texas A&M University will be modified with the capability to perform turbulent flame speed measurements. Turbulence will be generated with fans, and the experiment and turbulence level will be well characterized prior to performing experiments. Turbulent flame speeds will be measured as a function of turbulence level, mixture composition, and initial pressure. Correlations will be developed that relate the turbulent speed to the equivalent laminar flame speed for the same mixture and initial pressure.

Task 3 –Laminar Flame Speed Measurements with Diluents
Using the new, heated flame speed vessel, high-pressure experiments up to 20 atm will be conducted over a wide range of syngas mixtures. These mixtures will have realistic levels of diluents, with emphasis on high levels of water dilution. The heated facility will allow for such mixtures, with initial temperatures as high as 600 K possible. The resulting database will be compared with current chemical kinetics models and will be used as the baseline for the turbulent flame speed measurements.

Task 4 – NOx Mechanism Validation Experiments
These experiments will involve shock tubes to obtain data for validation of the NOx submechanism at realistic ranges of mixture composition, stoichiometry, and pressure. Emphasis will be placed on two types of experiments: 1) ignition experiments (both dilute and high concentration) containing initial levels of NO_2 and N_2O, to test the mechanisms in a global way, and 2) dilute experiments wherein key intermediate and NOx-related species profiles are measured using laser absorption and ir emission techniques. The resulting database will be compared to the NOx mechanism, and areas for improvement will be identified as needed.

Task 5 – Fundamental NOx Kinetics
Focus for this task will be on the direct measurement of specific rate coefficients to improve the accuracy of the NOx predictions at conditions involving high hydrogen and dilution levels. We anticipate the focus to be on the NNH pathway, and the rate measurement will be done in carefully designed shock tube experiments at controlled conditions.

Task 6 – Effect of Impurities on Syngas Kinetics
This task will involve primarily ignition measurements from the shock-tube experiments that contain realistic levels of syngas impurities. Consultation with industry will be helpful in identifying the likely impurities. Flame speed measurements can also be performed to assess the impact of the most important or likely impurities.

PROJECT RESULTS

The following twelve sections cover the main results of the 3-year project effort. They are divided into the following topics: laminar flame speed measurements of high-hydrogen blends; chemical kinetics of syngas and NOx; effects of impurities on the oxidation kinetics of syngas blends; turbulent flame speeds; and fundamental kinetics measurements using OH absorption.

LAMINAR FLAME SPEED CORRELATIONS

Fuel flexible operation of stationary gas turbines for integrated gasification combined cycle (IGCC) applications has triggered significant interest in the use of hydrogen-based fuels [Campbell et al., 2008]. Additionally, stringent NO_x emission standards and the focus on carbon-free operation have provided momentum in the design of modern, premixed combustors which utilize high-hydrogen-content fuels [Lacy et al., 2008]. The wide flammability limits ranging from 0.1 to 7.1 in equivalence ratio (fuel-to-air) and the high flame speeds at extremely fuel-lean conditions make hydrogen an attractive fuel option [White et al., 2006]. Hydrogen-fueled internal combustion engines are gaining popularity as well [Verhelst and Wallner, 2009]. Combustion processes at engine conditions are highly turbulent, and the flame speeds at such realistic conditions are often estimated from a functional relationship involving the laminar flame speed [Zimont and Lipatnikov, 1995]. The laminar flame speed is usually provided as input to computational fluid dynamics (CFD) codes in the form of lookup tables or as correlations [White et al., 2006]. Correlations can provide reliable flame speed estimates when they are based on experimental data or on multi-step chemistry models. Furthermore, they are computationally convenient and do not require expensive software.

Correlation development for the H_2/air system is impeded by two major difficulties. Firstly, the correlation performance cannot be verified experimentally as hydrogen flames are categorically unstable at elevated pressures. However, the hypothetical stable flame speeds predicted by the kinetics model serve as good estimates for engine design codes [Verhelst et al., 2011]. Secondly, the pressure dependency of hydrogen kinetics is extremely complex, and the correlations available in the literature often fail to adequately capture the model data due to inadequate functional formulation. As a result, the differences between the kinetic model predictions and the correlation estimates are often more than ±20% [Verhelst et al., 2011]. Hence there is a need for better correlations that reproduce the kinetic model calculations of laminar flame speeds with greater accuracy. To improve their accuracies at realistic conditions, the correlations in this study were developed at individual pressures. Though tedious, this approach leads to better agreement with the model (±13 cm/s) and represents the model data more accurately than existing correlations (as is shown later). It should be noted that the words ‘model’ and ‘kinetics model’ are used interchangeably in this paper.

The primary objective of this study was to develop flame speed correlations for pure hydrogen as well as for high-hydrogen-content (HHC) syngas blends at engine-relevant conditions. First, the correlations available in the literature for H_2/air are reviewed and summarized. The mechanism used for the chemical kinetic simulations is then validated in detail. The work presented in the subsequent sections of the paper can be divided into two parts: (1) correlation development for pure-hydrogen mixtures with various diluents, namely nitrogen (air) and helium; and, (2) determination of a correlation for a variety of HHC syngas blends directly from the pure-

hydrogen correlations instead of using the chemical kinetics model predictions for each individual blend. This approach can be taken for hydrogen-based fuels because syngas-blend chemistry is typically dominated by hydrogen chemistry.

Background Literature

Flame speed refers to the propagation velocity of a self-sustained flame into a combustible mixture. It exhibits a non-monotonic behavior with respect to equivalence ratio (ϕ), consistent with the lean and rich flammability limits (see various flame speed plots throughout this paper). Flame speed increases with higher unburnt gas temperature, and decreases at elevated pressures. It can be shown from several studies throughout the literature that the laminar flame speed can be compactly modeled as,

$$S_{L,u}^{\circ} = f(x_i)\left({}^{T}/_{T_o}\right)^{\alpha(x_i)}\left({}^{p}/_{p_o}\right)^{\beta(x_i)} \quad (1)$$

Where T_o and P_o are the reference temperature and pressure respectively; and f, α, and β are the pre-multiplication factor, temperature exponent, and pressure exponent, respectively. These factors are typically taken to be functions of one or more independent variables, x_i, such as the equivalence ratio and pressure. To determine these parameters, extensive numerical simulations covering a wide range of P, T, and ϕ are performed. Subsequently, several correlations have been proposed for a variety of fuels. Table 1 summarizes the working ranges for various correlations available in the literature for the H_2/air system.

Table 1 Summary of laminar flame speed correlations for H_2/air from the literature.

Reference	Pressure (atm)	Temperature (K)	Equivalence Ratio	Mechanism
Verhelst and Sierens (2003)	1-16	300-800	0.25-1.0	Yetter et al. (1991)
Gerke et al. (2010)	5-45	350-700	0.36-2.5	Ó Connaire et al. (2004)
Verhelst et al. (2011)	5-45	500-900	0.33-2.0	Konnov et al. (2004)
Present Study	**1-30**	**270-620**	**0.5-5.0**	**Kéromnès et al. (2011)**

Verhelst and Sierens (2003) reviewed in detail the existing correlations for the burning velocity of H_2/air mixtures for use in spark-ignition engine modeling codes, and more details can be found therein. In summary, they identified several discrepancies amongst the correlations in modeling the pressure effects on the hydrogen flame speeds, which they attributed to the fact that the experimental data that were used to develop the correlations were not corrected for flame stretch effects. To account for the highly nonlinear effects of pressure on the laminar flame speeds, they proposed a coupled formulation in which the pre-multiplication factors and the temperature exponents were functions of both the equivalence ratio and pressure, thus modifying Eqn. (1) to the form of Eqn. (2). This new form of the correlation agreed within ±10% of the kinetics model predictions. However, the pressure range covered was limited and was not pertinent to high-pressure environments of industrial combustion systems.

$$S_{L,u}^{\circ} = f(\phi, p)\left({}^{T}/_{T_o}\right)^{\alpha(\phi,p)} \quad (2)$$

Gerke et al. (2010) measured the laminar flame speeds for hydrogen-air mixtures at engine conditions in a rapid compression machine with optical access. They observed cellular flames which they called quasi-laminar flames, and predicted the flame speeds using OH chemiluminescence imaging as well as from the thermodynamic analysis of the pressure trace during the combustion event. Large uncertainties were associated with the measured flame speeds due to the unstable nature of the flames caused by intrinsic flame instabilities and due to the variability in pressure and temperature as a result of the compressions induced by the piston-like motion of the burnt gases. Such experimentally determined flame speeds represent unstable flames and cannot be directly compared with the flame speeds of the stretch-free and stable flames predicted by kinetics modeling. However, an important observation was that the ratios of the quasi-laminar flame speeds to the kinetic model predictions increased linearly with increase in equivalence ratio, thus providing a method to estimate the unstable flame speed at engine conditions from the kinetic model predictions.

More recently, Verhelst et al. (2011) presented an improved correlation with a wider range of validity than their previous study [Verhelst and Sierens, 2003], and showed that the improved correlation had a better predictive capability in comparison to the other existing correlations (Gerke et al., 2010; D'Errico, 2008). Despite using the coupled formulation, significant discrepancies (greater than 20%) were found between the correlation estimates and the input data. These trends further support the need for correlations with better functions, or at least a change in the methodology used to develop such correlations to improve their capabilities in reproducing the kinetic model data at elevated pressures and temperatures.

Correlation Formulation

As explained earlier, the laminar flame speed can be modeled in a compact form using Eqn. (1). For simplicity, we have assumed the three modeling parameters to be polynomial functions of equivalence ratio only, and are defined as,

- $f(\phi) = a_1 + a_2\phi + a_3\phi^2 + a_4\phi^3 + a_5\phi^4$
- $\alpha(\phi) = b_1 + b_2\phi + b_3\phi^2 + b_4\phi^3$
- $\beta(\phi) = c_1 + c_2\phi + c_3\phi^2$

In an attempt to decouple the nonlinear pressure dependency of the H_2/air system, correlations at individual pressures are formulated herein. Then for a fixed pressure, Eqn. (1) can be reduced to the following form after using f(ϕ) and α(ϕ) from above,

$$S^{\circ}_{L,u,P} = [a_1 + a_2\phi + a_3\phi^2 + a_4\phi^3 + a_5\phi^4]\left[T/T_o\right]^{(b_1+b_2\phi+b_3\phi^2+b_4\phi^3)} \quad (3)$$

To develop the correlation by determining the various α_i and f_i coefficients, the kinetic model predictions of the flame speeds at different initial temperatures (270-620 K) for a wide range of equivalence ratios (0.5-5.0), all at a fixed pressure, are provided as input. A surface is fitted over the input data thereby ensuring smooth interpolation within the encompassed domain space. The equation of this fitted surface denotes the correlation at that pressure. The coefficients in Eqn. (3) are adjusted until the residuals (defined as the difference between the correlation estimates and

the model predictions) are within the acceptable limits (here, ± 13 cm/s). Figure 1 shows one such surface fit for atmospheric H_2/air mixtures.

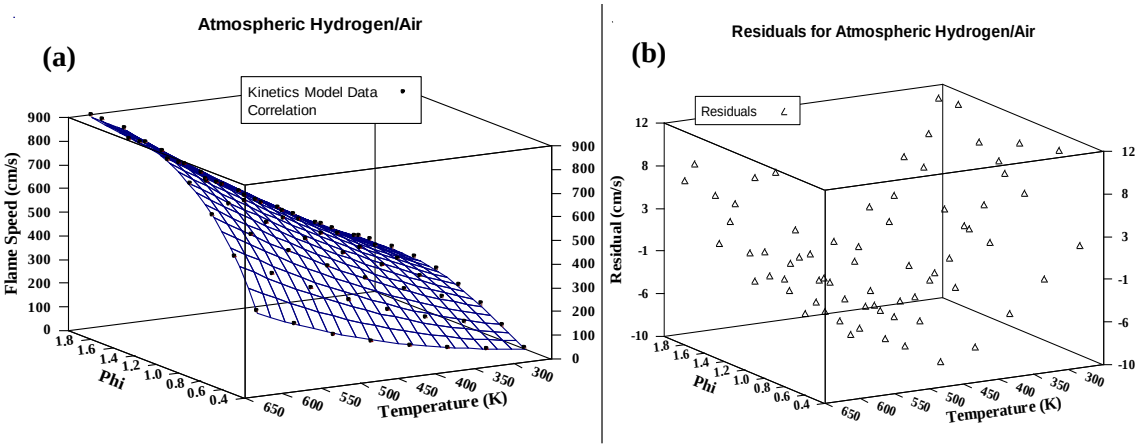

Fig. 1 (a) Correlation surface fit for atmospheric H_2/air for 270-620 K and $0.5 < \phi < 2.0$. The correlation (fitted surface) estimates the flame speed at any given ϕ, T. The kinetic model calculations used to develop the correlations are also shown (filled squares). (b) Residuals (difference between the model data and the correlation estimates) at various conditions. The excellent accuracy of the correlation is evident from the negligible residuals (±13 cm/s).

Mechanism Description

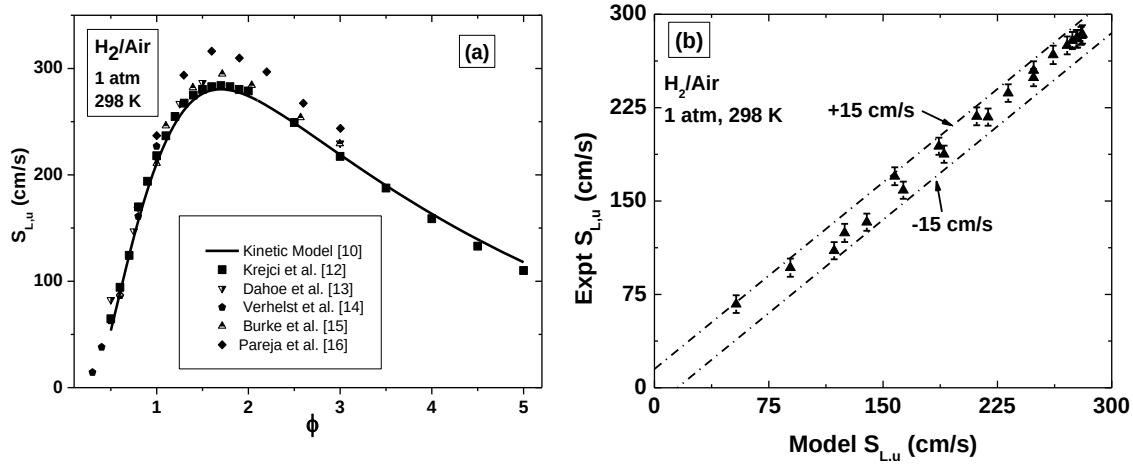

Fig. 2 (a) Experimental flame speed data (symbols) from various rigs for atmospheric H_2/air at 298 K. The kinetic model prediction (curve) is also shown. (b) Parity plot between the experimental data [Krejci et al., 2013] and the kinetic model prediction showing close agreement within ±15 cm/s.

The simulations in this study were performed using the updated mechanism by Kéromnès et al. (2013). This version of the mechanism is considered to be a significant improvement over the mechanism originally developed by Ó Connaire et al. (2004). The H_2/O_2 mechanism consists of 19 elementary reversible reactions, and was thoroughly validated using flame speed data from spherically expanding flame speed rigs and burner- stabilized flames, species composition data

from flow reactors, and ignition delay times from shock tubes. The working range for this mechanism is: pressures from 0.05 to 87 atm, temperatures ranging between 298 and 2700 K, and equivalence ratios from 0.6 to 6. The updated chemical kinetics mechanism was evaluated by comparing the simulation predictions for both the laminar flame speeds and the ignition delay times with the experimental measurements. Figure 2a shows the recent flame speed measurements from the authors' laboratory [Krejci et al., 2013] along with measurements from various rigs [Dahoe, 2005; Verhelst et al., 2005; Burke et al., 2009; Pareja et al., 2010] for atmospheric H_2/air mixtures. The model predicts the flame speeds within ±15 cm/s of the experimental measurements, as shown in Fig. 2b, which highlights the excellent predictive capability of the mechanism. The model performance at elevated pressures was assessed by ignition delay times from shock-tube experiments [Krejci et al., 2013] as stable flame speed data could not be obtained at those conditions in H_2/air mixtures (however, stable elevated-pressure data can be obtained when some or all of the N_2 is replaced by helium). Hence, the model satisfactorily captures the flame chemistry at all mixture strengths and over a wide range of pressures.

Parameter Space

The primary objective of this study was to develop correlations for hydrogen with various oxidizer-diluent mixtures, namely air and O_2/He (1:7), over a wide range of pressures and temperatures, outlined in the parameter space. At each individual pressure and temperature, an excursion of equivalence ratios ranging from extremely fuel-lean to fuel-rich was performed. These correlations then formed the framework upon which the correlation for high-hydrogen-content syngas blends of H_2/CO/H_2O was developed. To obtain the necessary model data, detailed chemical kinetic simulations were performed using PREMIX from Chemkin® (http://www.reactiondesign.com/products/open/chemkin.html.). Thermal diffusion was allowed, and mixture-averaged transport equations were used in the simulations. The adiabatic flame temperatures and the equilibrium temperatures were within 5 K of each other for all runs. This close agreement ensured convergence of solution over 3000 grid points. For the elevated-pressure simulations, water was initially added to the reactant mixture (2% of the fuel) and was then removed in the subsequent continuations as recommended by the mechanism developers to ensure failure-free results.

Table 2 Parameter space for PREMIX calculations of pure-hydrogen mixtures with various diluents is shown. Step size denotes the step-increments of the various parameters.

Parameters	**Range**	**Increment**
Pressure	1-30 atm	1,5,10,20,30 atm
Temperature	270-620 K	ΔT=50 K
Equivalence Ratio	0.5-2.0	$\Delta\varphi$=0.2
	2.0-5.0	$\Delta\varphi$=0.5

When presenting the results, the following convention is used: all experimental data (when available) are shown as filled symbols, and the corresponding model predictions are shown as open symbols. The correlations are plotted as dashed curves.

Pure-Hydrogen Mixtures

Table 3 H_2/air correlation at various pressures in the form of Eqn. (3)

	H_2/Air (0.5<φ<2.0)					H_2/Air (2.0<φ<5.0)				
	1 atm	**5 atm**	**10 atm**	**20 atm**	**30 atm**	**1 atm**	**5 atm**	**10 atm**	**20 atm**	**30 atm**
$\mathbf{a_1}$	-3	161	232.9	259.3	272.8	355.8	481.8	378.9	492.5	450.5
$\mathbf{a_2}$	-234.7	-970.8	-1228.7	-1281.3	-1316.4	16.2	-87.2	-31.2	-184.1	-190.6
$\mathbf{a_3}$	998.4	1902.6	2131.7	2081.5	2079.4	-24.7	-5.3	-20.8	21.1	25.9
$\mathbf{a_4}$	-673.4	-1111.7	-1197.3	-1147.1	-1141.8	2.53	1.38	2.8	-0.59	-1.05
$\mathbf{a_5}$	136.1	209.8	220.7	209.5	208.6			0		
$\mathbf{b_1}$	5.07	5.52	5.76	6.02	7.84	1.405	1.091	1.64	0.84	0.81
$\mathbf{b_2}$	-6.42	-6.73	-6.92	-7.44	-11.55	0.053	0.317	-0.03	0.56	0.64
$\mathbf{b_3}$	3.87	3.88	3.92	4.37	7.14	0.022	0	0.07	0	0
$\mathbf{b_4}$	-0.767	-0.728	-0.715	-0.825	-1.399			0		
$\mathbf{T_o}$	**320**									

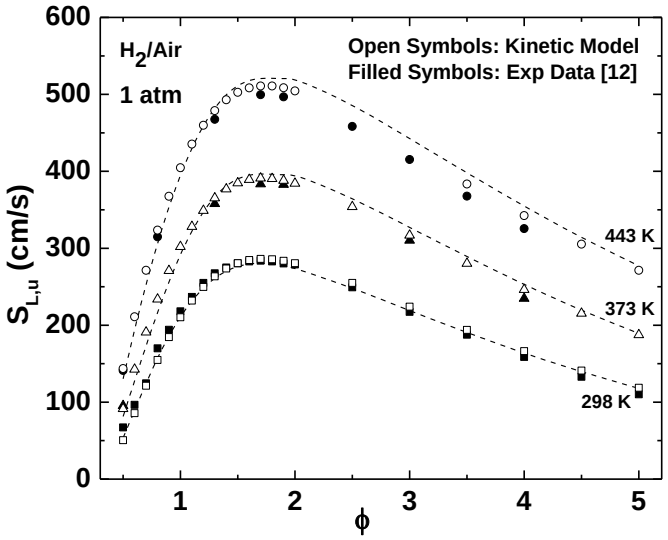

Fig. 3 Atmospheric H_2/air at different initial temperatures. Excellent agreement is seen amongst the experimental data [Krejci et al., 2013], the kinetics model predictions, and the correlation at all conditions.

H_2/Air Correlation. The correlations for the H_2/air system at various pressures are shown in Table 3. Figure 3 compares the flame speed measurements (experimental) with the correlation estimates for atmospheric H_2/air at three representative initial temperatures. The correlation matches the experimental data closely. The kinetics model predictions are also included for reference. There is excellent agreement between the correlation and the kinetics model over the entire range of equivalence ratios and temperatures. Figure 4 compares the correlation developed by Verhelst and Sierens (2003) with the correlation developed in this study for atmospheric

H_2/air at elevated temperatures. Despite a wider range of validity (300-800 K), the former correlation [Verhelst and Sierens, 2003] overestimates the flame speeds at higher initial temperatures, while the correlation developed herein is in closer agreement with the model as well as experimental data at all temperatures. A comparison of the overall performances of the two correlations was not possible since their parameter spaces were not exactly the same.

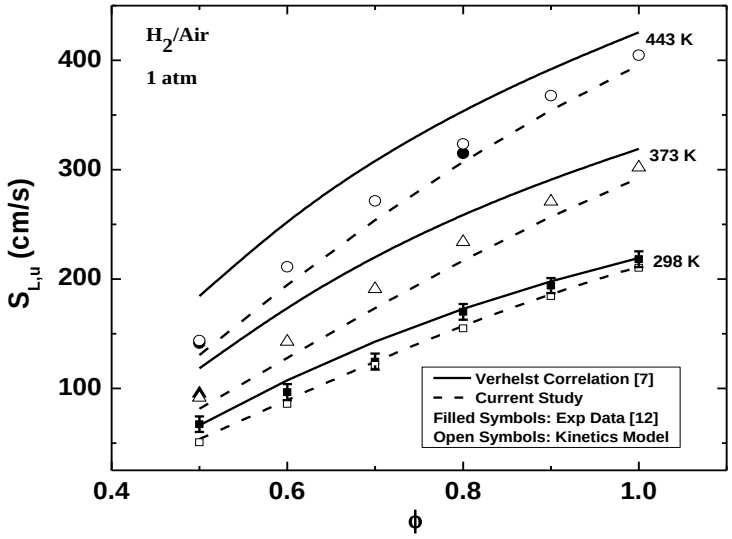

Fig. 4 Atmospheric H_2/air at elevated temperatures over the lean range of mixtures. Better agreement amongst the experimental data [Krejci et al., 2013] and model predictions and the correlation from this study (dashed curve) seen when compared to the correlation by Verhelst and Sierens (2003) (solid curve).

H_2/air mixtures simulated at elevated pressures, namely 10, 20 and 30 atm at 420 K are shown in Fig. 5. The correlation closely matches the model data at all conditions, and the scatter associated with the global formulation or the coupled formulation is not observed here due to the constant-pressure methodology used in this study. These correlations for elevated-pressure conditions cannot be verified experimentally as the flames tend to be unstable at those conditions due to diffusional instability. Therefore, a correlation-correlation comparison similar to the one presented in Fig. 4 is not possible due to lack of experimental data to benchmark them.

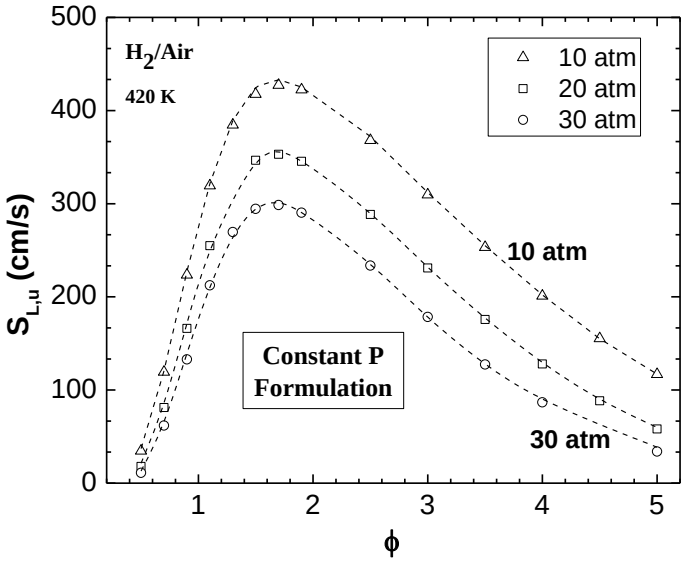

Fig. 5 High-pressure correlations for H_2/air. Kinetics model data are shown as open symbols. The constant-pressure formulation is used here, wherein correlations were developed at each pressure.

Table 4: Mean temperature coefficient for H_2/air for $0.5 \leq \phi \leq 1.0$

Reference	α(ϕ)
Gerke et al. (2010)	2.3 (for unstable conditions) 3.3 (for stable conditions)
Verhelst and Sierens (2003)	2 (1 atm); 2.5 (10 atm)
D'Errico et al. (2008)	2.7 (1 atm); 2.3 (30 atm)
Verhelst et al. (2011)	2.7 (5 atm); 3.3 (30 atm)

The temperature exponents of the H_2/air correlations at different pressures are plotted (Fig. 6) over the entire range of equivalence ratios covered in this study. The temperature exponents also exhibit a nonlinear relationship with respect to the equivalence ratio, but opposite to that of the laminar flame speed. A clear pressure dependency at fuel-rich conditions ($\varphi > 1.8$) is seen from the divergence of the exponents at different pressures. This divergence highlights the fact that the coupled correlation, deemed suitable to model the pressure dependency of the temperature exponent, is required only for the fuel-rich regime. The main objective of this study was to develop correlations pertinent to gas turbine operating conditions. At such lean conditions ($\varphi < 1$), a collapse of the curves at different pressures is observed, indicating only a weak dependence on pressure. In this regime, the temperature exponent, $\alpha(\varphi)$, has an average value of 2.5. This value agrees well with the similar averages estimated from the existing correlations reported in the literature (Table 4). It is also imperative to point out that this average value can only provide quick estimates for the flame speeds at different intermediate temperatures; nonetheless, to get an accurate result, the coefficient should be computed in its entirety.

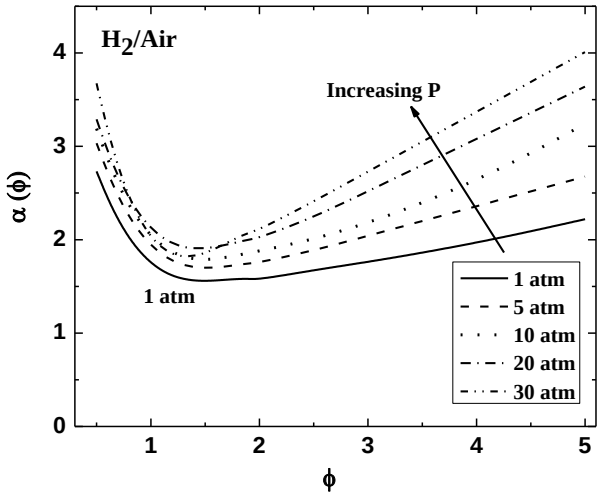

Fig. 6 Temperature exponent for H_2/air at different pressures. Unlike the fuel-rich cases, a collapse of the values in the fuel-lean regime, indicative of weaker pressure dependency, is evident.

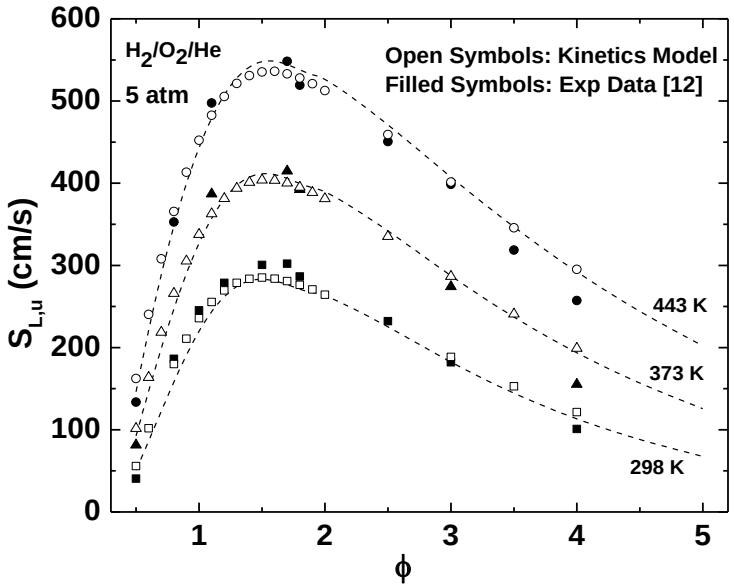

Fig. 7 5-atm H_2/O_2/He (1:7 O_2:He) mixtures at different initial temperatures. Unified agreement amongst the experimental data [Krejci et al., 2013], model predictions, and correlation estimates (dash lines) is observed.

H_2/O_2/He Mixtures. Helium is often used as a diluent instead of nitrogen to study the flame speeds of high-pressure hydrogen mixtures [Krejci et al., 2013; Tse et al., 2000]. Helium is found to suppress the onset of diffusional instability by increasing the Lewis number of the mixture [Tse et al., 2000]. Though a helium-based mixture may not be of practical relevance, it is of interest to the mechanism developers as it can be used to calibrate important reactions such as H + O_2+ M at elevated pressures and temperatures [Tse et al., 2000]. It also provides a method to

experimentally evaluate the predictive capability of the model at engine pressures, since stable flames that are unaffected by flame acceleration can be achieved at those conditions, unlike in H_2/air mixtures presented earlier. Flame speed computations at high pressures were performed using helium as the diluent. A dilution ratio of 1:7(O_2:He) was chosen to closely match the adiabatic flame temperatures of the pseudo-mixtures with those of the fuel-air mixtures, and this He level was successfully utilized in recent experimental measurements [Krejci et al., 2012]. Flame speed data for H_2/O_2/He mixtures at 5 atm and at elevated temperatures are shown in Fig. 7. The model captures the experimental data at all conditions. This agreement serves as a good indicator of the predictive capability of the model and adds more reliability to the correlations developed herein. The correlations for helium-based mixtures are shown in Table 5. Also, the correlation closely follows the kinetics model at all mixture strengths. To the authors' knowledge, correlations for H_2/O_2/He mixtures are presently not available in the literature, so a comparison of correlations is not possible.

Table 5 Correlation for H_2/O_2/He mixtures at various pressures in the form of Eqn. (3).

	H_2/O_2/He ($0.5<\varphi<2.0$)				**H_2/O_2/He ($2.0<\varphi<5.0$)**			
	5 atm	**10 atm**	**20 atm**	**30 atm**	**5 atm**	**10 atm**	**20 atm**	**30 atm**
$\mathbf{a_1}$	-35	30.7	120.9	152.8	542.5	470.8	648.2	548.8
$\mathbf{a_2}$	-160.9	-509.2	-900.2	-1019.4	-133.6	-91.2	-288.6	-235.3
$\mathbf{a_3}$	1051	1527.5	1971.2	2066.7	5.74	-7.49	45.8	31.9
$\mathbf{a_4}$	-766.4	-1027.8	-1243.9	-1279.4	0.53	1.77	-2.61	-1.26
$\mathbf{a_5}$	161.5	210.9	248.5	253	0.0			
$\mathbf{b_1}$	4.96	5.61	6.35	6.46	1.06	1.6	0.77	1.39
$\mathbf{b_2}$	-6.4	-7.57	-8.67	-8.67	0.33	-0.018	0.59	0.15
$\mathbf{b_3}$	4.03	4.75	5.34	5.24	0	0.071	0	0.095
$\mathbf{b_4}$	-0.813	-0.955	-1.048	-0.997	0.0			
$\mathbf{T_o}$	320							

Residual Analysis. To assess the accuracies of the correlations in a rigorous manner, residuals (i.e., the difference between the correlation and the kinetics model results) for the flame speed estimates were calculated for the entire parameter space. The computed residuals were then binned to generate the histograms at individual pressures as shown in Fig. 8. The residuals were normally distributed (unimodal) and their accuracy ranges can then be described by the parameters: mean (μ) and standard deviation (σ) (tabulated in Table 6). Also included are the 95% confidence intervals ($\mu \pm 2\sigma$) for the correlations at various pressures. This methodology implies that, for example, at atmospheric pressure, 95% of the correlation estimates in the parameter space are between -6.7 cm/s and 10.7 cm/s of the kinetics model predictions. This type of accuracy analysis is superior to merely stating the mean and standard deviation which corresponds only to a 68% confidence level. It should also be noted that the predictive capability of the correlations improves with pressure. Thus, the constant-pressure approach has drastically reduced the overall scatter between the correlation estimates and the model predictions to ± 13 cm/s.

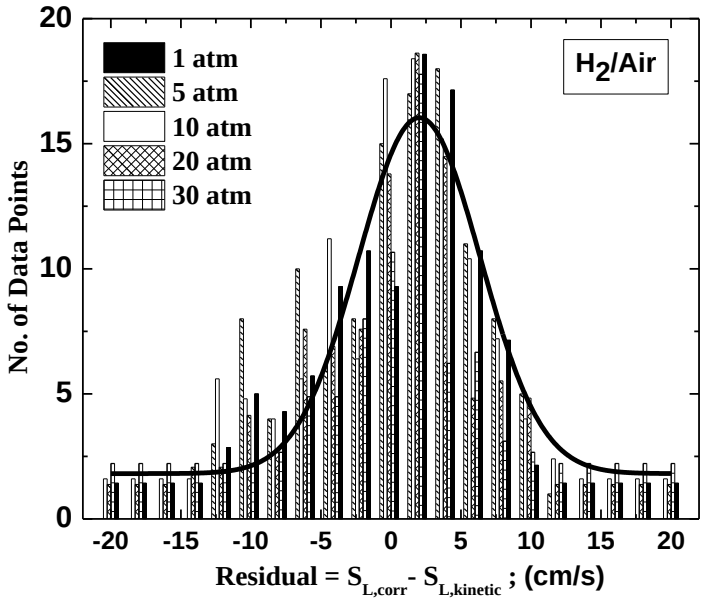

Fig. 8 Histograms of the residuals of H_2/air flame speeds at individual pressures. Normal distributions (Gaussian) were fitted to the histograms (1 atm curve is shown) to compute the 95% confidence intervals, thus yielding an overall scatter as low as ± 13 cm/s.

Table 6 95% confidence intervals for the H_2/air correlation at different pressures.

	μ	σ	95% Confidence Interval	
			Min (μ-2σ) **cm/s**	**Max** (μ+2σ) **cm/s**
1 atm	2.03	4.35	-6.7	10.7
5 atm	1.78	5.47	-9.2	12.7
10 atm	1.78	4.08	-6.4	9.9
20 atm	1.73	3.08	-4.4	7.9
30 atm	1.38	2.38	-3.4	6.1

A parity plot between the correlations and the kinetics model for H_2/air system at different pressures is shown in Fig. 9a. There is excellent agreement between both, and the scatter is negligible, which is typically not observed with the correlations reported in the literature. The 95% accuracy range (± 13 cm/s) is included for reference. A similar plot between the available experimental data and the correlations is shown in Fig. 9b. This comparison covers all conditions for which experimental data were presented in this paper. The slight scatter between them can be attributed to the difference between the kinetic model predictions and the experimental results. Since the model computations were used to develop the correlation, further improvements to the model will reduce the scatter between the actual measurements and the correlation predictions. Nevertheless, the agreement in Fig. 9b is still within ± 20 cm/s, predominantly.

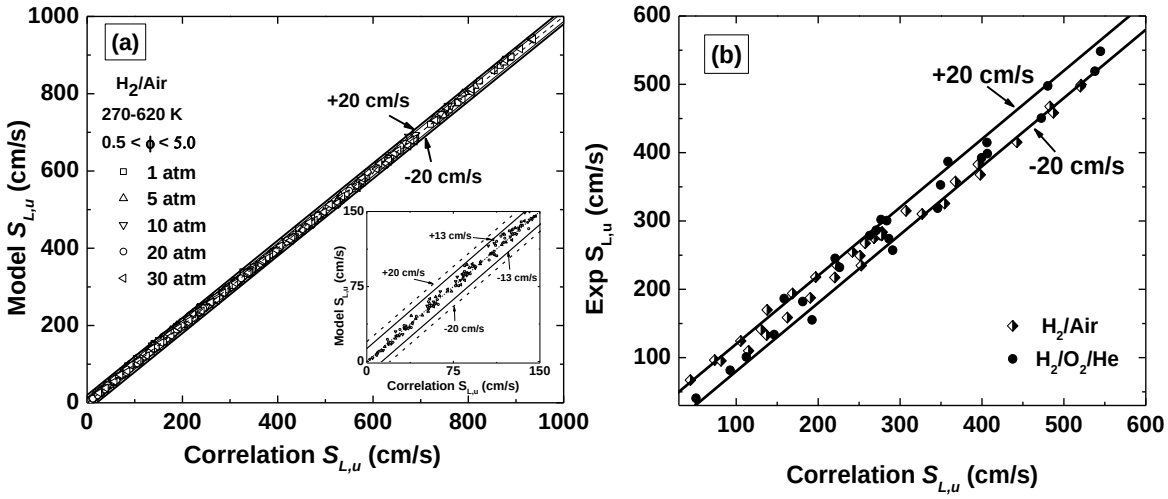

Fig. 9 (a) Model-Correlation parity plot for H_2/air for the entire parameter space. Both agree within ± 13 cm/s (95% confidence interval) at all conditions. For better visual clarity, flame speeds up to 150 cm/s are shown on the inset. (b) Parity plot between the available experimental data [Krejci et al., 2013] and correlation predictions for the pure-hydrogen mixtures with various diluents showing close agreement within ± 20 cm/s.

Global Pressure Correlation. A global pressure correlation of the form of Eqn (1) was also developed for the H_2/air system for the same parameter space (Eqs. 4 and 5). The flame speeds at elevated pressures for H_2/air were computed using the global correlation and are shown in Figure 10. It can be readily seen that the constant-pressure approach (Fig. 5) is better when compared to the global correlation in accurately capturing the kinetics model. Nevertheless, for φ <1.5, the global correlation captures the model estimates fairly accurately. Figure 11 shows the parity plots between the correlation predictions and model data for H_2/air. As the pressure is increased, the agreement between the model predictions and the correlation estimates dissipate, leading to increased scatter. While the majority of the correlation estimates are within ±15% of the kinetics model predictions, improvements are still needed to the proposed global correlation to better model the nonlinear pressure dependency.

For $0.5 < \varphi < 2.0$:

$$S_{L,u}^{\circ} = [168.3 - 1100.1\varphi + 2466\varphi^2 - 1449.2\varphi^3 + 267.6\varphi^4] * [{}^{p}/_{10}]^{(-0.71+0.8\varphi-0.25\varphi^2)} * [{}^{T}/_{500}]^{(5.61-7.75\varphi+5.54\varphi^2-1.61\varphi^3+0.151\varphi^4)} \quad (4)$$

For $2.0 < \varphi < 5.0$:

$$S_{L,u}^{\circ} = [856.7 - 158.8\varphi - 1.94\varphi^2 + 1.33\varphi^3] * [{}^{p}/_{10}]^{(0.075-0.072\varphi)} * [{}^{T}/_{500}]^{(1.3+0.275\varphi)} \quad (5)$$

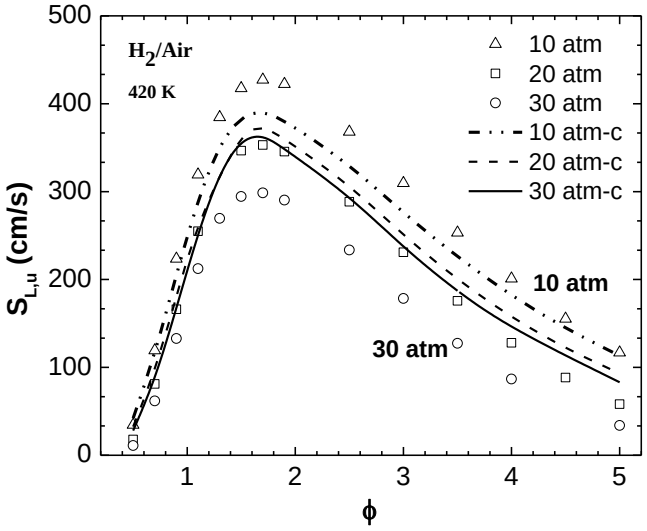

Fig. 10 Global correlation for H_2/air (Eqs. 4 and 5) which takes into account the nonlinear pressure dependency. The decreased accuracy is evident with the global correlation.

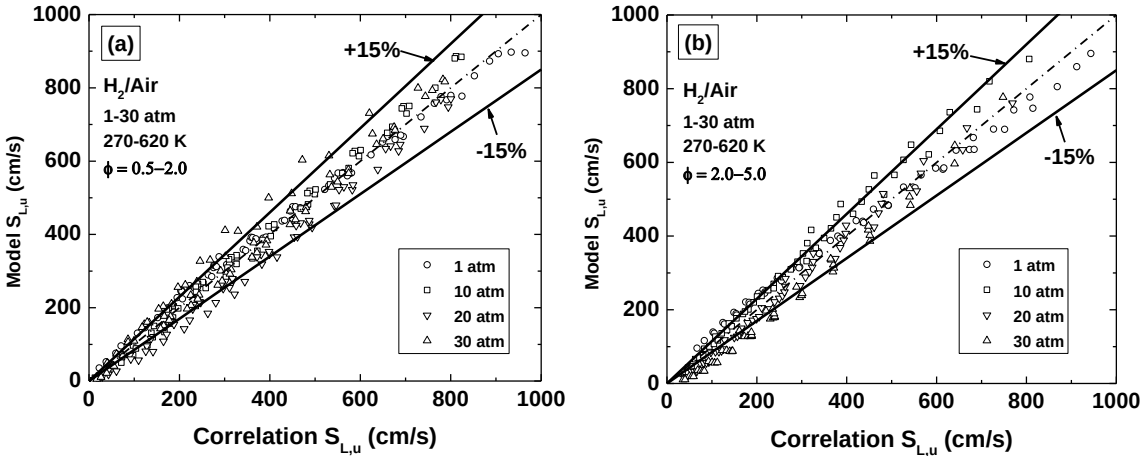

Fig. 11 Parity plots: Global pressure correlation and model predictions for H_2/air: (a) $0.5 < \phi < 2.0$ (b) $2.0 < \phi < 5.0$ for the entire range of pressures and temperatures. Correlation estimates are mostly within ± 15% the model predictions for both cases.

The advantage of the global correlation is its ability to model, even if not perfectly, the pressure dependency of the laminar flame speeds. Figure 12 shows the laminar flame speeds at three equivalence ratios, namely 0.5, 1.1, and 2.0; at two elevated temperatures 520 K and 620 K; and

over a wide range of pressures from 1 to 30 atm. A recent correlation which is based on the more-complex coupled formulation [Verhelst et al., 2011] is also included for comparison. The kinetic model predictions at those conditions are used to evaluate the predictive capabilities of both the correlations. Both relations follow the kinetics model closely for the fuel-lean case, but the latter fails to exhibit the curvature at higher equivalence ratios. This result could possibly be due to the fact the working range for the Verhelst et al. (2011) correlation starts at 5 atm instead of 1 atm used in this study.

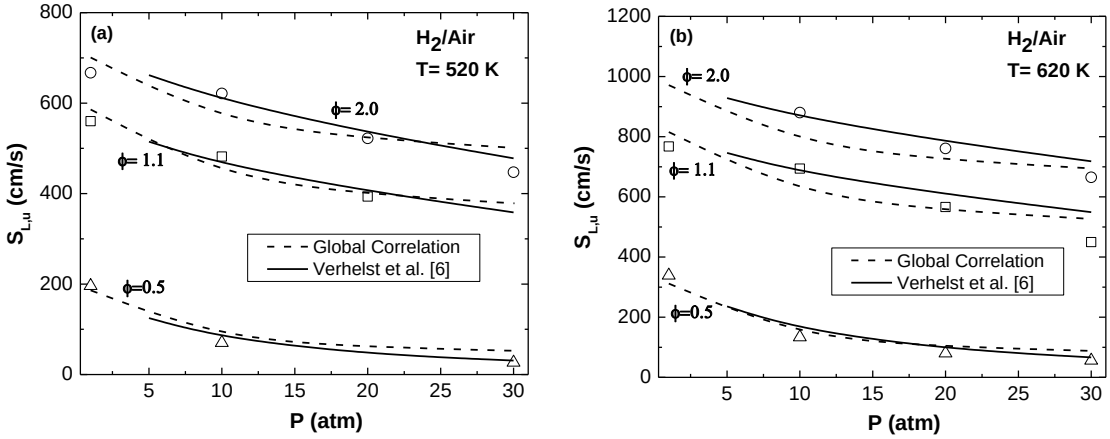

Fig. 12 Pressure dependency of H_2/air flame speeds at three equivalence ratios $\varphi = 0.5$, 1.1 and 2.0, and at elevated temperatures 520 K (a) and 620 K (b). The global correlation developed in this study agrees well with the full kinetics model (open symbols) despite higher data scatter when compared to the constant-pressure correlations. The coupled formulation Verhelst et al. (2011) is included for comparison.

The temperature exponent of the global correlation for hydrogen-air at different equivalence ratios is plotted in Fig. 13. Also included are the temperature exponents of the constant-pressure correlations at 1 and 30 atm. Since the global correlation spans the same range of pressures as the latter, its temperature exponent would be the mean of the two extremes (1 and 30 atm). An average value of 2.35 is obtained for the global temperature exponent for $0.5 \leq \phi \leq 1.0$. This value agrees well with the mean of 2.5 estimated earlier for the constant-pressure cases. This consensus further reinforces the argument that the temperature coefficient is only slightly pressure dependent, and that the effect of initial temperature on the laminar flame speed is satisfactorily captured by the global correlation.

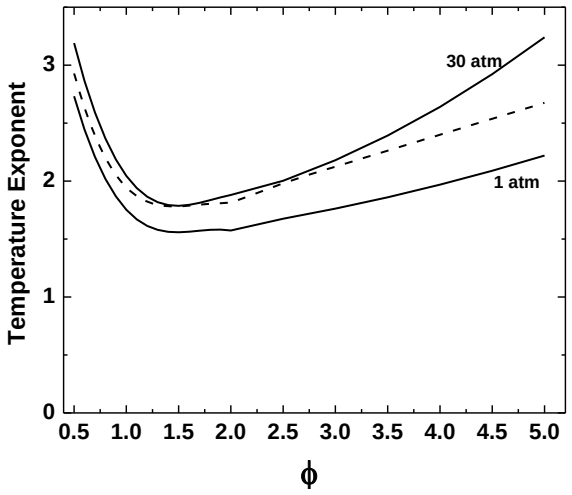

Fig. 13 Temperature exponents of the global correlation for H_2/air (dotted curve). The temperature exponent is found to be an average of the temperature exponents from the constant-pressure correlations at 1 atm and 30 atm (solid curves).

The analysis done so far is sufficient to summarize the advantages and disadvantages of both the approaches. The constant-pressure formulation provides flame speed estimates that are in better agreement with the kinetics model calculations even at elevated pressures and temperatures; but, it is slightly tedious as separate correlations are required at discrete pressures. The global correlations, however, are more convenient to implement, but their accuracies are compromised due to inadequacies in their functional forms.

Syngas Modeling

This section focuses on the development of a correlation for HHC syngas-type fuels. Synthetic gas or syngas is a hydrogen-based fuel blend with varying amounts of CO, CH_4 and other hydrocarbons [Moliere, 2000]. Its diverse composition makes it extremely challenging and computationally intensive for a single, comprehensive correlation to provide accurate flame speed estimates. Furthermore, the flame speed of a blend does not follow a simple linear mole fraction relation with its pure constituents [Lieuwen et al., 2008]. Hence, any correlation should accurately capture this nonlinear trend in the flame speed as a function of fuel compositional variation. However, HHC (containing at least 50% hydrogen in the fuel by volume) fuel blends of syngas mixtures of hydrogen and carbon monoxide tend to have chemical kinetic behavior similar to that of pure hydrogen. This observation was confirmed, for example, by insignificant deviations in the ignition delay times of different H_2/CO mixtures from the pure-hydrogen case [Krejci et al., 2013]. Whilst the diffusive and kinetic contributions of hydrogen to the flame speeds are found to be linear for fuel blends with trace amounts of hydrogen [Wu et al., 2011], an exponential amplification of the flame speeds with increase in hydrogen content is better suited for HHC blends due to the strong influence of hydrogen in such fuels. As a result, the laminar flame speed correlations for HHC blends can be derived using the pure-hydrogen flame speeds as a basis, as shown in Eqn. (5). This constraint significantly reduces the computational time by simplifying the correlations needed to model such a wide range of possible H_2/CO mixtures.

$$S_{L,u}(\phi, T, p, \lambda, \chi) = [k_1 \exp(m_1\lambda) + k_2 \exp(m_2\chi)]\left(S^{\circ}_{L,H_2}\right)^{c} \quad (6)$$

Where,

λ: Hydrogen Content in the fuel mixture (% volume)
χ: Water concentration in the fuel mixture (% volume of fuel)
S°_{L,H_2}: Pure [H_2/O_2/Diluent] flame speed at that p, T and φ
k_1, k_2, m_1, m_2 and c are the fitting constants.

To the authors' knowledge, this paper represents the first time that a correlation of this form has been proposed for H_2/CO-mixture laminar flame speeds. For obtaining the input data to develop the correlation, the design of experiments (DOE) methodology is appropriate and was employed in the study of Krejci et al. (2012) for syngas-type blends. This method provides an extensive excursion of the parameter space with the least number of experiments as opposed to a conventional parameterization scheme in which only one parameter is varied at a time. The factors that were varied (range shown in parentheses) included pressure (1-10 atm), temperature (323-423 K), hydrogen content in the fuel (5%-100%), and the water vapor levels in the mixture (0-15%). All atmospheric simulations were performed using nitrogen (air) as diluent, while elevated-pressure mixtures used helium dilution with a dilution ratio 1:7 (O_2:He). The DOE technique generated nine mixtures to be used as input to develop the correlation (shown in Table 7). The equivalence ratio was varied from 0.5-1.0 for each mixture due to its relevance to the gas turbine combustion processes.

To develop the correlation, the steam contaminant levels and percentages of hydrogen in the blends were provided as input. The pressure, temperature, and equivalence ratio dependency of each mixture was modeled through the laminar flame speeds of pure hydrogen at those conditions. The correlation coefficients were then adjusted to closely match the model data using the same surface fit method followed for pure-hydrogen mixtures to finally yield the correlation for HHC syngas,

$$S_{L,u}(\phi, T, p, \lambda, \chi) = [0.5 \exp\ (0.90\lambda) - 0.35 \exp(0.25\chi)]\left(S^{\circ}_{L,H_2}\right)^{1.02} \quad (7)$$

The developed correlation was experimentally verified by Krejci and coworkers for all mixtures except for mixture #3, as the pressure in mixture #3 was kept at 10 atm (as dictated by the DOE matrix) instead of changing it to 1 atm as was used in the experimental procedure [Krejci et al., 2012].

Table 7 DOE-mixtures matrix for the syngas-water mixtures. An excursion of ϕ=0.5-1.0 was done for each mixture, to form the parameter space to develop the syngas correlation (Eqn. (6)).

Mixture	*T (K)*	*P (atm)*	*χ(% by mole)*	*H_2:CO(λ)*
1	323	1	7.5	5:95
2	323	5	0	50:50
3	323	10	15	100:0
4	373	1	0	100:0
5	373	5	15	5:95
6	373	10	7.5	50:50
7	423	1	15	50:50
8	423	5	7.5	100:0
9	423	10	0	5:95

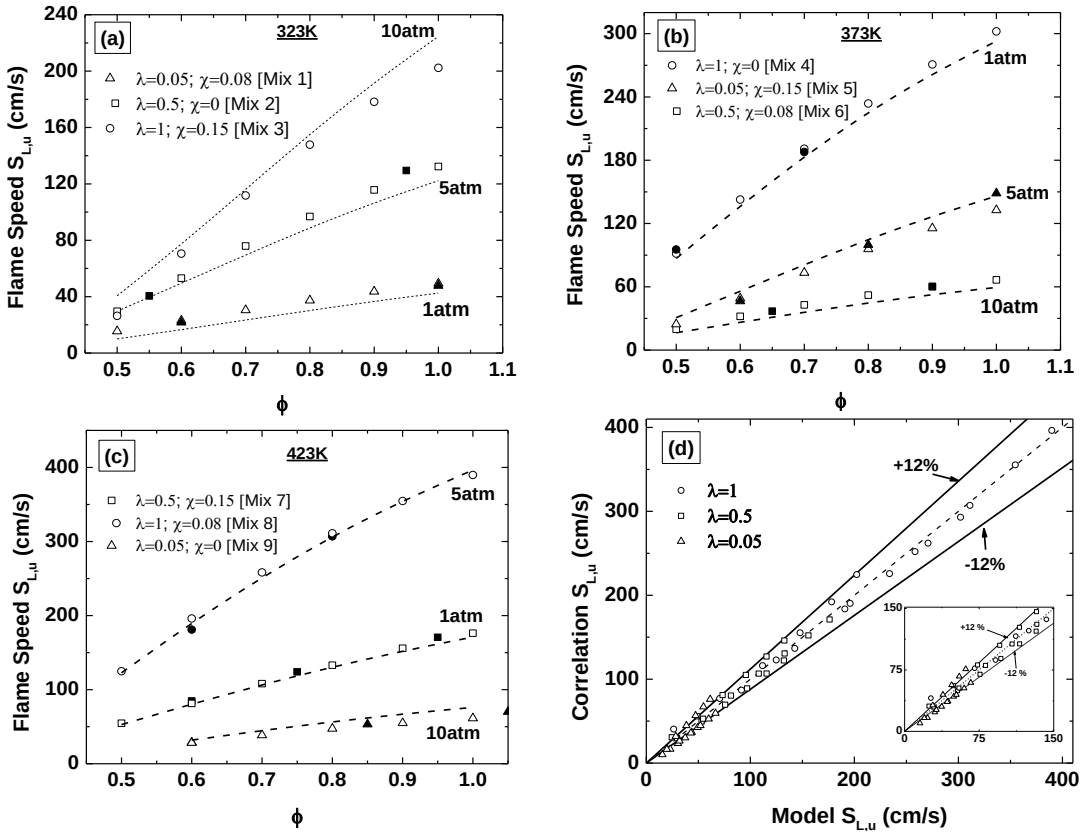

Fig. 14 Correlation predictions (Eqn. (7)) for the syngas mixtures (a-c). Symbols are based on the hydrogen content in the blend. Filled symbols are the experimental data [Krejci et al., 2012], and the open symbols represent the model predictions. The syngas correlation (dashed curves), based on H_2 chemistry only, agree within ± 12% of the kinetics model predictions which include CO chemistry as well (parity plot (d)).

Discussion

Figures 14a-c compare the correlation predictions with the experimental data and the model predictions for the nine syngas blends. As evident from the plots, the matrix has performed a wide excursion of all the parameters, and has significantly reduced the number of simulations required to develop the correlation. Figure 14d compares the model predictions with the

correlation estimates based on the hydrogen content in the fuel (α). The correlation estimates the flame speed within ±12% of the kinetic model prediction for mixtures with λ = 0.5 and 1.0. This trend highlights the strong masking effect of hydrogen on the properties of the blend, further supporting the modeling assumption used to develop the correlation. However, for λ = 0.05 mixtures, the correlations and the model seem to diverge (see inset in Fig. 14d). To extend the correlation to a generic syngas blend of H_2+CO+H_2O with CO concentrations approaching 100%, flame speed correlations for carbon monoxide should be incorporated as well. This additional work is however outside the scope of this study since the objective here is to develop correlations for lean mixtures of HHC blends with typical levels of hydrogen, which are of more interest to the gas turbine manufacturers.

To evaluate the capability of the correlation in modeling the impact of its parameters on the laminar flame speeds, several test cases within the validity range of the correlation were conducted. The primary reason for such an excursion was to assess the ability of the syngas correlation (based on the pure-hydrogen flame speed) to produce the correct behavior for hydrogen contents in between those in the original matrix (Table 8), particularly for cases with H_2 content between 5 and 50%. A DOE approach was used again to widely disperse the test scenarios. Table 8 compares the parameter space of the test case matrix with the one used to develop the correlation. As evident, the test case matrix explores conditions that are within the correlation matrix. Since P, T dependency of the blend was modeled using the pure-fuel relations, wider excursions of these variables, outside the correlation parameter space, but within the range of validity of pure-fuel cases were performed.

Table 8 Syngas parameter space explored using the DOE matrix approach to construct the correlation and the test scenarios.

	Correlation Matrix	**Test Case Matrix**
λ (%H_2 in the fuel mixture)	0.05, 0.5, 0.95	0.15, 0.4, 0.8
χ (% water in the fuel mixture)	0, 0.08, 0.15	0, 0.05, 0.1
P (atm)	1, 5, 10	10, 20, 30
T (K)	323, 373, 423	350, 450, 550
ϕ (GT regime)	0.5-1.0	0.5-1.0

Figures 15a-c show the test cases at various pressures 10, 20 and 30 atm. At each pressure, the blend composition and the unburnt temperature were varied. The correlation estimates agree well with the kinetics model predictions at those conditions (within ±12% as shown in Fig. 15d). These results highlight the fact that the correlation effectively captures the effect of the critical parameters affecting the laminar flame speeds of such syngas mixtures, and that the close agreement demonstrated earlier during the correlation formulation was not a mere consequence of curve-fitting. Thus, the proposed correlation is capable of estimating the flame speeds of lean syngas blends (H_2/CO), containing at least 15% hydrogen content, by using the simple hydrogen mechanism instead of the more complex syngas mechanism. Note that the correlation can still be used for hydrogen contents between 15 and 5%, but at slightly reduced accuracy.

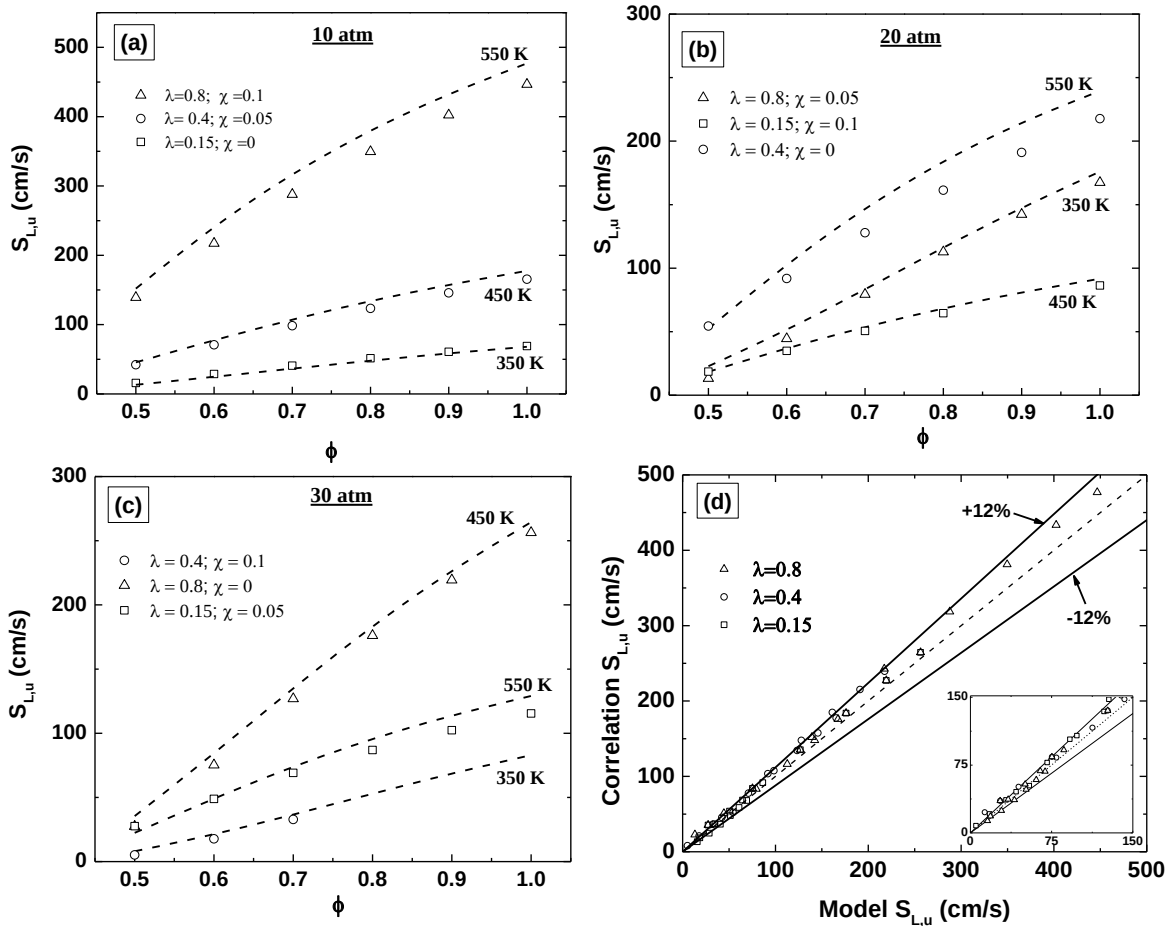

Fig. 15 Test cases (a-c) to verify the syngas correlation (Eqn. (7)). Symbols are based on the hydrogen content in the blend. The open symbols represent the model predictions. The dashed curves represent correlation predictions. The parity plot (d) between the correlation predictions and the model computations show close agreement within ±12%.

LAMINAR FLAME SPEEDS OF BASELINE HYDROGEN AND SYNGAS MIXTURES

The flame speed facility used in this study consists of two constant-volume cylindrical vessels. The first vessel is aerospace-grade aluminum and has an internal diameter of 30.5 cm with optical access using two fused quartz windows about 20 cm in diameter. This vessel is the facility's original flame speed bomb where more details about the vessel can be found in de Vries et al. (2011) and Lowry et al. (2011)0. The other vessel used in this study is a newly developed stainless steel vessel capable of performing experiments at initial temperatures up to 600 K and initial pressures up to 30 atm. The thick-walled vessel has an internal diameter of 31.8 cm and uses a similar optical access setup as the original flame speed facility which is discussed in Krejci et al. (2011).

The layout of the flame speed facility is shown in Fig. 16. Each vessel has its own thermocouple to monitor the initial gas mixture temperature. Each gas mixture is made using the partial-pressure method via 0–1000 Torr and 0–500 psi (34 atm) pressure transducers. Two additional pressure transducers with the same pressure capability are located near the stainless steel vessel to accurately monitor gas pressures at elevated temperatures. The purity of each gas used in this study is ultra-high purity grade, (≥ 99.9% for each primary gas). The filling and venting of gas mixtures are controlled remotely by electro-pneumatic valves. Additionally, the gas mixture is ignited remotely from a separate control room. The ignition consists of an adjustable, constant-current power supply, a 10-μF capacitor, an automotive coil, and a solenoid switch. The spark is created across two sharpened electrodes that are 0.9-mm (0.035 in) diameter Alloy X rods and are set at a variable gap.

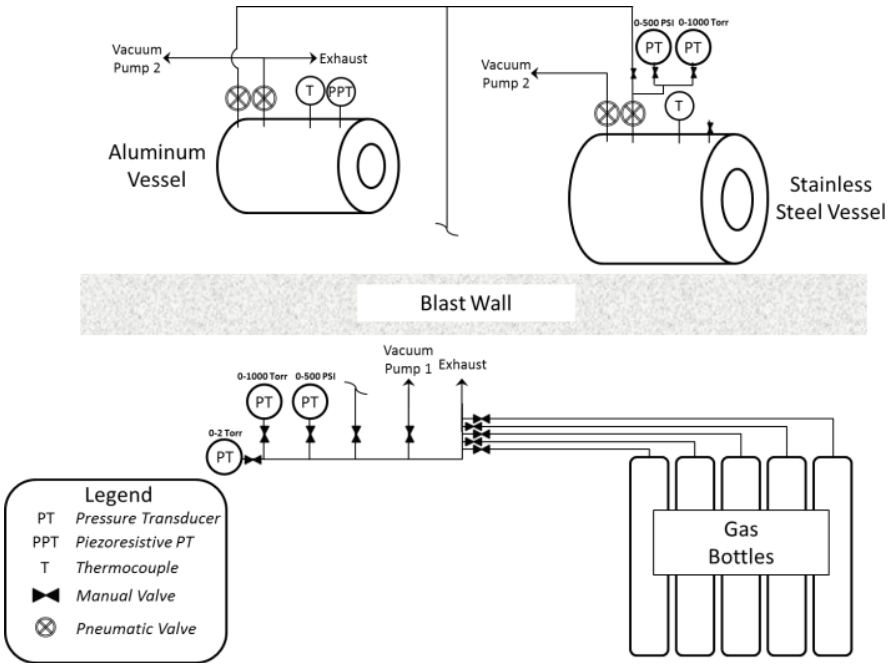

Fig. 16 Layout of the flame speed facility at Texas A&M University.

The experiment is visualized using a Z-type schlieren setup as suggest by Settles (2006)0. A schematic of the general optical setup is shown in Fig. 17. The source of light is generated by a

mercury arc lamp that is passed through a condenser lens before reflecting off the first 15.2 cm, f/8 parabolic mirror. The reflected light is passed through the vessel where it is reflected off a second 15.2-cm, f/8 parabolic mirror towards a high-speed camera. A circular pinhole aperture is used to cut off the light before entering the camera to intensify the density gradients as the flame spherically grows outwardly. The high-speed camera used to capture the event is a Photron FastCam SA 1.1. Example images from this study are shown in Fig. 18 to demonstrate the high quality-picture and the increase of flame instability with increasing pressure.

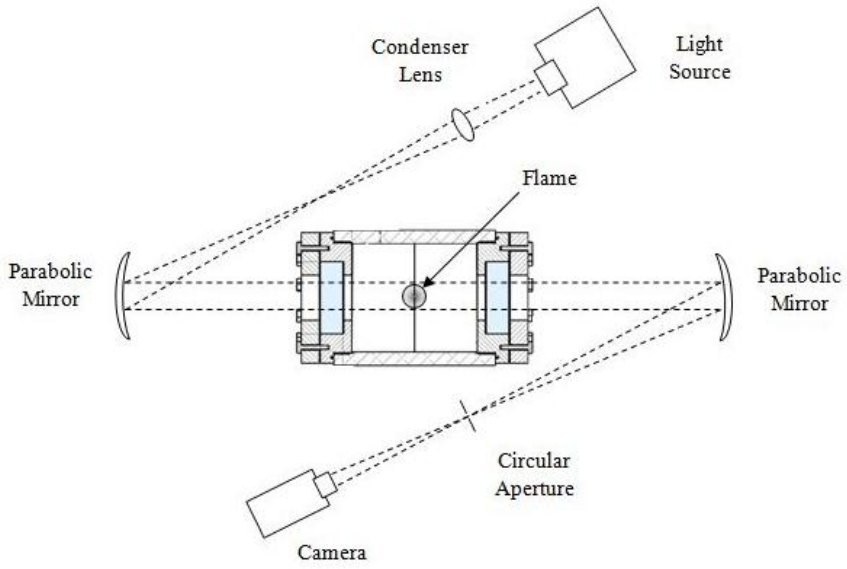

Fig. 17 Optical setup for high-speed schlieren system.

Data Analysis

After each experiment, the high-speed images are post processed using Matlab. A code has been developed and implemented to track the growth of the spherical flame in a similar manner as described by Lowry et al. (2011). Figure 9a shows a sample image of how the contrast of the image is changed so as to locate the outside edge of the flame, and Fig. 9b displays the original flame image with the flame edge detection and the six radial track points used to fit in a Euclidean circle algorithm.

The instantaneous flame radius given by the image post processing is analyzed using the linear relationship given by Eqns. 8-10 [Markstein, 1964; Dowdy et al., 1990; Brown et al., 1996].

$$S_b = S_b^o - L_{m,b}\alpha \tag{8}$$

Where S_b is the burned, stretched flame speed, S_b^o is the burned, un-stretched flame speed, $L_{m,b}$ is the burned Markstein Length and α is the flame stretch defined by

$$\alpha = \frac{1}{A}\frac{dA}{dt} = \frac{1}{4\pi R^2}\frac{d(4\pi R^2)}{dt} = \frac{2}{R}\frac{dR}{dt} \tag{9}$$

Equation 9 can be substituted into Eqn. 8 and integrated to result in Eqn. 10.

$$R = S_b^o \, t - 2L_{m,b} \, ln \, (R) + const \tag{10}$$

Where R is the instantaneous flame radius, and t is the corresponding time. Then the un-stretched flame speed and Markstein Length are obtained by using linear regression. The un-burned, un-stretched flame speed $S_{L,u}^o$ and Markstein Length $L_{m,u}$ are calculated by divided their respective burned values by the density ratio across the flame given by Eqn. 11.

$$\sigma = \frac{\rho_u}{\rho_b} \tag{11}$$

The density ratio is calculated using the authors' chemical kinetics model in Chemkin, using the STANJAN module [Reynolds, 1986].

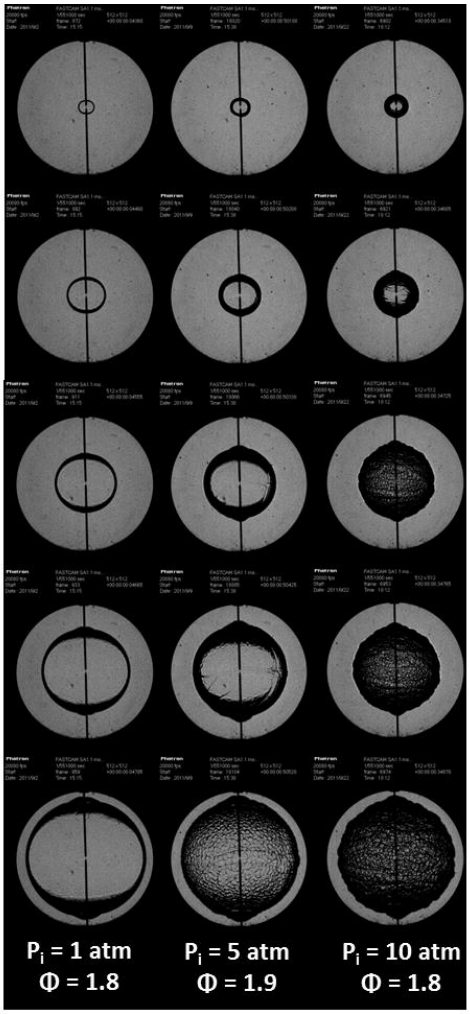

Fig. 18 Flame images for 1-atm (left), 5-atm (middle), and 10-atm (right) 50:50 H_2:CO. The oxidizer for the atmospheric experiment is air, while the oxidizer for the 5 and 10-atm experiments is 7:1 He:O_2.

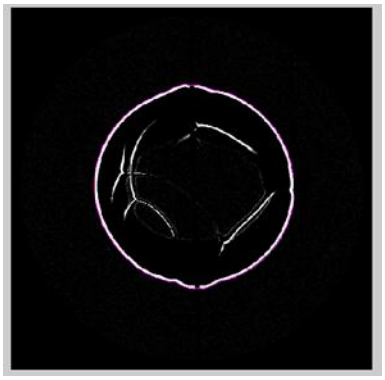

(a)

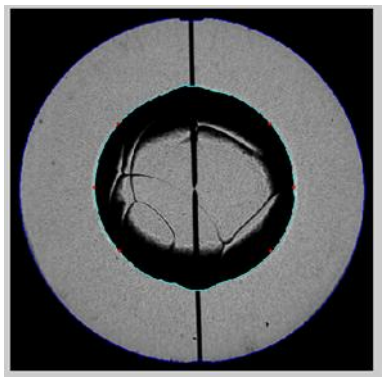

(b)

Fig. 19 Images from the flame detection program. (a) The contrast of the image is changed to locate the edge of the flame (b) The original image is shown with the edge detection.

Uncertainty Analysis

A brief overview of the uncertainty analysis is provided to demonstrate the repeatability for the experiments performed within this study. Systematic and random uncertainties were taken into account using the methods shown by Moffat (1988). The total experimental uncertainty, U_{S_L}, is given by Eqn. 12.

$$U_{S_L} = \sqrt{B_{S_L}^2 + \left(\frac{t_{M-1,95} S_{S_L}}{\sqrt{M}}\right)^2} \tag{12}$$

Where B_{S_L} is the total bias uncertainty, $t_{M-1,95}$ is the student *t* value at a 95% confidence interval and $M-1$ degrees of freedom, S_{S_L} is the standard deviation of repeated experiments, and M is the number of repeated experiments per condition. The total bias uncertainty, shown by Eqn. 13, includes u_i, the fixed error for each variable x_i, and S_L, the relationship between the flame speed and each variable x_i.

$$B_{S_L} = \sqrt{\sum_{i=1}^{n} \left(\frac{\partial S_L(x_i)}{\partial x_i} u_i\right)^2} \tag{13}$$

A relationship between each independent variable and the flame speed must be known to use this definition of the total bias uncertainty. A correlation is developed similar to that shown in Lowry et al. (2011)0. Table 9 and Fig. 20 show a characteristic data set of the uncertainty analysis. The total uncertainty percentage demonstrates good predictability of the data.

Table 9 Atmospheric hydrogen flame speed uncertainty.

ϕ	$S^0_{L,u}$ (cm/s)	U_{SL} (cm/s)	%
0.5	67.2	7.1	10.6
0.6	96.5	7.3	7.6
0.7	124.4	7.3	5.9
0.8	169.9	7.2	4.2
0.9	194.0	6.9	3.6
1.0	218.0	7.2	3.3
1.1	236.7	7.1	3.0
1.2	254.9	7.3	2.8
1.3	267.4	7.4	2.8
1.4	275.0	7.2	2.6
1.5	280.3	7.1	2.5
1.6	282.8	7.2	2.5
1.7	283.8	7.4	2.6
1.8	282.9	7.2	2.5
1.9	280.3	7.1	2.5
2.0	278.9	6.9	2.5
2.5	249.1	6.9	2.8
3.0	217.4	6.9	3.2
3.5	187.6	6.9	3.7
4.0	158.7	6.9	4.4
4.5	133.0	6.9	5.2
5.0	110.1	6.9	6.3

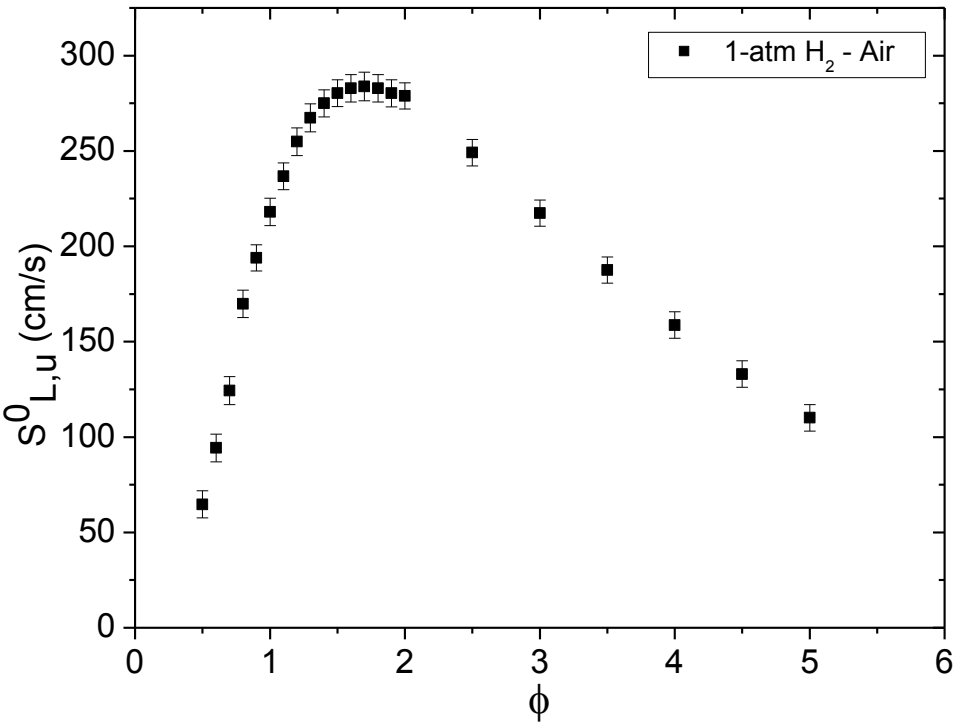

Fig. 20 Atmospheric hydrogen flame speed data with calculated uncertainty bars shown.

Computational Method

The detailed chemical kinetic mechanism utilized in this work is under constant development and optimization at the Combustion Chemistry Centre (NUI Galway). The $H_2/CO/O_2$ sub mechanism is based on the work of Ó Conaire et al. (2004) with several significant updates based on recent experimental and kinetic data. The changes are partially described in Kéromnès et al. (2011)0 and will be fully detailed in an upcoming publication.

Flame speed simulations were performed with the Premix module of Chemkin Pro (2010) using the multi-component transport equations. Solutions were converged to over 1000 grid points to essentially provide grid independent solutions. Shock-tube ignition delay simulations (see Tasks 4 and 6) were performed with the Aurora module assuming constant volume and constant energy conditions. Ignition delay time was defined as the time OH* reached 5% of its predicted maximum concentration. This definition essentially locates the onset of ignition, replicating well the experimental definition.

Results

This study includes experimental data from two gas dynamic experimental devices: constant-volume cylindrical bomb and high-pressure shock tube (see Tasks 4-6). The mixture compositions performed in the cylindrical bomb include hydrogen diluted with air at atmosphere pressure and three initial temperatures, hydrogen diluted with helium at two elevated pressures

and three temperatures, 50:50 H_2:CO diluted with air at 1 atm, and 50:50 H_2:CO diluted with helium at elevated pressures. For all elevated-pressure experiments, the oxidizer ratio was adjusted to a 7:1 He:O_2 ratio in order to increase the Lewis number of the mixtures and minimize hydrodynamic instabilities. Additionally, all initial temperatures have an uncertainty of ±3 K. Tables A1–A4 in the appendix provide the experimental results for all the conditions studied. Table 10 provides more details about the mixture compositions performed in this study for the laminar flame speeds.

Table 10 Experimental conditions for the cylindrical bomb measuring laminar flame speed.

H_2:CO	Temperature (K)	Pressure (atm)
100:0	298	1
		5
		10
	373	1
		5
	443	1
		5
50:50	298	1
		5
		10

Hydrogen. Figure 21 demonstrates an extensive literature comparison for atmospheric hydrogen-air at room temperature between the data herein and the experimental work done by Egolfopoulos and Law (1990); Vagelopoulos et al. (1994)0; Aung et al. (1997); Tse et al. (2000); Kwon and Faeth (2001)0; Lamoureux et al. (2003); Dahoe (2005); Verhelst et al. (2005)0; Burke et al. (2009)0; and Pareja et al. (2010). Since the H_2-O_2 chemical kinetic system has been well studied for the past few decades, it is expected that the agreement would be quite well between the data herein and previously published data, as shown in Fig. 21. However, unified agreement begins to dissipate at an equivalence ratio of about 1.0 and above. Additionally, when Fig. 21 is magnified to equivalence ratios below 1.0, as shown in Fig. 22, a potentially large variance exists amongst published flame speed data in a regime that typically has a distribution of about ±2 cm/s, such as the flame speed of methane-air 0Lowry et al., 2011]. The model exhibits excellent agreement with the new data of this study, reproducing it across the complete range of equivalence ratios. The model appears to slightly under predict the peak flame speed but is well within the experimental error bars depicted in Fig. 20.

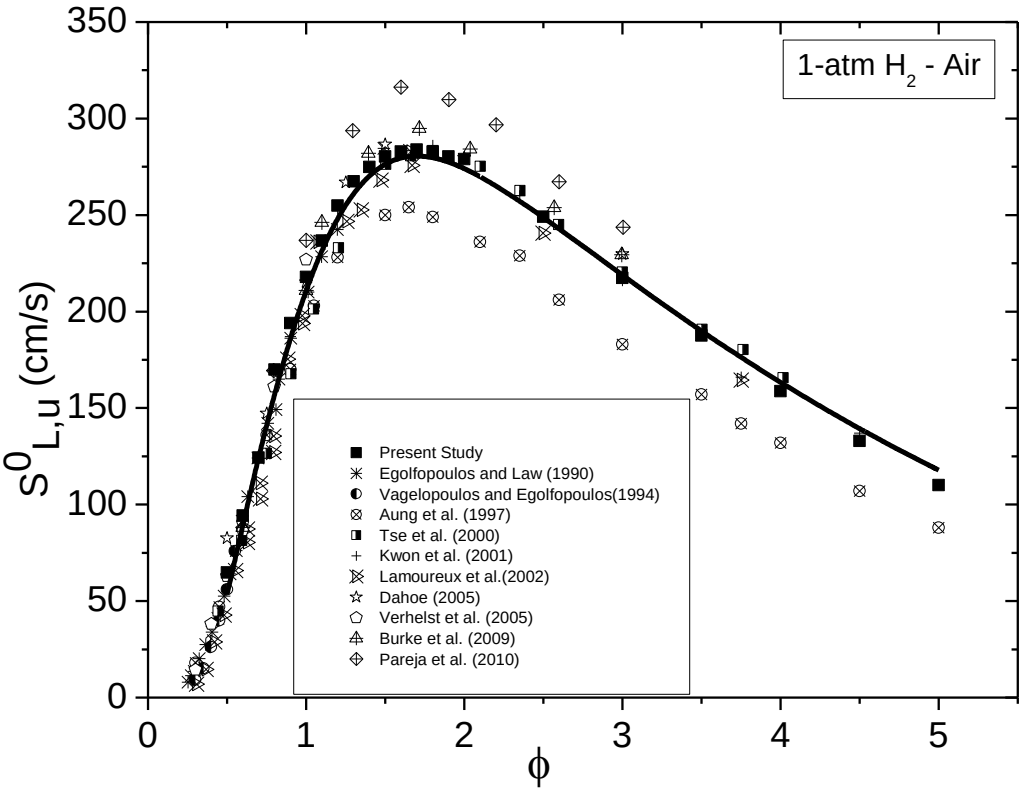

Fig. 21 Atmospheric hydrogen-air literature comparison to the data herein and the chemical kinetics model at standard temperature.

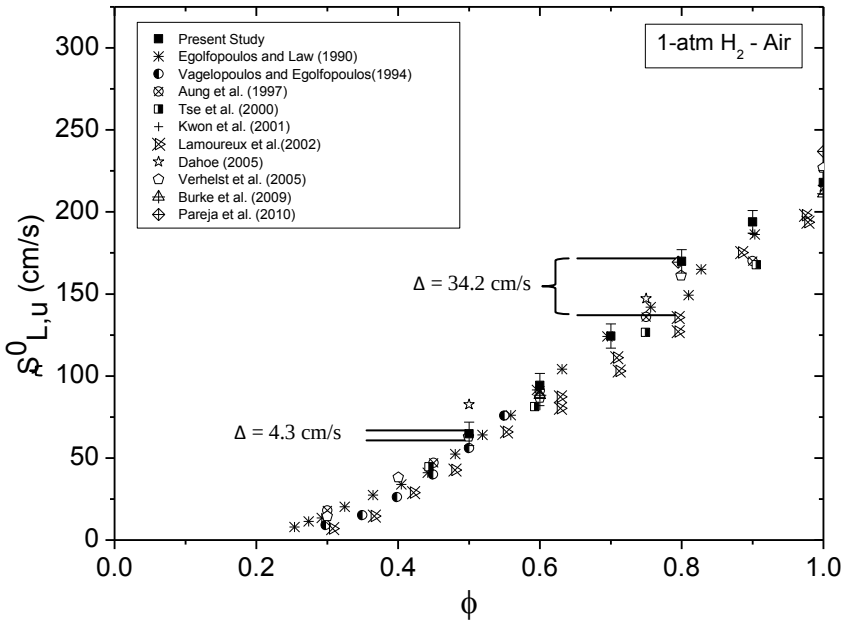

Fig. 22 Atmospheric hydrogen-air at equivalence ratios less than 1.0 demonstrating the increased distribution of laminar flame speed data.

Figure 23 explores the effects of pressure on hydrogen diluted with 7:1 $He:O_2$. With limited literature available at these pressures, this plot shows good agreement between the experimental data herein and data from Tse et al. (2000) at 5 atm. The model agrees quite well the 5 atm data obtained in this study, particularly under lean conditions and richer conditions ($\phi \geq 2$). However, the peak flame speed is underpredicted, with the model reproducing the existing data more accurately. The agreement deteriorates slightly with increasing pressure, with the model predicting a larger inhibiting effect of pressure than experimentally measured at an equivalence ratio around 1.5. Once again, the agreement at richer conditions is excellent.

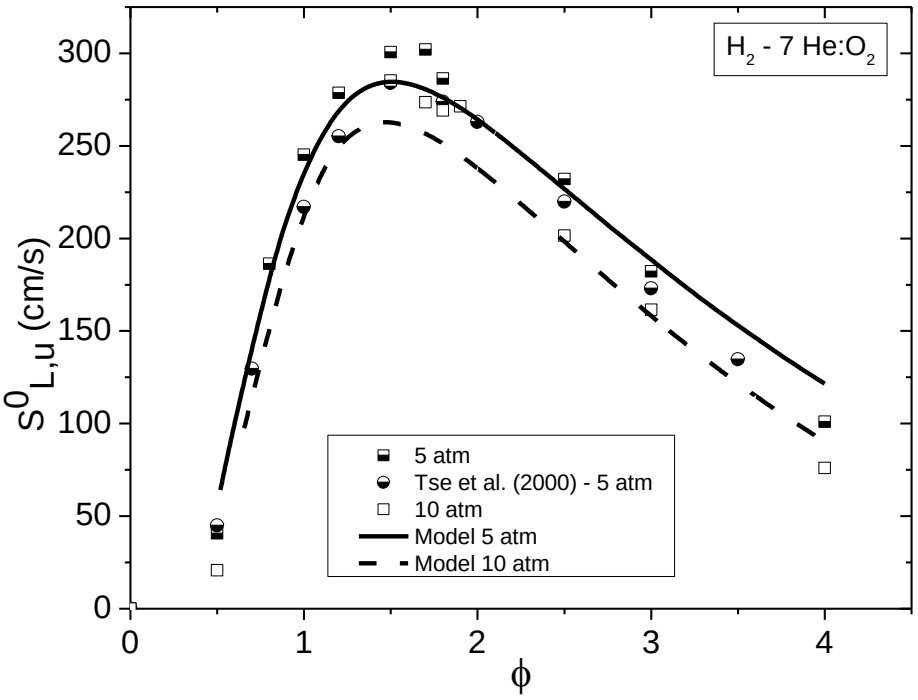

Fig. 23 Hydrogen diluted with $7He:O_2$ at 5 and 10 atm compared with the chemical kinetics model and data from Tse et al. (2000).

Figures 24 and 25 show the influence of initial pressures at elevated temperatures on the laminar flame speed. Hu et al. (2009) demonstrate excellent agreement for atmospheric hydrogen at elevated temperatures up to 443 K. Model agreement at 1 and 5 atm and elevated temperatures is excellent across the complete range of equivalence ratios.

Syngas. Figures 26 and 27 provide a baseline set of data for a common syngas (model) mixture with a 50:50 H_2/CO composition. The atmospheric syngas data herein, shown in Fig. 26, is compared with previously published data from McLean et al. (1994); Hassan et al. (1997); Sun et al. (2007); Natarajan et al. (2005); Burke et al. (2007); Prathap et al. (2008); Dong et al. (2009); and Bouvet et al. (2011). These data show a similar trend in agreement as seen with atmospheric hydrogen, where good agreement exists on the fuel-lean side, and discrepancies increase as the mixture becomes fuel rich. Once again, the model agreement with the data obtained in this study is excellent, with only minor disparities arising at high equivalence ratios.

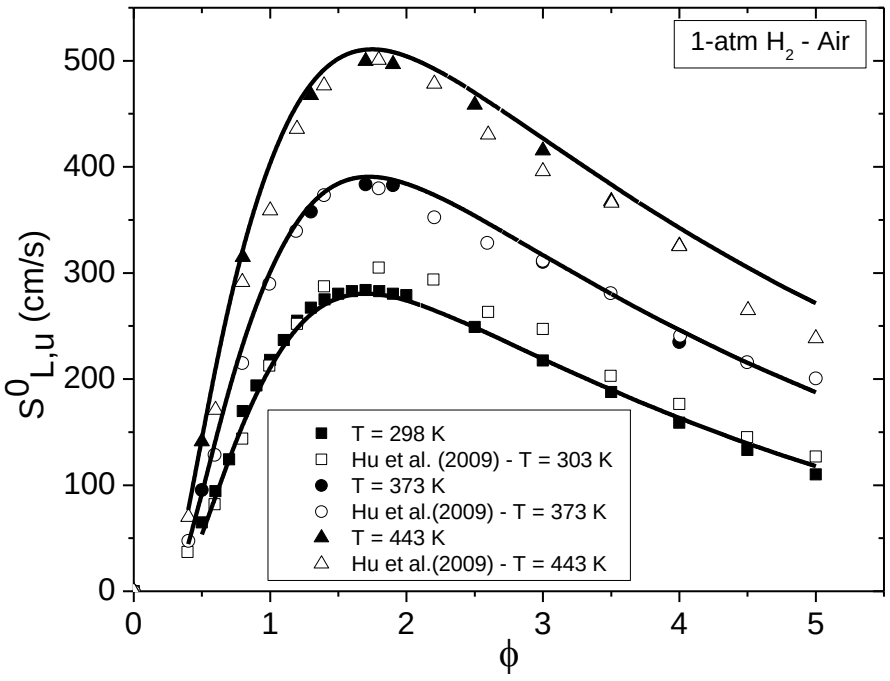

Fig. 24 Comparison of atmospheric hydrogen-air data herein, data from Hu et al. (2009), and the chemical kinetics model at elevated temperatures.

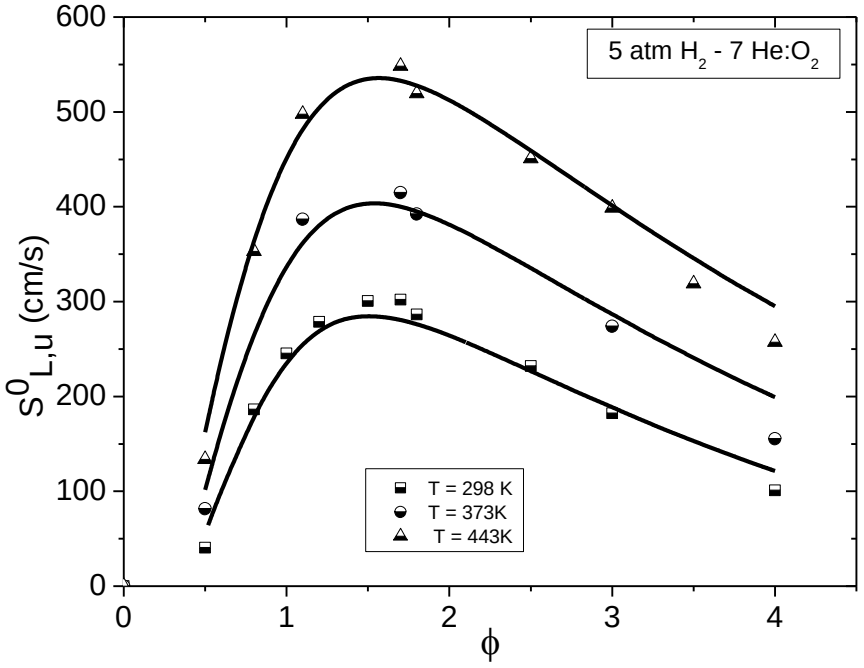

Fig. 25 Laminar flame speed of hydrogen diluted with 7:1 $He:O_2$ at 5 atm and elevated temperatures compared to the chemical kinetics model.

At elevated pressures, the 50:50 H_2:CO data herein are compared with Sun et al. (2007) and Natarajan et al. (2009) in Fig. 27. Overall agreement at both pressures is quite good. There are

some discrepancies around the peak flame speed at 10 atm which is under further investigation. This disagreement is also highlighted by the model, which predicts considerably lower reactivity at the elevated pressures, while reproducing the 5 atm data quite well.

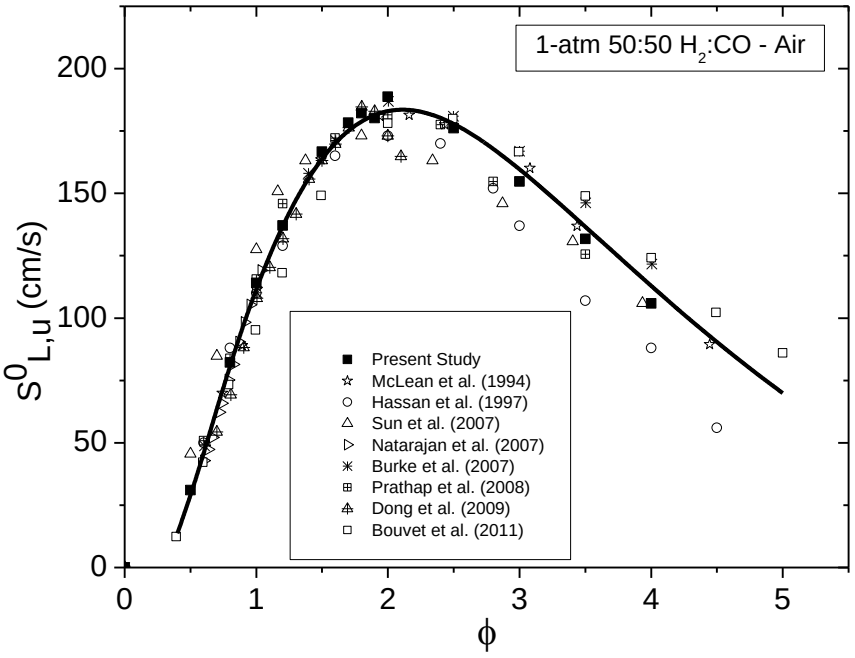

Fig. 26 Literature comparison of atmospheric 50:50 H_2:CO-Air with the data herein and the chemical kinetics model.

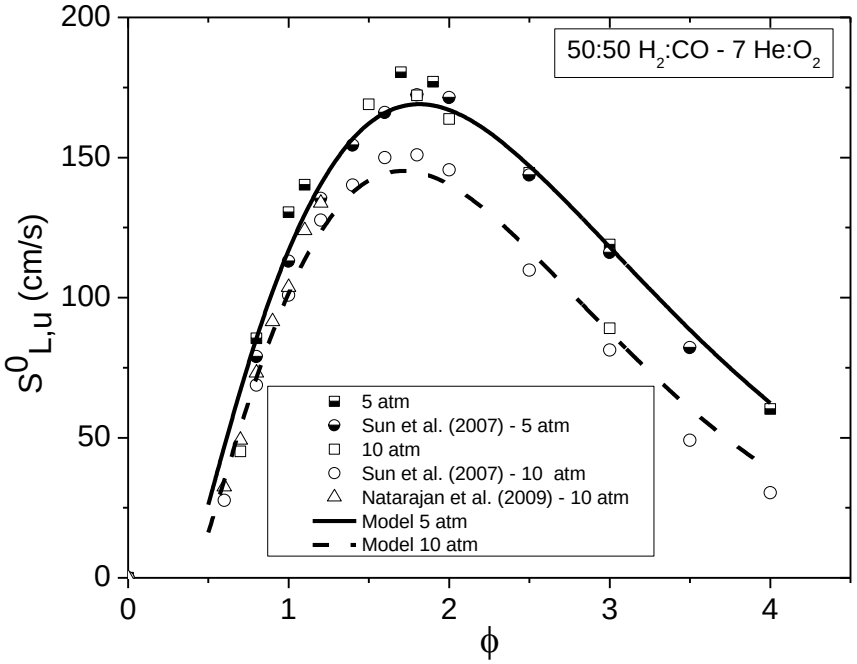

Fig. 27 Comparison of 5- and 10-atm 50:50 H_2:CO diluted with 7:1 He:O_2 with literature data and the chemical kinetics model.

SYNGAS FLAME SPEEDS WITH WATER ADDITION

Task 3 provided new data for nine mixtures that vary the concentration of carbon monoxide, hydrogen, and steam dilution at different initial pressures and temperatures over a wide range. In doing so, the target mixtures and conditions were selected using a Design-of-Experiments (DOE) approach so as to cover as comprehensive of a range as possible in an efficient manner. An updated chemical kinetics model is compared to the new data, and conclusions are drawn on the most influential factors on the laminar flame speed, mass burning rate, and the Markstein length. An overview of the experiments and results is provided below.

Experiment Approach and Design of the Experiment

This study investigated how the laminar flame speed is affected over a wide range of experimental conditions that are relevant to syngas fuel blends. Ideally, the experiments should be conducted over as wide of a range as possible of equivalence ratios (ϕ) for several syngas blends of H_2 and CO with varying levels of steam (0 – 15% by volume), initial pressure (1 – 10 atm), and initial temperature (323 – 423 K). The desired experimental conditions derived from these parameters are highly uncommon based on the available literature, lending to the significance of the experimental results presented herein. A DOE methodology was determined as the most efficient way to explore the entire range of variables shown in Table 11. Each factor was given three levels to provide greater detail over the range. Conditions relevant to gas turbine operating conditions set the overall ranges of the factors, while the specific levels were selected based on the capability of the experimental facility. Some consideration was also given to ensure some overlap with available data from the literature, for comparison.

Table 11 Four variables, each with three corresponding levels for the syngas experiments herein. The water dilution is on a mole percent of the total fuel mixture, including the H_2O.

Variable	***Level (1,2,3)***
Temperature (K)	323, 373, 423
Pressure (atm)	1, 5, 10
H_2O Dilution (% mole)	0, 7.5, 15
Syngas Comp. (H_2:CO)	5:95, 50:50, 100:0

With four factors at three levels, a full-factorial matrix would require an overwhelming 81 conditions to perform over the range of equivalence ratios between the lean and rich limits, resulting in over 1,000 total experiments without repeats. A DOE approach significantly reduces the required number of conditions while still covering the desired parameter space. To this end, a Taguchi L9 matrix was applied to the four experimental factors, reducing the number of experimental conditions to a total of nine.

This reduced matrix still allows for a comprehensive study over the entire range of parameters from fuel-lean to fuel-rich conditions without compromising the significance of the results. Applying the nomenclature of the L9 matrix to the factor levels in Table 11 provides the appropriate combinations for each factor and establishes the target test matrix listed as Table 12.

The steam dilution, $\chi = [X_{H2O}/(X_{H2}+X_{CO}+X_{H2O})]\times 100\%$, is defined as the mole percentage of the fuel mixture, and "X" denotes the mole fraction for each species in the fuel mixture. All nine conditions shown in the test matrix were tested over a full excursion of fuel-to-oxidizer equivalence ratios (~0.7-5.0) to obtain the experimental flame speed envelope. Note that the pressure had to be changed for experiment 3 from 10 atm to 1 atm due to the limitation of the water vapor pressure at the required water dilution level. Approximately 11 to 13 different equivalence ratios were tested at each condition in the test matrix, with the majority conducted around the peak flame speed value for greater resolution on the trend.

Table 12 Laminar flame speed matrix with 9 blends using four factors (Temperature (*T*), Pressure (*P*), Steam Dilution (χ), and Syngas Composition (H_2:*CO*)) at three levels.

Exp.	*T (K)*	*P (atm)*	*χ (% by mole)*	*H_2:CO*
1	323	1	7.5	5:95
2	323	5	0	50:50
3*	323	1	15	100:0
4	373	1	0	100:0
5	373	5	15	5:95
6	373	10	7.5	50:50
7	423	1	15	50:50
8	423	5	7.5	100:0
9	423	10	0	5:95

*Pressure should be 10 atm but changed to 1 atm due to high steam concentration

Kinetics Model

The detailed chemical kinetic mechanism utilized in this work is under constant development and optimization at the Combustion Chemistry Centre at the National University of Ireland Galway. The $H_2/CO/O_2$ mechanism is based on the work of Ó Conaire et al. (2004) with several significant updates based on recent experimental and kinetic data. The changes are partially described in Kéromnès et al. (2011). Flame speed simulations were performed with the Premix module of Chemkin Pro using the multi-component transport equations. Solutions were converged to approximately 1,000 grid points to provide grid-independent solutions.

Results

The results are shown graphically in the following paragraphs. Figure A and Fig. B show the un-burned, laminar flame speed as a function of equivalence ratio of the data herein compared to previously published data. It is important to validate moist mixtures to demonstrate the accuracy of the chosen method of introducing steam into each mixture. The data in these two figures are shown with experimental error bars demonstrating the relative uncertainty of the laminar flame speed measurements. The relative uncertainty is similar for the other figures presented thereafter but are not shown to better display the data trends. Figure A compares atmospheric 5:95 H_2:CO diluted with 7.5% steam at 323 K data to the data of Das et al. (2011) and the chemical kinetics model. The two experimental data sets show good agreement, within 2 cm/s, while the model also exhibits excellent predictive behavior at these fuel-lean conditions. Another validation plot is shown in Fig. B, where the focus is to demonstrate the elevated-temperature operational capability of the facility with a dry hydrogen-air mixture at one atmosphere. The data herein

agree well with both Hu et al. (2009) and the chemical kinetics model. It is also worthy to note that the peak flame speed is about 35% faster at 373 K than at 298 K, which indicates that the framing rate of the high-speed camera must be adjusted to capture the combustion event as temperature is increased above room temperature.

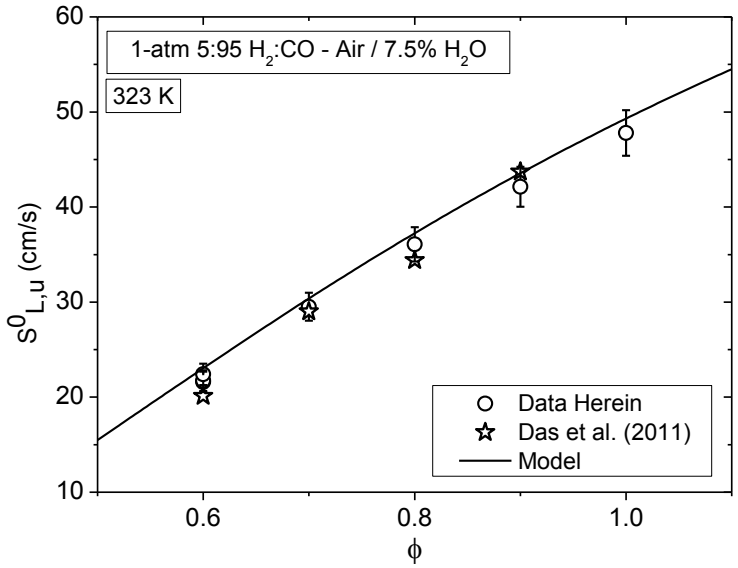

Fig. A Laminar flame speed for atmospheric 5:95 H_2:CO diluted with 7.5% H_2O at 323 K (Exp. 1 in Table 12) compared to data herein, the data of Das et al. (2011), and the chemical kinetics model.

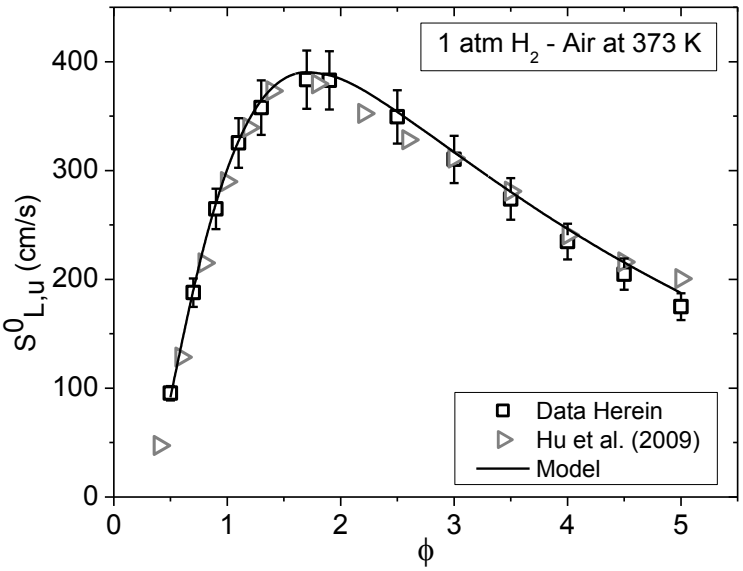

Fig. B Laminar flame speed for atmospheric 100:0 H_2:CO diluted with 0% H_2O at 373 K (Exp. 4 in Table 12) compared to the data herein, the data of Hu et al. (2009), and the chemical kinetics model.

For an initial preheat temperature of 323 K, Fig. 28 shows new laminar flame speed experimental data for the three syngas mixtures with different dilutions of steam at initial pressures of 1 and 5 atm (i.e., experiments 1, 2, and 3 in Table 12). From an equivalence ratio over the range of about 0.5 to 5.0, a distinct trend can be noticed where the peak flame speed appears shift to the fuel-rich end due mostly to the increased concentration of carbon monoxide. Typically, an increase in the initial pressure will shift the peak flame speed to the left, while an increase in carbon monoxide content will shift the peak to the right and broaden the flame speed "dome". The broadening of the flame speed "dome" physically represents the laminar flame speed becoming less influenced by the equivalence ratio as the carbon monoxide concentration is increased. This phenomenon is also shown in Sun et al. (2007) and is further addressed in the Discussion section below. The addition of steam appears to play only a small role in adjusting the peak flame speed at different equivalence ratios; rather, it slows the chemical kinetics of the combustible mixtures and decreases the flame speed. This effect of water addition on the chemical kinetics is discussed in a later section. The chemical kinetics model demonstrates good predictive behavior overall with discrepancies arising around the peak flame speed and as pressure is increased.

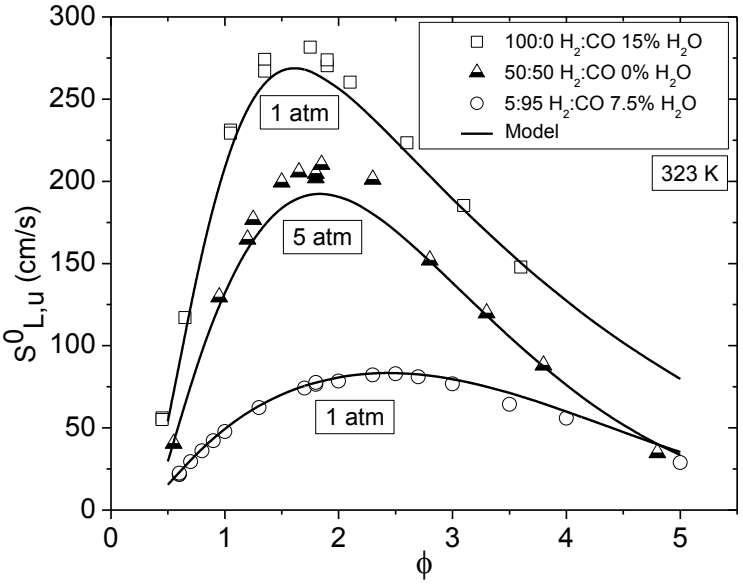

Fig. 28 Laminar flame speed for the three syngas compositions at 1 and 5 atm each at different steam dilutions initially heated to 323 K compared to the chemical kinetics model (Exps. 1, 2, and 3 in Table 12). Lines represent the model predictions for each mixture.

Figure 29 shows the laminar flame speed results for the middle initial temperature factor, 373 K (experiments 4, 5, and 6 in Table 12). This set of data demonstrates similar trends seen with Fig. 28 where an increase in the carbon monoxide concentration has a strong influence reducing the flame speed. Also the model shows good agreement over the entire range of equivalence ratios at one atmosphere but as the pressure increases up to 10 atm, the model fails to completely capture the trend around the peak.

How the laminar flame speed changes at an initial temperature of 423 K for the final three DOE conditions (experiments 7, 8, and 9 in Table 12) is shown in Fig. 30. The continual broadening of

the flame speed "dome" is still apparent with increasing carbon monoxide concentration at this elevated temperature. From analyzing the three presented plots, it can be theorized that the syngas composition has a strong influence on the laminar flame speed regardless of how the other parameters--temperature, pressure, and water dilution--are being varied at the same time. The chemical kinetics model continues to perform well with increasing temperature at low pressures, but struggles predicting the peak region and the extreme fuel-rich region as pressure increases above 5 atm.

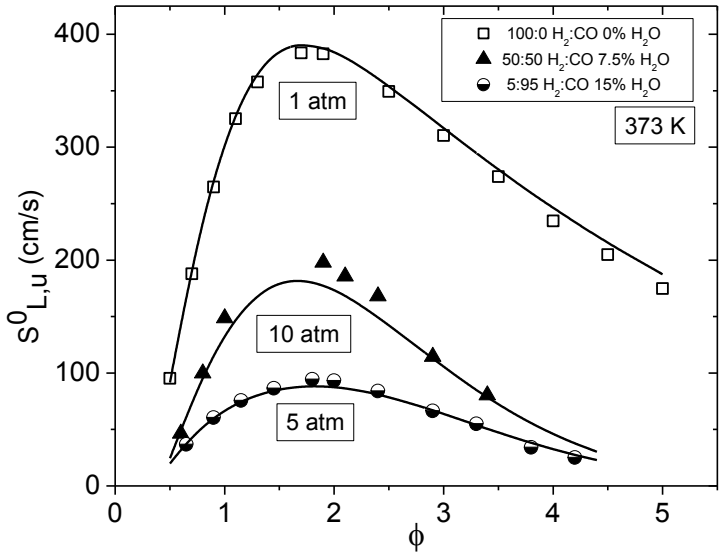

Fig. 29 Laminar flame speed for three syngas compositions at 1, 5, and 10 atm each at different steam dilutions initially heated to 373 K compared to the chemical kinetics model (Exp. 4, 5, and 6 in Table 12).

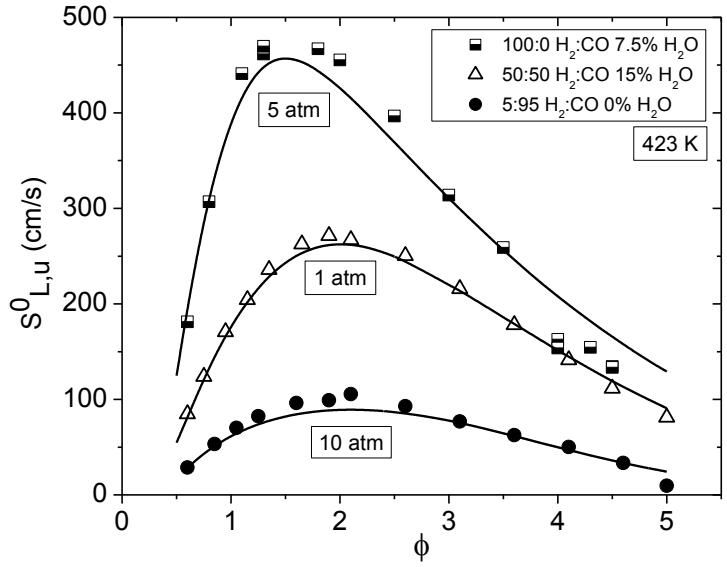

Fig. 30 Laminar flame speed for three syngas compositions at 1, 5, and 10 atm each at different steam dilutions initially heated to 423 K compared to the kinetics model (Exps. 7, 8, and 9 in Table 12).

Discussion

The DOE approach provides the capability to demonstrate the most influential factor(s) on the experiment. By following the parameter analysis outlined in Ross (2000), a performance sensitivity analysis was conducted for the laminar flame speed, mass burning flux, and the Markstein length. The mass burning flux, m^0, is equal to the laminar flame speed times the un-burned density. This parameter is a more-direct representation of the rate of the overall chemical reaction. The performance sensitivity calculation for each factor and equivalence ratio is the maximum difference between the averaged parameter value (i.e. laminar flame speed) at each DOE level (i.e. 1, 2, or 3). The performance sensitivity results help to explain the experimental data trends. Figure 31 shows the results of the analysis, where it is clear that the H_2:CO ratio of the syngas blend is by far the dominant effect on laminar flame speed over the range of conditions and mixtures explored.

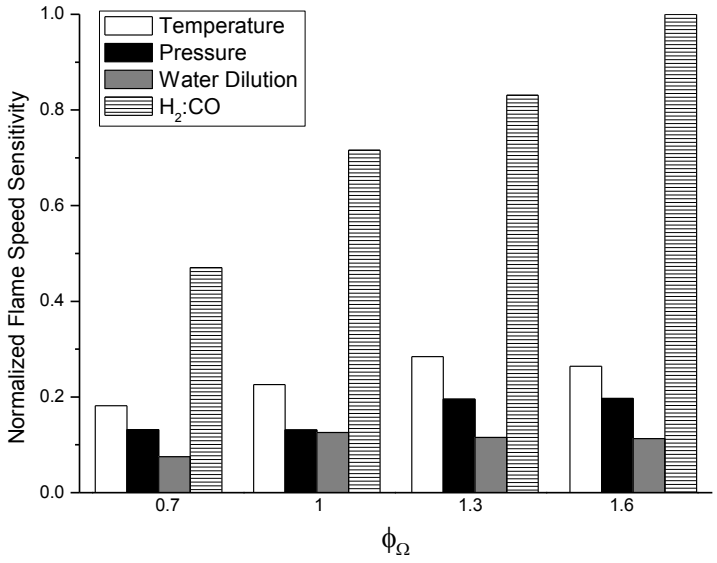

Fig. 31 Normalized flame speed sensitivity between the four factors studied (temperature, pressure, water dilution, and H_2:CO) at four oxygen equivalence ratios from fuel-lean to fuel-rich.

Based on the excellent behavior of the model when compared to the experimental data over the comprehensive range of conditions explored herein, the model can be used with confidence to study further the impact of water dilution on the laminar flame speed of syngas mixtures. Two mixtures featuring extreme H_2:CO dilutions were used to calculate laminar flame speed values at an equivalence ratio of 0.5, which is of relevance to the gas turbine industry. Figure 32 and Fig. 33 show the flame speed versus percent water dilution for temperatures of 323 and 423 K, respectively. For mixtures with higher concentrations of carbon monoxide (i.e., 5:95 H_2:CO), the water concentration has a small kinetic effect on the laminar flame speed. A slight increase in flame speed is seen for higher moisture concentrations at both of the temperatures at 1 atm and a subtle decrease in flame speed at 10 atm. As the concentration of CO in the fuel blend is reduced (i.e., 95:5 H_2:CO), the water has a much larger effect on the laminar flame speed; in fact, the presence of water has a negative effect on the flame speed. These results are similar to the trends presented by Das et al. (2011).

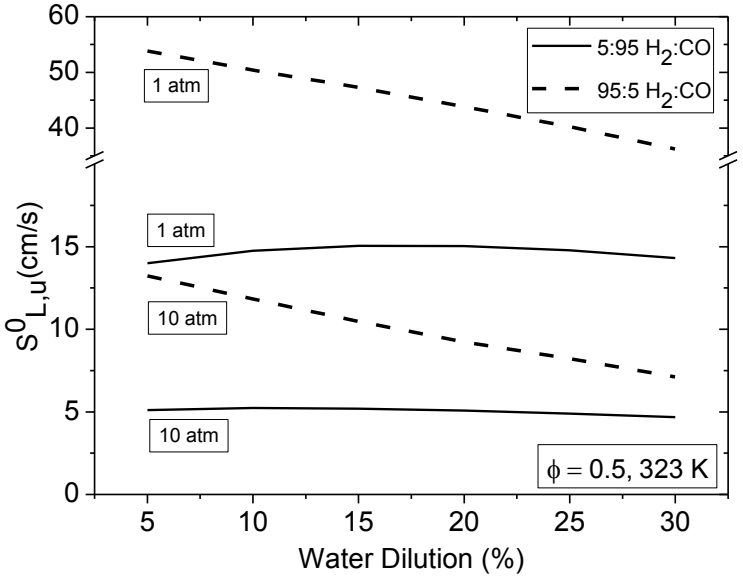

Fig. 32 Effect of water dilution on the laminar flame speed for 5:95 H_2:CO and 95:5 H_2:CO mixtures with air at 323 K and $\phi = 0.5$.

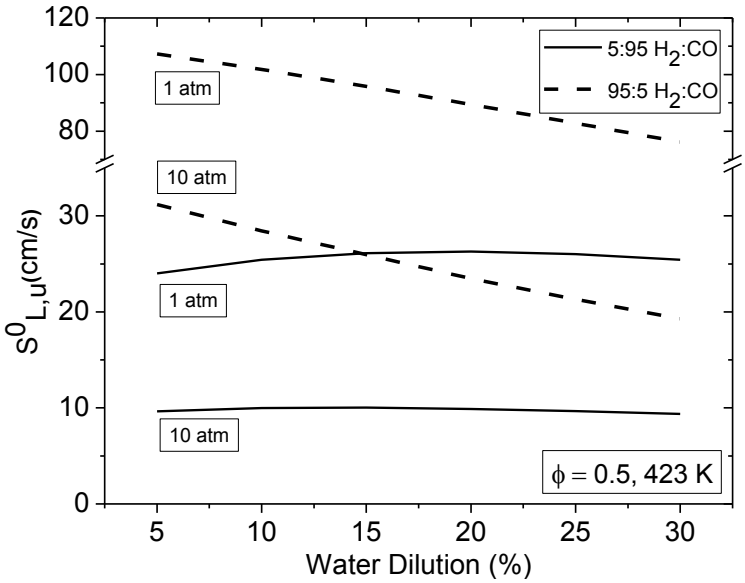

Fig. 33 Effect of water dilution on the laminar flame speed for 5:95 H_2:CO and 95:5 H_2:CO with air mixtures at 423 K and $\phi = 0.5$.

A reaction rate sensitivity analysis was performed using Chemkin Pro to explain the kinetic effect of water dilution at one atmosphere depicted in Fig. 32 and Fig. 33. The analysis was performed on the atmospheric mixtures at zero and 15% water dilution. Prior to analyzing the sensitivity results, it is necessary to decouple the thermal and chemical effects of water dilution. This separation was performed by diluting the mixture with a 'dummy' species (with identical thermochemistry as water) instead of water, thus reproducing the thermal effect of water, while excluding any chemical interactions.

N_2O KINETICS IN HIGH-H_2 MIXTURES

Interactions between hydrocarbons and NO during combustion have been investigated in various systems, and studies showed a promoting effect of small additions of NO on hydrocarbon combustion [Slack and Grillo, 1981; Faravelli et al., 2003; Dagaut et al., 2005; Sivaramakrishnan et al., 2007; Javoy et al., 2009]. According to Javoy *et al.* (2009), nitrous oxide can contribute significantly to the NO formation in high-pressure flames or under fuel lean conditions at low flame temperatures. Nitrous oxide is also a major, intermediate oxidizing species formed during the combustion of many solid propellants. As mentioned by Hong *et al.* (2011), the H_2/O_2 sub-mechanism is critical for the combustion of hydrocarbons because it contains many important elementary reactions involving radicals (H, O, OH, HO_2) that play a great role at every stage of the hydrocarbon oxidation process. From these fundamental perspectives, it is therefore clear that the understanding of the interactions between N_2O and the H_2/O_2 system is important. Ignition delay times (τ_{ign}) of N_2O-H_2-diluent mixtures have been studied in numerous works. A detailed summary is provided in Mathieu et al. (2012).

Hence, to make a significant contribution to the set of data on H_2/N_2O and to produce data for further validation of the NOx submechansim, the aim of this study was to acquire ignition delay times from $H_2/O_2/N_2O$ mixtures in dilute conditions using a shock tube for pressures up to around 32 atm. Experiments were conducted for mixtures of 1% H_2/1% O_2 into Ar (equivalence ratio (Φ) = 0.5) seeded with various amount of N_2O (100, 400, 1600, and 3200 ppm). Ignition delay time measurements were taken at the sidewall location, and results were compared to some recent measurements obtained under the same conditions with a neat 0.01 H_2/0.01 O_2/0.98 Ar mixture. Only one equivalence ratio was investigated during the present study since preliminary calculations and the recent experimental literature with H_2 or H_2/N_2O mixtures showed that there is little or no effect of the equivalence ratio on the ignition delay time for the mixtures of interest herein. Using models from the literature, a detailed kinetics model was built and validated to explain the experimental results.

Experiments

Experiments were performed at three different pressure conditions: around 1.6, 13, and 32 atm, at an equivalence ratio (Φ) of 0.5 for the H_2/O_2 mixture. Polycarbonate diaphragms were used for test pressures of 1.6 and 13 atm (0.25-mm and 2 × 1.02-mm thickness, respectively), while pre-scored aluminum diaphragms (2.29-mm thickness) were used for the 32-atm experiments. When polycarbonate diaphragms were used, a cross-shaped cutter was employed to facilitate breakage of the diaphragm and prevent diaphragm fragments from tearing off. Helium was used as the driver gas during this study.

Prior to every run, the driven section was vacuumed down to 2×10^{-5} Torr or better using a roughing pump and a Varian 551 Turbomolecular pump. The pumping time between experiments was minimized using a pneumatically driven poppet valve matching the inside diameter of the driven section and allowing for a passage of 7.62-cm diameter between the vacuum section and the driven tube. The pressure is measured using two MKS Baratron model 626A capacitance manometers (0-10 Torr and 0-1000 Torr) and an ion gauge for high vacuums. Test mixtures were prepared manometrically in a mixing tank of 3.05-m length made from stainless steel tubing with a 15.24-cm ID. The pressure in the mixing tanks was measured using a Setra GCT-225 pressure

transducer (0-17 atm). The mixing tank is connected to the vacuum system and can be pumped down to pressures below 1×10^{-6} Torr. The gases (H_2 (Praxair, 99.999%), O_2 (Praxair, 99.999%), N_2O (Praxair, 99.5%) and Ar (Acetylene Oxygen Company, 99.999%)) were passed through a perforated stinger traversing the center of the mixing tank to allow for rapid, turbulent mixing. To further ensure homogeneity through diffusion processes, mixtures were allowed to rest for at least 45 minutes prior to making the first run. No difference in the results was observed for longer mixing times. Conditions investigated during this study are provided in Table 13.

Table 13 Experimental conditions investigated behind reflected shock waves for the present study, with the exception of the baseline H_2-O_2 mixture data.

Mixture composition (mole fraction)	T_5 (K)	P_5 (atm)	Reference
0.01 H_2 / 0.01 O_2 / 0.98 Ar	960-1625	1.65 ± 0.15 atm	This project
	1085-1245	13.3 ± 1.0 atm	
	1160-1270	32.8 ± 1.5 atm	
0.01 H_2 / 0.01 O_2 / 0.0001 N_2O / 0.9799 Ar	950-1660	1.60 ± 0.17 atm	This study
	1090-1230	13.1 ± 0.3 atm	
	1150-1260	31.8 ± 1.1 atm	
0.01 H_2 / 0.01 O_2 / 0.0004 N_2O / 0.9796 Ar	940-1675	1.67 ± 0.25 atm	This study
	1075-1220	12.6 ± 0.8 atm	
	1145-1300	31.4 ± 1.0 atm	
0.01 H_2 / 0.01 O_2 / 0.0016 N_2O / 0.9784 Ar	950-1660	1.62 ± 0.20 atm	This study
	1080-1225	13.1 ± 0.6 atm	
	1125-1235	32.4 ± 1.0 atm	
0.01 H_2 / 0.01 O_2 / 0.0032 N_2O / 0.9768 Ar	975-1580	1.89 ± 0.28 atm	This study
	1085-1230	13.2 ± 0.4 atm	
	1130-1230	34.7 ± 0.7 atm	

Results

The effect of N_2O concentration on the ignition delay time of H_2/O_2 mixtures at around 1.6 atm is visible in Fig. 34. As can be seen, an addition of 100 ppm did not have any discernible effect on τ_{ign}. Above this level, it can be noticed that N_2O additions tended to decrease the ignition delay time at higher temperatures; at around 1650 K, the ignition delay time was reduced from about 95 μs for the neat H_2 case to approximately 40 μs when 3200 ppm of N_2O was added. This effect of N_2O induced a change in the apparent activation energy (Ea) for concentrations above 400 ppm, and the values of Ea extracted from Fig. 34 indicate an increase of Ea with the nitrous oxide concentration: Ea = 13.6±1.7 kcal/mol for the neat H_2/O_2 mixture, 13.9±1.0 kcal/mol with 100-ppm N_2O, 14.5±0.9 kcal/mol with 400 ppm, 16.6±1.3 kcal/mol with 1600 ppm, and 17.7±1.2 kcal/mol with 3200-ppm N_2O.

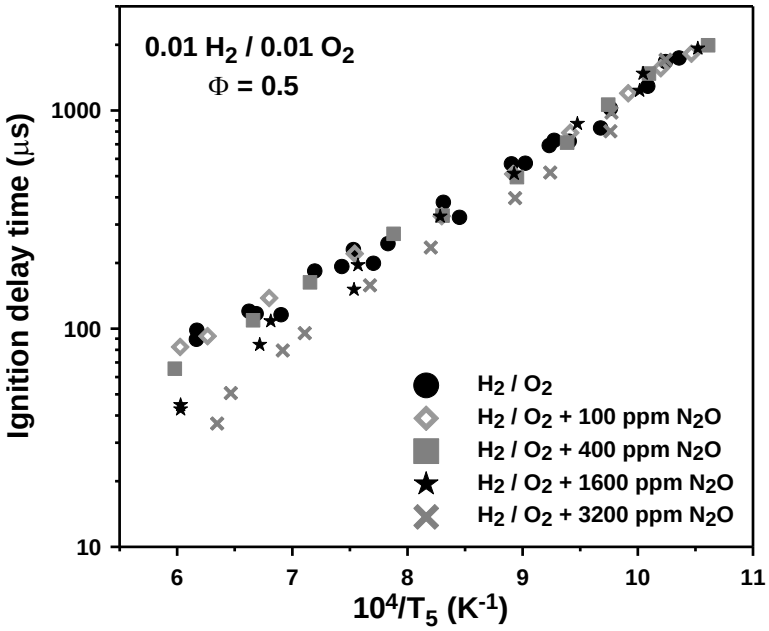

Fig. 34 Evolution at around 1.6 atm of the ignition delay time with the inverse of the temperature for H_2/O_2 mixtures with various amount of N_2O. The N_2O only seems to have an effect on ignition delay times at this pressure for the highest concentrations of N_2O and at the higher temperatures.

At a pressure around 13 atm (Fig. 35), it is visible that the data are not following a straight line but rather present a curvature at around 1150 K; this nonlinear behavior occurs for the neat H_2/O_2 mixtures as well as the ones with nitrous oxide. Similar to the data at 1.6 atm, no effect of nitrous oxide on the ignition delay time was detected with an addition of 100 ppm. However, for N_2O concentrations larger than 100 ppm, only a small (< 35%) decrease in the ignition delay time was observed, mostly on the low-temperature side. It is also interesting to note that the reduction in the ignition delay time does not really relate to the N_2O concentration, as for the other pressure conditions investigated. Indeed, the ignition delay times are essentially the same for the 400-, 1600- and 3200-ppm N_2O addition on the low-temperature side of the curve, within the accuracy of the ignition delay time measurement itself.

For the highest pressure investigated, around 32 atm (Fig. 36), the evolution of τ_{ign} in an Arrhenius graph displays the same linear decrease of the ignition delay time with the rise of the temperature observed at around 1.6 atm. The overall effect of N_2O is also similar (decrease of the ignition delay time with the increase of the nitrous oxide concentration), but unlike at the other two pressures (1.6 and 13 atm) this effect can be observed over the entire range of temperatures investigated and is visible even for 100 ppm of N_2O. For example, at around 1175 K, the ignition delay time was decreased from 1050 μs to 650 μs when 100 ppm N_2O was added. At this temperature, the ignition delay time was reduced to about 530 μs, 435 μs, and 330 μs with the 400-ppm, 1600 ppm, and 3200-ppm N_2O additions, respectively. A correlation between the ignition delay time, the temperature, and the N_2O concentration was derived from the data from Fig. 36 with a good r^2 value (0.972):

$$\tau_{ign}(\mu s) = 6.63 \times 10^{-14} \times [N_2O]^{-0.1} exp^{\left(\frac{-82.93\ (kcal)}{RT}\right)} \quad (14)$$

As can be seen from this correlation, the exponent on the N_2O concentration is quite small, indicating an overall limited effect of N_2O additions on the ignition delay time in the conditions of Fig. 36. It is worth noting that the activation energy does not vary much with N_2O addition. Overall, the activation energy was only slightly decreased by the presence of nitrous oxide: Ea = 90.5±12.7 kcal/mol for neat H_2, 86.8±11.7, 80.3±14.0, 80.2±13.1, and 77.6±12.0 kcal/mol for 100-, 400-, 1600-, and 3200-ppm N_2O addition, respectively.

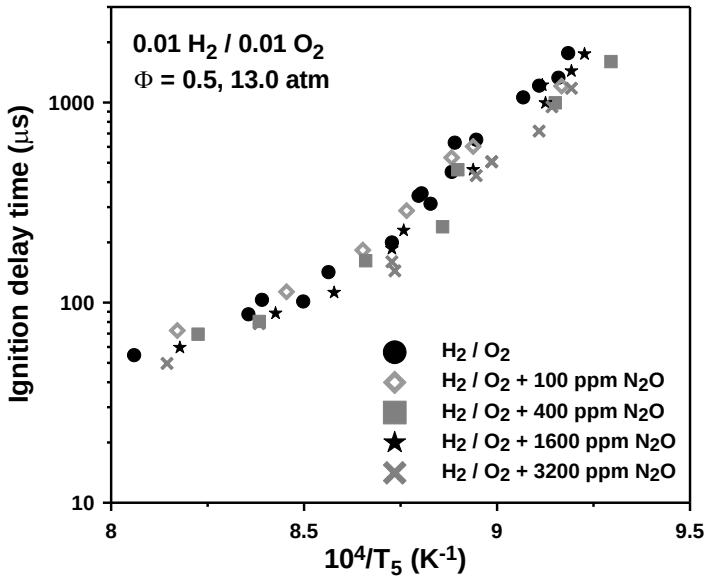

Fig. 35 Evolution at around 13 atm of the ignition delay time with the inverse of the temperature for H_2/O_2 mixtures with various amount of N_2O. There is only a slight reduction in ignition delay time due to N_2O addition at this pressure, and only for levels above 100 ppm.

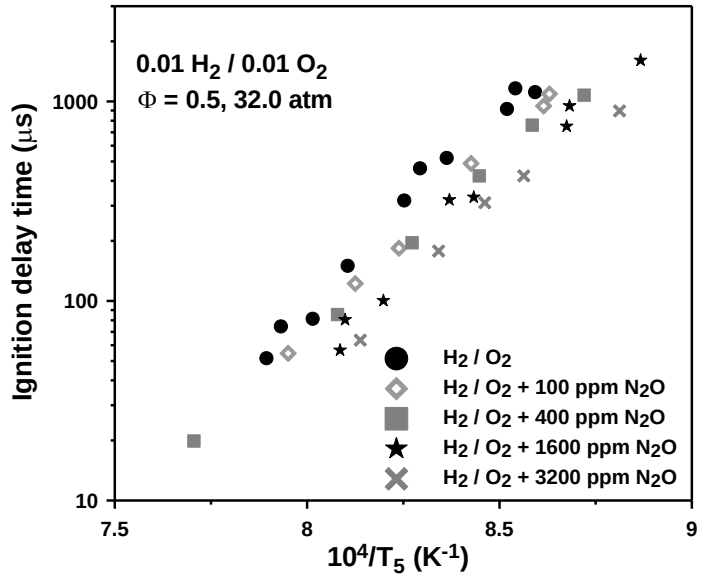

Fig. 36 Evolution at around 32 atm of the ignition delay time with the inverse of the temperature for H_2/O_2 mixtures with various amount of N_2O. At this pressure, the effect of N_2O addition is more noticeable over the entire range of temperatures and N_2O concentrations than in Figs. 34 and 35.

Kinetics Modeling

Several N_2O mechanisms [Mevel et al., 2009; Kosarev, 2007; Dayma and Dagaut, 2006; Konnov, 2009] were then successively merged into the NUIG mechanism and tested against the $H_2/O_2/N_2O$ ignition delay times data of this study. Note that the complete OH* sub-mechanism used herein [Hall and Petersen, 2004; 2006] was extended using the study of Hidaka *et al.* (1985a) to account for the OH* production from N_2O via $N_2O + H = N_2 + OH^*$. The effect of this reaction on the computed OH* profile is discussed later in this paper. The comparison between these mechanisms and the experimental data showed that all of them were equivalent at around 1.6 atm and offered excellent τ_{ign} predictions for temperatures above 1000 K. Below this temperature, the models tended to over-predict the ignition delay time (all mechanisms yielding the same result). However, at higher pressures, the ignition delay time was well captured by the models on the whole range of temperatures except for the mechanism from Dayma and Dagaut (2006) which was slightly over-reactive and tended to predict shorter delays than observed experimentally. For the highest pressure studied, the model from Dayma and Dagaut was still predicting too-short ignition delays and was therefore not considered further. It was also possible to eliminate the mechanism from Kosarev *et a*l. (2007) as this mechanism exhibited an activation energy that was much too low around 32 atm. The N_2O sub-mechanisms of Konnov (2009) and Mével *et al.* (2009) demonstrated equivalent and satisfying predictions over the whole range of temperatures and pressures investigated. It is however worth mentioning that the mechanism of Mével *et al.* is based, amongst others, on the mechanism of Konnov but was modified with the mechanism of Mueller *et al.* (2000) to allow for better predictions with NH_3 data [Davidson et al., 1990], as documented in Mevel *et al.* (2009). The NOx sub-mechanism of Mével *et al.* was therefore selected for this study as it is applicable over the largest range of components and conditions.

To allow for a better agreement with the data, the H_2-NUIG/N_2O-ICARE1 model was then slightly modified. The most important reactions influencing the ignition delay time and involving N_2O were determined through sensitivity analysis, and the N_2O sub-mechanism from Mével *et al.* (2009) was updated with reaction rates from the literature. More particularly, the primary calculation using sensitivity analysis showed that the reaction $N_2O + M \rightleftarrows N_2 + O + M$ was of primary importance. The reaction rate for this reaction was changed with the high- and low-pressure limiting rate coefficients recommended in the review of Baulch *et al.* (2005) instead of the value proposed by Zuev and Starikovskii (1991). This modification allows for a better agreement between the model and the data of this study. Finally, the rate coefficient for the reaction $N_2O + H \rightleftarrows N_2 + OH$ was also changed with the value suggested in Baulch *et al.* (2005), and the reaction $NH + NO \rightleftarrows NNH + O$ with the reaction rate from Bozelli *et al.* (1994) was added. The addition of this reaction improves the predictions of the model over the data for H_2/N_2O/diluent mixtures, especially for the data of Hidaka *et al.* (1985b), as shown later.

Results of these modifications are visible in Fig. 37 (a-l) with the data obtained during this study. As can be seen from this figure, the models of Kosarev *et al.* (2007) and Dayma and Dagaut (2006) did not allow for good predictions over the whole range of pressures and temperatures investigated. The mechanisms of Konnov (2009) and Mével *et al.* (2009) offered reasonable to good predictions, with the mechanism of Konnov performing better at 1.6 atm and for higher pressure when the concentration of N_2O exceed 400 ppm. In comparison, the model proposed in this study is in better agreement with the experimental data above 1.6 atm and shows

improvement compared to the models previously published. For the experiments at 1.6 atm (Fig. 37 (a)), the model offers good predictions but still shows a lack of reactivity for the temperatures below 1000 K for N_2O concentrations below 1600 ppm.

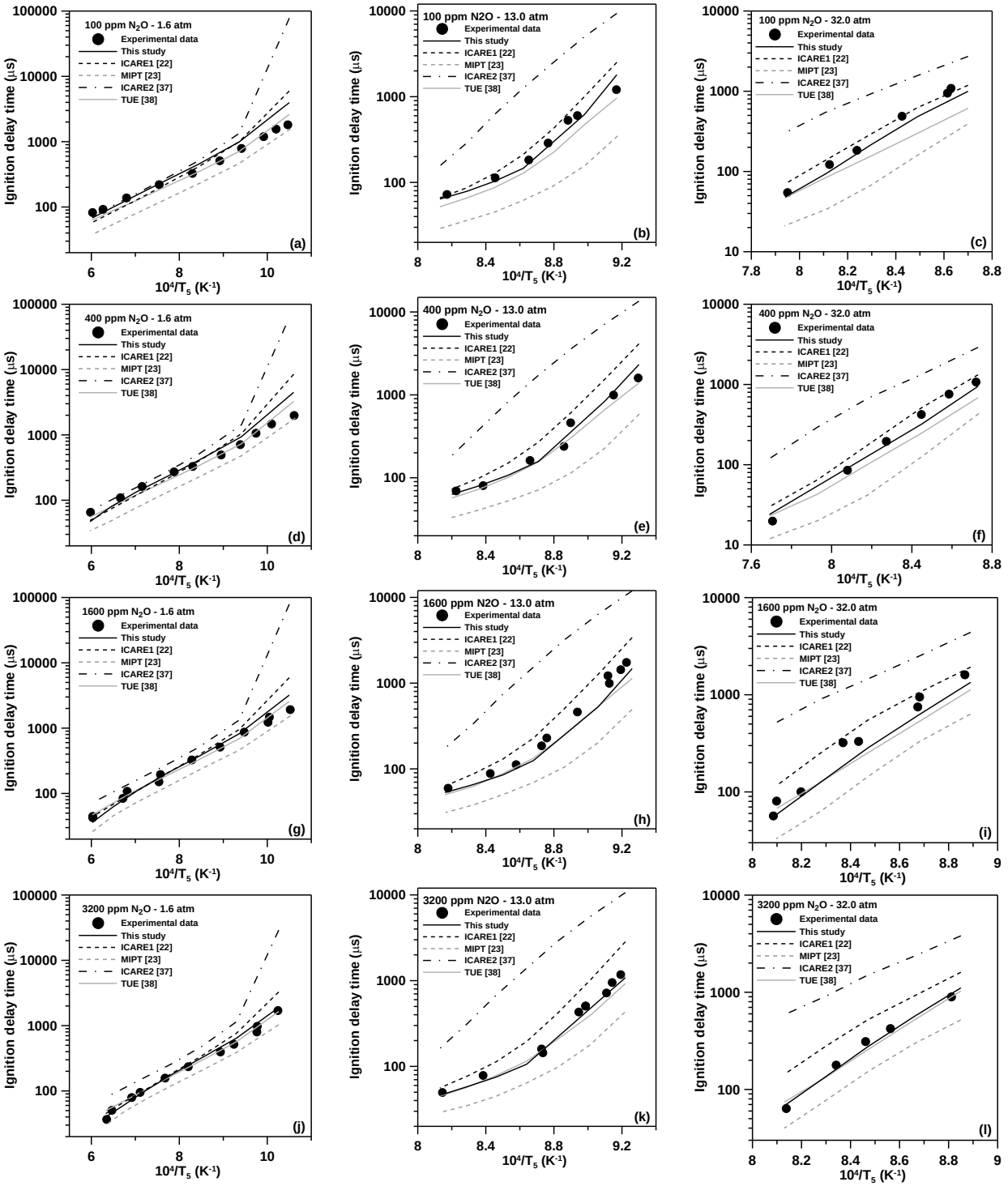

Fig. 37 Comparison between models and experiments for the ignition delay time of a 0.01 H_2/0.01 O_2 mixture diluted into Ar and doped with 100 (a-c), 400 (d-f), 1600 (g-i) and 3200 ppm (j-l) of N_2O at three different pressure conditions. Note that the reference numbers are taken from Mathieu et al. (2012).

As mentioned earlier, the H_2 chemistry is driving the combustion under the conditions of our experiments. Figures 34-36 also illustrate the important changes in the H_2 ignition behavior with pressure. Indeed, whereas τ_{ign} typically decreases with the increase in the pressure for hydrocarbons [Healy *et al*., 2010], important changes in the activation energy are visible with H_2 and, under our experimental conditions, the ignition delay time will actually increase with the pressure for some temperatures. This particular result with hydrogen is well known and is mentioned above. To summarize, the behavior observed is essentially due to the competition between two reactions:

$$H + O_2 \rightleftarrows OH + O \quad (R1)$$

$$H + O_2 + M \rightleftarrows HO_2 + M \quad (R2)$$

The chain-branching reaction (R1) is dominant at high temperatures and low pressures, whereas the termolecular reaction (R2) prevails for higher pressures. Reaction (R2) therefore plays a progressively more important role as the pressure increases and lowers the effect of the chain branching from reaction (R1). Reaction (R2) also forms a HO_2 radical which is much less reactive than the OH radical formed with (R1).

To explain the effect of N_2O addition on the ignition delay time of H_2/O_2 mixtures, a sensitivity analysis on OH* was performed using the model developed in this study, for the low- and high-temperature areas of each pressure condition investigated. Results for the conditions around 30 atm and for the low-temperature area (1130 K) are visible in Fig. 38 for the neat H_2 (a) and 3200-ppm N_2O (b) cases. For the neat-H_2 case, the most-sensitive reaction is the pressure-sensitive, inhibiting reaction $H + O_2 + Ar$ (or +M) $\rightleftarrows HO_2$ +Ar (or +M) (R2) closely followed by the branching and promoting reaction $H + O_2 \rightleftarrows O + OH$ (R1). These two reactions are discussed above, and their competition is mainly responsible for the trends observed for H_2 experiments. When 3200 ppm of nitrous oxide are added to the mixture, the reaction N_2O +M $\rightleftarrows N_2 + O$ +M (R3) appears in the 10 most-sensitive reactions. This reaction involving N_2O is releasing O radicals which can then react though the branching reaction (R4): $O+H_2 \rightleftarrows H+OH$ and therefore promotes the ignition of the mixture, as observed experimentally. As can be seen in Fig. 16, (R4) is more sensitive when 3200 ppm of N_2O are added. A similar conclusion on the role of N_2O can be given for the high-temperature condition, 1235 K at 32 atm, except that the reaction R3: N_2O +M $\rightleftarrows N_2 + O$ +M has a lower sensitivity.

For the lowest pressure investigated, the sensitivity analysis at 1.5 atm and 1050 K showed that reaction R3 is by far the most-sensitive reaction, followed by R4 (Fig. 39 (a)). The fact that R3 is the most-sensitive reaction while conversely the ignition delay time is not modified experimentally by the N_2O addition can be explained by the fact that the reaction rate for the pressure-dependent reaction R3 is low at these low-temperature and low-pressure conditions. A reaction pathway analysis showed that if N_2O is consumed *via* R3 at the very beginning of the reaction, the reaction $N_2O + H \rightleftarrows N_2 + OH$ (R5) overtakes R3 with time and eventually becomes the main channel for N_2O depletion after roughly one third of the ignition delay time.

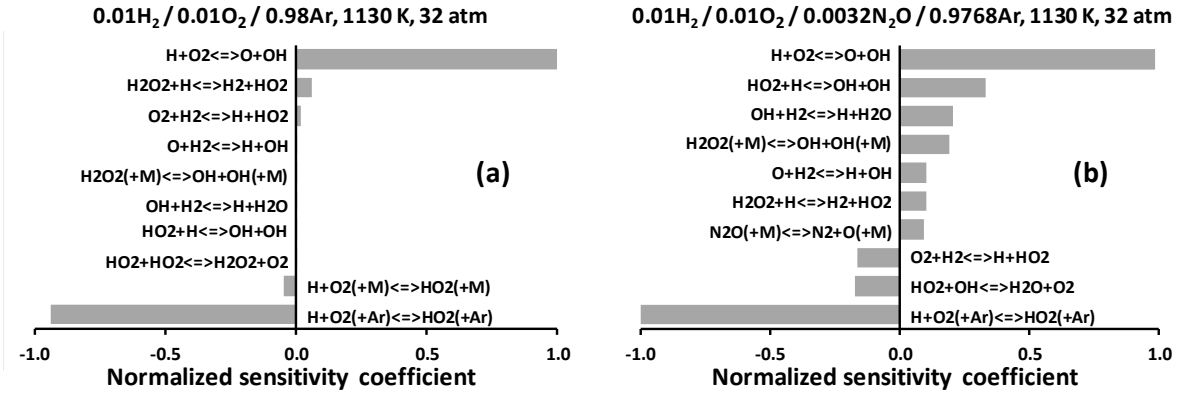

Fig. 38 Normalized sensitivity analysis on OH*at 1130 K and 32 atm for mixtures of 0.01 H_2/0.01 O_2/0.98 Ar (a) and 0.01 H_2/0.01 O_2/0.0032 N_2O/0.9768 Ar (b).

At the highest temperature studied (1650 K), the most-sensitive reaction is still R3 followed by $N_2O + H \rightleftarrows N_2 + OH^*$ (R6), R1, and R3 with R3 being significantly more sensitive than at low temperature (Fig.39 (a)). For the neat H_2 case, reaction R1 is the most-sensitive reaction at these conditions. The addition of N_2O therefore promotes the formation of the O radical through R3 and, at this high-temperature condition, these O radicals will then react quickly with H_2 (directly *via* R4 and indirectly *via* R4 and R5) and promote the reactivity. Note that at this low-pressure condition, as can be expected, the ignition delay time is not very sensitive to the reaction $H + O_2 + M \rightleftarrows HO_2 + M$ (R2).

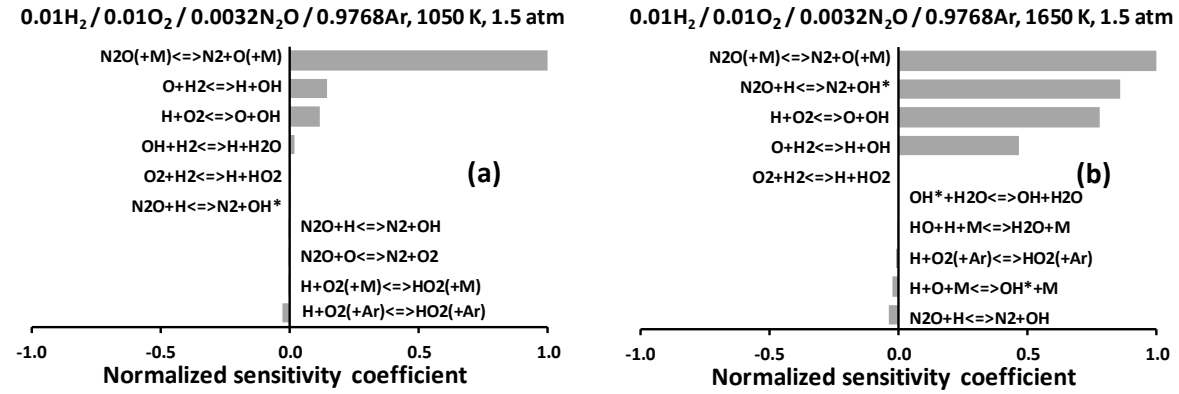

Fig. 39 Normalized sensitivity analysis on OH*at 1050 K (a) and 1650 K (b) for a mixture of 0.01 H_2/0.01 O_2/0.0032 N_2O/0.9768 Ar at 1.5 atm.

At the conditions herein, the reaction $N_2O + M \rightleftarrows N_2 + O + M$ (R3) therefore seems to be the main cause of the decrease in the ignition delay time when nitrous oxide is added to the mixture for the cases where any effect of N_2O addition is seen at all.

NO_2 KINETICS IN HIGH-H_2 MIXTURES

Interactions between hydrocarbons and NOx have been widely studied [Miller et al., 2005]. Typically, studies showed that small additions of NO result in a promoting effect on hydrocarbon combustion coupled with a rapid conversion of NO to NO_2 (referred to as mutual sensitization) [Sivaramakrishnan et al., 2007]. During the combustion of hydrocarbons, it is well known that the H_2/O_2 system is key as it contains many important elementary reactions involving radicals (H, O, OH, HO_2) that play a great role during the oxidation process. Hence, there is a fundamental interest in characterizing the interactions between the H_2/O_2 and the NOx systems.

These interactions were first studied by Slack and Grillo (1977) with shock-tube ignition delay time (τ_{ign}) measurements from H_2/air/NO or NO_2 mixtures and for pressures up to 2 atm. Mueller *et al.* (2000) investigated the NO and NO_2 concentration profiles with time in a flow reactor for a fuel rich mixture of $H_2/NO_2/N_2$ at 3 atm and around 830 K. They determined from their results a rate for the reaction $H_2 + NO_2 \rightleftarrows HONO + H$ which was in agreement with the calculated rate from Parks et al. (1998). They concluded that the reaction rate proposed in Slack and Grillo (1978), derived from τ_{ign} measured in Slack and Grillo (1977), was too fast because the τ_{ign} were subject to gas dynamic effects (due to the use of undiluted mixtures). More recently, Dayma and Dagaut (2006) used a jet-stirred reactor to investigate the oxidation of H_2/O_2 mixtures with various concentrations of NO or NO_2 and under various conditions (700-1150 K, 1 and 10 atm and equivalence ratios (Φ) from 0.1 to 2.5). Results confirmed the rate constants from Mueller et al. (2000) and Parks et al. (1998), and they concluded that τ_{ign} measurements for $H_2/O_2/NO_2$ mixtures were necessary to help in further validating the model.

The aim of the present study was therefore to measure τ_{ign} of $H_2/O_2/NO_2$ mixtures in a shock tube under dilute conditions (98-97.84% Ar) for mixtures and pressures (1.5-30 atm) that have never been heretofore investigated. Various amounts of NO_2 (100, 400 and 1600 ppm) were added to a H_2/O_2/Ar mixture to investigate the effect of the NO_2 concentration on τ_{ign}. The equivalence ratio was set to 0.5 for the other conditions. To assess the effect of NO_2 on τ_{ign}, results were compared to some recent τ_{ign} measurements obtained under the same conditions with a neat H_2/O_2 mixture obtained by the authors and presented in Keromnes *et al.* (2013).

Experimental set-up

Ignition delay times were measured behind reflected shock waves (RSW) in a single-diaphragm, stainless steel shock tube. The driven section is 15.24-cm i.d., 4.72-m long, and the driver section is 7.62-cm i.d., 2.46-m long. Wave speed was measured through five PCB-P113A piezoelectric pressure transducers, equally spaced alongside the driven section and mounted flush with the inner surface. Post reflected-shock conditions were determined using the measured incident wave speed extrapolated to the end wall in conjunction with the one-dimensional shock relations. This method was proven to maintain the uncertainty in the temperature determination behind RSW (T_5) below 10 K. Test pressure was monitored by one PCB-134A located at the endwall and one Kisler 603-B1 located at the sidewall, in the same plane as the sapphire window.

The driven section was evacuated using a roughing pump and a turbomolecular pump. The pumping time between experiments was minimized using a pneumatically driven poppet valve

matching the inside diameter of the driven section. Test mixtures were prepared manometrically in a stainless steel mixing tank. The gases were passed through a perforated stinger traversing the center of the mixing tank to allow for rapid, turbulent mixing. Conditions investigated during this study are summarized in Table 14.

Table 14 Experimental conditions investigated behind reflected shock waves.

Mixture (molar fraction)	T_5 (K)	P_5 (atm)	Reference
0.01 H_2/0.01 O_2 / 0.98 Ar	960-1625	1.5-34.3 atm	Kermones et al. (2013)
0.01 H_2 / 0.01 O_2 / 0.0001 NO_2 / 0.9799Ar	945-1640	1.5-35.3 atm	This study
0.01 H_2 / 0.01 O_2 / 0.0004 NO_2 / 0.9796 Ar	990-1565	1.4-35.9 atm	This study
0.01 H_2 / 0.01 O_2 / 0.0016 NO_2 / 0.9784 Ar	1035-1720	1.45-34.5atm	This study

Ignition delay times were measured at the sidewall location (16 mm from the endwall) using emission spectroscopy from the $A^2\Sigma^+ \rightarrow X^2\Pi$ transition of the excited-state hydroxyl radical (OH*) using an interference filter centered at 307±10 nm with a Hamamatsu 1P21 photomultiplier tube. The ignition delay time is defined as the time between the passage of the reflected shock wave, indicated by a pressure jump in the signal delivered by the sidewall pressure transducer, and the intersection of lines drawn along the steepest rate-of-change of OH* de-excitation and a horizontal which defines the zero-concentration level.

Results

At around 1.5 atm (Fig. 40), it is visible that an addition of 100 ppm of NO_2 has no discernable effect on H_2 τ_{ign}. With 400 ppm of NO_2, a small increase in τ_{ign} can however be observed below 1215 K. For the highest NO_2 concentration, 1600 ppm, a clear inhibiting effect on τ_{ign} can be observed, and it is visible that the importance of this effect grows as the temperature decreases.

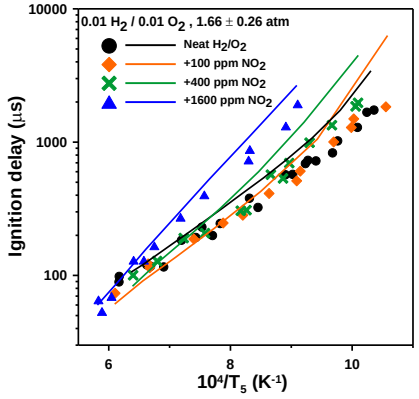

Fig. 40 Effect of NO_2 concentration on the ignition delay time for H_2/O_2 mixtures around 1.5 atm. Lines correspond to the model.

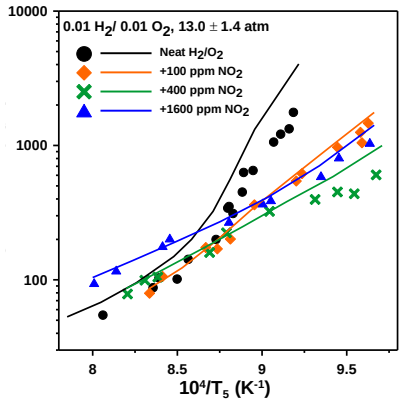

Fig. 41 Effect of NO_2 concentration on the ignition delay time for H_2/O_2 mixtures around 13 atm. Lines correspond to the model.

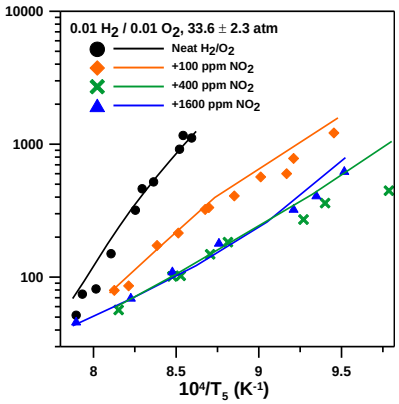

Fig. 42 Effect of NO_2 concentration on the ignition delay time for H_2/O_2 mixtures around 30 atm. Lines correspond to the model.

At around 13.5 atm (Fig. 41), a noticeable effect on τ_{ign} can be observed with 100 ppm of NO_2. Indeed, the change in the slope observed below 1140 K for the neat H_2 case, corresponding to a rapid increase in τ_{ign}, is cancelled by the 100-ppm NO_2 addition. With 400 ppm of NO_2, ignition delay times above 1140 K are still identical to those of H_2. Nevertheless, the reactivity is further increased below this temperature, leading to a new change in the slope. It is worth noting that the temperature at which the slopes change is the same (around 1140 K) for the neat hydrogen mixture and for the 400-ppm NO_2 case. Finally, an addition of 1600 ppm NO_2 still decreases τ_{ign} above 1140 K compared to the neat H_2 mixture, but the resulting delays are now longer than for the 400-ppm case, even for temperatures above 1140 K.

As can be seen in Fig. 42, for the experiments at around 30 atm, the reactivity of the mixture increases significantly for the lower temperatures studied when NO_2 is added to the mixture. As for the 10-atm case, τ_{ign} decreases with the increase in the NO_2 concentration from 0 to 400 ppm of NO_2. However, an addition of 1600 ppm of NO_2 results in an ignition delay time that is shorter than the neat H_2/O_2 mixture but longer than for the 400-ppm NO_2 case.

Kinetics modeling

Several H_2/NOx chemical kinetics models have been used: the mechanisms from Dayma and Dagaut (2006) (with the high-pressure updates in the NOx chemistry from Sivaramakrishnan et al. (2007)), Rasmussen *et al.* (2008) and Konnov (2009), each coupled with the OH* sub-mechanism from Hall and Petersen (2006). Results of this comparison showed that there is no currently existing model from the literature capable of reproducing correctly the data over the whole range of conditions investigated herein.

To assess the validity of the NOx sub-mechanisms separately from the baseline H_2/O_2 chemistry, the neat H_2/O_2 data from Kermones et al. (2013) were modeled with the aforementioned NOx mechanisms, which include the H_2-O_2 chemistry. Results showed that the mechanisms were not capable of predicting the neat H_2/O_2 τ_{ign}. Several mechanisms were tested against these H_2/O_2 data and it was found that the C0-C4 mechanism from Healy *et al.* (2010) offered the best predictions over the whole range of pressure investigated. This mechanism was therefore selected as a base for the H_2/O_2 sub-mechanism.

The NOx chemistry from the mechanisms of Dagaut *et al.*, Rasmussen *et al.* and Konnov were then successively merged into this H_2/O_2 sub-mechanism and tested against the $H_2/O_2/NO_2$ data. Results showed that the experimental trends were better reproduced by the NOx sub-mechanism of Dagaut *et al.* over the entire range of conditions. Concerning the rate of the reaction H_2+NO_2 ⇄ HONO+H, Dagaut *et al.* uses the rate proposed in Mueller et al. (2000). The reaction rate from Slack and Grillo (1978) was tried, and the results showed a poor agreement with the data, especially for the 13- and 30-atm conditions. The reaction rate of Parks *et al.* (1998) was also tried, and predictions were notably improved over the entire range of conditions investigated. Results provided by this mechanism (H_2/O_2 from Healy et al. (2010), NOx from Sivaramakrishnan et al. (2007) and Dayma and Dagaut (2007) with the reaction rate for H_2+NO_2 ⇄ HONO+H from Parks et al. (1998)) are visible in Figs. 40-42. As can be seen, this mechanism captures well the experimental trends and allows for good predictions for the higher temperatures.

Discussion

The mechanism employed to model the data was then used to interpret the results by reaction path and sensitivity analyses. The sensitivity analysis was made by determining the ignition sensitivity coefficient (σ) for every reaction of the kinetics model. The ignition sensitivity coefficient was determined with the following equation:

$$\sigma = \frac{\Delta\tau}{\Delta K} \times \frac{K_{nominal}}{\tau_{nominal}} \approx \frac{\tau_{(2)} - \tau_{(0.5)}}{1.5\tau}$$

Where K is the rate constant of the chemical reaction considered, $\tau_{(2)}$ is the delay time determined with the rate constant of the corresponding reaction multiplied by 2, $\tau_{(0.5)}$ is the delay time of the corresponding reaction multiplied by 0.5, and τ is the nominal ignition delay time.

Sensitivity analyses were performed on the low- and high-temperature areas of every mixture and pressure condition investigated (1100 and 1650 K at 1.6 atm, 1110 and 1250 K at 13.5 atm and 1050 and 1250 K at 32 atm). An example of the sensitivity analysis results is provided in Fig. 4 for the neat H_2/O_2 (a), and for the additions of 100 (b), 400 (c) and 1600 ppm (d) of NO_2, at 13.5 atm and at 1110 K.

It is visible in Fig. 43 (a) that the most sensitive reactions for the H_2/O_2 system at 1110 K are an inhibiting reaction: $H + O_2 (+M) \rightleftarrows HO_2 (+M)$ (R1), followed by the branching reaction: $H+O_2 \rightleftarrows O+OH$ (R2). The sensitivity analysis at a higher temperature, 1250 K, showed an inverse order for these two reactions. The well-known competition between these reactions explains why τ_{ign} increases very rapidly with the decrease of the temperature with the neat H_2/O_2 mixture.

Several reactions promote the reactivity of the mixture in the presence of NO_2, namely: $NO_2+H_2 \rightleftarrows HONO+H$ (R3), $NO+HO_2 \rightleftarrows NO_2+OH$ (R4), $NO_2+HO_2 \rightleftarrows HONO+O_2$ (R5) and $NO_2+H \rightleftarrows NO+OH$ (R6). According to the reaction path analysis, the main path for NO_2 consumption is (R6), which produces NO and a radical OH. Most of this NO will then be recycled to NO_2 by converting a HO_2 radical into a more reactive radical OH *via* the reaction (R4). These two reactions explain the important effect on the reactivity of a small amount of NO_2 (100 ppm). This mechanism has been documented numerous times in the literature [Sivaramakrishnan et al., 2007; Slack and Grillo, 1977; Dayma and Dagaut, 2006; Rasumussen et al., 2008].

The NO_2 can also react with H_2 or a radical HO_2 to form HONO through reactions (R3) and (R5), respectively. This HONO will later decompose into NO and OH through: $HONO (+M) \rightleftarrows OH+NO (+M)$ (R7). Increasing the NO_2 concentration from 100 to 400 ppm leads to further changes in the most-sensitive reactions (Figs. 43 (b) and (c)). It is first noticeable that the most-sensitive reaction is now the promoting reaction (R2) instead of (R1). Also, the sensitivity of (R3) is significantly more important, due to the higher occurrence of NO_2 molecules in the mixture. This reaction (R3) will produce H radicals which will enhance (R2). The reaction (R3) will then generate OH radicals directly *via* (R7) and then indirectly *via* reaction (R7) followed by (R4) and is therefore responsible of the further reduction in τ_{ign} for the lower temperatures when increasing the NO_2 concentration from 100 to 400 ppm.

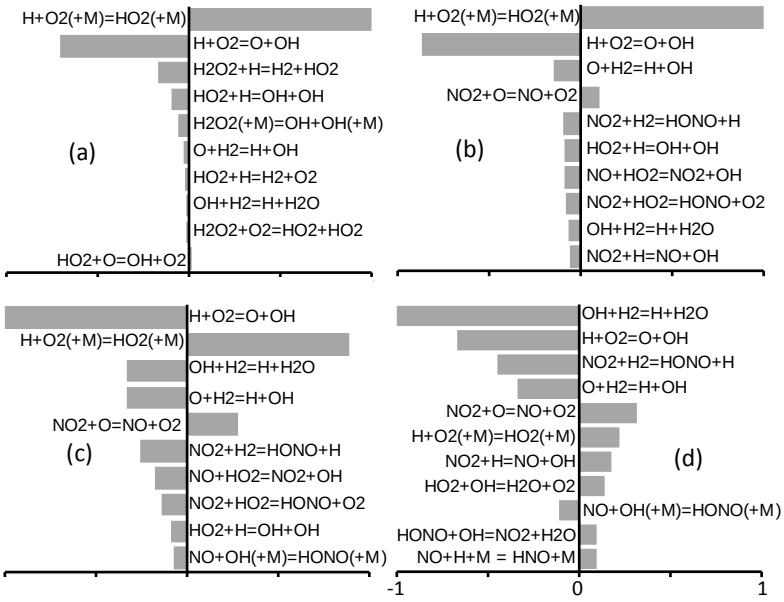

Fig. 43 Normalized ignition sensitivity coefficient (σ) for a neat mixture of H_2/O_2 (a) (98% Ar) at $\phi = 0.5$, 13.5 atm and with 100 (b), 400 (c) and 1600 ppm of NO_2 (d).

With an addition of 1600 ppm of NO_2, many changes in the most-sensitive reactions are visible (Fig. 43 (d)). First, the most-sensitive reaction is now the propagating chain reaction $OH+H_2 \rightleftarrows H+H_2O$ (R8) instead of the chain-branching reaction (R2) for the 400-ppm NO_2 case. This propagating reaction (R8) was determined as the main oxidation pathway of H_2 in Healy et al. (2010), and a similar conclusion was found here. As stated in Healy et al. (2010), (R8) also contributes to the NO formation *via* (R6), and this NO will then produce OH radicals *via* (R4) that will contribute to (R8). Reaction (R8) is followed by (R2) and (R7) in sensitivity, the latest still gaining in importance as the NO_2 concentration is increased. However, the large proportion of HONO produced allows it to react with OH: $HONO+OH \rightleftarrows NO_2+H_2O$ (R9) (Fig.43 (d)). This reaction is partly compensating for the promoting effect of (R7). Three other inhibiting reactions appeared with 1600-ppm NO_2: $NO_2+H \rightleftarrows NO+OH$ (R10), $HO_2+OH \rightleftarrows H_2O+O_2$ (R11) and $NO+H+M \rightleftarrows HNO+M$ (R12). Overall, the fact that (i) the most-sensitive reaction is a propagating chain instead of a branching chain; (ii) (R9) is partly compensating for (R7); and (iii) inhibiting reactions (R10), (R11) and (R12) are present explain the results at 1600-ppm NO_2, where the delay is still decreased compared to the neat H_2/O_2 system but is increased compared to the 400-ppm case.

On the high-temperature side (1250 K) at 13.5 atm and for the 100-ppm NO_2 case, the most-sensitive reaction involving NO_2 is (R6) (σ=0.06). The radical OH produced by this reaction will then react with H_2 *via* (R8) (σ=-0.14), which is less reactive and sensitive under this condition than (R2) (σ=-1). The addition of 100 ppm of NO_2 would therefore tend to decrease the reactivity of the mixture, but this effect is compensated by (R3) (σ=-0.05). This scenario could explain the fact that, at this temperature, an addition of 100 ppm of NO_2 has no effect on τ_{ign}, and a similar conclusion can be provided for the 400-ppm case. For the 1600-ppm addition case, some reactions involving NO_2 are showing a relatively important sensitivity: (R10) (σ=0.32) and $NO_2+O \rightleftarrows NO+O_2$ (R13) (σ=0.37). The OH formed *via* (R10) and by the subsequent reaction (R4)

will then react with H_2 *via* (R8) which is the most-sensitive reaction instead of the branching reaction (R2) (σ=-0.73) for smaller amounts of NO_2. This reaction path explains the increase in τ_{ign} at 1250 K and at around 13 atm when 1600 ppm of NO_2 are added.

At 30 atm, the effect of the NO_2 addition is mostly visible for the lower temperatures. The sensitivity analysis showed that at 1050 K the two most-sensitive reactions are, by decreasing order, (R1) and (R2) for the H_2/O_2 mixture and for NO_2 additions up to 400 ppm. The decrease in τ_{ign} observed by additions of NO_2 up to 400 ppm is due to promoting reactions involving NO_2 which are principally, at 400 ppm, (R3) (σ=-0.54), (R4) (σ=-0.46) and (R10) (σ=-0.33). At 1600 ppm of NO_2, the most-sensitive reaction is now the reaction (R8) followed by (R2), the reaction (R1) being only the sixth most sensitive reaction (σ=0.30). This result is due to the high concentration of NO_2 which induces the production of OH radical *via* (R3) (σ=-0.46) followed by (R7). It is worth noting that all the five other important reactions implicating NO or NO_2 are inhibiting reactions. Indeed, the production of HONO through (R3) is also responsible for the important role played by the termination reaction (R9) (σ=0.32). Inhibiting termination reactions (R13) and (R12) also play an important role under these conditions. Most of the HNO reacts with NO_2 *via* $HNO+NO_2 \rightleftarrows HONO+NO$ (R15). Therefore, an addition of 1600 ppm of NO_2 at 32 atm has a promoting effect on the H_2/O_2 τ_{ign} by promoting the reaction (R8) instead of (R1), explaining why τ_{ign} are shorter than for the H_2/O_2 case, but this 1600-ppm addition also induces an inhibiting effect, mostly through termination reactions (R9) and (R13), explaining why τ_{ign} are longer than for the 400-ppm NO_2 case.

For the lowest pressure investigated, at 1100 K, the reaction (R1) is not as important as for the higher pressures (σ=0.22) with the neat H_2/O_2 mixtures. The promoting effect *via* (R4) and (R6) observed for higher pressures is therefore minimized. Indeed, the analysis showed that the most-sensitive reaction was (R3) for the 100- and 400-ppm NO_2 cases, followed by (R2) (which is the most sensitive for the neat H_2/O_2 mixture). This HONO will then produce OH (*via* (R14) and (R7)) which will promote (R8). The reaction path also showed that a large portion of this HONO was involved in some inhibiting reactions, notably (R9) (29.5%) and (R15) (16.8%). The termination reaction (R13) was also relatively important under these conditions. Overall, the addition of NO_2 is therefore having an inhibiting effect due the strengthening of the propagating channel (R8) at the expense of the branching channel (R2). For the 1600-ppm NO_2 addition case, (R8) is again reinforced and is now the most sensitive reaction before (R2) (σ=-0.48); (R3) being only the sixth most sensitive reaction (σ=-0.17). Some other inhibiting reactions are also appearing, such as $NO_2+H \rightleftarrows NO+OH$ (also reinforcing (R8)) and $NO_2+O \rightleftarrows NO+O_2$, explaining the important inhibiting effect on τ_{ign} of 1600 ppm of NO_2 at these conditions.

AMMONIA OXIDATION KINETICS

Ammonia (NH_3) is an impurity commonly found in gaseous fuels derived from gasification processes of biomass or coal [Xu et al. (2011)] and is one of the largest source of nitrogen leading to NO formation during coal combustion [Mendiara and Glarborg (2009)]. Depending on the conditions under which fuels are burned, the ammonia can either be converted to NO (fuel-NOx formation mechanism) or N_2 [Kohse-Höinhaust et al. (1989), Mendiara and Glarborg (2009)]. Ammonia also has a key role in de-NOx processes [Salimian et al. (1984), Kohse-Höinhaust et al. (1989)] and can be used directly as a fuel in internal combustion engines [Pratt and Starkman (1969), Duynslaegher et al. (2012)] or as a hydrogen vector [Duynslaegher et al. (2012)]. To control these NOx formation/removal mechanisms or to use NH_3 as a fuel efficiently, it is therefore mandatory to understand the details of the combustion of ammonia in a wide range of conditions.

A large number of detailed combustion mechanisms containing ammonia sub-mechanisms are currently available in the literature [Duynslaegher et al. (2012), Mével et al. (2009), Dagaut et al. (2008), Dagaut and Nicolle (2005), Hughes et al. (2001), Mueller et al. (2000), Smith et al. (1999), and Miller and Bowman (1989)]. Unfortunately, large discrepancies can be seen amongst predictions from these mechanisms, making difficult the choice of a reliable mechanism for the industry. Ignition delay time (τ_{ign}) is a convenient measurement to assess the overall validity of the combustion chemistry of a fuel at given conditions. Although many studies focused on the ignition delay time measurement of ammonia mixtures two or three decades ago [Takeyama and Miyama (1965 (a, b), 1966 (a, b), 1967), Miyama and Endoh (1967 (a, b)), Bull (1968), Miyama (1968 (a, b)), Bradley et al. (1968), Drummond, (1972), Fujii et al. (1981)], these studies did not report the pressure and temperature conditions accurately. Also, except for the study of Drummond (1972), there is no study available for pressures above 10 atm.

The aim of this study was therefore to measure ignition delay times for NH_3 mixtures highly diluted (98-99% Ar dilution) in a shock tube. Experiments were performed behind reflected shock waves for pressures around 1.4, 11, and 30 atm and for equivalence ratios set to 0.5, 1.0, and 2.0. Detailed kinetics mechanisms from the literature were then tested against these data to assess their validity.

Methods

The single-diaphragm, stainless steel, shock tube has a driven section of 15.24-cm i.d., 4.72-m long, and a driver section of 7.62-cm i.d., 2.46-m long. A schematic of the shock-tube setup can be found in Mathieu et al. (2012). Five PCB P113A piezoelectric pressure transducers, equally spaced alongside the driven section and mounted flush with the inner surface were used along with four Fluke PM-6666 timer/counter boxes to measure the incident-wave velocities. A curve fit of these four velocities was then used to determine the incident wave speed at the end wall location. Post reflected-shock conditions were obtained using this extrapolated wave speed in conjunction with one-dimensional shock relations and the initial conditions at the test region. This method was proven to maintain the uncertainty in the temperature determination behind reflected shock waves (T_5) below 10 K [Petersen et al. (2005)]. Test pressure was monitored by one PCB 134A located at the end wall and one Kisler 603 B1 located at the sidewall, in the same plane as the observation window (Sapphire, located 16 mm from the end wall). Non-ideal

boundary layer effects measured by the change in pressure (dP/dt) behind the reflected shock wave were determined to be less than 2% per ms for all experiments. The corresponding increase in temperature for these dP/dt levels would be less than 10 K for the longest ignition delay times reported in this study and therefore does not have a noticeable impact on the results herein.

Experiments were performed at three different pressure conditions (around 1.4, 11, and 30 atm), and three equivalence ratios (ϕ), 0.5, 1.0, and 2.0. Polycarbonate diaphragms were used for test pressures of 1.4 and 11 atm (0.25-mm and 2 × 1.02-mm thickness, respectively), while pre-scored aluminum diaphragms (2.29-mm thickness) were used for the 30-atm experiments. When polycarbonate diaphragms were used, a cross-shaped cutter was employed to facilitate breakage of the diaphragm and prevent diaphragm fragments from tearing off. Helium was used as the driver gas during this study.

The driven section was vacuumed down to 2×10^{-5} Torr or better using a roughing pump and a Varian 551 Turbomolecular pump prior to every run. The pumping time between experiments was minimized using a pneumatically driven poppet valve matching the inside diameter of the driven section and allowing for a passage of 7.62-cm diameter between the vacuum section and the driven tube. The pressure was measured using two MKS Baratron model 626A capacitance manometers (0-10 Torr and 0-1000 Torr) and an ion gauge for high vacuums. Test mixtures were prepared manometrically in a mixing tank of 3.05-m length made from stainless steel tubing with a 15.24-cm ID. The pressure in the mixing tanks was measured using a Setra GCT-225 pressure transducer (0-17 atm). The mixing tank is connected to the vacuum system and can be pumped down to pressures below 1×10^{-6} Torr. The gases (Ammonia (Praxair, 99.9% purity diluted in 94.92 % Ar (99.999 %)), O_2 (Praxair, 99.999 %), and Ar (Acetylene Oxygen Company, 99.999 %)) were passed through a perforated stinger traversing the center of the mixing tank to allow for rapid, turbulent mixing. To further ensure homogeneity through diffusion processes, mixtures were allowed to rest for at least 1 hour prior to making the first run. No difference in the results was observed for longer mixing times. Since NH_3 adsorbs on stainless steel [Roose et al. (1981), Kohse-Höinghaust et al. (1988)], the mixing tank and shock-tube surfaces were passivated with NH_3 before the mixture preparation and before each experiment (introduction of around 100 torr of NH_3 for at least 5 minutes and then vacuumed for 5 minutes with the rough pump, until around 40 mtorr, typically). Conditions investigated during this study are provided in Table 15.

Table 15 Experimental conditions investigated behind reflected shock waves.

Mixture composition (mole fraction)	Equivalence ratio (ϕ)	T_5 (K)	P_5 (atm)
0.004 NH_3 / 0.006 O_2 / 0.99 Ar	0.5	1925-2480 1625-2015 1560-1895	1.4 ± 0.1 atm 10.9 ± 0.5 atm 28.7 ± 1.0 atm
0.005715 NH_3 / 0.004285 O_2 / 0.99 Ar	1.0	1985-2490 1660-2080 1565-1930	1.4 ± 0.1 atm 10.8 ± 0.4 atm 28.7 ± 1.0 atm
0.01143 NH_3 / 0.00857 O_2 / 0.98 Ar	1.0	1825-2455 1615-2085 1565-1870	1.4 ± 0.1 atm 10.5 ± 0.4 atm 28.6 ± 0.6 atm
0.007373 NH_3 / 0.002727 O_2 / 0.99 Ar	2.0	1990-2360 1650-2040 1580-1910	1.4 ± 0.1 atm 10.6 ± 0.6 atm 28.9 ± 1.5 atm

The ignition delay time was measured using the chemiluminescence emission from the $A^2\Sigma+ \rightarrow X^2\Pi$ transition of the excited-state hydroxyl radical (OH*) using an interference filter centered at 307 ± 10 nm with a Hamamatsu 1P21 photomultiplier tube. The ignition delay time is defined herein as the time between the passage of the reflected shock wave, indicated by a pressure jump in the signal delivered by the sidewall pressure transducer, and the intersection of lines drawn along the steepest rate-of-change of OH* de-excitation and a horizontal line which defines the zero-concentration level, as can be seen in Fig. 44. Time zero is defined as the time of arrival of the reflected shock wave at the sidewall measurement location. Note the typical OH* profiles for NH_3, where the OH* signal does not come back to zero and stays flat for a few hundreds of microseconds after the ignition. All of the data signals were recorded through a 14-bit GageScope digital oscilloscope with sampling rates of 1 MHz or greater per channel.

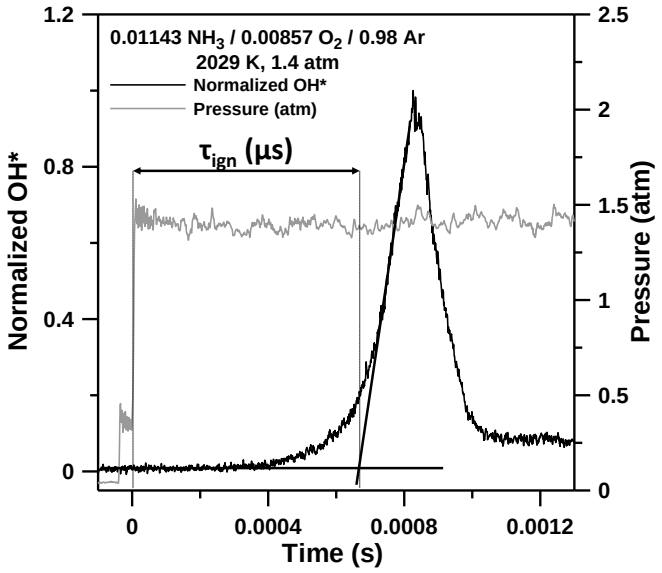

Fig. 44 Typical pressure and OH* profiles and method of determination of the ignition delay time.

There are essentially two sources of uncertainties in the ignition delay time: the uncertainty in the determination of the temperature behind the reflected shock wave (T_5) and the uncertainty associated with the determination of the steepest rate of change from the OH* profile. The temperature determination is the most important uncertainty and, as mentioned earlier, the experimental setup and method used allow for a determination of T_5 within less than 10 K. The second source of uncertainty is typically smaller than the uncertainty in the temperature, and is neglected. Overall, the total uncertainty in τ_{ign} reported in this study is estimated to be 10% (which also includes the minimal temperature variation with facility dP/dt).

Results and Discussion

Equivalence ratio effect. The equivalence ratio effects on ammonia ignition delay times are visible in Fig. 45 at pressures around 1.4 atm (a), 11 atm (b), and 30 atm (c). As can be seen, at pressures of 11 atm and above, the ignition delay time obtained at ϕ = 1.0 and 2.0 are very similar, while τ_{ign} obtained at ϕ = 0.5 are shorter (by a factor around 1.5). At the lowest pressure investigated, around 1.4 atm (a), the equivalence ratio seems to have only a moderate effect on τ_{ign}. At the stoichiometry and at this low-pressure condition, ignition delay times seem to be longer than for the other conditions but τ_{ign} at ϕ = 0.5 are similar at high temperatures while τ_{ign} compare with those obtained at ϕ = 1 on the low-temperature side. The activation energies (Ea) extracted from Fig. 45 show that Ea does not vary much with the equivalence ratio at 11 atm and above (Ea = 39.5, 40.1 and 40.1 kCal/mol at 11 atm for ϕ = 0.5, 1.0 and 2.0, respectively and Ea = 42.5, 42.0 and 44.1 kCal/mol at 30 atm for ϕ = 0.5, 1.0 and 2.0, respectively). However, it seems that Ea increases with the equivalence ratio for the lowest pressure investigated: Ea = 44.6, 51.7 and 56.3 kCal/mol for ϕ = 0.5, 1.0 and 2.0, respectively, at 1.4 atm.

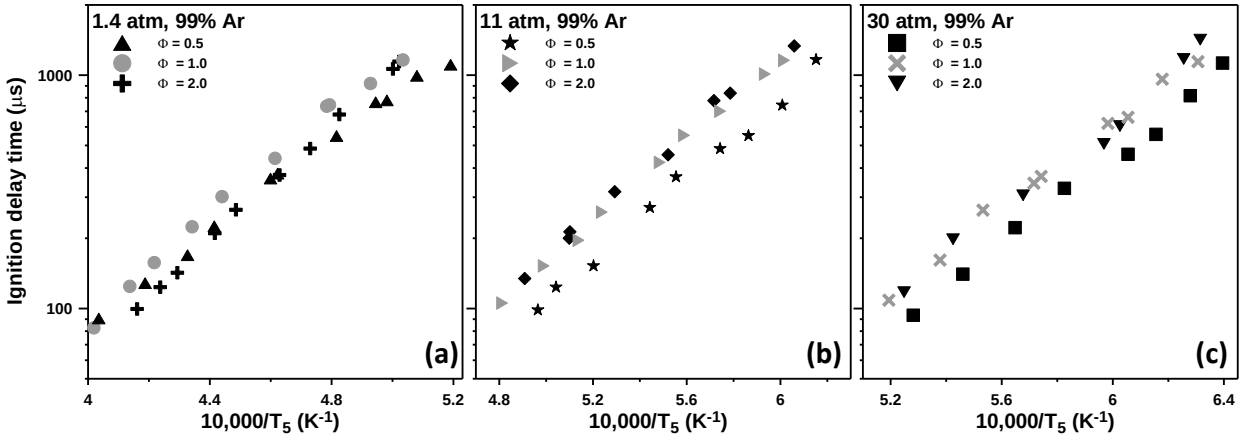

Fig. 45 Effects of the equivalence ratio on the ignition delay time of NH_3 mixtures diluted in 99% Ar at around 1.4 atm (a), 11 atm (b), and 30 atm (c).

Pressure effect. As can be seen in Fig. 46 (a-d), there is an important effect of pressure on the ignition delay time, for all the equivalence ratios and Ar dilution studied. Indeed, it is visible that the ignition delay time decreases with the increase in the pressure. A factor around 7 is found between τ_{ign} obtained at 1.4 and 11 atm at 2000 K for all conditions investigated, while factors of

1.8, 1.9, and 2.2 were found at 1700 K between τ_{ign} obtained at 11 and 30 atm for ϕ = 0.5, 1.0 (at both dilution level), and 2.0, respectively.

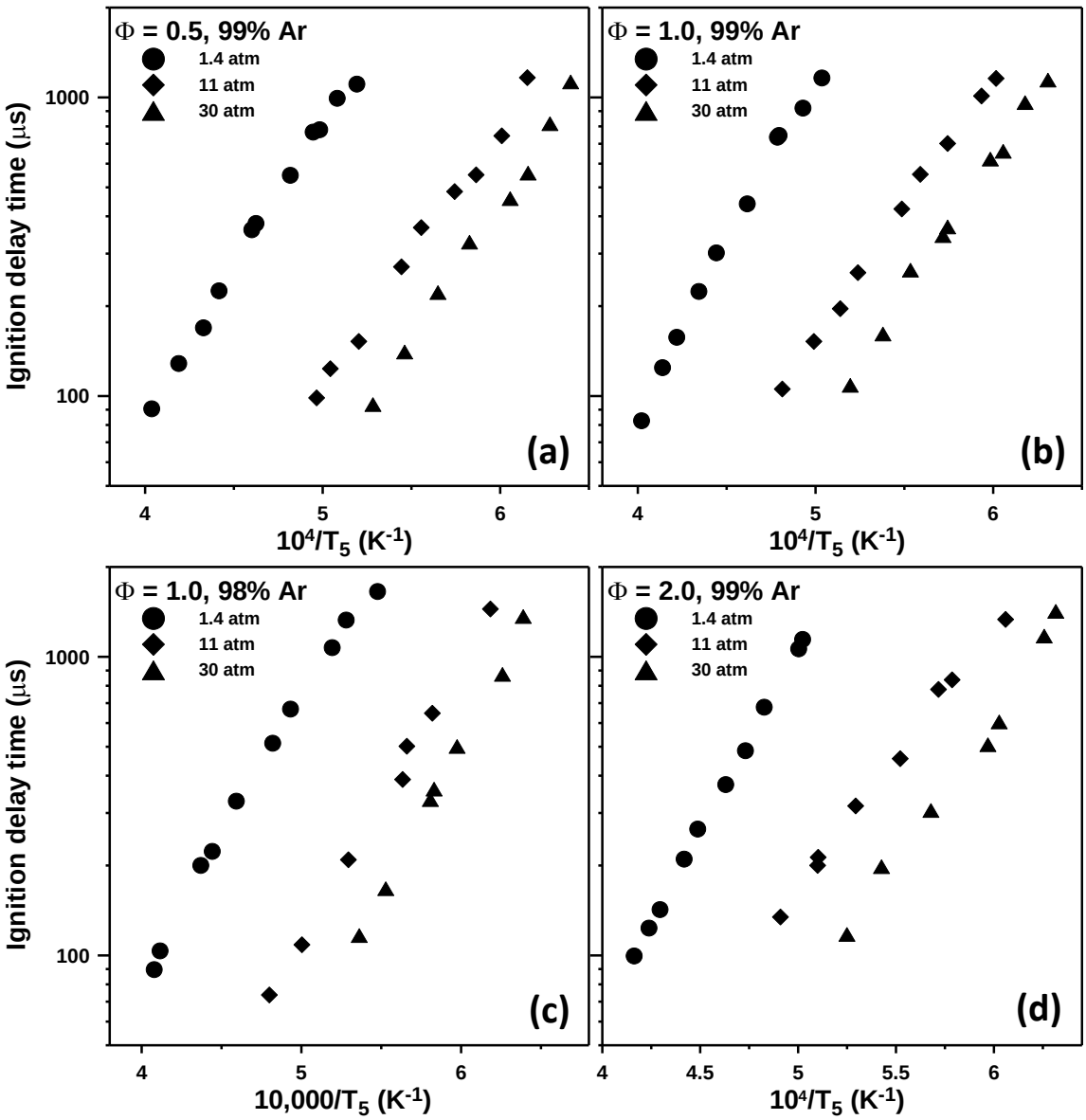

Fig. 46 Effects of the pressure on the ignition delay time of NH_3 mixtures diluted in 99% Ar at around 1.4 atm (a), 11 atm (b) and 30 atm (c).

Fuel Concentration Effect. By comparing the data obtained at ϕ = 1.0 for the 98% and 99%dilutions in Ar, Fig. 47, one can see the effect of the dilution level on the ignition delay time. As can be seen in this figure, at around 1.4 atm (a), the ignition delay time is typically shorter for the 98% dilution case. However, the ignition delay times tend to converge toward a similar value as the temperature increases, and it can be seen that τ_{ign} are similar above 2270 K. For higher pressure, 11 atm (b) and 30 atm (c), the ignition delay times are also shorter for the lowest dilution ratio and also tend to converge toward a similar value at a given temperature. However,

at these high pressures, one can see that ignition delay times converge toward the same value for the lowest temperatures investigated. Activation energies for the mixtures with 98% Ar dilution are 42.0, 43.0, and 46.7 kCal/mol at 1.4, 11, and 30 atm, respectively. These values compare with the value obtained for the 99% Ar dilution, except for the low-pressure case where Ea is higher for the highest dilution level (51.7 kCal/mol).

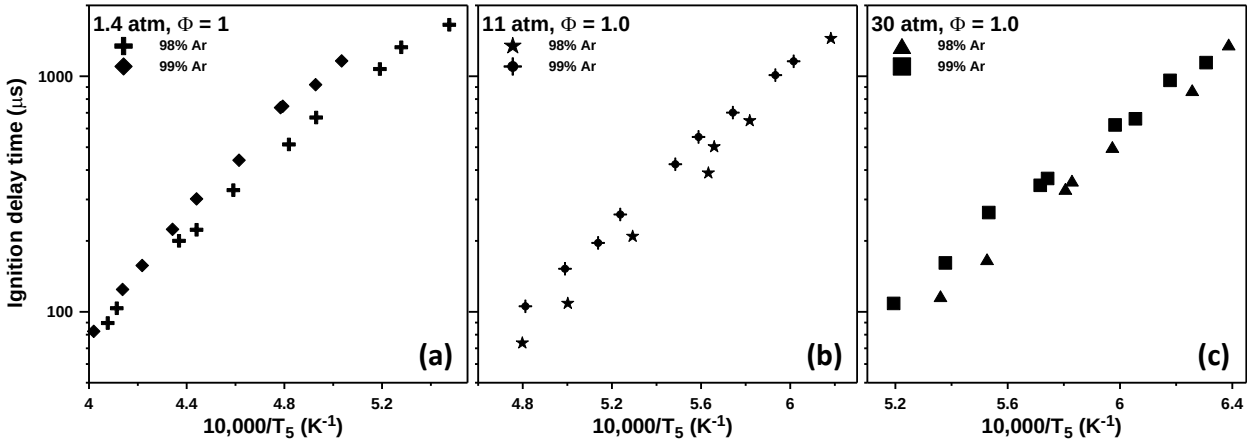

Fig. 47 Effect of the dilution (98 and 99% Ar) on the ignition delay time of NH_3 at around 1.4 atm (a), 11 atm (b), and 30 atm (c) at $\phi = 1.0$.

Using the shock-tube data presented herein, it was possible to derive the following correlation ($r^2 = 0.955$):

$$\tau_{ign}(\mu s) = 16.81.10^{-3}\varphi^{0.18}P^{-0.89}\exp\left(44.11\ (kCal)/RT_5\right)$$

Models Comparison. To assess the validity of the aforementioned detailed kinetics models, data from this study were modeled with mechanisms available in the literature. To do so, whenever necessary, the OH* model from Hall and Petersen (2006) was merged to these detailed kinetics mechanisms. Due to the large differences in the ignition delay time and shape of the computed OH* profiles with the profiles obtained experimentally, it was found necessary to add the reaction $N_2O + H = N_2 + OH^*$ from Hidaka et al. (1985) to the OH* mechanism from Hall and Petersen (2006). Some representative experimental profiles obtained at various conditions have been modeled using the mechanism from Dagaut et al. (2008) along with the OH* chemistry from Hall and Petersen (2006) with and without the reaction from Hidaka et al. (1985). These profiles are visible in Fig. 48 and, as can be seen, this combination of reactions allow for a good modeling of both the experimental profiles and ignition delay times, whereas a strong disagreement in the shape ((a) and (c)) and in the ignition delay time was observed without the OH* formation from N_2O and H. Note that the normalized OH* profile does not reach 1 in Fig. 48(c) because the computed OH* profile is increasing after the visible peak and reach its maximum value after the time frame of Fig. 48(c).

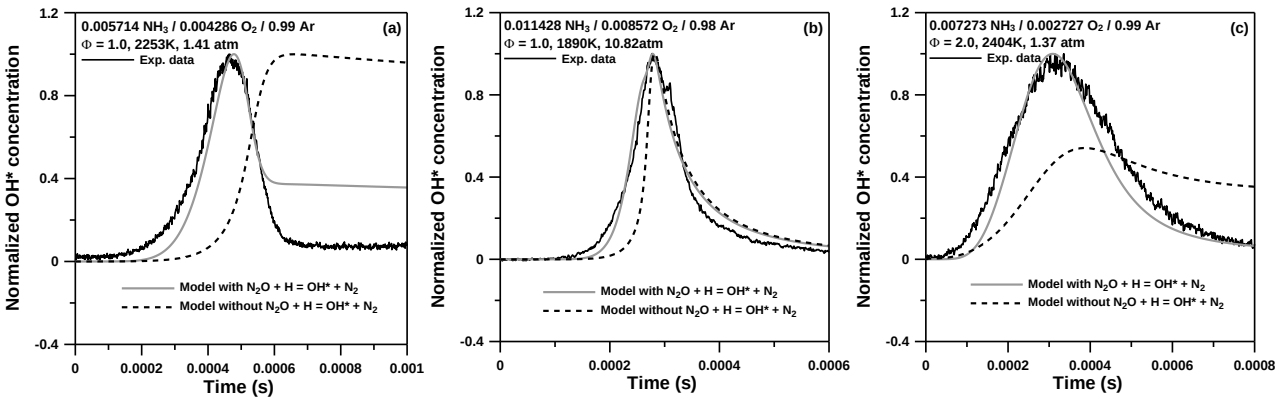

Fig. 48 Comparison of the temporal evolution of the experimental and computed OH* profiles. Model: Dagaut et al. (2008) along with the OH* chemistry from Hall and Petersen (2006) with and without the reaction from Hidaka et al. (1985), for various conditions representative of the present study.

Using this complete OH* sub-mechanism, the comparison between some selected and representative data from this study and the models is visible in Fig. 49. Note that the results from the mechanism of Smith et al. (1999), (GRI 3.0 mechanism) are not included in this figure. Indeed, this mechanism does not contain the dissociation reaction $NH_3 + M = NH_2 + H + M$. This reaction is very important to initiate the combustion of NH_3. As a result, this mechanism is significantly too slow, from at least one order of magnitude, compared to the experimental data. As can be seen in Fig. 49, the mechanism of Dagaut et al. (2008) is predicting the experimental data with high accuracy. The predicted ignition delay times are well captured for pressures higher than 1.4 atm, whatever the ammonia concentration and the equivalence ratio. At around 1.4 atm, however, the model tends to be slightly under-reactive but is still the closest of the mechanisms. The model of Dagaut and Nicolle (2005), although too reactive, also provides relatively acceptable results. Then the model of Miller and Bowman (1998) generally presents a too-high activation energy and mediocre prediction of τ_{ign}. The other mechanisms are somewhat close to each other in terms of predictions and are significantly too reactive. However, note that the mechanism of Duynslaegher et al. (2012) was developed for low-pressure conditions only, and that the model of Mével et al. (2009) is essentially a model describing the combustion of H_2/N_2O mixtures but with an ammonia sub-mechanism. The results in Fig. 49 are representative of the results obtained for the other conditions investigated.

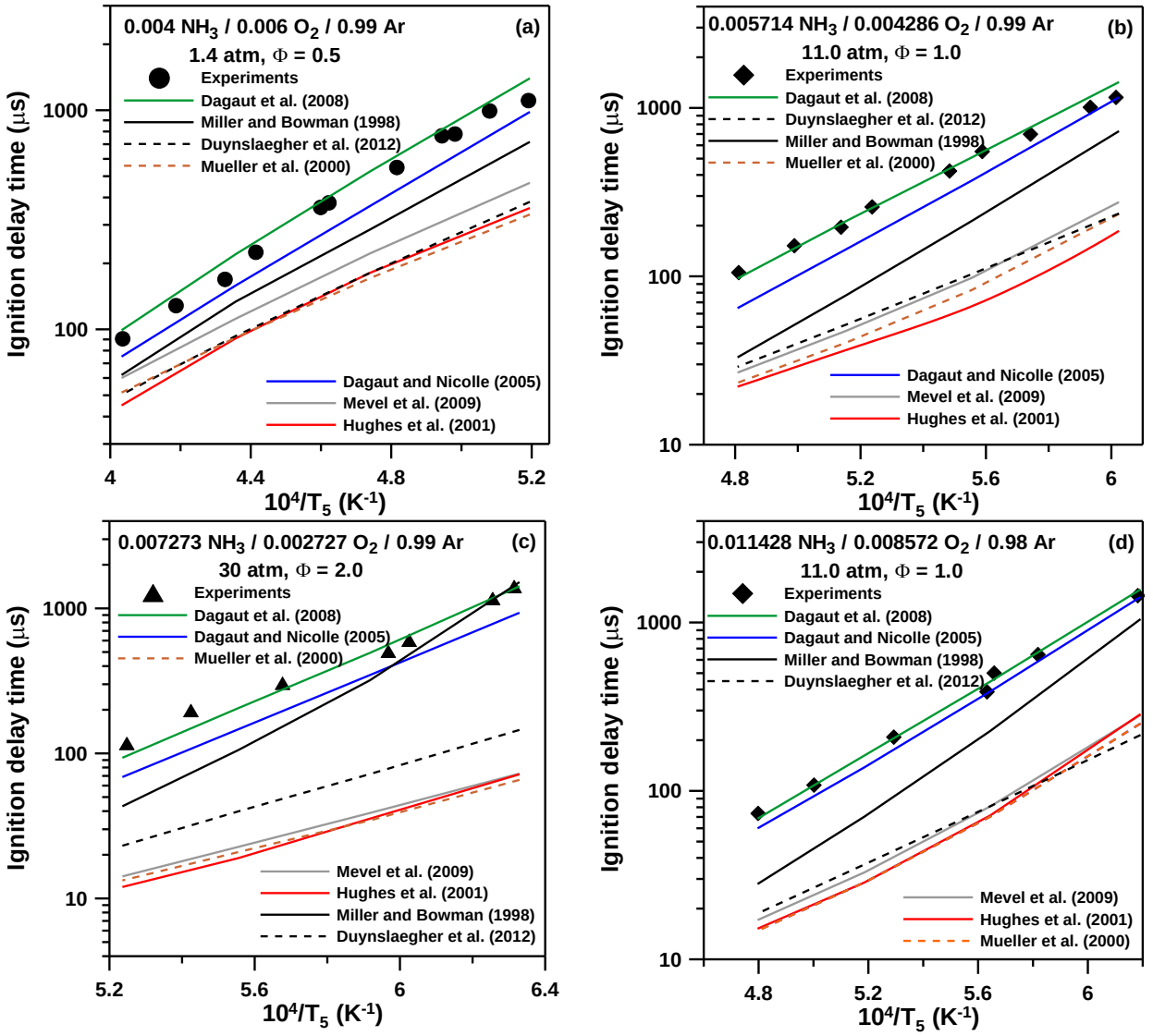

Fig. 49 Comparison between models from the literature and selected, representative data from this study. (a): 1.4 atm, ϕ = 0.5, 99% Ar; (b): 11.0 atm, ϕ = 1.0, 99% Ar; (c): 30 atm, ϕ = 2.0, 99% Ar; (d): 11.0 atm, ϕ = 1.0, 98% Ar.

As seen previously, the N_2O chemistry seems to be of great importance for the NH_3 combustion as the reaction $N_2O + H = N_2 + OH^*$ is critical for the determination of the ignition delay time. To assess the validity of the N_2O sub-mechanism in the mechanism of Dagaut et al. (2008), $H_2/O_2/N_2O$ results from Mathieu et al. (2012) were modeled. As can be seen in Fig. 50, the model of Dagaut et al. (2008) does not predict very well these data and is significantly under-reactive. To better estimate whether this discrepancy was due to the H_2/O_2 sub-mechanism or to the N_2O sub-mechanism, the hydrogen mechanism from Kéromnès et al. (2013) was merged to the model of Dagaut et al. (2008). The same H_2 mechanism is used in the work of Mathieu et al. (2012). As can be seen, results are significantly improved using this H_2 mechanism. However, the predicted ignition delay times are now slightly too short. Although acceptable, the predictions could probably be improved. Note that this replacement of H_2/O_2 chemistry has nearly no effect on the predictions for NH_3 ignition. A future work will then be needed to

improve the model of Dagaut et al. (2008) merged with the H_2/O_2 mechanism from Kéromnès et al. (2013). The aim of this model will be then to model NH_3 data from this study and the literature as well as the H_2/NO_2 [Mathieu et al. (2013)] and H_2/N_2O [Mathieu et al. (2012)] data to propose a consistent base model. This base model for mixtures involving H_2 and NH_3/NOx species will then later be extended to hydrocarbons/NH_3/NOx interactions.

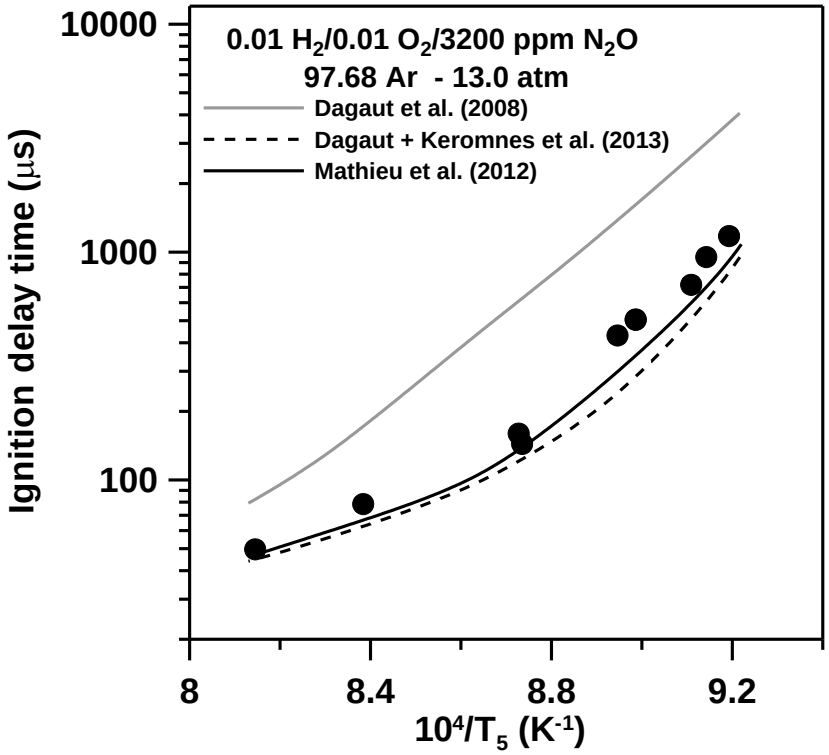

Fig. 50 Comparison between the 0.01 H_2 / 0.01O_2 / 0.0032 N_2O / 0.9768 Ar data at around 13 atm from Mathieu et al. (2012) with the models of Dagaut et al. (2008), the model of Dagaut et al. (2008) merged with the H_2 mechanism from Kéromnès et al. (2013) and the model from Mathieu et al. (2012).

HYDROGEN SULFIDE OXIDATION KINETICS

It is well known that some impurities, even in very low concentration, can induce measurable and sometimes large changes in the combustion properties of a fuel (see Glarborg (2007) for N, S, Cl, and K/Na species). Amongst these impurities, H_2S is a common one that can be found in syngas produced from biomass or coal (up to 1% mol. [Xu et al., 2011]), but can also be present in natural gases (up to 80% v/v [Cerru et al., 2006]) in addition to being a by-product of the oil industry. Hydrogen sulfide and SO_2 are generally removed through a sulfur recovery procedure that uses the modified Claus process ($3\ H_2S + {}^3/_2\ O_2 \rightarrow SO_2 + H_2O + 2\ H_2S$ (1173-1473 K) followed by $2\ H_2S + SO_2 \rightleftarrows {}^3/_2\ S_2 + 2\ H_2O$ (440-640K)). Unfortunately, due to both the limited available literature data (see Cerru et al. (2006) and reference herein) and the very large number of sensitive reactions with significant rate uncertainty [Zhou et al., 2013], the high-temperature chemistry of sulfur species is still poorly understood. This lack of understanding leads to difficulties in the design of emissions control and energy production (gas turbine using syngas) processes.

To better understand the high-temperature chemistry of H_2S and to set a base for the comprehension of the interactions between H_2S and hydrocarbons, a detailed knowledge of the interactions between H_2S and the H_2/O_2 system is of paramount importance. Indeed, the H_2/O_2 sub-mechanism is critical for the combustion of hydrocarbons as it contains many important elementary reactions involving radicals (H, O, OH, HO_2) which play a great role at every stage of the hydrocarbon oxidation process.

However, to the best of our knowledge, there is only one study on the interactions between H_2/O_2 and H_2S. These interactions have been investigated in a shock tube at low pressure and high temperatures by Bradley and Dobson (1967), with a relatively low level of Ar dilution, 86-88% by volume. Note that the body of work on H_2S combustion itself is also rather limited. The earliest work (before the 1970's) on sulfur species is summarized in Cullis and Mulcahy (1972) and, more recently, the high-pressure shock-tube ignition delay time measurements in air by Frenklach et al. (1981) and a few studies on thermal decomposition behind reflected shock waves [Bowman and Dodge, 1977]; or in flow reactors [Zhou et al., 2013; Binoist et al., 2003] have appeared. However, for the latter technique, the study of Zhou (2009) proved the possibility of having catalytic effects by silica surfaces on H_2S, resulting in misleading results such as in Binoist et al. (2003). These catalytic effects seem to be suppressed after a B_2O_3 coating is applied, even though Zhou et al. could not prove that this coating has no effect on H_2S oxidation reactivity. Hence, they concluded their recent study by underlining the need for improvements in both their experimental setup and the sulfur mechanism they developed [Zhou et al., 2013].

To investigate and clarify the interactions between the H_2/O_2 and H_2S sub-systems, the main aim of the present study was to acquire ignition delay times from $H_2/O_2/H_2S$ mixtures in dilute conditions (around 98% Ar) using a shock tube for pressures from around 1.6 atm up to around 33 atm. Note that the shock tube is a technique well known for its ability to perform high-temperature chemical kinetic investigations without wall surface effects [Tsang and Lifshitz, 2001], avoiding the possible catalytic effects often observed with silica in flow reactors. The present paper is outlined as follows. Details of the experiments conducted for mixtures of H_2/O_2 in Ar seeded with various amount of H_2S are presented, and the results are compared to recent measurements obtained with neat hydrogen mixtures (under similar conditions and in the same

experimental apparatus [Kermones et al., 2013]. Modern, detailed kinetics models are then used to predict these data. Finally, a detailed kinetics model was built using existing models from the literature and is outlined herein; this model is then used to help explain the experimental results of this study.

Experimental Procedure

Experiments were carried out in a stainless steel, single-diaphragm, shock tube (15.24-cm i.d., 4.72-m long for the driver and 7.62-cm i.d., 2.46-m long for the driven section). The inside of the driven section was polished to a surface finish of 1 μm root mean square roughness (RMS) or better. Five PCB P113A piezoelectric pressure transducers alongside the driven section and mounted flush with the inner surface were used in association with four Fluke PM-6666 timer/counter boxes to measure the incident-wave velocities. A schematic of the shock-tube setup is provided elsewhere [Mathieu et al., 2012]. A curve fit of the four incident wave velocities was used to determine the incident wave speed at the endwall location. Post reflected-shock conditions were obtained using this extrapolated wave speed in conjunction with one-dimensional shock relations and the initial conditions at the test region. This method was proven to maintain the uncertainty on the temperature determination behind reflected shock waves (T_5) below 10 K [Petersen et al., 2005]. Test pressure was monitored by one PCB 134A transducer located at the end wall and one Kisler 603 B1 located in the same plane as the observation window (Sapphire, 16 mm from the endwall). Polycarbonate diaphragms were used for test pressures of 1.6 and 13 atm (0.25-mm and 2 × 1.02-mm thickness, respectively), while pre-scored aluminum diaphragms (2.29-mm thickness) were used for the 33-atm experiments. When polycarbonate diaphragms were used, a cross-shaped cutter was employed to facilitate breakage of the diaphragm and to prevent diaphragm fragments from tearing off. Helium was used as the driver gas during this study.

The driven section was vacuumed down to 10^{-3} Pa or lower using a roughing pump and a Varian 551 Turbomolecular pump prior to every run. The pumping time between experiments was minimized using a pneumatically driven poppet valve matching the inside diameter of the driven section and allowing for a passage of 7.62-cm diameter between the vacuum section and the driven tube. The pressure was measured using two MKS Baratron model 626A capacitance manometers (0-10 Torr and 0-1000 Torr) and an ion gauge for high vacuums. Test mixtures were prepared manometrically in a mixing tank of 3.05-m length made from stainless steel tubing with a 15.24-cm ID. The pressure in the mixing tanks was measured using a Setra GCT-225 pressure transducer (0-17 atm). The mixing tank is connected to the vacuum system and can be pumped down to pressures below 10^{-4} Pa. The gases (H_2 and O_2 (Praxair, 99.999%), H_2S (Praxair (99.9% purity), 1.01% diluted in Ar (99.999% purity)) and Ar (Acetylene Oxygen Company, 99.999%)) were passed through a perforated stinger traversing the center of the mixing tank to allow for rapid, turbulent mixing. To further ensure homogeneity through diffusion processes, mixtures were allowed to rest for at least 45 minutes prior to making the first run. No difference in the results was observed for longer mixing times. Conditions investigated during this study are provided in Table 16. All mixtures had an equivalence ratio (ϕ) of 0.5.

Table 16 Experimental conditions investigated behind reflected shock waves.

Mixture composition (mole fraction)	T_5 (K)	P_5 (atm)	Reference
0.01 H_2 / 0.01 O_2 / 0.98 Ar	960-1625	1.65 ± 0.15 atm	[Keromnes et al., 2013]
	1085-1245	13.3 ± 1.0 atm	
	1160-1270	32.8 ± 1.5 atm	
0.01 H_2 / 0.01 O_2 / 0.0001 H_2S / 0.9799 Ar	1045-1575	1.83 ± 0.2 atm	This study
	1100-1260	12.9 ± 0.5 atm	
	1160-1270	34.1 ± 1.5 atm	
0.01 H_2 / 0.01 O_2 / 0.0004 H_2S / 0.9796 Ar	1180-1650	1.70 ± 0.1 atm	This study
	1090-1370	12.8 ± 0.6 atm	
	1150-1295	35 ± 1.0 atm	
0.01 H_2 / 0.01 O_2 / 0.0016 H_2S / 0.9784 Ar	1305-1860	1.63 ± 0.05 atm	This study
	1150-1430	12.2 ± 0.6 atm	
	1110-1360	32.3 ± 3.0 atm	

The ignition delay time (τ_{ign}) was measured using the chemiluminescence emission from the $A_2\Sigma^+ \rightarrow X_2\Pi$ transition of the excited-state hydroxyl radical (OH*) using an interference filter centered at 307 ± 10 nm with a Hamamatsu 1P21 photomultiplier tube. The ignition delay time is defined herein as the time between the passage of the reflected shock wave, indicated by a pressure jump in the signal delivered by the sidewall pressure transducer, and the intersection of lines drawn along the steepest rate-of-change of OH* de-excitation and a horizontal line which defines the zero-concentration level, as can be seen in Fig. 51. Time zero is defined as the time of arrival of the reflected shock wave at the sidewall measurement location. All of the data signals were recorded through a 14-bit GageScope digital oscilloscope with sampling rates of 1 MHz or greater per channel.

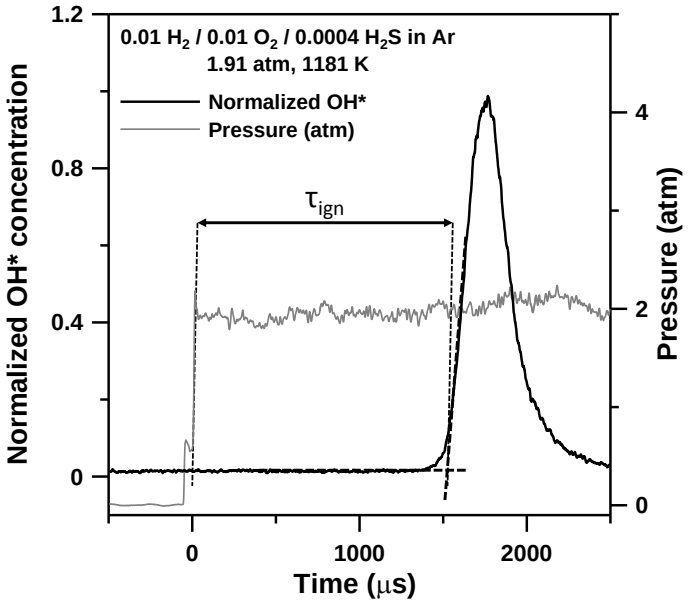

Fig. 51 Typical OH* and pressure profiles obtained during this study and determination method for the ignition delay time.

Two sources of uncertainties lead to a global uncertainty of about 10 % in the ignition delay time. These are the uncertainty in the determination of the temperature behind the reflected shock wave (T5) and the uncertainty associated with the determination of the steepest rate of change from the OH* profile. The temperature determination is the most important uncertainty and is related to: 1) the determination of the initial post-shock T_5 from the measured incident-shock velocity (< 10 K, as mentioned above), and 2) non-ideal boundary layer effects which are linked to the change in pressure (dP_5/dt) behind the reflected shock wave. These non-ideal effects were determined to be less than 2% P_5 increase per ms for all experiments. The corresponding increase in temperature for these dP_5/dt levels would be less than 10 K for the longest ignition delay times reported herein. The recent study of Burke et al. (2012) confirms this assessment using the data of Pang et al. (2009) for H_2-O_2 mixtures highly diluted in argon. Indeed, it can be seen in Burke et al. (2012) that the difference in the ignition delay time of hydrogen mixtures induced by pressure increases of 2% and 6.5% per ms become noticeable only for times longer than 2 ms, a time larger than the longest ignition delay time reported in the present study. The second source of uncertainty associated with the determination of the steepest rate of change from the OH* profile is typically smaller than the uncertainty in the temperature and can be neglected. Ignition delay time measurements along with corresponding conditions behind reflected shock waves are provided as supplementary material.

Experimental Results

H_2S Concentration Effects on the Ignition Delay Time. The effects of H_2S addition on the ignition delay time of a H_2/O_2/Ar mixture at around 1.6 atm are visible in Fig. 52. As can be seen, the addition of H_2S notably increases τ_{ign} at this pressure condition. An addition of only 100 ppm nearly doubles the ignition delay time around 1050 K, compared to the neat mixture. However, at higher temperatures (above 1350 K), one can see that there is almost no influence of this small H_2S addition. For a 400-ppm H_2S addition, the ignition delay time is further increased but follows the same trend as the 100-ppm addition. The reactivity is indeed much more decreased on the low-temperature side (a factor of 4 is observed at 1175 K compared to the mixture without H_2S) than on the high-temperature side (an increase in the delay time by 25% at 1640 K). At 1600 ppm of H_2S, the ignition delay time is greatly increased over the whole range of temperatures investigated. This increase is still more important at low temperature than at high temperature; the ignition delay time is increased by a factor of 7 at 1300 K and by a factor of 3 at 1640 K. Note that the activation energy (Ea) derived from the data in Fig. 51 seems to be increased by H_2S addition for concentrations up to 400 ppm (Ea = 13.8 kcal/mol for the neat mixture and 17.3 kcal/mol and 21.8 kcal/mol for the 100 ppm and 400 ppm H_2S additions, respectively). Above this concentration of 400 ppm H_2S, it seems that the activation energy no longer increases with H_2S concentration (Ea = 21.6 kcal/mol for the 1600-ppm H_2S addition).

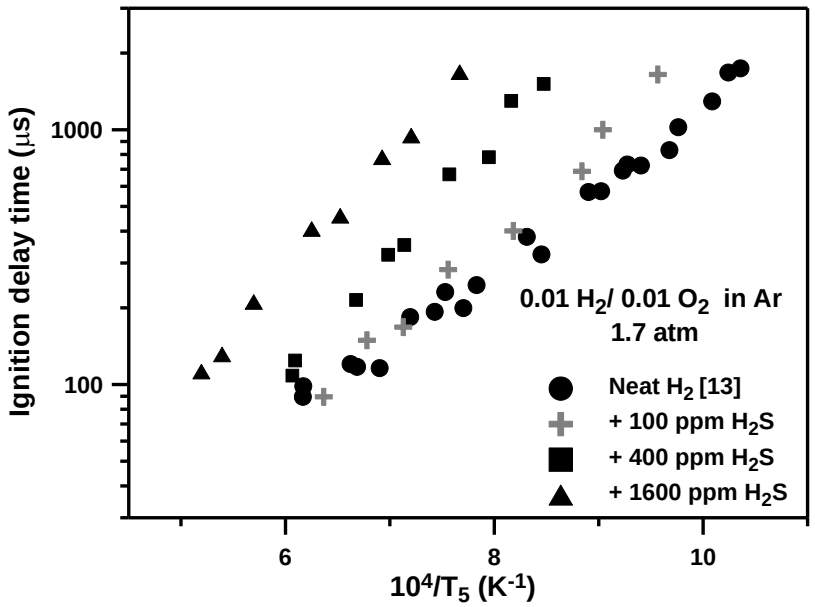

Fig. 52 Evolution of the ignition delay time with the inverse of the temperature at around 1.6 atm for H_2/O_2 mixtures with various concentrations of H_2S.

At a higher pressure, around 13 atm, it is visible in Fig. 53 that H_2S addition also has a dramatic effect on the ignition delay time of H_2/O_2 mixtures. Nonetheless, it is interesting to see that the effect on τ_{ign} takes place mainly on the high-temperature side at this pressure condition. Hence, ignition delay times are the same for the neat mixture and the mixture with 100 ppm of H_2S for temperatures below 1135 K. At the highest temperature investigated, 1240 K, the ignition delay time is increased by around 65% (from to 55 to 90 μs) by the 100-ppm H_2S addition. With an

addition of 400 ppm of H_2S, the ignition delay time is multiplied by two at around 1100 K and increased by a factor of 4.5 at 1220 K. At 1600 ppm of H_2S, the ignition delay time is increased between 8 and 10 times over the range of temperature that is common between the neat and 1600-ppm mixtures. Another interesting result associated with the addition of H_2S is the fact that the curvature of the data visible for the neat H_2 mixture is no longer observed when H_2S is present. Also, although a unique activation energy cannot be directly derived from the neat H_2/O_2 data due to this slight curvature, one can see that Ea decreases as the H_2S concentration increases: Ea = 46.7 kcal/mol for the 100-ppm H_2S addition, 31.6 kcal/mol for the 400 ppm addition, and 27.4 kcal/mol at 1600-ppm H_2S.

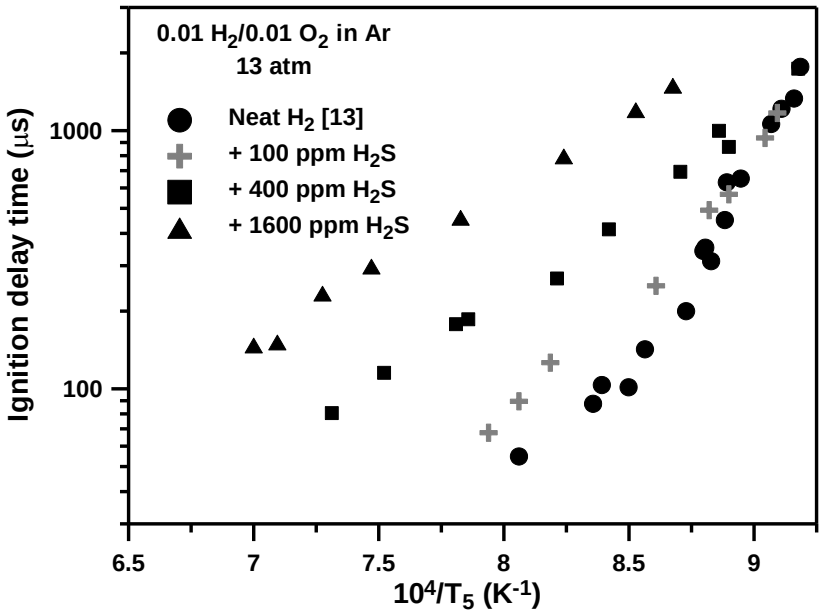

Fig. 53 Evolution of the ignition delay time with the inverse of the temperature at around 13 atm for H_2/O_2 mixtures with various concentrations of H_2S.

At higher pressure (Fig. 54), as also seen in the data at 13 atm, the effects of H_2S addition are mostly visible on the high-temperature side. It is nonetheless visible that there is little difference in ignition delay times more or less around 1150 K, whatever the H_2S concentration. An addition of 100 ppm of H_2S leaves the ignition delay time nearly unchanged, even if τ_{ign} seems to be slightly shorter on the low-temperature side. With a larger addition of H_2S, 400 ppm, the ignition delay time is significantly increased at high temperature (by a factor near to 2.5 at 1265 K), whereas τ_{ign} are slightly lower than the ones from the neat H_2 mixture below 1190 K. This behavior is amplified for the 1600-ppm H_2S addition, with an increase in τ_{ign} by a factor of more than 6 at high temperatures. These changes in the slope of the data are visible in the activation energy derived from Fig. 54: Ea = 90.4 kcal/mol for the neat mixture, 72.6 kcal/mol for the 100-ppm H_2S addition, 52.9 kcal/mol for the 400-ppm addition, and 32.2 kcal/mol at 1600-ppm H_2S.

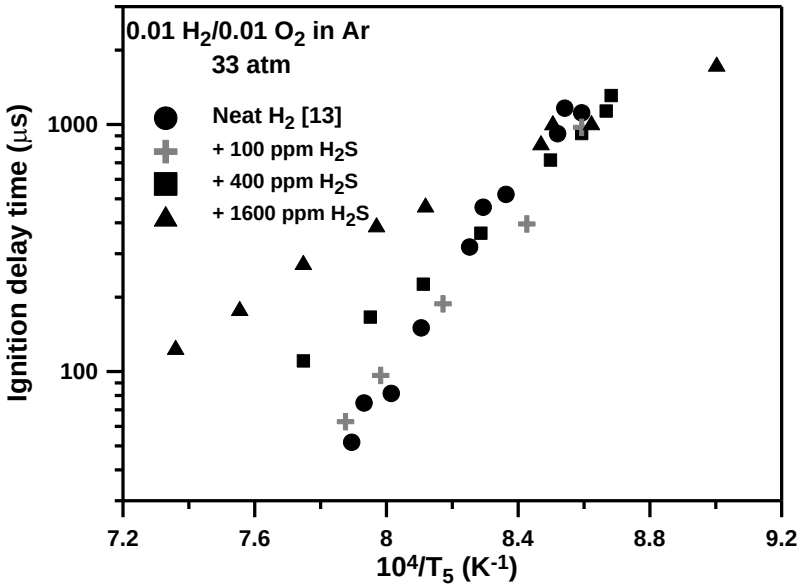

Fig. 54 Evolution of the ignition delay time with the inverse of the temperature at around 33 atm for H_2/O_2 mixtures with various concentrations of H_2S.

Pressure Effects on the Ignition Delay Time. The effect of pressure on the ignition delay time can be seen in Fig. 55 for the neat mixture and for the mixture doped with 1600 ppm of H_2S. As can be seen, the typical pressure behavior for hydrogen, explained in detail in [Kermones et al., 2013], is no longer visible when 1600 ppm of H_2S are added. Indeed, it appears that the 1600-ppm H_2S mixture behaves like a hydrocarbon would behave when the pressure is increasing: a decrease in the ignition delay time is observed, proportionally to the increase in pressure.

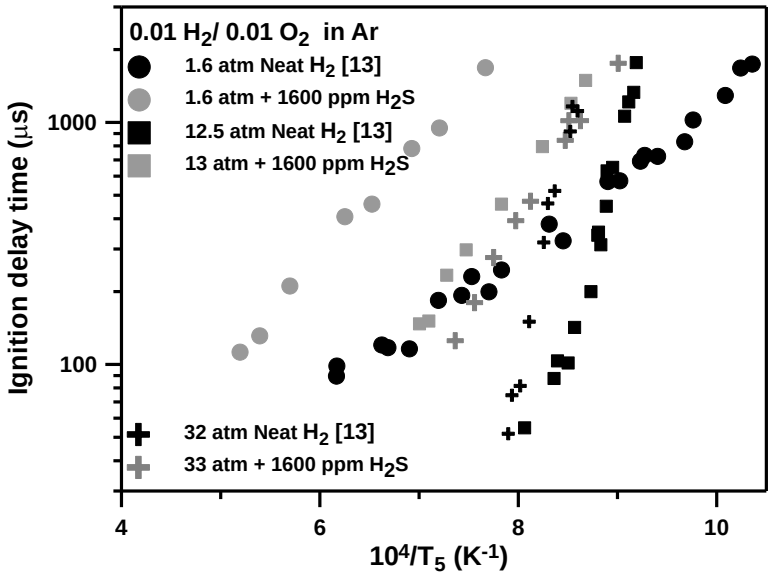

Fig. 55 Evolution of the ignition delay time with the inverse of the temperature at around 1.6, 13, and 33 atm for a neat H_2/O_2 mixture and for a the same mixture doped with 1600 ppm of H_2S.

Comparison with Models from the Literature

The present data were first compared to the following models from the literature which contain sub-mechanisms for H_2, H_2S, and SO_2: the SOx mechanism from Leeds [Hughes et al., 2001], the CO/NO/SO_2 mechanism from Mueller et al. [Mueller et al., 2000], the mechanism on the effect of SO_2 on NO reduction by NH_3 from Dagaut and Nicolle (2005), the reduced mechanism on H_2S pyrolysis and oxidation from Cerru et al. (2005, 2006), and the detailed H_2S mechanism from Zhou et al. (2013). Note that the SOx chemistry from the first three mechanisms is based on the work from Glarborg et al. (1996; 2001; 2003). As can be seen in Fig. 56, the mechanism from Leeds [Hughes et al., 2001] predicts well the data at 1.6 atm (Fig. 56 (a), (d) and (g)) and relatively well the data at higher pressure for the 100-ppm H_2S case (Fig. 56 (b) and (c)). However, at around 13 atm and 33 atm, data for H_2S concentrations larger than 100 ppm are poorly predicted, especially on the low-temperature side where the model is largely too reactive (a factor of 7 is observed at the lowest temperature for the 33-atm, 1600-ppm case). Similar behavior can be observed for the model from Mueller et al. (2000), even though their model is closer to the data at these low temperatures, high pressures, and high H_2S concentrations (factor of 3.3 at the lowest temperature for the 33-atm, 1600-ppm case). The mechanism from Dagaut and Nicolle (2005) also offers reasonably good predictions at around 1.6 atm and for higher pressure for the 400-ppm H_2S case. However, predictions are not very good for larger (1600 ppm) or smaller (100 ppm) H_2S concentrations, with the τ_{ign} at 100-ppm H_2S being largely over-predicted, whereas the τ_{ign} at 1600 ppm are mostly under-predicted.

The model from Cerru et al. (2005, 2006) predicts relatively well the data at 13 atm with 1600 ppm H_2S. For the other pressure conditions at this concentration, the reactivity of the model seems too low (ignition delay times are too long). The data at 1.6 atm and with 100- and 400-ppm H_2S are relatively well predicted, notably with the lowest H_2S concentration. However, for pressures above 1.6 atm, the model predicts ignition delay times that are significantly too small. These results seem to indicate that the hydrogen chemistry is poorly treated in the model of Cerru et al., especially for the reactions involving HO_2. Finally, the most recent mechanism from Zhou et al. (2013) shows the closest overall agreement with the data over the models tested. However, although predictions are fairly good at 1.6 atm and for the 400-ppm cases (from 1.6 to 33 atm), the other conditions, while better predicted than the other models, are not within a satisfactory agreement with the data. One can notice the need for an increase in the overall reactivity of the model for the conditions at 100 ppm of H_2S, whereas a decrease in the reactivity would be necessary for the 1600-ppm H_2S cases. Thus, the current set of data highlights the need for improving the H_2S chemistry, especially for pressures above 10 atm.

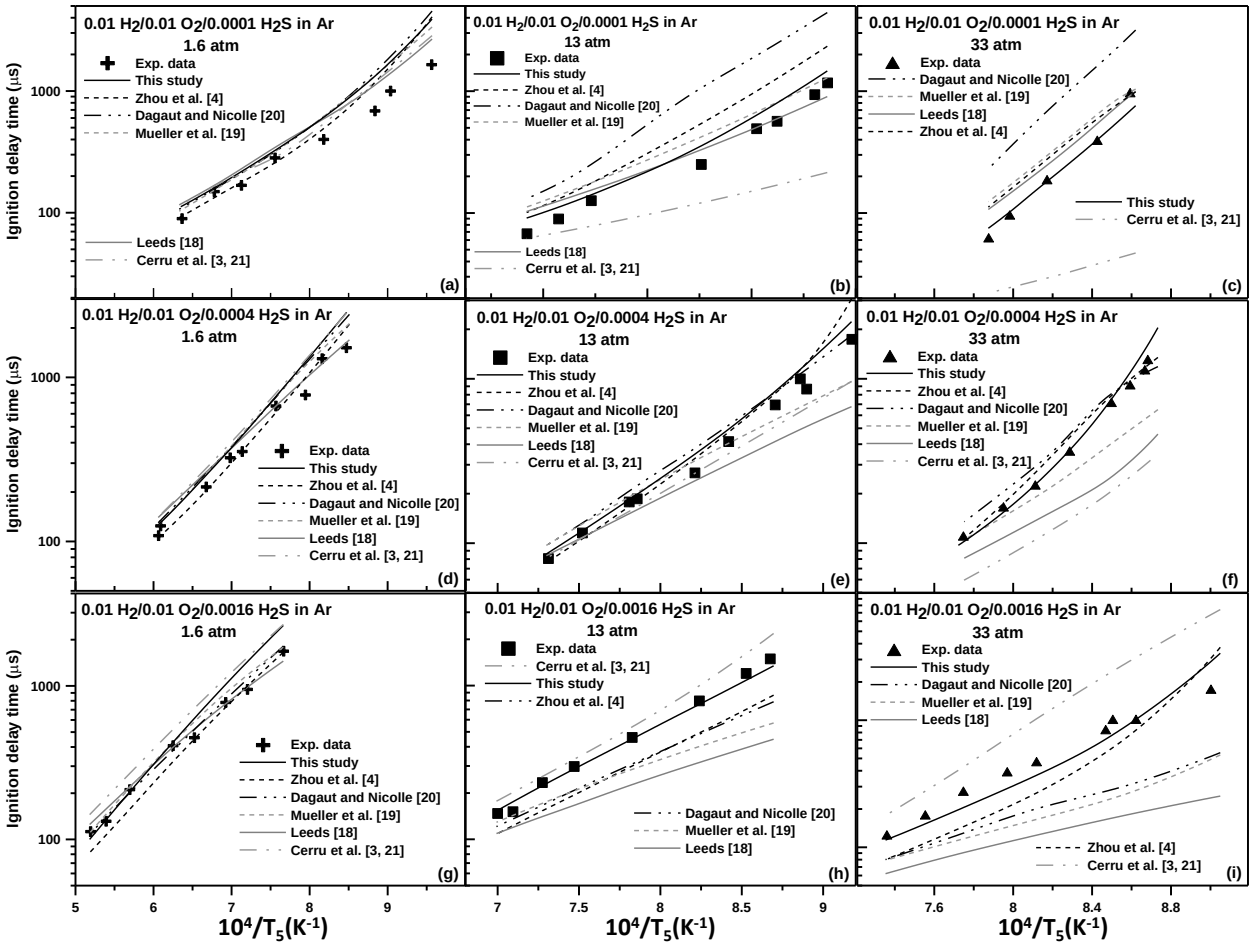

Fig. 56 Comparison between the results of the present study and predictions from several models from the literature. (a) – (c) 100-ppm H_2S addition; (d) – (f) 400-ppm H_2S addition; (g) – (i) 1600-ppm H_2S addition.

Kinetics Model Improvements

To improve the predictions on the new $H_2/O_2/H_2S$ data, the mechanism from Zhou et al. (2013) was selected as a base for the H_2S-related chemistry. Indeed, Fig. 56 shows that this mechanism offers predictions that are, overall, in closer agreement with the data than the other mechanisms available. Also, one can observe the completeness of this mechanism compared to the other models from the literature, especially at the level of the interactions between sulfur-containing species and radicals (through the presence of species like HSSH, HSS, etc. that are coming from the reaction between SH radicals). Although the model from Cerru et al. provides acceptable results when the concentration of H_2S is high or when the pressure is around 1.6 atm, this model was not selected as it does not include the whole S-S chemistry. This S-S chemistry seems to be very important for H_2S oxidation, as mentioned in [Cerru et al., 2005], especially for fuel rich conditions. Also, the model reaction path for the SH radical is still uncertain in the work of Cerru et al. (2005, 2006), while this aspect was covered in more detail by Zhou et al. (2009, 2013). Note that the models of Leeds [Hughes et al., 2001], Mueller et al. (2000), and Dagaut and

Nicolle (2005) do not contain a submechanism for the interactions between sulfur-containing species and radicals.

To improve the model, the H_2/O_2 chemistry of the Zhou et al mechanism was first exchanged with the recent hydrogen mechanism from Kéromnès et al. (2013). This change has nearly no impact on the predictions for the data of Zhou et al. (2013). This modification can be justified by comparing in Fig. 57 the results of the mechanisms considered in this study against the neat $H_2/O_2/Ar$ ignition data recently performed in our laboratory and presented in Kéromnès et al., (2013) (again, the neat H_2/O_2 data have been performed under very similar conditions to the H_2S-doped data from the present study). As can be seen, the mechanism of Kéromnès et al. shows the best agreement with the data over the range of conditions investigated. In more detail, predictions with the mechanism from Kéromnès et al. are in excellent agreement with the data around 13 atm (Fig. 57 (b)), whereas a large discrepancy is observed for the other mechanisms at low temperatures. At around 32 atm (Fig. 57 (c)), the mechanism from Kéromnès et al. offers the best predictions above 1200 K. Below this temperature, the mechanism from Zhou et al. (which contains the H_2 chemistry from Li et al. (2004)) is however closer to the data. The other mechanisms used are notably not reactive enough at this higher-pressure condition, with the exception of the model from Cerru et al. (2005, 2006). Note that, at this high-pressure condition, the experimental slope is better reproduced by the model of Kéromnès et al. than the model from Zhou et al. (2013). These two high-pressure conditions, where the model of Cerru et al. performs very poorly, confirm the former assessment on the ability of this mechanism to represent correctly the HO_2 chemistry.

Finally, at around 1.6 atm (Fig. 57 (a)), one can see that the models are close to each other and within a fair agreement with the data above 1100 K, with the mechanism of Zhou et al. having good agreement, while the other mechanisms are slightly under-reactive. However, below this temperature, the mechanisms of Dagaut and Nicolle, Zhou et al., and Mueller et al. start deviating rapidly and predict ignition delay times that are too long. This overprediction is less the case for the mechanism from Leeds and Kéromnès et al. even though the discrepancy with the data is larger at this low-temperature condition than above 1100 K. Note that the model from Cerru et al. is the only one to not deviate from the data below 1100 K.

The selection of the H_2/O_2 mechanism from Kéromnès et al. along with the H_2S chemistry of Zhou et al. was therefore used in the present effort as a base to further develop the H_2S model. Note that the hydrogen mechanism from Kéromnès et al. also compared more favorably than a large number of H_2/O_2 mechanisms against these shock-tube ignition delay time data, as can be seen in Mathieu et al. (2012).

Using this intermediate base mechanism, sensitivity analyses on OH* were then performed on the high- and low-temperature side of each pressure/H_2S concentration condition to identify the important reactions controlling the ignition of the $H_2/O_2/H_2S/Ar$ mixtures. As also found by Zhou et al. (2013), the model showed large sensitivity to the rates of a significant number of reactions, listed below, for the full set of conditions investigated during this study.

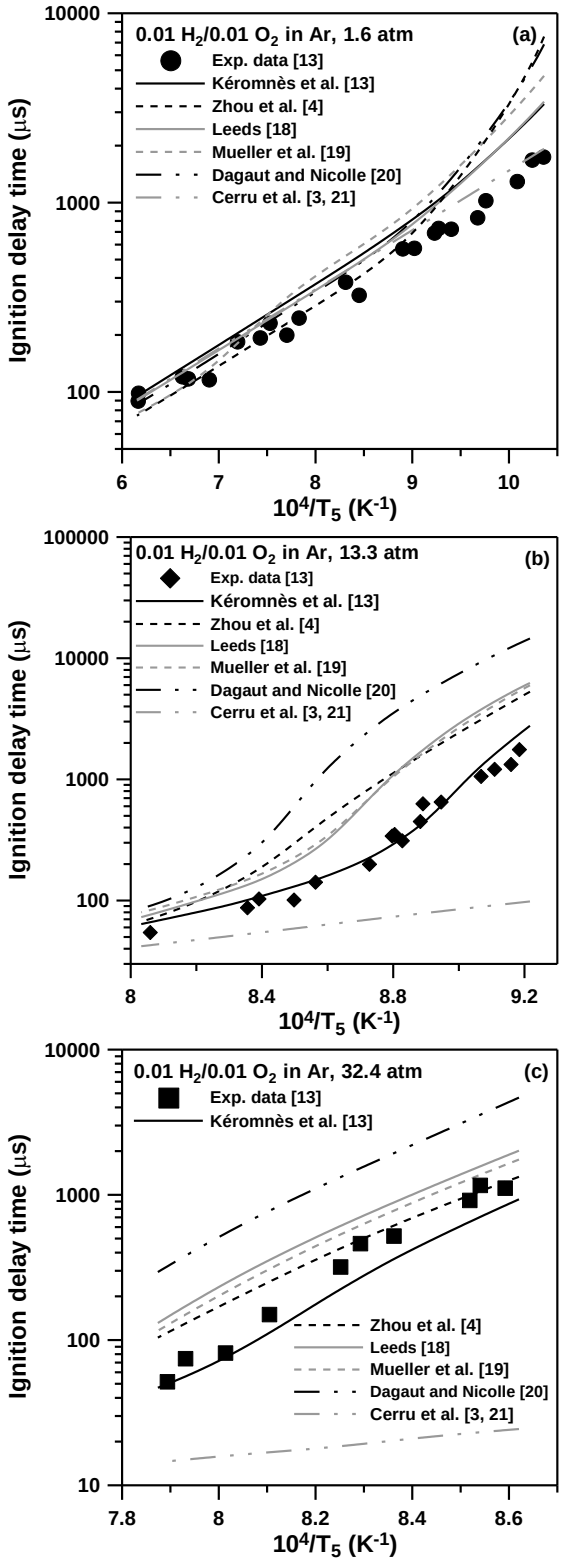

Fig. 57 Comparison between the 0.01 H_2 / 0.01 O_2 /0.98 Ar data from [13] (i.e., no H_2S) and the results provided by the H_2S mechanisms considered in this study and the syngas mechanism from Kéromnès et al. (2013).

$H + O_2 \rightleftarrows O + OH$ (r1)
$H + O_2 (+ Ar) \rightleftarrows HO_2 (+ Ar)$ (r2)
$HO_2 + H \rightleftarrows OH + OH$ (r3)
$H_2S + H \rightleftarrows SH + H_2$ (r4)
$S + O_2 \rightleftarrows SO + O$ (r5)
$SO + O_2 \rightleftarrows SO_2 + O$ (r6)
$SH + HO_2 \rightleftarrows HSO + OH$ (r7)
$SH + HO_2 \rightleftarrows H_2S + O_2$ (r8)
$H_2O_2 + SH \rightleftarrows H_2S + HO_2$ (r9)
$H_2S + S \rightleftarrows SH + SH$ (r10)
$SH + SH (+ M) \rightleftarrows HSSH (+ M)$ (r11)
$S + SH \rightleftarrows S_2 + H$ (r12)
$H + HSS \rightleftarrows SH + SH$ (r13)

Reactions (r1)-(r3) are related to the H_2/O_2 mechanism extensively validated in Keromnes et al. (2013) and are therefore excluded from modification. Similarly, even if the range of validation does not fully cover the conditions investigated in this study, reactions (r4)-(r6) are considered to be relatively well known compared to the other sensitive reactions of the H_2S sub-mechanism. Hence, these reactions have also been left unchanged (see Peng et al. (1999), Lu et al. (2004), and Garland (1998) and the discussions in Zhou (2009) for the value used for (r4), (r5), and (r6), respectively). Hence, improvement to the model was rather focused on the reactions (r7)-(r13) for which the reaction rates can be estimated to be known with less accuracy. During this study, it has been elected to implement only minor variations of the reaction rates considered for change (with a variation no larger than a factor of 3, corresponding to the error factor in the reaction rate calculated in Zhou (2009) and a value also adopted by Zhou et al. (2013) to adjust their mechanism to some experimental conditions in Zhou et al. (2013)). Better results would have been possible with greater freedom, but we chose to stay as close as possible to the reaction rates evaluated via high-level calculations, when no other reasonable option was possible.

Predictions using the intermediate mechanism consisting of H_2/O_2 chemistry from Kéromnès et al. and the H_2S chemistry from Zhou et al. (2013) showed that an increase in the reactivity was needed for the 100-ppm H_2S addition cases below 30 atm, whereas a decrease in the reactivity was needed for the 30-atm cases and for the 1600-ppm H_2S, 10-atm case (predictions at 400-ppm H_2S, 10 atm were relatively accurate). For the 100-ppm addition case, sensitivity analysis also showed that amongst the ten most-sensitive reactions, reactions involving sulfur-containing species were only reactions between sulfur-containing species and a radical from the H_2/O_2 radical pool. However, for higher H_2S concentrations, numerous reactions between sulfur species were sensitive. To reduce the number of parameters to modify at the same time, we first optimized reactions between sulfur-containing species and the H_2/O_2 radical pool ((r7)-(r9)) using the data at 100 ppm H_2S, where the interactions between sulfur species can be considered negligible (no effect on the predictions for the 100-ppm data was observed by modifying the reaction rates of (r10)-(r13)). Then, the data at 1600 ppm of H_2S were used to optimize the remaining reactions (r10)-(r13). In both cases, the 400-ppm data were used to adjust the level of modifications as these data were shown to be sensitive to both the interactions between H_2/O_2 and sulfur species and the interactions between the sulfur-containing species themselves.

Reactions between Sulfur Species and Species from the H_2-O_2 Mechanism. Reaction r7 (SH + HO_2 ⇄ HSO + OH) was the most important promoting reaction involving a sulfur species at low temperature for the 30-atm, 100-ppm H_2S case, making this reaction a good candidate to be adjusted to better fit the data. The reaction rate employed in Zhou et al. (2013) is the value that has been calculated in Zhou (2009). This value is around ten times higher than the value estimated in Alzueta et al. (2001) (which is the value used in the Leeds] and Dagaut and Nicolle mechanisms) and close to the value used in the mechanism of Mueller et al. (2000)] in the range of temperature investigated during the present study. The present study showed that reducing the reaction rate by a factor of three allows for better predictions at high-pressure conditions. The final reaction rate is therefore in closer agreement with the earlier literature [Alzueta et al., 2001] and still within the estimated error reported for the rate calculation in Zhou (2009).

$$k(r7) = 8.2\times10^{7}T^{1.477}\exp(2.17 \text{ kcal mol}^{-1}/RT)$$

$$SH + HO_2 \rightleftarrows H_2S + O_2 \qquad (r8)$$

This reaction channel, not present in the other mechanisms considered in the present study, is an important terminating channel which has a very important inhibiting effect at low-temperature and high-pressure conditions, where the H_2/O_2 chemistry is dominated by H + O_2 (+ Ar) ⇄ HO_2 (+ Ar) (r2). This reaction rate was first estimated by Frenklach et al. (1981). More recently, this reaction rate was calculated by Montoya et al. (2005) and by Zhou (2009). The latest estimation led to a slightly slower reaction rate. Although it would have been interesting to use the fastest reaction rate to decrease the reactivity of the model at low temperature for the 100-ppm, 30-atm case, the present work showed that a small increase in the rate of (r8) has a large impact on the cases at 400- and 1600-ppm H_2S addition, leading to computed ignition delay times that are rapidly significantly too large, whereas the reactivity is not changed much for the 100 ppm, 30-atm case. Therefore, to be able to significantly decrease the reactivity at 100 ppm, 30 atm without jeopardizing the predictions at larger concentrations, this reaction rate was decreased by 1.2:

$$k(r8) = 3.17\times10^{4}T^{2.775}\exp(1.53 \text{ kcal mol}^{-1}/RT)$$

Note that this modification of the reaction rate is well below the estimated error for the calculated value of (r8) (estimated error is a factor of 3 in Zhou (2009)).

$$H_2O_2 + SH \rightleftarrows H_2S + HO_2 \qquad (r9)$$

As mentioned by Zhou (2009), and showed by the sensitivity analysis in the current study for all pressure conditions, the SH + H_2O_2 channel is important to describe the H_2S combustion chemistry under fuel lean conditions. The reaction (r9) was also not included in the other sulfur mechanisms considered in the present study and was only roughly estimated at low pressure and room temperature in Friedl et al. (1985). This reaction has a promoting effect on the ignition delay time under the conditions of the present study and has a smaller impact on the ignition delay time than the two aforementioned reactions between SH and HO_2 ((r7) and (r8)). The calculated reaction rate used in the Zhou et al. (2013) mechanism was divided by two, the final reaction rate being $k(r9) = 2.79\times10^{4}T^{2.823}\exp(-8.67 \text{ kcal mol}^{-1}/RT)$ cm^3 mol^{-1} s^{-1}. Note that in the

study of Friedl et al. (1985), the measured reaction rate at 298 K is $< 5\times10^{-15}$ cm^3 mol^{-1} s^{-1} for the sum of the following reactions:

$$\begin{aligned} H_2O_2 + SH &\rightarrow H_2S + HO_2 \\ &\rightarrow HSOH + OH \\ &\rightarrow HSO + H_2O \end{aligned}$$

At 298 K, the reaction rate calculated by Zhou (2009) is therefore higher than the reaction rate estimated experimentally. Hence, the lower value adopted in the present study brings the reaction rate for (r9) closer to the only measurement available in the literature.

Reactions between Sulfur-Containing Species. The branching reaction r10 ($H_2S + S \rightleftarrows SH + SH$) was found to be the most-sensitive promoting reaction involving sulfur species for the 1600-ppm H_2S cases above 1.6 atm. The value used in Zhou et al. (2013) was calculated in Zhou (2009), whereas the mechanisms of Dagaut and Nicolle and Mueller et al. use the value determined experimentally by Woiki and Roth (1994). However, Shiina et al. (1996) criticized the photolysis of CS_2 at 193 nm as the source of S atoms in the study of Woiki and Roth. Indeed, Shiina et al. found that the photolysis of H_2S was also significant at this wavelength. The generation of S atoms by photolysis of COS at 248 nm as suggested by Shiina et al. apparently avoids these problems. In the present study, the reaction rate calculated in Zhou (2009) was divided by 1.75 to obtain better agreement with the 1600-ppm H_2S data at high pressure.

$$k(r10a) = 4.22\times10^{6}T^{2.297}\exp(-9.01 \text{ kcal mol}^{-1}/RT)$$
$$k(r10b) = 6.74\times10^{17}T^{-1.685}\exp(-5.98 \text{ kcal mol}^{-1}/RT)$$

$$SH + SH (+ M) \rightleftarrows HSSH (+ M) \qquad (r11)$$

The reaction rate for r11 above has never been measured experimentally but was first calculated by Sendt et al. (2002). The calculated reaction rate showed unusual temperature dependence at low temperatures and, because of this unusual temperature dependence, Cerru et al. (2006) estimated this reaction rate by analogy with the reaction $OH+OH +M \rightleftarrows H_2O_2 + M$ from Atkinson et al. (1997) but divided this rate by 2 to match the high-temperature reverse rate suggested by Sendt et al. (2002). More recently, Zhou (2009) performed high-level calculations, and the result indicates that the inclusion of more reaction channels for the intermediate adduct HSSH* was necessary to compute the rate constants. A new reaction rate was then proposed, and this reaction (r11) was found to be of great importance in the experimental conditions, for the 1600-ppm H_2S cases, at pressures of 10 atm and above and for the lowest temperatures, as (r11) was the most-sensitive inhibiting reaction at these conditions with the intermediate mechanism. Although results at 10 atm, 1600-ppm H_2S tend to indicate that this reaction rate should be increased to match the experimental results, it was found that the important curvature observed on the low-temperature side of the 30-atm, 1600-ppm H_2S case (see Fig. 56 (i)) was due to this terminating reaction. Since this curvature was not observed experimentally and led to significant discrepancy between the model and the data at these extreme conditions, the reaction rate of (r11) was reduced to mitigate this curvature behavior. Thus, the calculated reaction rate by Zhou et al. (2013) was divided, within the boundaries defined earlier, by a factor of 3:

$$k(r11) = 1.15\times10^{12}T^{0.155}\exp(1.43 \text{ kcal mol}^{-1}/RT)$$
$$\text{LOW} / 7.76\times10^{30}T^{-4.943}\exp(-2.0 \text{ kcal mol}^{-1}/RT)$$
$$\text{TROE}/ 1.0 \ \ 254 \ \ 2373/$$

This new reaction rate allows for a significant reduction of the curvature observed on the low-temperature side for the 1600-ppm H_2S, 30-atm case, as can be seen in Fig. 56 (i) by comparing the computed results from the model of Zhou et al. and the modified model of this study. However, even though the curvature has been significantly reduced, this behavior is still observed and should be eliminated. This persistent trend would indicate the need for a better estimation of this reaction rate, as results tend to show that the reaction rate of (r11) needs to be further reduced or modified at the temperature-dependence level.

$$S + SH \rightleftarrows S_2 + H \qquad (r12)$$

This inhibiting reaction (r12) was found to be relatively important at all pressures studied for the 1600-ppm H_2S addition case. The reaction rates reported in the literature [Mihelcic, 1970] or used in the mechanisms of Dagaut and Nicolle and Mueller et al. are very close to each other and correspond to a reaction rate that has been estimated at 300 K. The value adopted in the Leeds mechanism was three times higher but is still significantly lower than the value estimated by high-level calculation in Zhou (2009). Better agreement with the data of the present study was found when the calculated reaction rate from Zhou (2009) was multiplied by 2.5:

$$k(r12) = 8.3\times10^{12}T^{0.543}\exp(-0.03 \text{ kcal mol}^{-1}/RT)$$

$$H + HSS \rightleftarrows SH + SH \quad (r13)$$

Reaction r13 has never been measured experimentally but was calculated by Sendt et al. (2002). However, according to Zhou (2009), the QRRK treatment used to determine this reaction rate was inadequate. It was indeed noted that the equilibrium constant reproduced by calculating the rate coefficients in both directions separately differs from the equilibrium constant derived from thermodynamic values by a factor of 5. A new reaction rate was calculated in Zhou (2009). Multiplying the reaction rate of this inhibiting reaction by 2 led to improvements in the model predictions against the data from this study.

$$k(r13a) = 3.01\times10^{8}T^{1.551}\exp(1.03 \text{ kcal mol}^{-1}/RT)$$
$$k(r13b) = 8.38\times10^{18}T^{-1.563}\exp(-0.26 \text{ kcal mol}^{-1}/RT)$$

An overview of the changes in the H_2S mechanism operated in this study and in the study of Zhou et al. (2013) is visible in Table 17. Note that Zhou et al. (2013) employed various scaling factors depending on the conditions to model. It is also worth mentioning that (r7) and (r8) were not among the most-sensitive reactions in the conditions investigated by Zhou et al. This difference in sensitivity when compared to the present data probably explains why it was not deemed necessary to modify these reactions.

Table 17 Overview of the reaction rates that have been modified from the H_2S model of Zhou et al. (2013). The scaling factor represents the absolute value of the factor by which the reaction rate was modified. A scaling factor of 1.0 means that the reaction rate was not changed.

	Scaling factor	
Reaction	This study	Zhou et al. (2013)
$H_2S+S \leftrightarrows SH+SH$ (r10)	1.75	0.8-2.8
$SH+SH+M \leftrightarrows HSSH (+ M)$ (r11)	3.0	1.0-3.0
$SH + HO_2 \leftrightarrows HSO + OH$ (r7)	3.0	1.0
$SH + HO_2 \leftrightarrows H_2S + O_2$ (r8)	1.2	1.0
$H_2O_2 + SH \leftrightarrows H_2S + HO_2$ (r9)	2.0	1.0
$S + SH \leftrightarrows S_2 + H$ (r12)	2.5	1.0
$H + HSS \leftrightarrows SH + SH$ (r13)	2.0	1.0

These changes in the aforementioned reaction rates lead to changes in the ranking of the sensitive reactions. A comparison between sensitivity analyses before and after the modifications is shown in the Discussion section.

Model Validation

The results of this mechanism against the data of this study are visible in Fig. 56. As can be seen, the modifications adopted to improve the model of Zhou et al. are overall providing better predictions than the original model, with an evident improvement at around 13 atm, for all H_2S concentrations. The agreement with the data at around 13 atm was important as the baseline $H_2/O_2/Ar$ data (Fig. 57 (b)) are particularly well predicted by the model of Kéromnès et al. at this pressure condition. At a pressure around 35 atm, predictions are improved for the 100-ppm case where good agreement is seen except for the lowest temperature investigated. At 400 ppm, the modified model is in good agreement with the data, although the original model of Zhou et al. seems to be closer to the experimental data on the low-temperature side. However, note that the trend of the computed results is now in better agreement with the trend followed by the experimental data. For an addition of 1600 ppm of H_2S, the agreement of the modified model with the data is better than for any other model, even though a rapid increase of the predicted ignition delay time, not observed experimentally, can be seen at the low-temperature extremity. Note that this increase in the ignition delay time at low temperature has been greatly mitigated compared to the model of Zhou et al. (2013). At around 1.6 atm, one can see that the models are close to each other in terms of predictions, with all models being in reasonable agreement with the data and with the Leeds mechanism being slightly better than the others. One can however see that the model from the present study is not reactive enough at low temperatures at this pressure condition. This under-predicted reactivity is partly due to the H_2/O_2 mechanism itself, as can be seen in Fig. 57 (a), where the model is showing some discrepancy with the data under these conditions.

The present model was also compared with other models from the literature against the data from Frenklach et al. (1981), where the ignition delay time was measured for various concentrations of H_2S in air at high pressures. As can be seen in Fig. 58, the models from Leeds and Mueller et al. are close to each other but are significantly too reactive. Ignition delay time predictions are between 10 and 40 times shorter than the experimental τ_{ign}. Although the model of Dagaut and

Nicolle is closer to the data than the two aforementioned models, the predictions are also not satisfactory (ignition delay times are between 6.5 and 15 times shorter than the data). The model of Zhou et al. is, in comparison, close to the data even though the activation energy is too high, resulting in ignition delay times that are too short at high temperatures (by a factor of 2.5-3) and too long at low temperatures (factor 1.5-3).

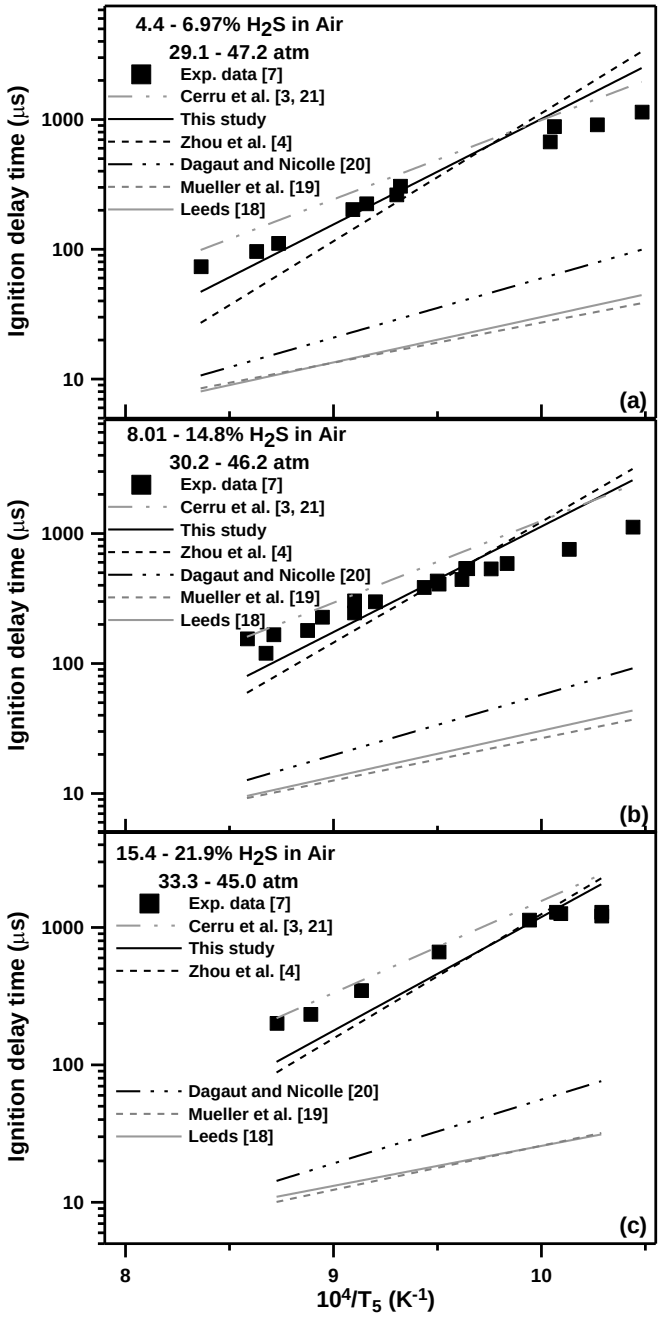

Fig. 58 Comparison of the results from Frenklach et al. (1981) with the predictions from the model of this study and recent literature models.

The reduced model of Cerru et al. (2005, 2006) was validated using this dataset and shows relatively good agreement with the results of Frenklach and coworkers. The activation energies are notably closer to the ones derived from the experimental data. Finally, after the modifications described earlier, the model proposed in the present study exhibits an activation energy that is slightly too high but reduced when compared with the model of Zhou et al. (2009). This result leads to better predictions against the Frenklach et al. data (by a factor between 1.5 and 2 on the high- and low-temperature sides).

It seems, however, possible to further improve the model especially at low temperatures for concentrations between 8 and 15% of H_2S and at high temperature for H_2S concentrations above 15%. The analysis of the ten most-sensitive reactions on the ignition delay time showed that only two reactions were inhibiting τ_{ign}: (r11) and, to a lesser extent, the reaction SH+HSS ⇄ $H_2S + S_2$. This result would indicate the need for a better estimate of the reaction rates for the SH self-reaction system involving HSS and HSSH. One can note that, again, experimental results seem to show that (r11) needs to be further reduced or that the temperature dependence term of (r11) needs to be revised. The good results yielded by the mechanism of Cerru et al. (2005, 2006) can indeed be explained by the low value for the rate of (r11) they adopted.

The modeling of the data from Frenklach et al. and of the high-H_2S concentration (1600 ppm) data from the present study, especially at 10 atm and above, demonstrates the insufficiencies of the SO_2 mechanisms from the literature in reproducing correctly the H_2S data. As described above, the reaction between sulfur containing species seems to be very important in the conditions of the Frenklach et al. (1981) study. The deficiencies in the models of Leeds [Hughes et al., 2001], Mueller et al. (2000), and Dagaut and Nicolle (2005) in predicting these results can therefore be attributed to the lack of S-S chemistry in those mechanisms. To simplify the subsequent figures and shorten the discussion, the mechanisms from Leeds, Nicolle and Dagaut, and Mueller et al. will therefore not be considered further in this study.

Several decades ago, Bradley and Dobson (1967) studied the ignition behind reflected shock waves of $H_2S/H_2/O_2$ mixtures in Ar (86-88% dilution) by following the SO_2 and OH light absorption at low pressure and high temperature. Ignition delay time results for the OH appearance from a 4% H_2S / 6% O_2 / 2% H_2 / 88% Ar mixture, along with computed results from the models considered in this study, are visible in Fig. 59. As can be seen, the models of the present study and the model from Zhou et al. (2013) have a somewhat similar activation energy that seems higher than for experiments (which cannot be determined accurately due to the noticeable scattering of the data). The mechanism of Zhou et al. seems too reactive over most of the temperature range, whereas the mechanism of the present study provides good predictions at the highest temperature and is in reasonable agreement with the data at the lowest temperature. Bradley and Dobson also published a similar study on H_2S/O_2/Ar mixtures [Bradley and Dobson, 1967]. However, the scatter in the results was this time too large to be considered as useful data to validate a model. Note that the model from Cerru et al. (2005, 2006) was not used here due the significant concentration of H_2 and the poor prediction performances of this model with H_2, as seen earlier.

Hawboldt et al. (1998, 2000) studied the pyrolysis of H_2S and related species in a plug flow reactor at atmospheric pressure. Figure 60 presents the results of the normalized H_2 conversion

obtained at (a) 1123 K and (b) 1423 K for the pyrolysis of a 1.14% H_2/ 1.8% S_2 mixture in N_2. At 1123 K, Fig. 60a, the models from Zhou et al. (2013) and from this study provide equivalent results and are over-estimating the conversion of H_2. At higher temperature, Fig. 60b, the mechanisms are still providing similar predictions on the maximum H_2 converted. Although the maximum of H_2 conversion is well captured by the models, the mechanisms are still slightly under-reactive during the first 0.2 s. The mechanism of Cerru et al. (2005, 2006), in comparison, is more reactive in these conditions and yields a much higher H_2 conversion at 1123 K, significantly above the experimental results. At 1423 K, however, the reactivity of the first 0.2 s is correctly reproduced by this model. The maximum of H_2 conversion, although slightly above the other models, is also correctly reproduced by the Cerru et al. model.

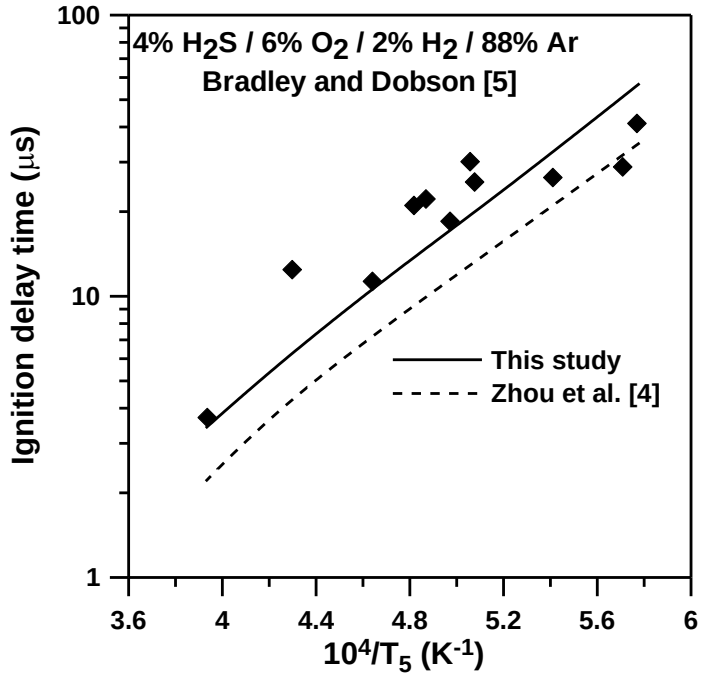

Fig. 59 Ignition delay time deduced from the OH appearance for a 4% H_2S / 6% O_2 / 2% H_2 / 88% Ar mixture from Bradley and Dobson (1967).

The recent data of Zhou et al. (2013) were computed using their model along with the mechanisms from Cerru et al. (2005, 2006) and from this paper. Results for the 100-ppm H_2S / 1000 ppm O_2 and 520-ppm H_2S / 1000-ppm O_2 cases are visible in Fig. 61a and Fig. 61b, respectively. As can be seen, the mechanism of Zhou et al. is in good agreement with the data for SO_2 formation and H_2S depletion for the 100-ppm H_2S condition. The model from the present study, in comparison, presents a reactivity that is significantly too slow as the computed profiles are shifted toward higher temperatures by 50 K. At these conditions, the model of Cerru et al. is even less reactive than the other models, with the reactivity starting at around 1065 K, more than 100 K from what was observed experimentally by Zhou et al. (2013). At the larger H_2S concentration, 520 ppm, the model of Zhou et al. is significantly too reactive, predicting a total consumption of H_2S at around 980 K where a temperature of 1050 K was observed

experimentally. As for the last condition, the model of the present study is not reactive enough, with the total consumption of H_2S being predicted at around 1130 K. At this high H_2S concentration, the mechanism of Cerru et al. is also not reactive enough. Indeed, their model predicts a reactivity that starts at around 1065 K, similar to the former condition, which is around 70 K higher than the experimental observation. Note that the total consumption of H_2S is reached at nearly the same temperature for the model of the present study and for the model of Cerru et al., even if the shape of the experimental profile seems to be better predicted by the latter.

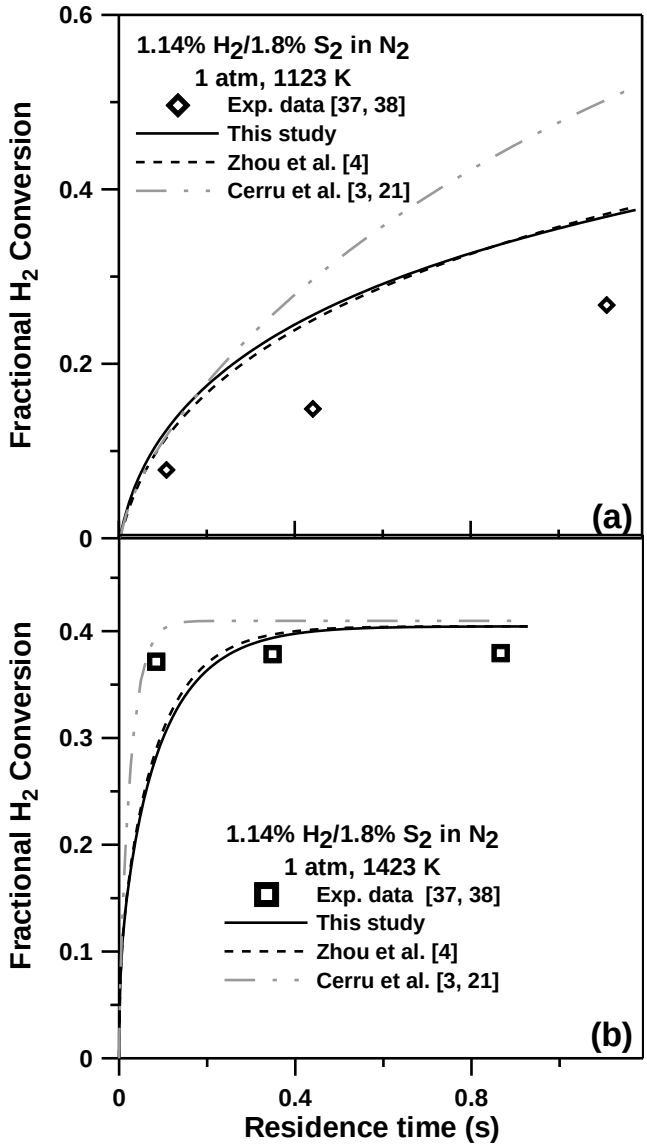

Fig. 60 Evolution of the normalized H_2 conversion in a plug flow reactor for a mixture of 1.14% H_2/ 1.8% S_2 in N_2 at (a) 1123 K and (b) 1423 K from Hawboldt et al. (1998, 2000). Lines are model predictions.

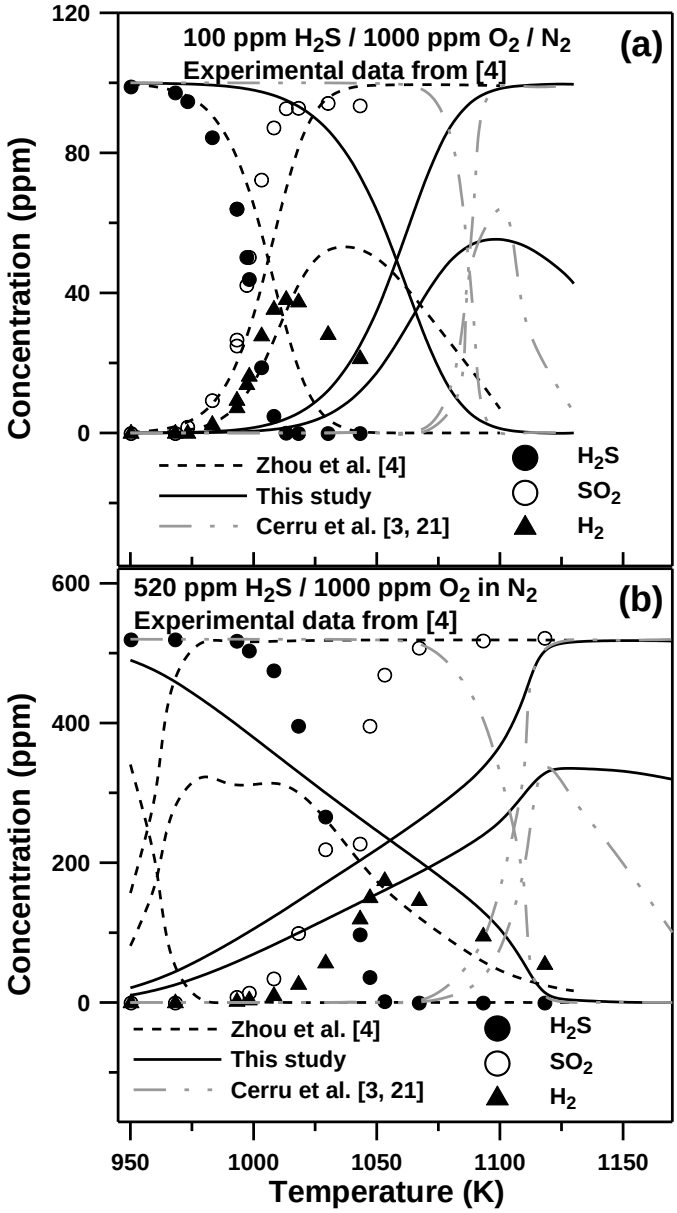

Fig. 61 H_2S, SO_2 and H_2 concentrations as a function of temperature for (a)100 ppm H_2S/1000 ppm O_2/N_2 and (b) 520 ppm H_2S/1000 ppm O_2/N_2 mixtures. Dashed line: model from Zhou et al. (2013). Continuous line: this study. Grey dashed line: Cerru et al. (2005, 2006).

Discussion

During this study, several kinetics models have been tested against shock-tube and flow reactor data. If the SO_2 models from Leeds, Mueller et al. (2000) and Dagaut and Nicolle, which all contain a H_2S sub-mechanism, are excluded (because the H_2S chemistry is not developed enough), these models were able to predict the available body of shock-tube data within a factor 3 (except for the data containing H_2 with the Cerru et al. (2005, 2006) model, see above). However, none of the H_2S mechanisms can reproduce the flow reactor data when H_2S is a

reactant. In their study, Zhou et al. (2013, 2009) observed a catalytic surface effect of the SiO_2 walls of their reactor, at both pyrolysis and oxidation conditions. Zhou (2009) noticed that this catalytic effect was not always reported in some other literature studies and concluded that these contradictory observations on the effect of silica can be attributed to the different surface conditions of the reactors. To avoid this issue, Zhou et al. used a B_2O_3 coating which significantly reduced the reactivity of their experimental system, even though they were not able to exclude heterogeneous surface reactions after application of this coating.

As seen above, the model of Zhou et al. (2013) is too reactive for most of the conditions of their own study, and these authors had to modify different reaction rates from one experimental condition to the other to obtain good predictions. The Zhou et al. model was however not reactive enough to predict reactivity for the H_2S pyrolysis data from Hawboldt et al. (1998, 2000) as they had to multiply all the reaction rates by 2 to obtain some agreement with the data in Zhou et al. (2013). To match shock-tube data, the model of this study reduced the overall reactivity of the Zhou et al. H_2S sub-mechanism. This decrease in reactivity leads to strong under-predictions of the reactivity for the flow reactor data of Zhou et al., for all conditions. Then, similarly to the model of Zhou et al., no reactivity was predicted in the conditions of the H_2S pyrolysis data of Hawboldt et al. (1998, 2000). Concerning the modeling of the results from Zhou et al. (2013), the difference in the models' predictions in Fig. 61 is mainly due to the reaction $H_2S+S \rightleftarrows 2\ SH$ (r10) which has been identified as the most important promoting reaction in Zhou et al. (2013) and in most of the conditions of this study, with the 1600-ppm H_2S addition. The reaction rate for this reaction was divided by 1.75 in the present study to decrease the reactivity of the mechanism and to better represent the shock-tube results on the low-temperature side and high-pressure conditions for the 1600-ppm H_2S case.

Note that increasing (r10) and changing a few other reaction rates (such as increasing (r11)) could have led to similarly good predictions of the shock-tube data at 10 atm, 1600-ppm H_2S. However, the necessary increase in (r11) also rapidly lengthens the predicted ignition delay times, far above the experimental data, for the 33-atm, 1600-ppm H_2S case at low temperature (with an increase in the pronounced curvature seen with the model of Zhou et al.) and for the Frenklach et al. data. Finally, the model from Cerru et al. behaves like the model proposed in this study on the data of Zhou et al. (2013) and Hawbolt and coworkers (1998, 2000), with an even slower reactivity against the data of Zhou et al. (2013). However, it is worth noting that these three models were able to predict relatively well the depletion of H_2 in H_2/S_2 pyrolysis conditions as observed experimentally in Hawbolt's work. This result could indicate either the presence of catalytic reactions with H_2S on the reactor walls, even with a B_2O_3 coating, or that some reaction pathways that are important under these conditions are missing from the model. Accurate reaction rate measurements for (r10) and (r11), over large ranges of temperature and pressure, would therefore be necessary to remove any ambiguity in this regard.

As the flow reactor data are ambiguous and since shock tubes operate without wall surface effects, only shock-tube results were considered relevant to validate the model herein. To explain the results of the present work, sensitivity and reaction pathway analyses were conducted using the model proposed in the study. Typical examples of sensitivity analyses on OH* are visible in Fig. 62 for the neat H_2/O_2 mixture and for the mixture seeded with 1600 ppm of H_2S at 1.7, 13, and 33 atm (at 1300, 1240, and 1265 K, respectively) and in Fig. 63 for the comparison of the

results between the base model (Zhou and coworkers) and the model proposed in this study, at 1160 K, 33 atm and with 1600 ppm of H_2S. As can be seen in these figures, the addition of H_2S leads to a significant increase in the number of sensitive reactions on the ignition delay time. Indeed, while the ignition of the neat H_2/O_2 mixture is mostly sensitive only to 2 reactions, (r1) and (r2), several reactions involving sulfur species are also of great importance on the ignition delay time predictions when H_2S is added to the mixture, as mentioned in Zhou et al. (2013). Note that the sensitivity analyses described below were performed with the model proposed in this study.

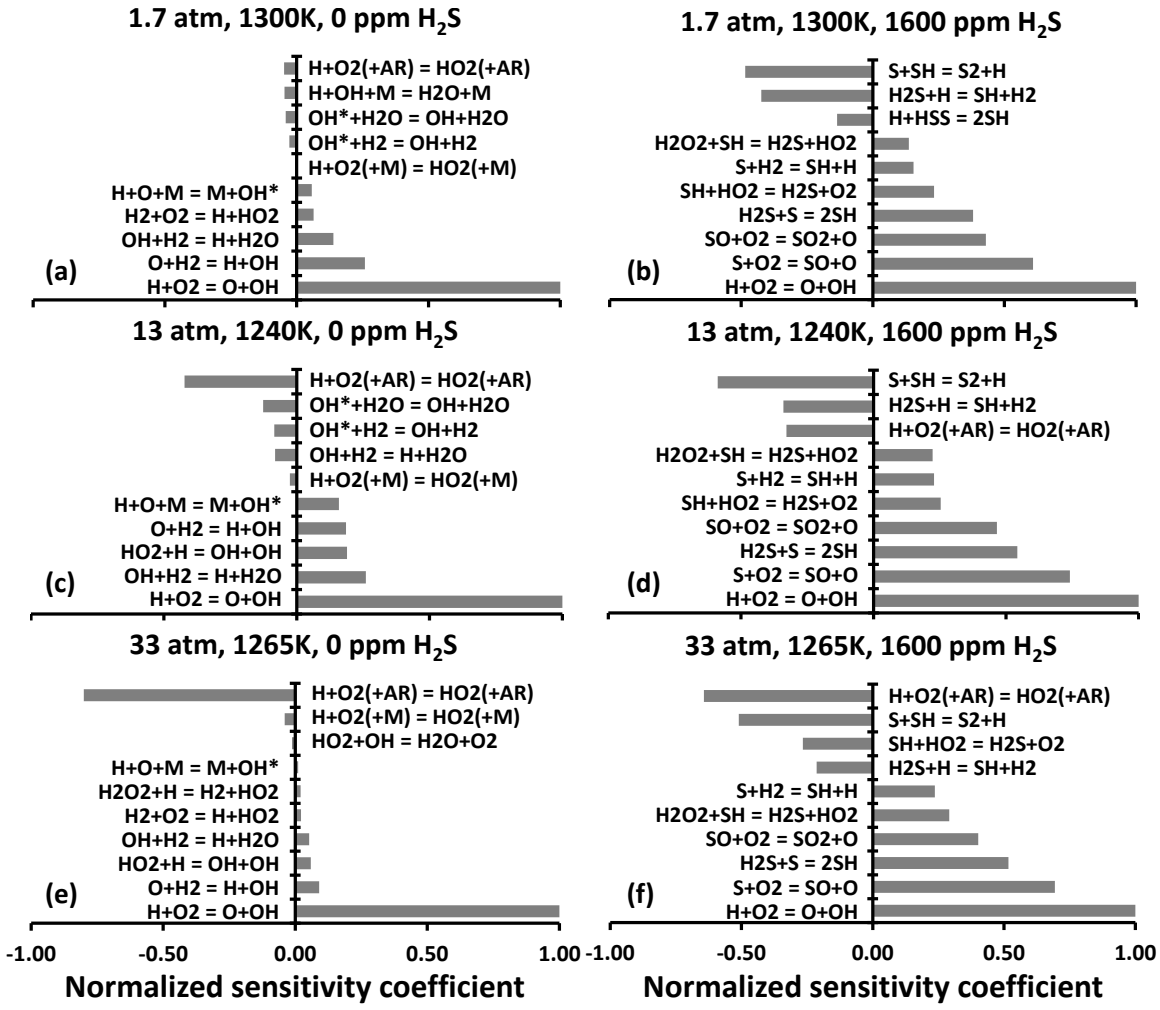

Fig. 62 Example of sensitivity analyses on OH* for the neat H_2/O_2 mixture at (a) 1.7 atm, 1300 K; (c) 13 atm, 1240 K; and (e) 33 atm, 1265 K and for the mixtures seeded with 1600-ppm H_2S under the same conditions ((b), (d) and (f), respectively).

At 1.7 atm, the addition of H_2S typically decreases the reactivity of the mixture. This effect is visible over the entire range of temperatures investigated for concentrations of H_2S above 100 ppm. At 100 ppm H_2S, the increase in the ignition delay time is mostly occurring on the low-

temperature side, with ignition delay times being roughly the same with the neat H_2 mixture at the highest temperatures investigated. The sensitivity analysis on OH* performed at this pressure condition (1045 K (neat H_2, 100 ppm), 1175 K (neat H_2, 100 and 400 ppm), 1300 K and 1620 K (0, 100, 400 and 1600 ppm for both temperatures)), showed that the branching reaction $H+O_2 \rightleftarrows OH+ O$ (r1) is always the most-sensitive reaction at 1.7 atm, regardless of the H_2S concentration or the temperature. For the neat hydrogen mixture, the propagating reaction $H+O_2+Ar \rightleftarrows HO_2+Ar$ (r2) is the most-sensitive inhibiting reaction, with a relatively small sensitivity coefficient (σ) value due to the low-pressure condition. When H_2S is added to the mixture, however, the reaction $S + SH \rightleftarrows S_2 + H$ (r12) (in reverse), closely followed by $H_2S + H \rightleftarrows SH + H_2$ (r4), become the most-sensitive inhibiting reactions, with a sensitivity coefficient significantly larger than (r2) for the neat H_2 mixture case. This result is visible in Fig. 62 (a) and (b) and is also valid for the other temperatures considered.

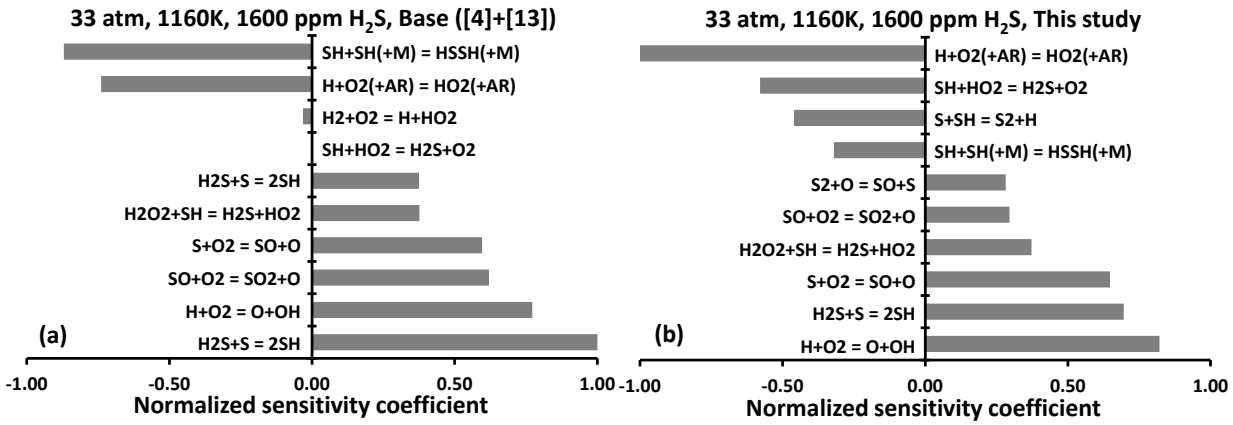

Fig. 63 Comparison of the sensitivity analysis on OH* between: (a) the base model (H_2 chemistry from Keromnes et al. (2013) and H_2S chemistry from Zhou et al. (2013)) and, (b) the revised model from this study at 1160 K and 33 atm for the mixture with 1600 ppm of H_2S.

A reaction pathway analysis showed that H_2S is mostly (more than 75%) consumed via (r4) and, to a lesser extent, via $H_2S + O \rightleftarrows SH + OH$ (r14) and $H_2S + OH \rightleftarrows SH + H_2O$ (r15). The H_2S is therefore consuming the radicals H though (r4), hence inhibiting (r1) and decreasing the reactivity of the mixture. This inhibitive effect is visible in Fig. 64 where it can be seen that the H_2S concentration decreases before the ignition (corresponding to the sharp rise in the OH concentration), while SH accumulates in the mixture and the H_2 concentration increases via (r1). The H_2S can therefore be viewed as a sink for H radicals, preventing (r1) to take place and trigger the ignition. It is worth mentioning that the radical SH is mostly consumed via $SH + H \rightleftarrows S + H_2$ (r16) and $SH + O \rightleftarrows SO + H$ (r17). At the peak of SH, the reaction $HSS + H \rightleftarrows 2SH$ (r13) is also relatively important. The influence of the H_2S chemistry before the ignition delay time, where the formation and accumulation of SH takes place, is observed for all the other conditions investigated, whatever the pressure, temperature, or H_2S concentration, in the range of conditions investigated. Note that this influence of H_2S was also the case for the model of Zhou et al., before the modifications made during the current study.

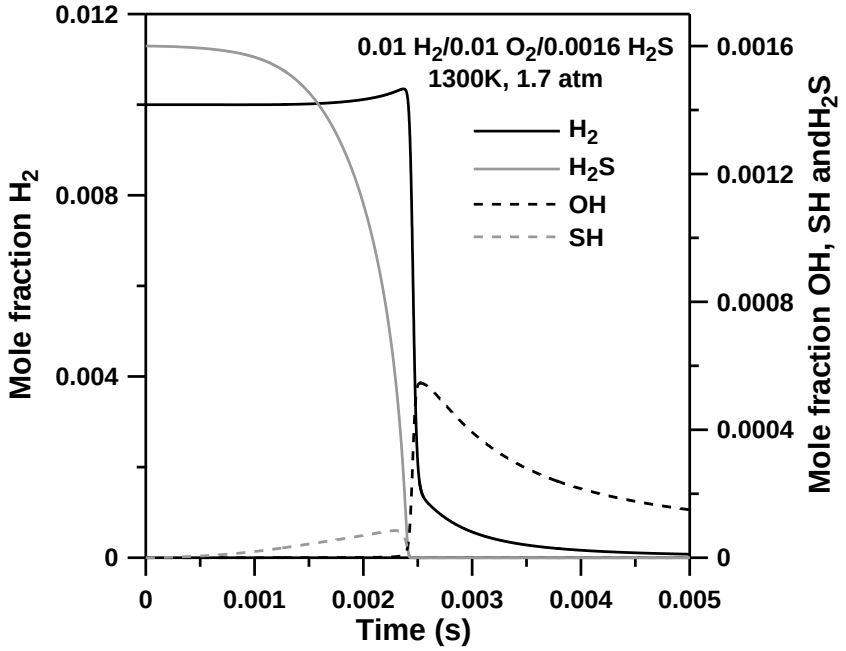

Fig. 64 Computed time histories for H_2, OH, H_2S, and SH for a 0.01 H_2/0.01 O_2/0.0016 H_2S/0.9784 Ar mixture at 1.7 atm and 1300 K.

At 33 atm, the sensitivity analyses show that (r4) is relatively less important, as this reaction has a smaller sensitivity coefficient or is no longer among the 10 most-sensitive reactions in some cases. This decrease in importance of (r4) indicates a slight change in the way the H_2S chemistry decreases the overall reactivity of the mixture. For the 100-ppm H_2S case, it is visible in Fig. 64 that the ignition delay time is almost not modified by the H_2S addition. On the low-temperature side, at 1160 K, the sensitivity analysis does not show any difference with the neat mixture concerning the two most-sensitive reactions ((r1) and (r2)). In addition to (r4), two reactions involving sulfur-containing species are in the ten most-sensitive reactions at this temperature, with a small sensitivity coefficient. These reactions are (r8) SH + HO_2 ⇄ H_2S + O_2 (terminating and, hence, inhibiting reaction) and (r7) SH + HO_2 ⇄ HSO + OH (propagating and, overall, promoting). At 1160 K, the reaction rates between (r7) and (r8) are close and these reactions are almost compensating for each other. This offsetting effect and the small concentration of H_2S explain the absence of effects of the H_2S addition on the ignition delay time at low temperature.

At the highest temperature investigated with 100 ppm of H_2S, 1265 K, the inhibiting reaction H_2S + H ⇄ SH + H_2 (r4) is the most-sensitive reaction involving a sulfur species, although the normalized sensitivity coefficient is small (σ = -0.07, σ(r1) = 1.0 and σ(r2) = -0.72). The SH radicals produced will then react with H, O, OH, and HO_2 radicals and eventually form SO which will react with O_2 to give SO_2 and a radical O (r6). It is also interesting to note that before ignition, most of the H_2O_2 is coming from H_2S + HO_2 ⇄ H_2O_2 + SH (r-9). This H_2O_2 can then react with SH and give back H_2S and HO_2. This later reaction competes with the strongly branching reaction H_2O_2 + M ⇄ 2OH + M (r18). Overall, at this low concentration of H_2S, the

inhibiting reaction (r4) $H_2S + H \rightleftarrows SH + H_2$ is counterbalanced by the reaction (r6) and by the formation of H_2O_2 which then reacts through (r9) and (r18).

For larger concentrations of H_2S, such as 1600 ppm, the results are different depending on the temperature. At the highest temperature investigated with H_2S, around 1360 K, the sensitivity analysis shows that the branching reaction (r1), $H + O_2 \rightleftarrows OH + O$, is significantly more important than the reaction (r2) ($H + O_2 + M \rightleftarrows HO_2 + M$, with M=Ar in that case) ($\sigma(r1) = 1.0$ and $\sigma(r2) = -0.39$). As for the low-pressure condition, the presence of H_2S will impact the overall chemistry before the ignition by consuming important radicals via H_2S + radicals (H, O, OH) $\rightleftarrows$ SH + products (H_2, OH, H_2O). This radical consumption will delay the ignition delay time by slowing down the formation of radicals, notably by the reaction $H_2S + H \rightleftarrows SH + H_2$ (r4) which limits the branching via (r1). Note that the SH will then give S and SO which will provide some O radicals via $S + O_2 \rightleftarrows SO + O$ (r5) and $SO + O_2 \rightleftarrows SO_2 + O$ (r6) and contribute to some important promoting reactions (notably $O + H_2 \rightleftarrows OH + H$). This pathway is in competition with the terminating reaction where SH is consumed without participating to the formation of O radicals $SH + SH (+M) \rightleftarrows HSSH (+M)$ (r11).

For the lowest temperature investigated with 1600 ppm of H_2S (1110 K), it is worth noting that this temperature is significantly lower than for the neat hydrogen addition (1160 K) for a similar ignition delay time. Therefore, this effect at lower temperature indicates an increase in the reactivity, and this temperature (1110 K) is the only experimental condition where this behavior was observed. At this specific condition, there is still production of SH via the reactions between H_2S and radicals (H, O, OH, and HO_2). This consumption of radicals limits the important reaction for H_2 oxidation, namely $H + O_2 \rightleftarrows OH + O$ (r1) and $H + O_2 + M \rightleftarrows HO_2 + M$ (r2), the latter being important at this high-pressure/low-temperature condition ($\sigma(r1) = 0.64$ and $\sigma(r2) = -1.0$). Most of the SH will then quickly form SO which will then form SO_2 via the reaction $SO + O_2 \rightleftarrows SO_2 + O$ (r6) and react through $SH + SH \rightleftarrows H_2S + S$ (r-10). The S formed will then react through r5 (followed by (r6)). To summarize, the formation of HO_2 is limited by the presence of H_2S via the consumption of H radicals (and also most of the SH reacts through $SH + HO_2 \rightleftarrows H_2S + O_2$ at the ignition event) whereas the SH will then lead to the formation of an O radical via (r5) and (r6). These O radicals will then react through $O + H_2 \rightleftarrows OH + H$ and, overall, promote the reactivity of the mixture. The importance of this pathway of O formation via SH radicals is illustrated by the fact that the termination reaction $SH + SH + M \rightleftarrows HSSH + M$, inhibiting the O formation by competing with (r-10), is of great importance at this condition.

At 13 atm, the results can be explained by the same mechanism as at 33 atm, 1600 ppm and high temperature described above. This similarity is illustrated by the important sensitivity coefficient of the reaction promoting the formation of O as it can be seen at 1600 ppm, 1240 K, for example where (r5) is the second most-important promoting reaction ($\sigma(r5) = 0.74$) after (r1) ($\sigma(r1) = 1.0$) followed by $SH + SH \rightleftarrows S + H_2S$ (r-10) and $SO + O_2 \rightleftarrows SO_2 + O$ (r6) ($\sigma(r\text{-}10) = 0.54$ and $\sigma(r6) = 0.47$, while the most-inhibiting reaction, (r2), has a $\sigma(r2) = -0.59$).

Finally, as mentioned earlier in this paper, modifications to the reaction mechanism do have a slight impact on the reactions predicted to be most sensitive to the ignition process. An example of this change is provided in Fig. 63, where the sensitive reactions to OH* are compared between the base mechanism (H_2 chemistry from Kermones et al. (2013) and H_2S chemistry from Zhou et

al. (2013)) (a) and the modified mechanism as described above (b). This representative example is taken at 1160 K, 33 atm and for the highest H_2S concentration investigated (1600 ppm). As can be seen, most of the reactions are identical. Only the reaction $H_2+O_2 \leftrightarrows H+HO_2$ in (a), a reaction with a relatively low sensitivity, has been replaced in (b) by the reaction $S+SH \leftrightarrows S_2+H$. However, one can notice that the order and normalized sensitivity coefficient of almost all the reactions are different after the reaction rates were changed during the model optimization procedure. Notably, the most promoting and inhibiting reactions in (a) ((r10) and (r11), respectively) were reactions involving sulfur-containing species, whereas the most-sensitive reactions are (r1) and (r2), respectively, in (b), which is typical for a H_2-dominating combustion.

BIO-DERIVED SYNGAS WITH IMPURITIES

The large variety of feedstock and methods for syngas production lead to great disparities in its composition, *i.e.*, variations in the H_2/CO ratio along with various concentrations of N_2, H_2O, CO_2, CH_4, and impurities [Göransson et a., 2011; Chacartegui et al., 2011]. These disparities in the composition introduce numerous control issues for premixed combustion [Richards et al., 2011] which complicate gas turbine design and operation. Indeed, depending on the mixture, auto-ignition can occur in the premixer which leads to overheating and subsequent damage to the fuel injector [Richards et al., 2011]. It is therefore important to understand the influence of the other species found in a real syngas on the ignition characteristics of the H_2/CO system.

The aim of the work presented in this section was to measure τ_{ign} for a mixture representative of a real syngas produced from biomass, but in a shock-tube experiment that is highly diluted in argon to avoid any non-ideal ignition behavior. The composition of the baseline syngas fuel was determined by averaging the components of 23 bio-syngas mixtures from the literature; and the effect of each additional component (CO_2, H_2O, CH_4) on the ignition properties of the baseline syngas (BS) studied in Krejci et al. (2013) was investigated by adding them separately. Since impurities such as ammonia can be present in the fuel [Higman and van der Burt, 2008] and can potentially have an impact on τ_{ign}, the study of an additional 200 ppm of NH_3 was conducted with the baseline mixture and with the full mixture. The composition of all the mixtures investigated is provided in Table 18.

These mixtures were studied at an equivalence ratio set to 0.5 and for three pressure conditions (around 1.6, 12.5, and 32 atm). Presented in the following sections is an overview of the experimental setup, followed by the results of the shock-tube experiments. A comparison of several chemical kinetics models over the range of the data is then performed, and the experimental results are discussed based on detailed kinetics modeling.

Table 18 Composition of the mixtures investigated.

Mixture name	% H_2	% CO	% O_2	% CH_4	%CO_2	% H_2O	%NH_3	% Ar
Neat H_2	1.0	0.0	1.0	0.0	0.0	0.0	0.0	98.0
BS (Krejci, 2013)	0.50	0.50	1.0	0.0	0.0	0.0	0.0	98.0
BS-CH_4	0.406	0.406	1.113	0.075	0.0	0.0	0.0	98.0
BS-CO_2	0,46	0,46	0,93	0.0	0,15	0.0	0.0	98.0
BS-H_2O	0.444	0.444	0.889	0.0	0.0	0.223	0.0	98.0
BS-NH_3	0.50	0.50	1.0	0.0	0.0	0.0	0.02	97.98
Biosyn	0.29659	0.29659	0.95013	0.08924	0.15748	0.20997	0	98.0
Biosyn-NH_3	0.29659	0.29659	0.95013	0.08924	0.15748	0.20997	0.02	97.98

Results

Results obtained at a pressure on the order of 1.6 atm for the Neat H_2, BS, BS-CO_2, BS-H_2O, BS-CH_4, and the full syngas mixture derived from biomass are visible in Fig. 65. As can be seen, the difference between the Neat H_2 and the BS mixtures is small and, overall, slightly longer τ_{ign} (around 15%) were found for BS. The addition of water to BS only slightly decreased τ_{ign}, and

the results were similar to those of the Neat H_2. No appreciable differences between BS and BS-CO_2 were observed under these conditions, whereas an addition of CH_4 tended to increase the ignition delay times below 1230 K. The comparison between Biosyn, BS, and BS-CH_4 showed that τ_{ign} is further increased, compared to BS-CH_4, for temperatures below 1550 K.

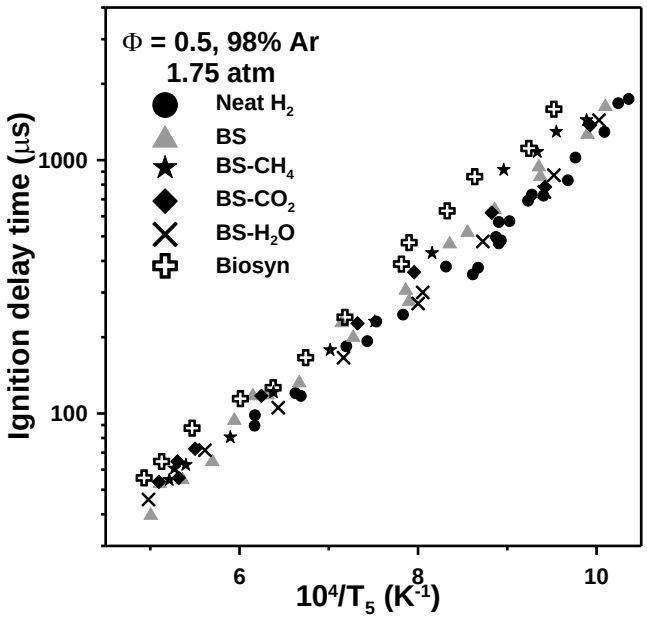

Fig. 65 Effect of the composition on the ignition delay time for a syngas with a H_2/CO ratio set to 1 and at a pressure around 1.6 atm.

For the intermediate pressure investigated (Fig. 66), differences in τ_{ign} are more significant amongst the mixtures, although the trends observed in Fig. 65 at around 1.6 atm were the same as those near 12.5 atm. Indeed, ignition delay times of the BS mixture were also slightly longer than for Neat-H_2 (above 1135 K), and the addition of water resulted in similar τ_{ign} between BS-H_2O and Neat H_2 over most of the temperature range investigated. Although the addition of CO_2 did not show any appreciable effect on the ignition delay time, the addition of CH_4 increased τ_{ign} significantly compared to results obtained for BS. A factor of 6 between τ_{ign} of BS and BS-CH_4 was found at around 1150 K, the amplitude of this change being decreased as the temperature increased. This increase in τ_{ign} for the lower temperatures was more important for the Biosyn mixture. The curvature in the delay time visible between 1180 and 1280 K for the Neat H_2, BS and the ternary mixtures was not observed for Biosyn, and the activation energy for Biosyn was determined to be 45.2 kcal/mol.

At a pressure around 32 atm, most of the differences amongst the mixtures were visible for the higher temperatures (Fig. 67), and differences between the syngas mixtures and Neat-H_2 were typically less important than for the other pressure conditions investigated. No appreciable difference amongst Neat-H_2, BS, and BS-CO_2 was observed. Water addition however still exhibited a small, promoting effect on the ignition delay time, and τ_{ign} were overall slightly shorter than those of the Neat-H_2 mixture. The addition of CH_4 near 32 atm showed an inhibiting

effect on τ_{ign}, but this effect was visible only for temperatures above about 1220 K. At the highest temperature investigated, a factor of 2 was found between the delay time from BS and BS-CH_4. Results for Biosyn showed that τ_{ign} were a bit higher than for the other mixtures considered below 1250 K. Above this temperature, ignition delay times fell between those of BS-CH_4 and those of the other mixtures.

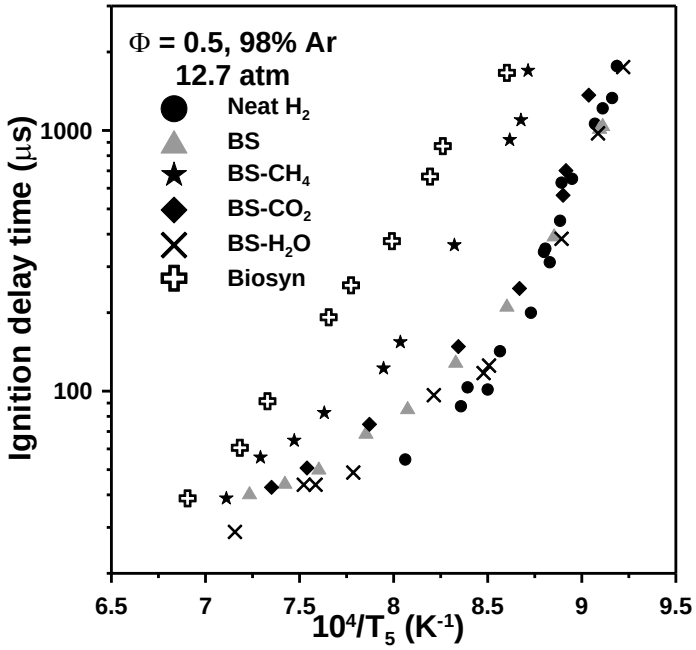

Fig. 66 Effect of the composition on the ignition delay time for a syngas with a H_2/CO ratio set to 1 at a pressure around 12.5 atm.

The effect of the NH_3 impurities was first studied by adding 200 ppm of ammonia to the BS mixture. As can be seen in Fig. 68, this NH_3 addition had a very limited influence on τ_{ign}. At around 1.6 atm, a small decrease in the ignition delay time was observed when NH_3 impurities were present. This decrease was also observed for the intermediate-pressure condition but only for temperatures above 1315 K. For the highest pressure investigated, however, no influence of NH_3 on τ_{ign} was visible.

The influence of NH_3 on the ignition delay time was also investigated with the Biosyn mixture (Fig. 69). It can be seen that under these conditions, no effect of the 200-ppm NH_3 addition was discernible between results obtained with the neat Biosyn and the Biosyn-NH_3 mixtures.

Discussion

During this study, the addition of some compounds showed an influence compared to the ignition delay time of the baseline syngas mixture, while others did not. More particularly, CH_4 was found to have an important inhibiting effect on τ_{ign}. A sensitivity analysis was conducted at 12.5 atm, 1150 K for the BS and the Biosyn mixtures with the mechanism of Li *et al.* (2007). The sensitivity analysis on OH* showed that the four most sensitive reactions were identical between the two mixtures: $H+O_2 \rightleftarrows O+OH$, $H+O_2\ (+M) \rightleftarrows HO_2\ (+M)$, $CO+O_2 \rightleftarrows CO_2+O$ and

$O+H_2 \rightleftarrows H+OH$ (by decreasing sensitivity coefficient value). However, the fifth most sensitive reaction was a promoting reaction for the BS mixture ($HO_2+H \rightleftarrows H_2+O_2$, in reverse), whereas an inhibiting reaction involving CH_4 was found with the Biosyn mixture ($CH_4+OH \rightleftarrows CH_3+H_2O$). This reaction seems to be mostly responsible for the decrease in the reactivity observed for the Biosyn and BS-CH_4 mixtures. Note that two other reactions involving CH_4 appeared during the sensitivity analysis ($CH_3+HO_2 \rightleftarrows CH_4+O_2$ (promoting) and $CH_4+O \rightleftarrows CH_3+OH$ (inhibiting)) but these reactions are of smaller importance (eighth and ninth most sensitive reactions, respectively) and are compensating for each other. This decrease in reactivity for the methane-containing mixtures at 12.5 atm also explains the fact that τ_{ign} are longer than at 30 atm (lower importance of $CH_4+OH \rightleftarrows CH_3+H_2O$ above 12.5 atm).

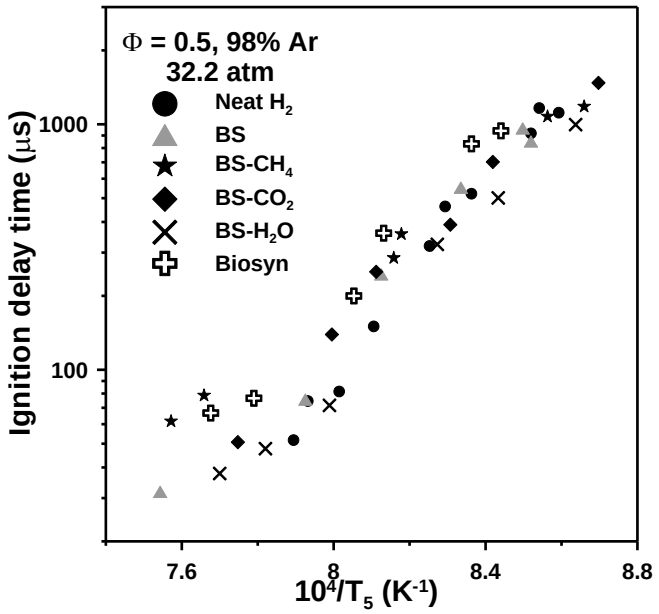

Fig. 67 Effect of the composition for a syngas with a H_2/CO ratio set to 1 at a pressure around 32 atm.

The reasons for the lack of effects on τ_{ign} of an addition of 200-ppm NH_3 was also investigated numerically with the NH_3 chemistry of Konnov (2009) merged to the mechanism of Li *et al.* (2007). A sensitivity analysis on τ_{ign} was conducted for Biosyn and Biosyn-NH_3 and showed that only two reactions involving NH_3 appear in the 15 most-sensitive reactions: $NH_3+O \rightleftarrows NH_2+OH$ (promoting) and $NH_3+OH \rightleftarrows NH_2+H_2O$ (inhibiting reaction). These two reactions are of very little importance (last and thirteenth reactions in terms of absolute sensitivity coefficient, respectively). A further analysis showed that NH_3 does not react (constant concentration) before the ignition starts nor does it interact with the radical pool. However, between 1/3 and 1/2 of the NH_3 is converted to NO (fuel NO formation) during the ignition process. Therefore, due to its lack of reactivity, NH_3 does not have a direct impact on τ_{ign} at the present conditions but can indirectly have a great influence on the combustion in gas turbines *via* the presence of NOx, if an exhaust gas recirculation strategy is used.

Concerning the water addition effect, a small decrease in the ignition delay time was observed experimentally, but this decrease was not predicted by any of the models. To assess where the discrepancy between the models and the experiment lies, water concentration measurements

were performed by laser absorption to verify the concentration of water in the shock tube prior to each experiment. It was determined that the original mixtures were correct (see next section).

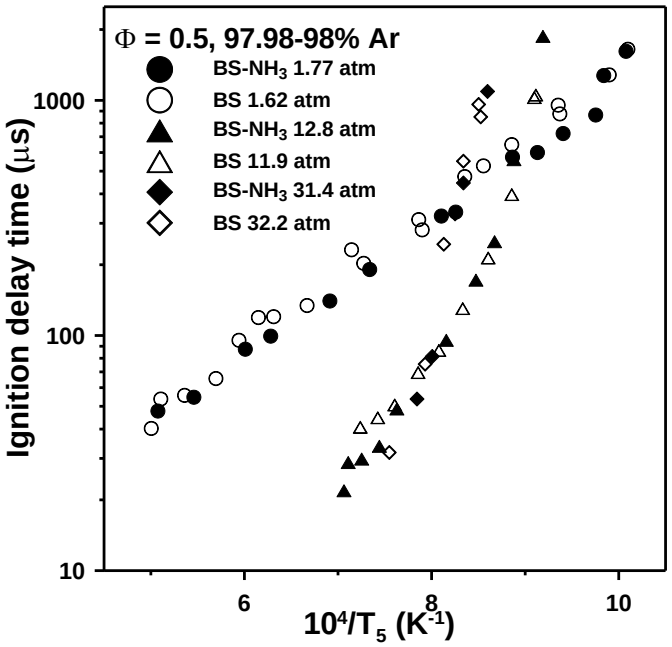

Fig. 68 Effect of an addition of 200 ppm of NH_3 on the ignition delay time of the BS mixture for 3 three different pressures: around 1.6, 12.5, and 32.0 atm.

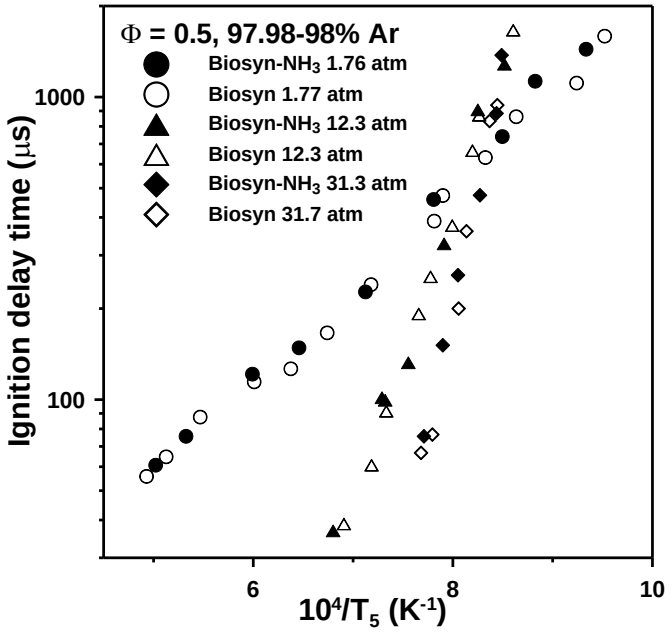

Fig. 69 Effect of an addition of 200 ppm of NH_3 on the ignition delay time of the Biosyn mixture at 3 three different pressures: around 1.6, 12.5, and 32.0 atm.

COAL-DERIVED SYNGAS WITH IMPURITIES

Coal has been used as a source of energy for several centuries but has long been criticized because of the release of toxic products (sulphur-containing compounds and oxides of nitrogen, or NOx) during its combustion, in addition to the production of CO_2. With natural coal reserves being larger than oil and gas, it is however anticipated that energy production from coal will continue for many years to come. Hence, because of environmental concerns, methods have been developed to use coal as a cleaner energy source. One possible method is to convert coal into synthetic gas (syngas), a process that allows for the removal of most of the particulates, along with sulphur and NOx compounds.

Ideally, syngas is mostly composed of H_2 and CO, in various proportions, but real syngas can also contain small hydrocarbons, H_2O, N_2, and CO_2 in reasonable amounts as well as traces of undesirable impurities such as NH_3 and H_2S [Mathieu et al., 2013a]. These variations in syngas composition are due primarily to the large variety of feedstock and production processes. The compositional variation leads to a large deviation in combustion properties, which, in turn, make the optimization of stable, high-efficiency gas turbines challenging [Richards et al., 2001]. To better optimize gas turbines, well-validated chemical kinetics models for realistic mixtures are therefore desirable. Unfortunately, there are very few data on complex, realistic syngas compositions to help in validating these models.

While H_2/CO mixtures have been studied in numerous conditions (see Mathieu et al. (2013a) and references therein), more-realistic mixtures have hardly been investigated. Indeed, aside from the addition of CO_2 [Natarajan et al., 2005; Wang et al., 2013; Petersen et al., 2007) [Prathap et al., 2008], H_2O [Das et al., 2011], CH_4 [Mathieu et al., 2013b], or NH_3 [Mathieu et al., 2013b] to CO/H_2, only a syngas derived from a wood gasification process [Herzler et al., 2012] and a bio-syngas averaged from real compositions [Mathieu et al., 2013b] were studied, both in shock tubes. The comparison between a binary CO/H_2 fuel blend and realistic practical bio-syngas mixture with the same CO/H_2 ratio and under the same conditions in the previous study by the authors [Mathieu et al., 2013b] showed important differences in terms of ignition delay time (τ_{ign}) and stressed the importance of studying complex, realistic mixtures to validate models. The aim of the present study was therefore to extend the earlier work by the authors toward ignition delay time measurements for a realistic, coal-derived syngas. A practical coal syngas was derived by averaging the compositions of 40 real coal-syngases (see Mathieu et al., 2013a), leading to a 40/60 ratio between H_2 and CO and the presence of CH_4, CO_2, and H_2O in the fuel blend. The effect of these components was investigated in the present paper by adding them individually to the baseline H_2/CO mixture. Finally, the effect of the addition of impurities such as NH_3 and H_2S was studied, on both the baseline CO/H_2 and the realistic, averaged, fuel blend. Note that mixtures of H_2/CO with H_2O or NH_3 have already been investigated in Mathieu et al. (2013b), at identical conditions. Since the results from that study did not show any appreciable effect of these two species on τ_{ign}, the individual effects of H_2O and NH_3 addition on the binary baseline mixture were not investigated in the present study.

Mixtures were studied in dilute conditions, to avoid non-ideal ignition behaviour observed with real fuel-air mixtures [Petersen et al., 2007], and at an equivalence ratio (ϕ) set to 0.5 to be representative of lean conditions in gas turbine engines. In addition, the authors have shown in previous studies that the ignition behaviour of hydrogen-based fuel blends is not very dependent

on the stoichiometry for equivalence ratios between about 0.3 and 2.0 [Kermomnes et al., 2013; Krejci et al., 2013]. Three pressure conditions were investigated: around 1.7, 13, and 32 atm. The details of the mixture composition are provided in Table 19.

Table19 Composition of the mixtures investigated in the shock tube, in % volume.

Mixture	% H_2	% CO	% O_2	% CH_4	%CO_2	% H_2O	%NH_3	% H_2S	% Ar
Neat H_2	1.0	0.0	1.0	0.0	0.0	0.0	0.0	0.0	98.0
BS	0.40	0.60	1.0	0.0	0.0	0.0	0.0	0.0	98.0
BS-CH_4	0.385	0.578	1.022	0.015	0.0	0.0	0.0	0.0	98.0
BS-CO_2	0.38	0.57	0.96	0.0	0.09	0.0	0.0	0.0	98.0
BS-H_2S	0.4	0.6	1.0	0.0	0.0	0.0	0.0	0.005	97.995
Csyn	0.3297	0.4554	0.8538	0.0172	0.1032	0.2407	0.0	0.0	98.0
Csyn-imp	0.3297	0.4554	0.8538	0.0172	0.1032	0.2407	0.02	0.005	97.975

The experimental setup used during this study is presented in the next section, followed by the experimental results. These data are then compared to several recent detailed kinetics models from the literature. Results are then discussed in terms of a chemical analysis derived from the detailed kinetics modeling.

Experimental Setup

Shock Tube. Ignition delay times were measured behind reflected shock waves (RSW) in a single-diaphragm, stainless steel shock tube (15.24-cm i.d., 4.72-m long and 7.62-cm i.d., 2.46-m long for the driven and driver sections, respectively). The wave speed, extrapolated to the endwall, was measured using five PCB-P113A pressure transducers to determine post reflected-shock conditions in conjunction with the one-dimensional shock relations. The uncertainty in the temperature behind the RSW (T_5) was proven to be maintained below 10 K using this method [Petersen et al., 2005]. A Kistler 603-B1 transducer, located in the same plane as the sapphire observation window (16 mm from the endwall), and a PCB-134A transducer, located at the endwall, were used to monitor the test pressure. Polycarbonate and pre-scored aluminum diaphragms were used for experiments up to 13 atm and 32 atm, respectively. Further details on the shock tube are available in Aul et al. (2013).

Test mixtures were prepared manometrically in a mixing tank (stainless steel, 3.05-m length and 15.24-cm ID). The gases were passed through a perforated tube traversing the mixing tank to allow for rapid, turbulent mixing. The test section was evacuated to 2×10^{-5} Torr or better before each experiment. The possible formation of $FeCO_5$ from the CO cylinder was minimized using a gas cylinder made of aluminium and a gas supply tubing of Teflon from the bottle to the experiment. Since NH_3 adsorbs on stainless steel, the mixing tank and shock-tube surfaces were passivated with NH_3 before each mixture preparation and experiment. The passivation method was as follows: introduction of around 100 torr of NH_3 for at least 5 minutes and then vacuuming for 5 minutes with the rough pump (until around 30-40 mtorr, typically) before filling the driven tube with the mixture (or the mixing tank with the mixture components). Care was also taken for the mixtures containing water vapour to ensure that there was no condensation or other losses in water between the mixing tank and the shock tube; details on the water monitoring diagnostic are

presented later in this paper. Conditions investigated during this study are summarized in Table 20.

Table 20 Experimental conditions investigated behind RSW. Fuel names are as defined in Table 19.

Mixture	T_5 (K)	P_5 (atm)	Source
Neat H_2	960-1625	1.65 ± 0.15	Keromnes (2013)
	1085-1245	13.3 ± 1.0	
	1160-1270	32.8 ± 1.5	
BS	1015-1845	1.73 ± 0.22	Mathieu (2013)
	1090-1445	12.6 ± 0.8	
	1140-1300	31.5 ± 0.9	
BS-CO_2	1025-1875	1.75 ± 0.26	This study
	1105-1450	12.9 ± 0.7	
	1160-1305	31.5 ± 1.1	
BS-CH_4	1010-2010	1.71 ± 0.22	This study
	1095-1400	12.9 ± 0.8	
	1170-1290	31.7 ± 1.4	
BS-H_2S	1050-1785	1.85 ± 0.26	This study
	1095-1340	13.0 ± 0.6	
	1165-1295	32.6 ± 1.6	
Csyn	1050-1705	1.85 ± 0.22	This study
	1095-1400	13.2 ± 1.1	
	1170-1315	32.6 ± 0.8	
Csyn-imp	1050-1740	1.84 ± 0.19	This study
	1095-1410	12.9 ± 0.8	
	1180-1300	33.0 ± 0.9	

Ignition Delay Time Setup. The ignition delay time was defined as the time between the passage of the RSW and the intersection of lines drawn along the steepest rate-of-change of OH* de-excitation (i.e., chemiluminescence) and a horizontal which defines the zero-concentration level, as documented in Mathieu et al. (2014). The emission spectroscopy from the $A^2\Sigma^+ \rightarrow X^2\Pi$ transition of the excited-state hydroxyl radical (OH*) was followed at the sidewall location using an interference filter centered at 307 ± 10 nm with a Hamamatsu 1P21 photomultiplier tube in a custom housing.

Uncertainties in τ_{ign} are due to (i) the uncertainty in T_5 determination, and (ii) the uncertainty associated with the determination of the steepest slope from the OH* time history profile. The temperature determination is the most important one and, for some of the high-pressure conditions of this study, can lead to a relatively significant uncertainty. The second source of uncertainty is typically smaller and can be neglected. The total uncertainty on τ_{ign} reported in this study is between around 10% at the lower pressures (1-15 atm) and 20% at around 30 atm. These uncertainties take into account the non-ideal boundary layer effects measured by the change in pressure (dP/dt) behind the RSW, which for the shock tube, mixtures, and time scales utilized is almost negligible. Due to the dilution level used, these non-ideal effects are mainly due to the facility and not to any heat release from chemical reaction. The change in pressure was

determined to be less than 2%/ms during this study and in other hydrogen-based studies from our group with similar dilution levels [Petersen et al., 2007; Keromnes et al., 2013]. Some representative OH* and pressure profiles are visible in Fig. 70.

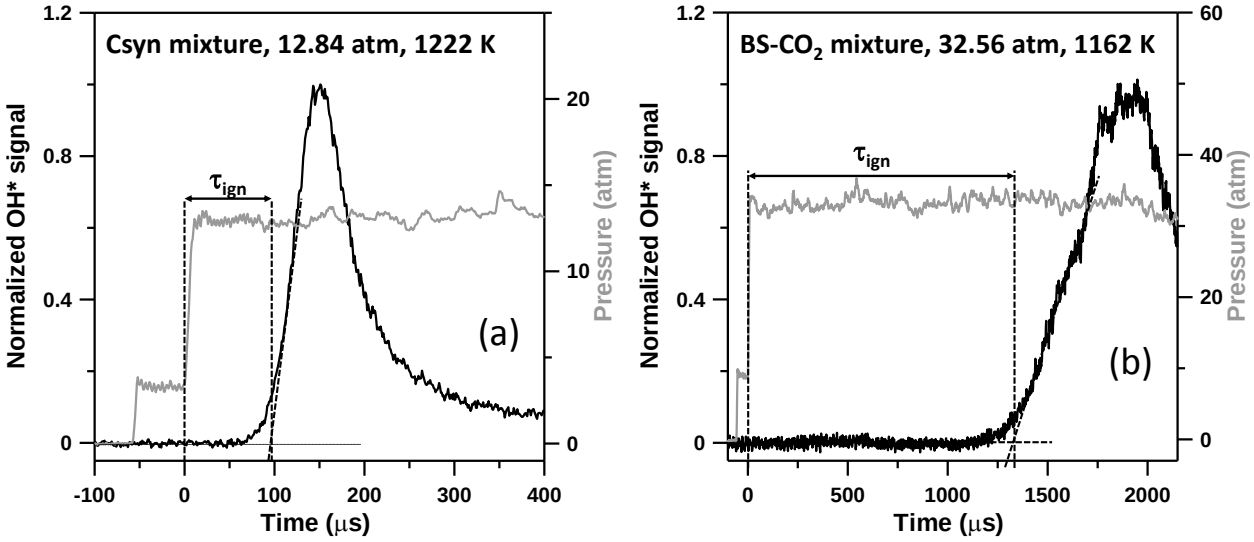

Fig. 70 Typical OH* and pressure profile observed during this study and determination method for the ignition delay time. (a) Csyn mixture, 12.84 atm, 1222 K and (b) BS-CO_2 mixture, 32.56 atm, 1162 K.

Measurements with the H_2O Absorption Diagnostic. When working with mixtures containing water vapor in an unheated shock tube, care must be taken to ensure that the mixture being shock heated is indeed the mixture that was made in the mixing tank. There are at least 3 possible mechanisms for creating uncertainty in the final water partial pressure in the shock tube: 1) adsorption onto the shock-tube walls; 2) local, transient condensation within the tube while filling (if gas compression makes the local water partial pressure above the vapor pressure); and, 3) expansion of the mixture when moving from the higher-pressure mixing tank to the shock tube under vacuum pressure causing local condensation due to low, local temperatures created during the expansion process. The best way to ensure the amount of water vapor in the tube is to measure it directly, and this was done using laser-light absorption at frequency ν governed by the Beer-Lambert relation:

$$I_T / I_0 = \exp\left(-k_\nu P X_i L\right) \tag{15}$$

which describes the relation between the ratio of the transmitted (I_T) and incident (I_0) intensities; the spectral absorption coefficient k_ν (atm^{-1} cm^{-1}); pressure, P (atm); mole fraction of the absorbing species i, X_i; and path length, L (cm). The light source was a Toptica Photonics DL100L tunable diode laser (TDL) with a DC 110 laser controller, operated near 1.38 μm and used to measure water absorption in the ν1+ν3 transition band of H_2O near 1387.877 nm.

The spectral parameters listed above, namely k_v, were calculated for H_2O using HITRAN 2004 and a Voigt fit for the spectral line to account for Doppler and collision broadening. The argon broadening coefficients were not obtainable by HITRAN but were estimated for the selected transitions by using an argon-to-air broadening ratio described by Negali et al. (2000) near 1405 nm. A schematic of the optical diagnostic setup is visible in Fig. 71.

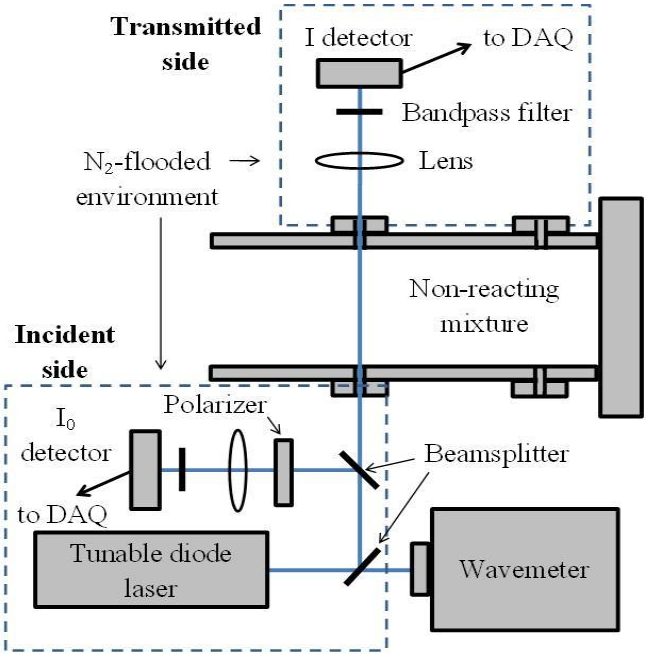

Fig. 71 Schematic of the water absorption diagnostic setup used during this study.

The incident laser beam was split three ways: into a Burleigh WA-1000 wavemeter with an uncertainty of ±1.0 ppm, into a Newport 2317 Large-Area Balanced Photoreceiver with bandpass filters centered at 1384±5 nm (I_0), and through the shock tube onto another Newport 2317 Photoreceiver (I_T). An adjustable polarizer on the incident side was used to balance the incident and transmitted signals prior to filling the tube with a mixture containing water. A DI-158U DAQ system monitored the output from the photoreceivers. Two separate, custom-made boxes isolated the incident and transmitted sides, and nitrogen was purged into the boxes to prevent ambient water vapor from interfering with the measurement. In addition to the WA-1000 wavemeter, the selected transition line was validated by analyzing the absorption using pure water vapor as described by Barrett (2009).

Measurements of the water partial pressure in the shock-tube test section were performed over a range of pressures that covers the fill pressures utilized in the shock-tube experiments. The main H_2O-containing mixture in Table 19 (Csyn) was used to fill the tube, and the results are shown in Fig. 72, which compares the TDL-measured water partial pressure with the mixture partial pressure (from the tank). As shown, the water vapor in the tube agrees within 5% of the target mixture value. The slope of the line fit in Fig. 72 produces the measured mole fraction of 0.0023, which compares well with the target value of 0.0024 and is within the uncertainty of the TDL

measurement. It can therefore be concluded that there is no appreciable uncertainty in the water content of the shock-heated mixtures studied herein.

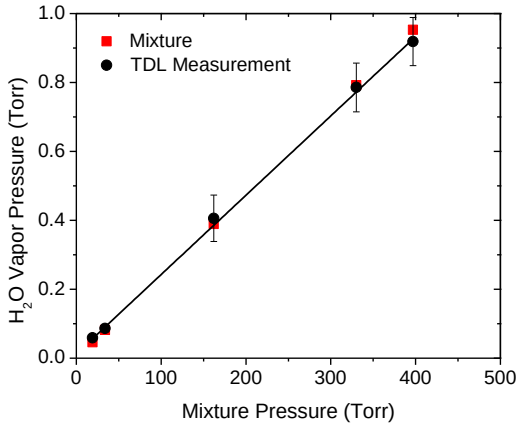

Fig. 72 Measured water partial pressure compared to the tank mixture value over a range of typical shock-tube fill pressures. The slope of the measured P_{H2O} produces a water mole fraction of 0.0023, which agrees within 5% of the target value in Table 19.

Results

Composition Effect on the Ignition Delay Time. The effects of syngas composition on τ_{ign} at the lowest pressure investigated are visible in Fig. 73. As can be seen, the ignition delay times for the baseline 60 CO/40 H_2 mixture are slightly longer, between 10 and 50% (for high and low temperatures, respectively), than for the neat H_2 mixture. An addition of CO_2 to the BS mixture does not change the ignition delay time, whereas the addition of a small concentration of methane seems to bring τ_{ign} closer to the neat hydrogen data. Although H_2S was introduced at a very small concentration (Table 19), it has a noticeable effect on τ_{ign}. Indeed, τ_{ign} is increased by nearly a factor of two at 1050 K and by around 35% at 1785 K, compared to the BS mixture. The results for the realistic coal syngas mixture are between those of the neat H_2 and BS mixtures, indicating only a small influence of the CO_2, CH_4, and H_2O addition under these conditions. Noticeable changes are observed for the Csyn blend in the presence of both impurities (NH_3 and H_2S) via the Csyn-imp mixture in Fig. 73; τ_{ign} is increased by 50% at the lowest temperature investigated and decreased by around 25% at 1740 K.

At around 13 atm, Fig. 74, the difference between the neat H_2 and the BS mixture is more important than at 1.7 atm. Indeed, if τ_{ign} remains the same or nearly so at the lowest temperature investigated, the addition of CO nearly doubles τ_{ign} at 1245 K. However, it is interesting to note that the CO_2, CH_4, and H_2S additions did not affect τ_{ign} at 13 atm. On the other hand, the realistic mixture (Csyn) shows some noticeable differences above 1200 K, where the ignition delay time is shorter than for the baseline mixture with just CO and H_2 (up to a factor around 2). In the presence of impurities (i.e., Csyn-imp), the reduction in τ_{ign} is still observed but seems to be slightly reduced compared to what was seen at 1.7 atm.

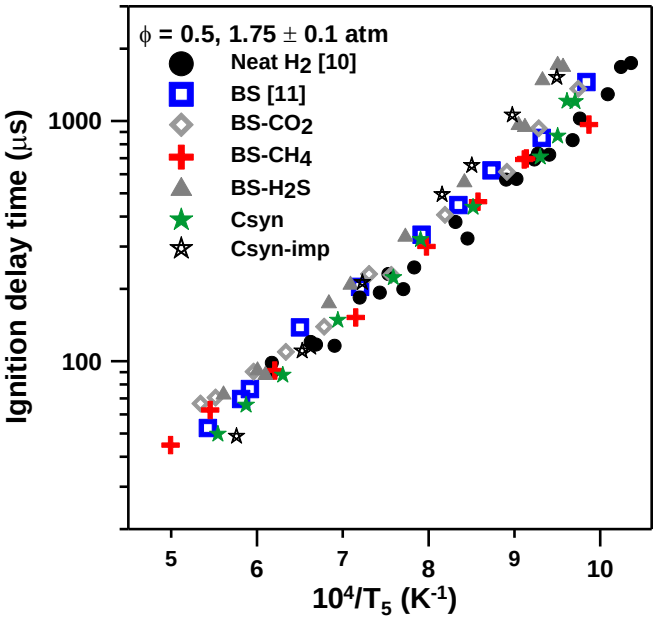

Fig. 73 Composition effect on the ignition delay time at around 1.7 atm. Fuel mixtures are as defined in Table 19.

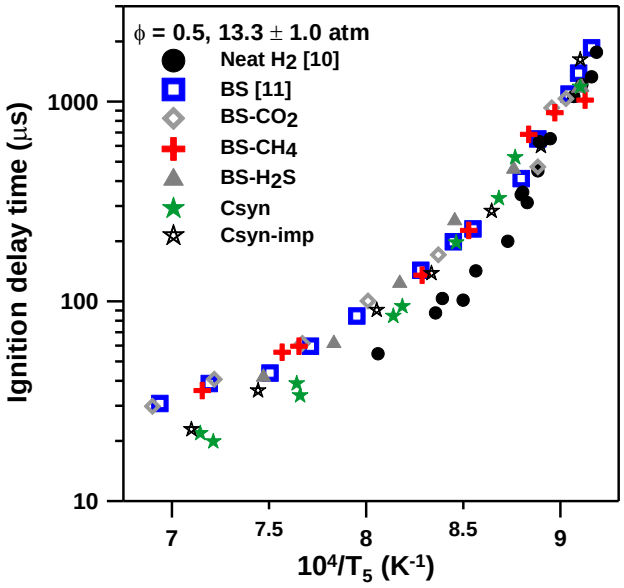

Fig. 74 Composition effect on the ignition delay time at around 13 atm. See Table 19 for fuel compositions.

At the highest pressure investigated, Fig. 75, results are mostly the same for the neat H_2, the BS, and the BS-H_2O, BS-CH_4 and BS-H_2S mixtures below 1200 K. Above this temperature, ignition delay times tend to be longer than for the neat H_2 mixture (up to around 30% at the highest temperature investigated). For the Csyn mixture, τ_{ign} are similar to the baseline mixture below 1200 K. Above this temperature, ignition delay times seem to be longer by about 35 to 50%. It is worth noting that the addition of H_2S alone to the H_2/CO baseline fuel blend decreases τ_{ign} below

1250 K. This effect is however almost not observed at all for the full mixture with impurities (Csyn-imp).

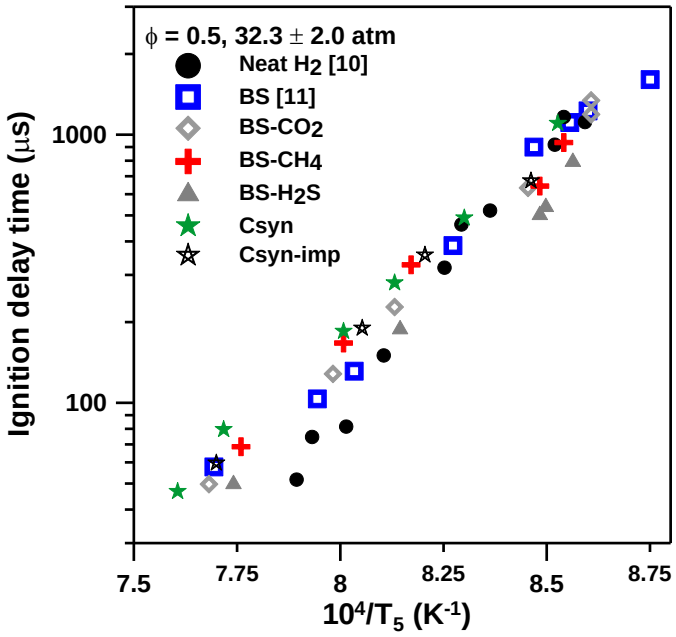

Fig. 75 Composition effect on the ignition delay time at around 32 atm. Fuel compositions are in Table 19.

Pressure and Composition Effects on the Ignition Delay Time. Since results for the coal syngas investigated in the present study have been obtained under similar conditions (same ϕ, pressure range, and dilution level) to the bio-syngas investigated in Mathieu et al. (2013b), results are compared in Fig. 76 to determine the relative importance of the syngas composition on τ_{ign}. As can be seen, the difference is relatively large between these two types of syngases. At the lowest pressure investigated, τ_{ign} for the bio-syngas are between 50% (high temperatures) and 75% (low temperatures) longer than for the coal-syngas blend. This difference is even larger at around 13 atm where a factor between 3 (high temperatures) and 5 (low temperatures) was observed. For the highest pressure investigated, however, there is no appreciable difference between the two fuel blends. Since the ignition delay times are very close between a 50/50 and a 60/40 CO/H_2 ratio (baseline bio- and coal-syngas, respectively) [Krejci et al., 2013], and since both H_2O and CO_2 addition did not exhibit any significant effect on τ_{ign} (this study and Mathieu et al. (2013b)), one can conclude that the differences in τ_{ign} between the bio- and coal-syngas are primarily due to the CH_4 concentration, which is around 5.2 times higher in the bio-syngas mixture. For reference, the composition of the bio-syngas mixture was 0.0029659 CO/0.0029659 H_2/0.0015748 CO_2/0.0008924 CH_4/0.0020997 H_2O/0.0095013 O_2/0.98 Ar (mol.) [Mathieu et al., 2013b].

Figure 76 also allows the effect of pressure on τ_{ign} for the Csyn mixture to be visualized. As can be seen, the increase in pressure has a significant and distinctive effect on τ_{ign}. When compared to typical hydrocarbon fuels, where an increase in pressure typically decreases τ_{ign} for a given temperature [Healy et al., 2010], the behavior observed from an increase in pressure for these

syngas mixtures corresponds to what is commonly observed with H_2 mixtures [Keromnes, 2013]. That is, significant changes of slope on an Arrhenius plot are observed depending on the pressure condition. For example, below 1150 K, τ_{ign} are notably longer for the 13-atm case than for the 1.7-atm condition, while τ_{ign} are higher for the 32-atm data than for the 13-atm data. This pressure dependence is similar for baseline, realistic, and pure-H_2 fuels (Figs. 71-73), indicating that the H_2 chemistry dominates under these conditions, even in the presence of the small amount of CH_4 in the Csyn fuel blend.

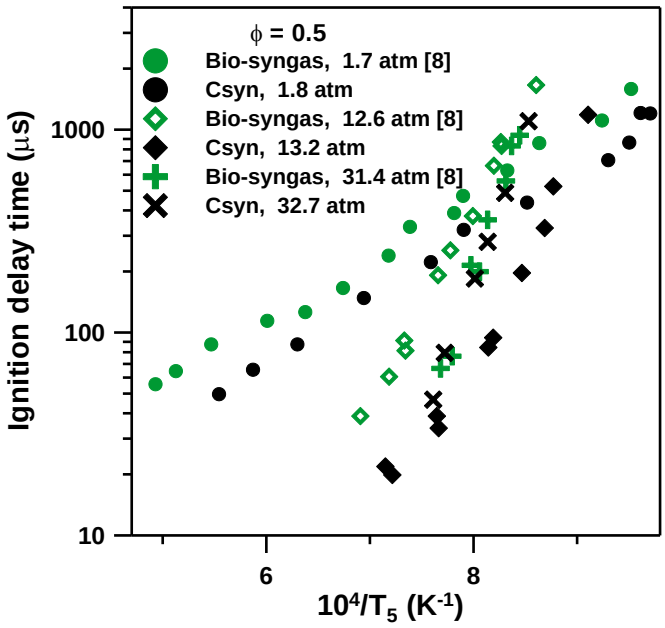

Fig. 76 Comparison between the ignition delay times of a coal- and biomass-derived syngases at around 1.7, 13, and 32 atm.

Comparison with Detailed Kinetics Models from the Literature. The data presented herein were compared to predictions from several detailed chemical kinetics mechanisms from the literature: the C0–C4 mechanism from Wang et al. (2007) (USCII), the C1 model from Li et al. (2007) (PRCT), the mechanism from Konnov (2009), and the C0–C3 mechanism from Metcalfe et al. (2013) (NUIG). When necessary, the OH* sub-mechanism from Hall and Petersen (2006) was merged with each model since OH* was used in the experiments to determine τ_{ign}. Results are visible in Fig. 77 for the baseline CO/H_2 (BS) ((a)-(c)) and for the neat coal syngas (Csyn) ((d)-(e)) mixtures. The comparisons amongst the models and the other data are visible in the supplementary material section. Note that none of the models used herein contain a H_2S or a NH_3 sub-mechanism (except Konnov (2009) for NH_3). Since a H_2/H_2S mechanism has been recently validated in similar conditions by Mathieu et al. (2014) with the same H_2 chemistry as used in the NUIG model, these two mechanisms were merged together along with the recent OCS mechanism from Glarborg and Marshall (2013), to account for possible CO/H_2S interactions. However, since adding and validating the NH_3 sub-mechanism to the models is beyond the scope of this study, no model comparison was made for the Csyn-imp mixture containing NH_3.

As can be seen in Figs. 77 (a) and (d), the low-pressure data are correctly reproduced by all the models. The models of NUIG, PRCT, and USCII are however slightly under-reactive. The model of Konnov is closer to (d) or even perfectly reproduces (a) the experimental results for the baseline mixture at 1.65 atm. At 11 atm, the models from NUIG and PRCT still yield nearly the same result. Data for the baseline mixture (b) are almost perfectly reproduced by these two models, while the trend is also well captured by the models from Konnov and USCII. For the Csyn mixture (e), the trend is captured by the models but τ_{ign} is over-predicted by a factor of 2 above 1200 K. Below this temperature, the USCII model is in agreement with the data, while the NUIG and Li et al. models are slightly over-predicting τ_{ign}. The ignition delay times computed with Konnov's model tend to be too short at the lowest temperature investigated for this intermediate-pressure condition.

At 32 atm, the baseline data (c) are well reproduced by the NUIG and PRCT models. The experimental trend is correctly predicted by the USCII mechanism, but τ_{ign} are too short. The model of Konnov is significantly too reactive for temperatures below 1250 K. For the Csyn mixture (f), the NUIG model reproduces the data nearly perfectly. Very good agreement was also observed with the PRCT model, for which τ_{ign} are slightly shorter than for the NUIG model. As for the baseline mixture, the USCII model reproduces the experimental trend for the Csyn blend but is too reactive, while the model from Konnov is significantly excessively reactive above 1250 K. Overall, this study shows that the models from Metcalfe et al. (2013) and Li et al. (2007) seem most suitable to model τ_{ign} for syngas mixtures over the entire range of conditions herein.

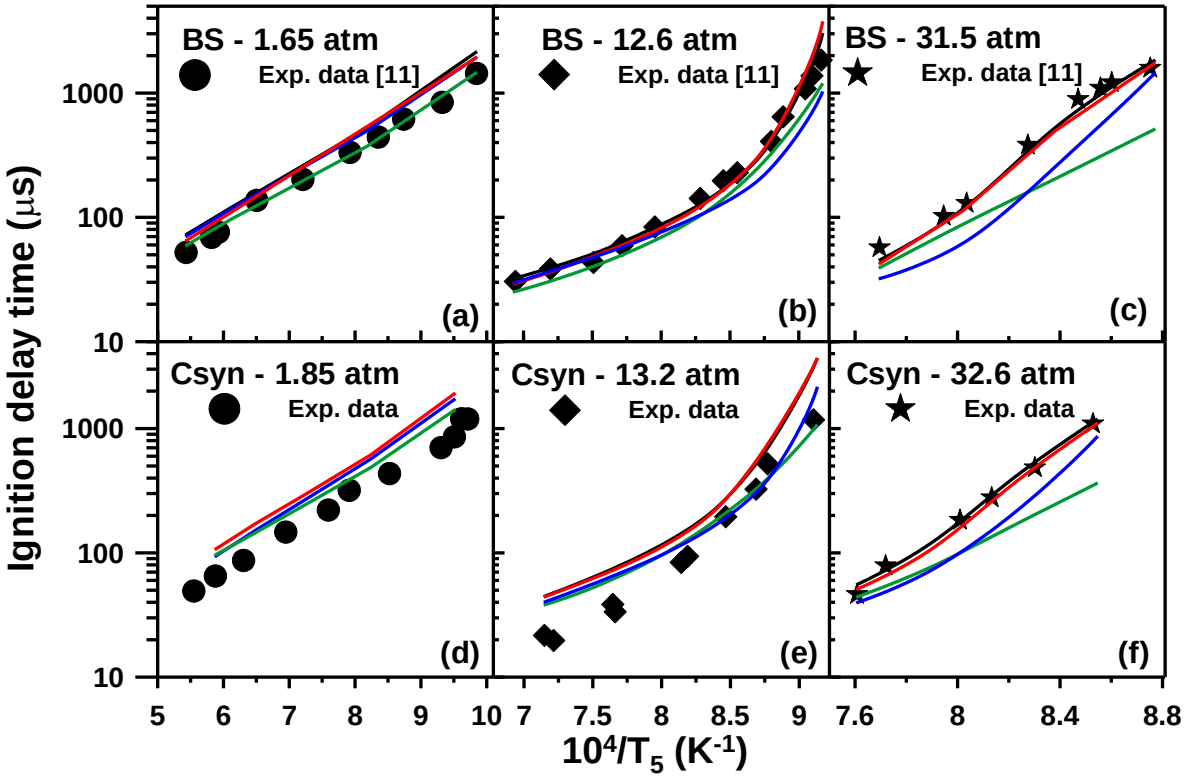

Fig. 77 Comparison between experiments and models for the BS mixture at around 1.7 (a), 13 (b), and 32 atm (c) and for the Csyn mixture at around 1.7 (d), 13 (e), and 32 atm (f). Black line: NUIG [Metcalfe et

al., 2013], red line: PRCT [Li et al., 2007]], blue line: USCII [Wang et al., 2007], and green line: Konnov (2009).

A comparison between the BS-H_2S mixture data and the NUIG model merged with H_2S [Mathieu et al., 2014] and OCS [Glarborg and Marshall, 2013] sub-mechanisms is visible in Fig. 78. As can be seen, experimental trends are well captured by this model, although the predicted τ_{ign} are slightly longer than the experimental ones.

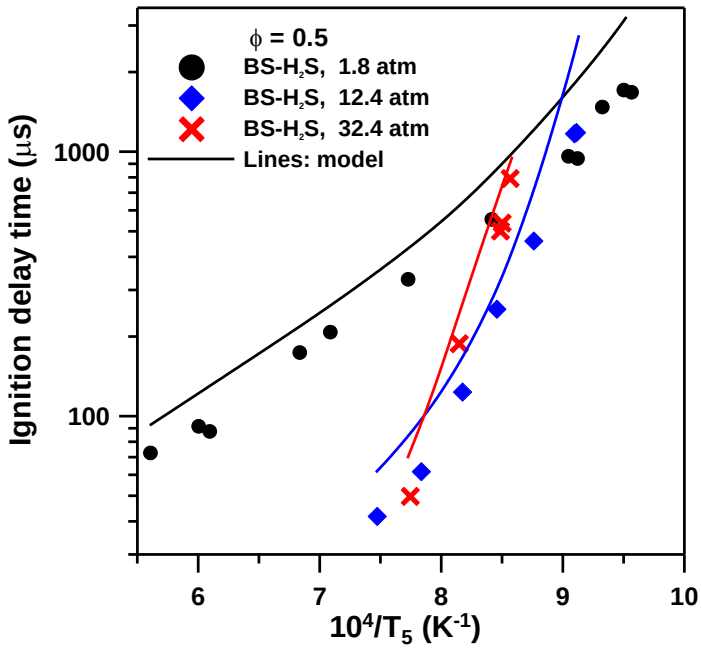

Fig. 78 Comparison between the experiments and the model (H_2/CO from Metcalfe et al. (2013)], H_2S from Mathieu et al. (2014) and OCS from Glarborg and Marshall (2013)) for the BS-H_2S mixture.

Discussion

The effect of various added species on the ignition delay times of a CO/H_2/O_2 mixture diluted in Ar was investigated in this study. Overall, the impacts of these additions were not significant, with the hydrogen chemistry still being dominant over the conditions investigated. Results were captured and well predicted by recent models from the literature, except for the high-temperature region around 13 atm for the Csyn mixture, where the models were not reactive enough. A similar observation was made by the authors at these same conditions for a biomass-derived syngas [Mathieu et al., 2013b]. Since the τ_{ign} data are in contrast well predicted at these conditions for the baseline mixtures doped with only CO_2, CH_4, or H_2O, this result could indicate that some interactions could exist between CH_4, CO_2, and/or H_2O when all three exist in a realistic fuel blend (which relates directly or indirectly to OH formation) that are not well considered by the current models.

Concerning the impurities, a lack of effect on τ_{ign} of NH_3 addition to syngas was previously investigated by the authors for a bio-syngas blend [Mathieu et al., 2013b]. A chemical analysis

showed that NH_3 does not react appreciably prior to the ignition event. However, computations showed that a significant proportion of NH_3 is subsequently converted to NO, which can induce important changes in the combustion properties in case of a burned-gas recirculation strategy.

Some noticeable effects were observed with H_2S addition (BS-H_2S mixture), notably at low temperature for the lowest- (increase in τ_{ign} with H_2S addition) and highest-pressure (decrease in τ_{ign}) cases. These effects were investigated using sensitivity and reaction pathway analyses. For the low-pressure case, the analysis showed that the decrease in the reactivity is mostly due to the reaction $H_2S+H \rightleftarrows SH+H_2$, which inhibits the most-sensitive reaction $H+O_2 \rightleftarrows OH+O$ by competing for H atoms. The complete mechanism for the increase in the reactivity at low temperature/high pressure was detailed in Mathieu et al. (2014). Note that there is no reaction involving CO and any sulfur-containing species among the 10 most-sensitive reactions under these conditions.

EFFECT OF IMPURITIES ON SYNGAS COMBUSTION AT ENGINE CONDITIONS

Synthetic gas or syngas, a gaseous mixture composed ideally of CO and H_2, can be produced from a large variety of feedstock (coal, biomass, waste, and natural gas) and production methods. These characteristics make syngas an attractive fuel to produce clean energy efficiently, with fuel supply flexibility and security for power systems such as gas turbines. However, this large variety of feedstock and production methods induces a large variation in the syngas composition where, in addition to the CO and H_2, can be found reasonable amounts of small hydrocarbons, CO_2, H_2O, N_2, and impurities such as NH_3, HCN, COS, NOx and H_2S.

A literature survey on the two types of feedstock considered for this study, coal and biomass, highlighted this high variation in the syngas composition (note that several gasification methods were employed to produce these syngases). For instance, a total of 23 different compositions were found for a real biomass-derived syngas where the H_2 mole percentage varies between 5 and 50.4% and the CO percentage between 8.1 and 50% [Zhang, 2010; Göransson et al., 2011; Chacartegui et al., 2011; Munasinghe and Khanal, 2010]. Overall, the average CO/H_2 mole ratio in these bio-derived syngases was 50/50. Several other compounds such as N_2, CH_4, C_2H_2, C_2H_4, C_2H_6, CO_2, H_2O, and impurities such as NH_3, NOx, and SO_2 have been reported as well. The same exercise has been done for a coal-derived syngas with an average composition determined from 40 real, coal-syngas mixtures (compositions taken from Zhang (2010); Chacartegui et al. (2011); Munasinghe and Khanal, 2010; among several others). The H_2/CO mole ratio was determined to be 40/60 for this average coal-syngas. It has been found that the proportion of hydrocarbons was typically higher for the biomass-derived syngas and that the impurities can be different amongst specific blends. This trend was confirmed by the study of Xu et al. (2011), where the nature and maximum concentration of hydrocarbons and contaminates reported in the literature were listed for both types of syngas.

Although the laminar flame speed (S_L) and ignition delay time (τ_{ign}) of basic H_2/CO mixtures have been investigated thoroughly in recent years, there is however very little information on the fundamental combustion of more-complex and realistic mixtures. Thus, only the influences of carbon dioxide [Natarajan et al., 2005; Burke et al., 2010], steam [Das et al., 2011], and nitrogen [Prathap et al., 2008] on flame speed have been studied, whereas the addition of hydrocarbons to a H_2/CO mixture is still an area requiring investigation. For the ignition delay time, except for a recent study on an average bio-syngas mixture by the authors [Mathieu et al., 2013], only CO_2 addition effects have been investigated over the past few years [Mathieu et al., 2013; Petersen et al., 2007; Peschke and Spadaccini, 1985]. During the recent bio-syngas study, the average H_2/CO mole ratio was found to be equal to 1.0, and the influence of the mixture composition (addition of CH_4, CO_2, H_2O, and NH_3) on the ignition delay time of this 1:1 CO/H_2 mixture has been investigated in a shock tube under various-pressure conditions. Results showed that the composition of the syngas can induce noticeable variations in the ignition delay time, especially at temperatures above 1250 K and for pressures of 12.5 atm or lower, indicating a need for more studies on the effect of syngas composition on combustion properties such as ignition delay time.

Consequently, because of this lack of experimental background on realistic syngas blends, it is difficult for gas turbine manufacturers to design engines that can operate efficiently and safely with this wide range of fuel compositions. Using a state-of-the-art C0-C5 detailed kinetics mechanism the aim of the larger effort from the present authors is therefore to investigate

numerically the effect of the syngas composition on some fundamental combustion properties of premixed systems, such as laminar flame speed and ignition delay time, at realistic engine operating conditions.

More specifically, the present study focused on the effect of the presence and concentration of hydrocarbon addition to baseline (CO/H_2) coal- and biomass-derived syngases. Details on the modeling procedure and mixtures investigated are covered first, followed by the results. This latter section covers the neat baseline mixtures, the effect of hydrocarbon addition to the baseline mixtures, and the averaged syngas mixtures. Several mechanisms from the literature will be compared as well, against some selected conditions. A discussion of the results with emphasis on the significant kinetics reactions is provided in the latter portion of this section of the report.

Modeling Procedure

The detailed chemical kinetics model used herein is based on the C0–C5 mechanism developed at the National University of Ireland, Galway (NUIG) [Metcalfe et al., 2013]. Note that the flame speed calculations were performed using the high-temperature version of the NUIG model, where low-temperature species (peroxy radicals, alkyl hydroperoxides, ketohydroperoxides, etc.) and reactions were removed. The complete mechanism is 1805 reactions and 316 species, while the high-temperature mechanism is 188 species and 1273 reactions.

Mixtures Investigated

To investigate the effect of hydrocarbons on the combustion properties of interest herein (ignition delay time and laminar flame speed), the two first mixtures studied were the neat, baseline CO/H_2 mixtures in air for the coal- and bio-derived syngas (60/40 and 50/50 (mole ratio), respectively). The hydrocarbons (CH_4, C_2H_6, C_2H_4, and C_2H_2) were then individually added to these baseline mixtures to study their respective influence on the combustion properties at the relative proportions that one would find them in the respective two types of syngas. Depending on the concentration reported in the literature, various concentration levels were investigated in some cases. For example, the maximum concentration of methane reported in a biomass-derived syngas is 15%, and an average value of 8.5% was determined. The effect of methane concentration was therefore investigated at 5, 8.5, and 15% for the ignition delay time with the baseline bio-syngas.

Averaged mixtures were then defined and studied for the coal- and bio-derived syngases (base H_2/CO, hydrocarbons, and diluents). The composition of the mixtures investigated in this study is provided in Table 21 for the bio-derived syngas and in Table 22 for the coal-derived syngas. Note that only the mixtures with the highest concentration for CH_4 were investigated for the flame speed.

Ignition delay time computations were performed at 1, 10, and 35 atm between 900 and 1400 K and equivalence ratios ϕ = 0.5 and 1.0. The ignition delay time was determined using the step rise in the OH* signal, which occurs at the ignition, as visible in Fig. 79. As can be seen in this figure, using this definition of the ignition delay time with the pressure signal would have yielded a similar result even though a slow and very moderate pressure increase can be observed after 0.42 s, before the ignition.

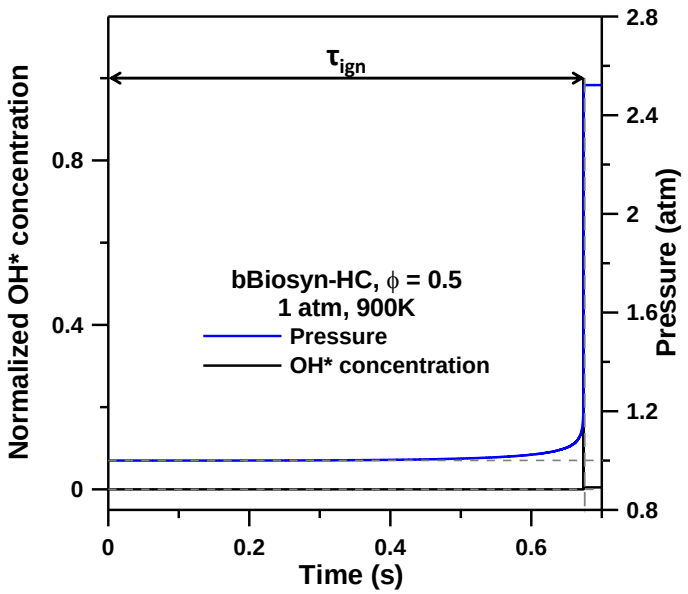

Fig. 79 Determination method for the ignition delay time using the computed pressure and normalized OH* concentration profiles.

Flame speed computations were performed at 1 and 15 atm; between ϕ = 0.5 and 3.0; and for unburned gas temperatures (Tu) of 300 and 500 K.

Model Validation

Several base mechanisms are available in the literature, each of these mechanisms being validated against a large body of data. However, as mentioned in the introduction section, there are very few experimental results available on realistic syngas compositions. Thus, the recent bio-syngas shock-tube results presented in Mathieu et al. (2013) were used as a benchmark to evaluate the detailed kinetics mechanisms available. These data have been taken at pressure conditions similar to the pressures investigated in the present study. Figure 80 shows the data from Mathieu et al. (2013) and the results provided by the kinetics model from NUIG Metcalfe et al. (2013), the mechanism from Wang and coworkers (referred to as USC hereafter) [Wang et al., 2007], and the mechanism from Petrova and Williams (2006) (SD). As can be seen, the NUIG model is closer to the data at around 1.6 atm, more particularly below 1250 K where the other models deviate from the experimental results. At around 12.5 atm, all the models deviate from the data above 1325 K. Below this temperature, the model from NUIG is on top of the experimental values while the mechanisms from USC and SD slightly under- and over-predict the ignition delay time, respectively. At around 32 atm, the NUIG model is very close to the data over almost the entire range of temperatures investigated. One can however notice that the mechanism seems to be slightly under-reactive for the highest temperatures. The USC model captures the trend of the experimental data but over-predicts the ignition delay time. At 32 atm, the SD model is close to the experimental values on the low temperature side but rapidly deviates and largely over-predicts the ignition delay time as the temperature increases.

This result demonstrates the relevance of the mechanism used in this study to conduct a numerical investigation for the temperature and pressure range relevant to gas turbines. Nonetheless, a mechanisms comparison over a few selected conditions is carried out later in this paper, to provide the reader with some estimation on the detailed kinetics model effect.

The results are presented as follows. The calculations for the neat baseline mixtures (CO and H_2 only) are covered first, followed by the effect of the additional hydrocarbons on the baseline mixtures. In the final section, the averaged syngas mixtures including all species are considered. For each general category, the ignition delay time results are discussed first, followed by the laminar flame speed results.

Neat Baseline Mixtures

Ignition Delay Time. The evolution with the temperature of the ignition delay times for the two neat baseline mixtures ($50CO/50H_2$ for the bio-derived syngas and $60CO/40H_2$ for the coal-derived syngas, mole ratio) at the three pressure conditions investigated can be seen in Fig. 81. It is visible that this slight variation in the CO/H_2 proportion does not significantly change the predicted ignition delay times; all the curves are close to each other and follow the same trend for a given pressure. One can however notice that the ignition delay times are slightly shorter for the bio-syngas mixture, which contains the higher proportion of H_2.

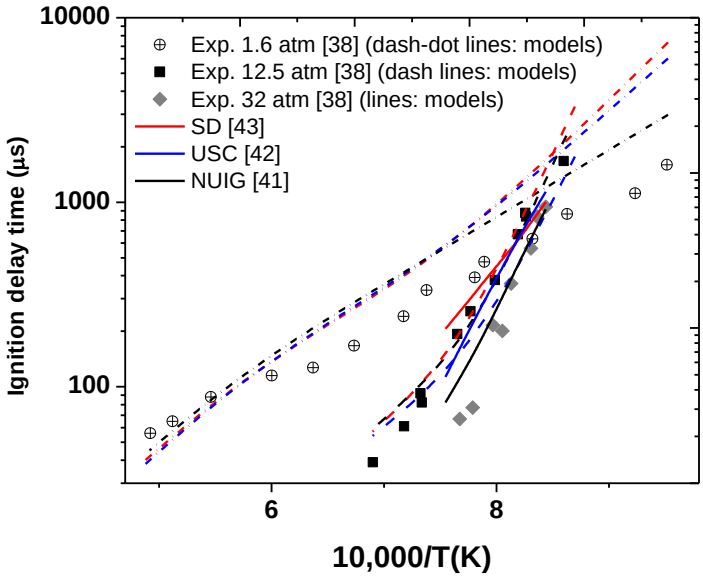

Fig. 80 Comparison with the bio-syngas shock-tube results from Mathieu et al. (2013) and models from the literature.

Since the CO/H_2 mole ratio can vary significantly for both types of syngas, two other extreme mixtures, $75H_2/25CO$ and $25H_2/75CO$ were tested in similar conditions. As can be seen, even if the difference in the ignition delay time can be relatively important between these two extremes, the trends for each pressure condition are the same, indicating that the H_2 chemistry is dominating in these syngas mixtures. A similar conclusion was reached for various H_2/CO syngas mixtures in Herzler and Naumann (2008) and Krejci et al. (2012). The effects of

hydrocarbon addition on the shape of the ignition delay time plots, as seen later in this study, are therefore primarily due to the effect of these additions on the H_2 chemistry.

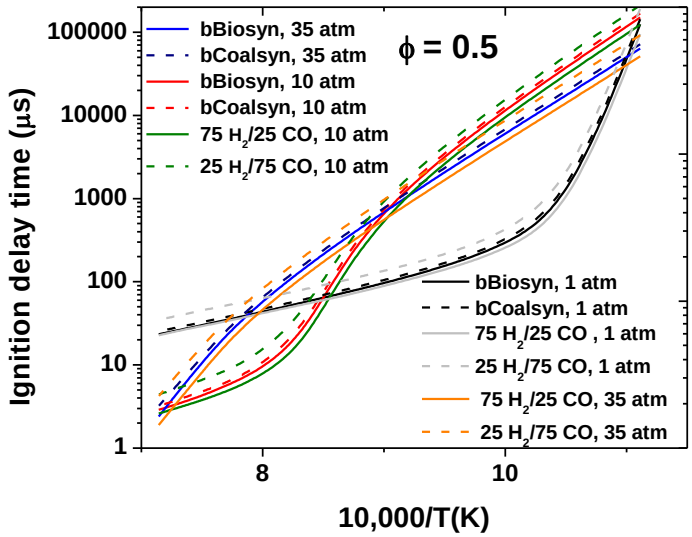

Fig. 81 Evolution of the ignition delay time with the temperature at three pressure conditions, 1, 10, and 35 atm and at an equivalence ratio of 0.5. Mixtures are CO/H_2 in air with the following CO/H_2 mole proportions: 75/25, 60/40 (bCoalsyn), 50/50 (bBiosyn) and 25/75.

Another thing that can be observed in Fig. 81 is the important pressure effect on the ignition delay time. Indeed, ignition delay times can actually be shorter at 1 atm than at 10 and 35 atm, depending on the temperature, and a crossover between the results at 10 and 35 atm can also be observed at around 1100 K. All these pressure/temperature behaviors are in fact due to the well-known competition between a few reactions in the H_2 chemistry, as documented in Keromnes et al. (2013) and discussed later.

Note that some studies showed a large difference between the ignition delay time predicted by detailed kinetics models and the ignition delay times determined experimentally by shock tube [Petersen et al., 2007] and rapid compression machine [Walton et al., 2007] for syngas /air mixtures at high pressure/low temperature conditions. This discrepancy is in fact due to non-ideal ignition behavior during the experiments, with a mild pre-ignition rise in pressure and, therefore, in temperature. Note that this phenomenon is not observed with dilute mixtures.

The effect of the equivalence ratio was also investigated on the ignition delay times of the baseline coal- and bio-derived syngases, as seen in Fig. 82, where results for $\phi = 0.5$ and 1.0 can be compared. Results show that there is nearly no effect of the equivalence ratio at a pressure of 1 atm. However, for pressures above 1 atm, it can be seen that ignition delay times are lower at $\phi = 1$ than at $\phi = 0.5$, especially on the low-temperature side of the graph, where a reduction in τ_{ign} larger than 33% is observed.

Table 21 Biosyngas mixtures investigated (mole fraction).

Mixture	H_2	CO	CH_4	C_2H_6	C_2H_4	C_2H_2	H_2O	N_2	CO_2
bBiosyn	50.00	50.00	—	—	—	—	—	—	—
bBiosyn-CH_4Lo	47.50	47.50	5.00	—	—	—	—	—	—
bBiosyn-CH_4Av	45.75	45.75	8.50	—	—	—	—	—	—
bBiosyn-CH_4Hi	42.50	42.50	15.00	—	—	—	—	—	—
bBiosyn-C_2H_6	49.60	49.60	—	0.80	—	—	—	—	—
bBiosyn-C_2H_4	47.35	47.35	—	—	5.30	—	—	—	—
bBiosyn-C_2H_2	49.65	49.65	—	—	—	0.70	—	—	—
bBiosyn-HC	39.10	39.10	15.00	0.80	5.30	0.70	—	—	—
Biosyn	21.75	21.75	8.50	—	—	—	20.00	13.00	15.00

Table 22 Coalsyngas mixtures investigated (mole fraction).

Mixture	H_2	CO	CH_4	C_2H_6	C_2H_4	C_2H_2	H_2O	N_2	CO_2
bCoalsyn	40.00	60.00	—	—	—	—	—	—	—
bCoalsyn-CH_4Av	39.36	59.04	1.6	—	—	—	—	—	—
bCoalsyn-CH_4Hi	37.04	55.56	7.40	—	—	—	—	—	—
bCoalsyn-C_2H_6	39.32	58.98	—	1.70	—	—	—	—	—
bCoalsyn-C_2H_4	39.96	59.94	—	—	0.10	—	—	—	—
bCoalsyn-C_2H_2	39.948	59.922	—	—	—	0.13	—	—	—
bCoalsyn-HC	36.268	54.402	7.40	1.70	0.10	0.13	—	—	—
Coalsyn	23.48	35.22	1.60	—	—	—	21.80	8.50	9.40

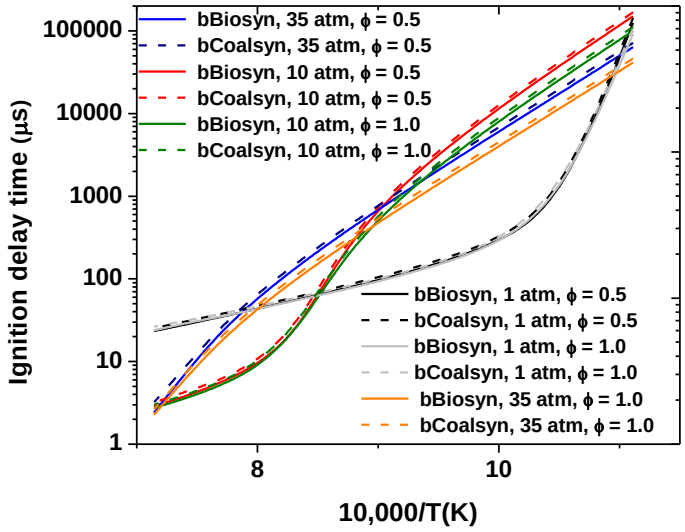

Fig. 82 Evolution of the ignition delay time with the temperature and the equivalence ratio at three pressure conditions, 1, 10, and 35 atm for the bCoalsyn ($60CO/40H_2$) and bBiosyn ($50CO/50H_2$) mixtures.

Laminar Flame Speed. The effect of the baseline CO/H_2 mixtures on the laminar flame speed was also investigated. Figure 83 presents the results obtained at 1 atm for an inlet temperature of 300 K. As can be seen, the difference between a $50CO/50H_2$ (bBiosyn) and a $60CO/40H_2$ (bCoalsyn) mixture can be relatively important, especially at fuel rich conditions. Not surprisingly, the blend with the lower amount of H_2 has the lower flame speed, but the difference can be up to 30 cm/s. At the extreme conditions investigated (15 atm, 500 K), it is visible in Fig. 84 that the difference between these two mixtures is even larger, the flame speed being around 225 cm/s for the bCoalsyn mixture and 270 cm/s for the bBiosyn mixture at $\phi = 2.1$.

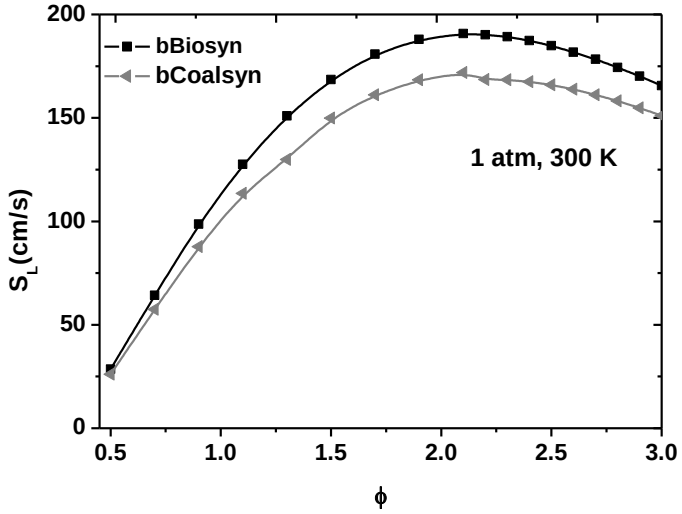

Fig. 83 Laminar flame speeds for the baseline bio-syngas and coal-syngas mixtures (bBiosyn and bCoalsyn) at 1 atm and an inlet temperature of 300 K.

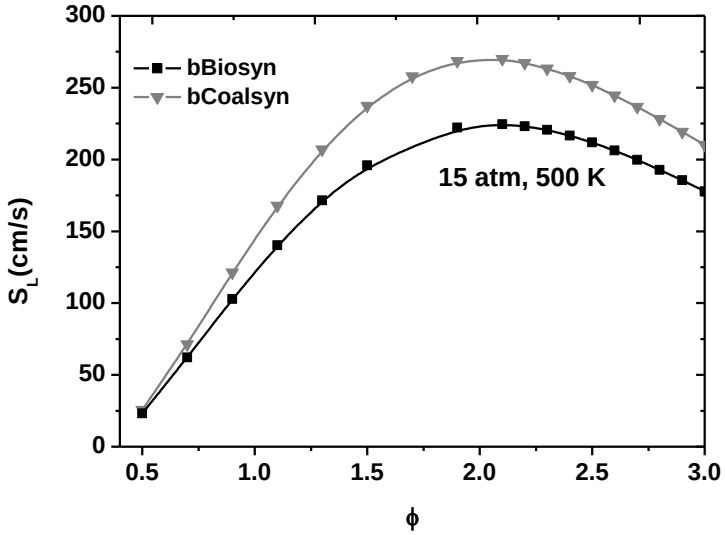

Fig. 84 Laminar flame speeds for the baseline bio-syngas and coal-syngas mixtures (bBiosyn and bCoalsyn) at 15 atm and an inlet temperature of 500 K.

Hydrocarbon Addition to the Baseline Mixtures

Ignition Delay Time. The effect of hydrocarbon addition to the baseline bio-derived syngas is visible in Figs. 85 (1 atm), 86 (10 atm), and 87 (35 atm). At 1 atm, it can be seen that the addition of hydrocarbons tends to increase τ_{ign} over the entire range of temperature. However, one can notice that a small decrease in the ignition delay time can be observed when C_2H_2 is added. Additions of methane seem to generally reduce the reactivity of the mixture on the high-temperature side of the curve, whereas C_2H_6 and C_2H_4 reduce the reactivity on the low-temperature side. For the fuel mixture with all the hydrocarbons together, at their highest concentrations (bBiosyn-HC mixture), it can be seen that the effects of the hydrocarbons are cumulative, with ignition delay times that are similar to the bBiosyn-C_2H_4 mixture on the low-temperature side and similar to the bBiosyn-CH_4Hi mixture on the high-temperature side.

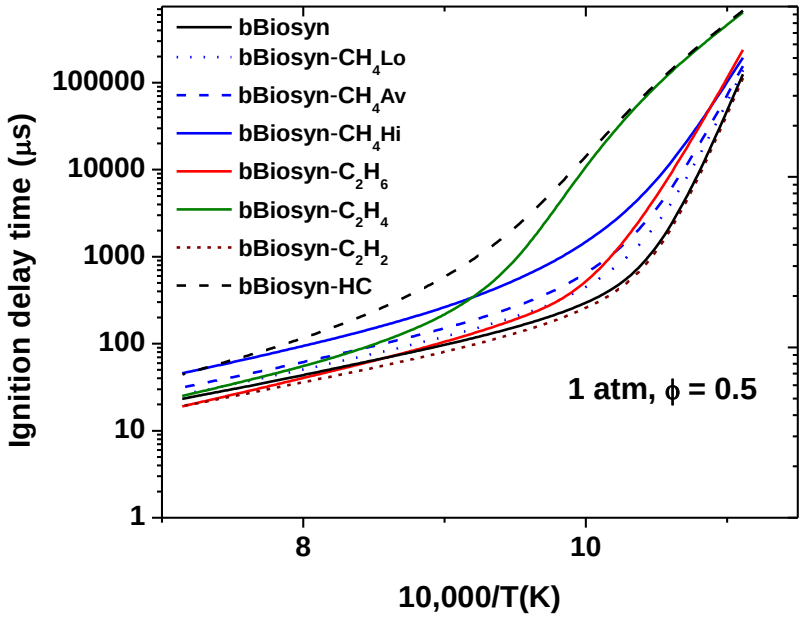

Fig. 85 Effect of hydrocarbon addition on the ignition delay time of the bBiosyn mixture at 1 atm and at an equivalence ratio of 0.5.

At higher pressures, 10 and 35 atm (Figs. 86 and 87), it can be seen that the addition of hydrocarbons impacts the ignition delay time only on the high-temperature side, above 1100 K. A small increase in the mixture reactivity is still observed with the 0.7% C_2H_2 addition, whereas the curvature induced by the H_2 chemistry for the neat baseline mixture (bBiosyn) is reduced by the other hydrocarbons as the ignition delay time is increased. At these high pressures, the ignition delay time of the bBiosyn-HC mixture is very close to the τ_{ign} of the bBiosyn-CH_4Hi mixture.

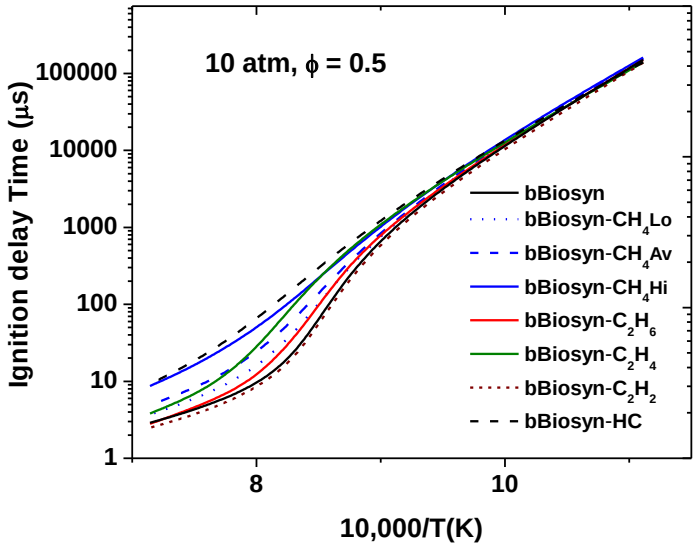

Fig. 86 Effect of hydrocarbon addition on the ignition delay time of the bBiosyn mixture at 10 atm and at an equivalence ratio of 0.5.

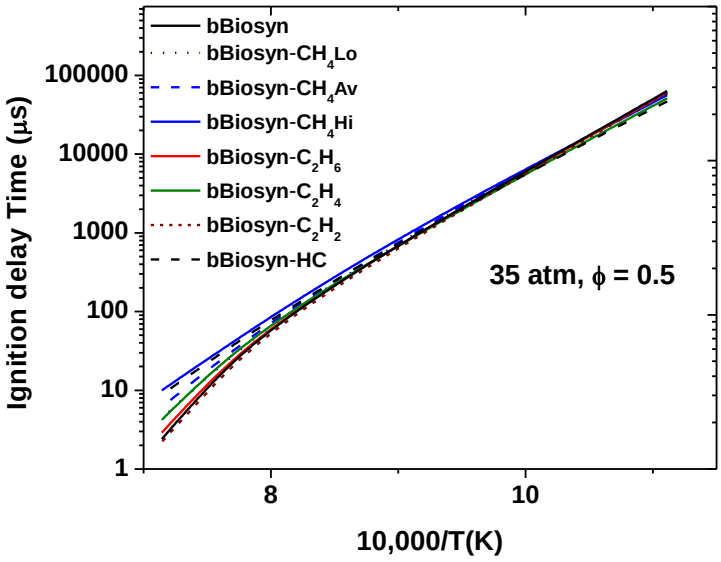

Fig. 87 Effect of hydrocarbon addition on the ignition delay time of the bBiosyn mixture at 35 atm and at an equivalence ratio of 0.5.

Figure 88 shows the effect of pressure and equivalence ratio on the bBiosyn-HC mixture. As can be seen, the effect of the equivalence ratio depends on the pressure regime. Indeed, ignition delay times are longer at $\phi = 1$ than at $\phi = 0.5$ at 1 atm, whereas an opposite trend is observed at higher pressures. Also, when comparing results at $\phi = 0.5$ with the bBiosyn mixture in Fig. 81, one can see that the pressure effect on τ_{ign} is less dramatic when hydrocarbons are present in the fuel composition.

Compared to the bio-derived syngas mixtures, coal-derived syngas typically contains a smaller amount of hydrocarbons (except C_2H_6 according to Xu et al. (2011)). The specific hydrocarbons are nevertheless the same, and the trends observed with the biomass-derived syngas are logically somewhat similar, but less pronounced, for the coal-derived syngas. The effects of hydrocarbon addition on the bCoalsyn mixture at 1 atm are visible in Fig. 89. It is shown in this figure that, as for the b-Biosyn mixture, the τ_{ign} for the bCoalsyn-C_2H_6 mixture (ζC_2H_6 = 1.7%) are longer than for the bCoalsyn-CH_4Hi mixture (ζCH_4 = 7.4%) below 1100 K. Above this temperature, the addition of methane demonstrates the highest increase in the ignition delay time of all the single hydrocarbons. Again, as for the bio-syngas mixture, the mixture with all the hydrocarbons together at their highest concentrations (bCoalsyn-HC mixture) shows ignition delay times that are similar to the bCoalsyn-C_2H_6 mixture on the low-temperature side and similar to the bCoalsyn-CH_4Hi mixture on the high-temperature side.

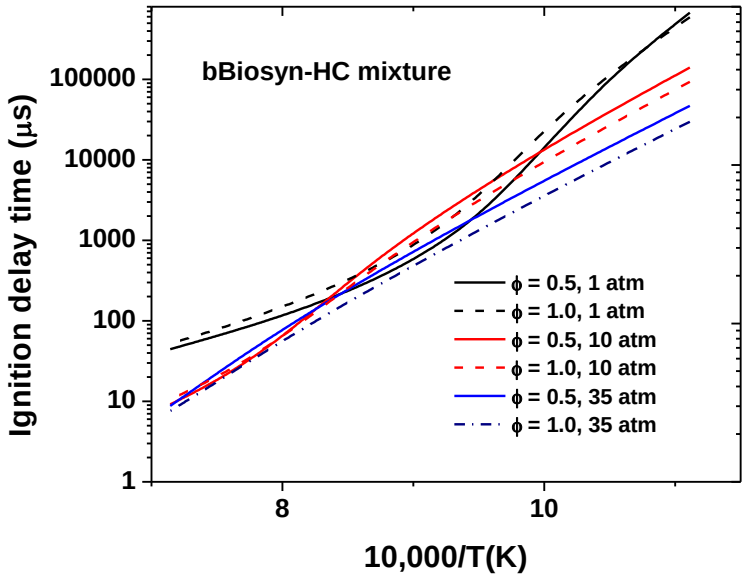

Fig. 88 Pressure and equivalence ratio effect on the ignition delay time of the bBiosyn-HC mixture at 1, 10 and 35 atm.

At higher pressures, 10 atm (Fig. 90) and 35 atm (Fig. 91), the behaviors observed for the bBiosyn mixture are also observed for the bCoalsyn mixture. Indeed, effects of the hydrocarbon addition are visible only at high temperature; methane shows the most-prominent effect of all of the single hydrocarbons, and the bCoalsyn-HC mixture shows the longest ignition delay time.

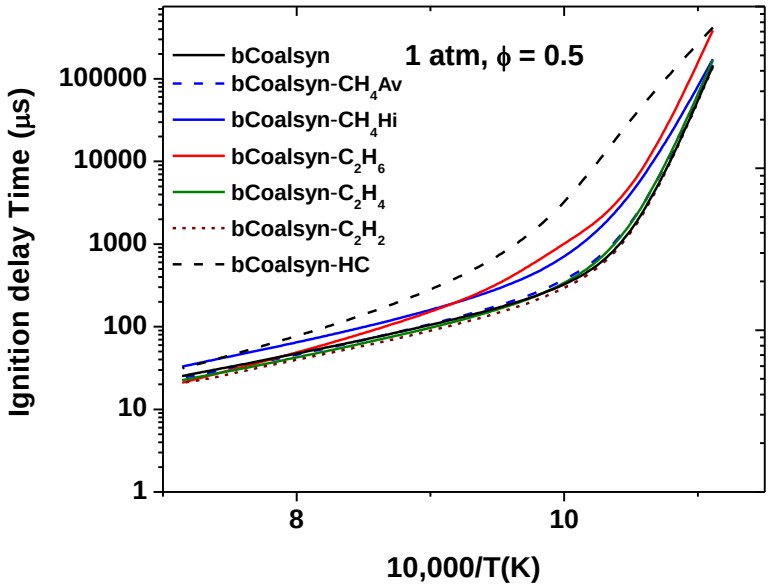

Fig. 89 Effect of hydrocarbon addition on the ignition delay time of the bCoalsyn mixture at 1 atm and at an equivalence ratio of 0.5.

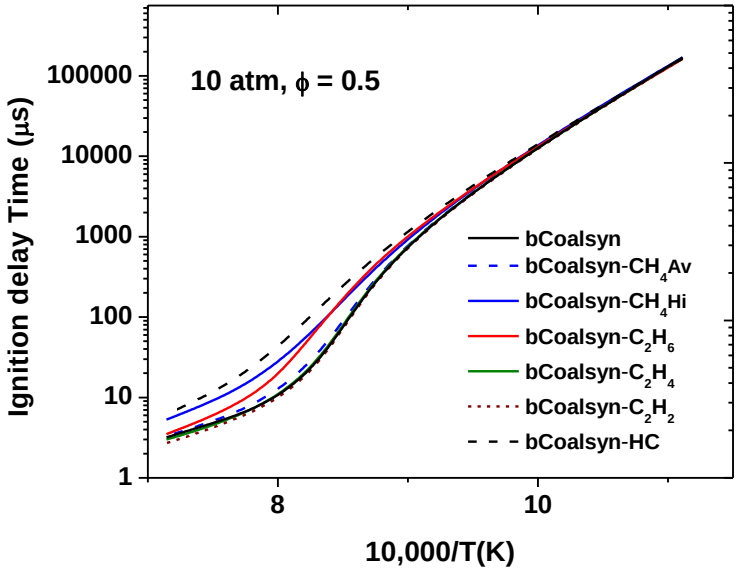

Fig. 90 Effect of hydrocarbon addition on the ignition delay time of the bCoalsyn mixture at 10 atm and at an equivalence ratio of 0.5.

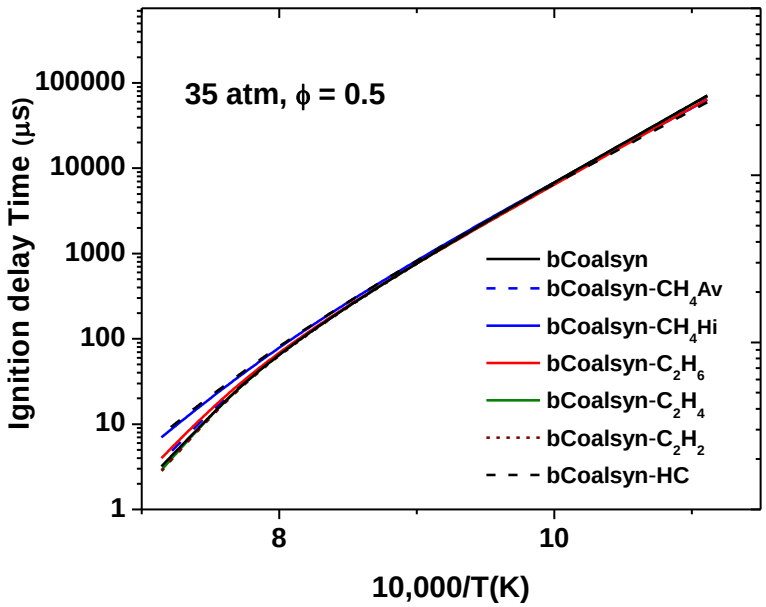

Fig. 91 Effect of hydrocarbon addition on the ignition delay time of the bCoalsyn mixture at 35 atm and at an equivalence ratio of 0.5.

The equivalence ratio and pressure effects on the ignition delay times of the bCoalsyn-HC mixture are visible in Fig. 92. At 1 atm, the increase in the equivalence ratio leads to slightly longer ignition delay time, generally between 1000 and 1250 K.At 10 atm, a slight increase in the ignition delay time can also be observed above 1200 K, whereas a small decrease in τ_{ign} is observed at lower temperatures. At 35 atm, an increase in the equivalence ratio leads to a decrease in the ignition delay time. This decrease is amplified as the temperature is reducing.

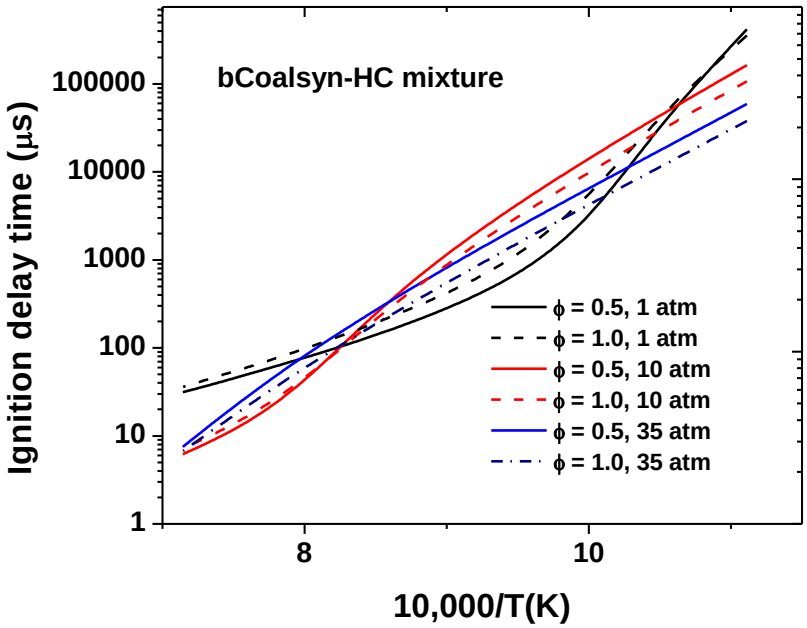

Fig. 92 Pressure and equivalence ratio effect on the ignition delay time of the bCoalsyn-HC mixture.

Flame Speed. The effect of hydrocarbon addition on the laminar flame speed of the bBiosyn mixture at 1 atm and at an inlet temperature of 300 K is visible in Fig. 93. At these conditions, one can see that the behaviors observed for the ignition delay time are also visible on the laminar flame speed. Indeed, a very small increase of the laminar flame speed can be seen for the addition of C_2H_2 for ϕ lower than 1.5 (a small decrease in S_L is however observed for equivalence ratios larger than 2.0) whereas the addition of CH_4, C_2H_6, and C_2H_4 decreases notably the laminar flame speed, especially at fuel rich conditions. The decrease of the flame speed is however very important for C_2H_6 and, to a lesser extent, to C_2H_4 compared to CH_4 given their respective concentrations (0.8, 5.3, and 15%). Finally, it is visible that the flame speed is significantly smaller for the bBiosyn-HC mixture, where all the hydrocarbons are present, with nearly a factor of 2 lower peak flame speed compared to the bBiosyn blend. At an equivalence ratio of 2.0, the laminar flame speed is more than 10 times higher for the bBiosyn mixture than for the bBiosyn-HC mixture.

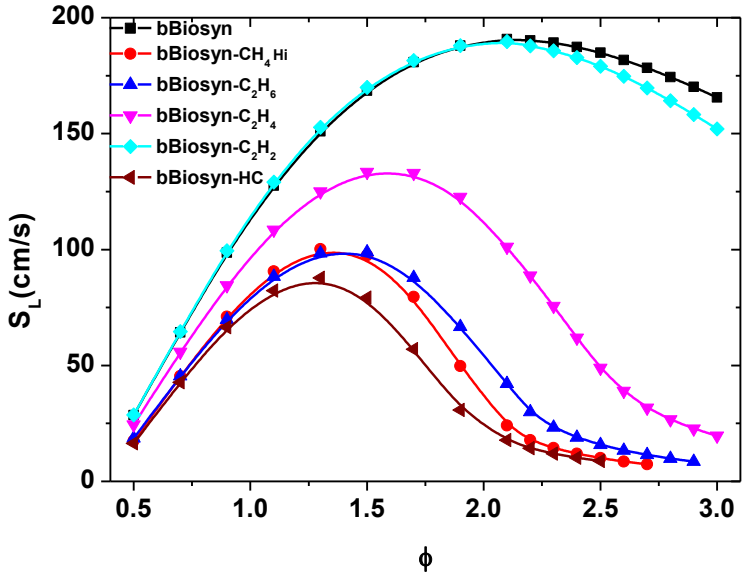

Fig. 93 Laminar flame speed as a function of hydrocarbon addition for the baseline bio-syngas mixture (bBiosyn) at 1 atm and at an inlet temperature of 300 K.

For a higher inlet temperature of 500 K, Fig. 94, similar observations can be made. It can also be seen that an increase in the unburned gas temperature by 200 K leads to an increase of the laminar flame speed by a factor slightly larger than two at 1 atm.

As can be seen by comparing Fig. 93 (1 atm) and Fig. 95 (15 atm), an increase in the pressure is translated into a reduction of the flame speed by around 40% for the baseline mixture. This important reduction in the flame speed is also observed for the mixtures with hydrocarbons in even higher proportions. Note that at this high pressure, the C_2H_2 behavior is slightly amplified with larger increases (below $\phi = 1.9$) and decreases (above $\phi = 1.9$) of the laminar flame speed.

Figure 96 shows computed results for a high pressure of 15 atm and with an inlet temperature of 500 K. At this high-pressure/high-temperature condition, it is visible that the effect of CH_4 and

C_2H_6 addition on the laminar flame speed can be clearly distinguished below ϕ = 1.25, which was not the case for the lower-pressure conditions investigated (Figs. 93 and 94). It can be seen that the laminar flame speed of the bBiosyn-HC mixture is very close to the flame speed yielded by the mixture with methane alone, indicating a stronger influence of methane as the pressure increases. This effect was also observed for the lower gas temperature (Fig. 95). Finally, one can note that the significant increase in the flame speed with the increase of the unburned gas temperature observed at 1 atm is also observed at 15 atm (Figs. 95 and 96).

Although the hydrocarbon concentration is typically smaller for a coal-syngas mixture, it is however interesting to notice that the concentration of C_2H_6 can be higher than for a bio-derived syngas according to Xu et al. (2011) (1.7 versus 0.8%, respectively). As seen above, the addition of C_2H_6 demonstrated an important impact on the laminar flame speed of the baseline bio-syngas mixture. Although the hydrocarbon concentration is typically smaller for a coal-syngas mixture, it is however interesting to notice that the concentration of C_2H_6 can be higher than for a bio-derived syngas according to Xu et al. (2011) (1.7 versus 0.8%, respectively). As seen above, the addition of C_2H_6 demonstrated an important impact on the laminar flame speed of the baseline bio-syngas mixture.

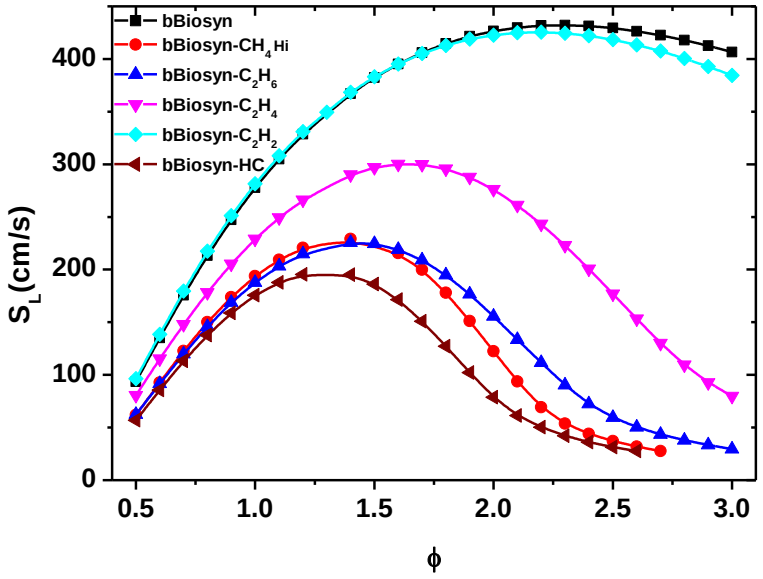

Fig. 94 Laminar flame speed as a function of hydrocarbon addition for the baseline bio-syngas mixture (bBiosyn) at 1 atm and at an inlet temperature of 500 K.

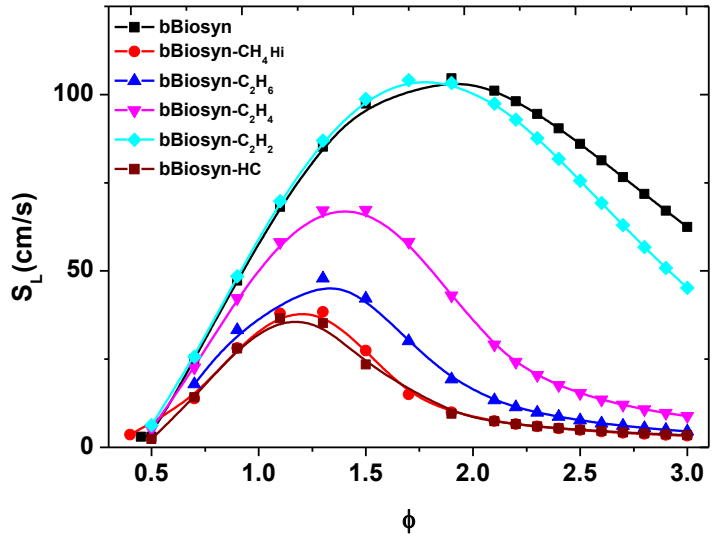

Fig. 95 Laminar flame speed as a function of hydrocarbon addition for the baseline bio-syngas mixture (bBiosyn) at 15 atm and at an inlet temperature of 300 K.

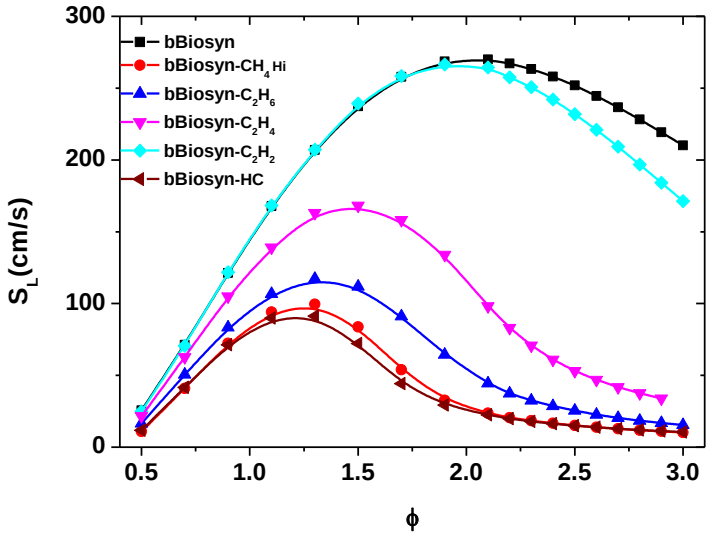

Fig. 96 Laminar flame speed as a function of hydrocarbon addition for the baseline bio-syngas mixture (bBiosyn) at 15 atm and at an inlet temperature of 500 K.

At 1 atm and at an inlet temperature of 300 K, it can be seen in Fig. 97 that below ϕ =1.7 the laminar flame speed is slower for an addition of 1.7% ethane than for an addition of 7.4% of methane. Above this equivalence ratio, the laminar flame speed of the mixture containing methane is dropping rapidly, and the shape of the curve for the bCoalsyn-HC mixture is similar to the curve for the bCoalsyn-CH_4 Hi mixture. It is also worth noting that the laminar flame speed is increased by methane addition below ϕ =1.3 for the coal-syngas, and this increase was not observed with the bio-syngas mixture, as noted above.

At higher pressure, 15 atm (Fig. 98), similar behaviors are observed except that the laminar flame speed of the mixture containing methane is no longer presenting a higher flame speed than the baseline mixture on the fuel lean side. For an inlet temperature of 500 K, higher flame speeds are observed but behaviors at 1 and 15 atm (Fig. 99 and 100, respectively) are the same as those at 300 K.

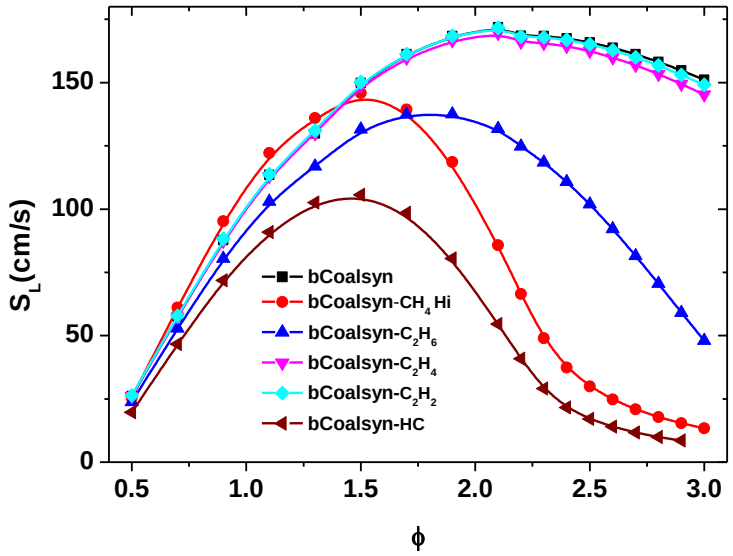

Fig. 97 Laminar flame speed as a function of hydrocarbon addition for the baseline coal-syngas mixture (bCoalsyn) at 1 atm and at an inlet temperature of 300 K.

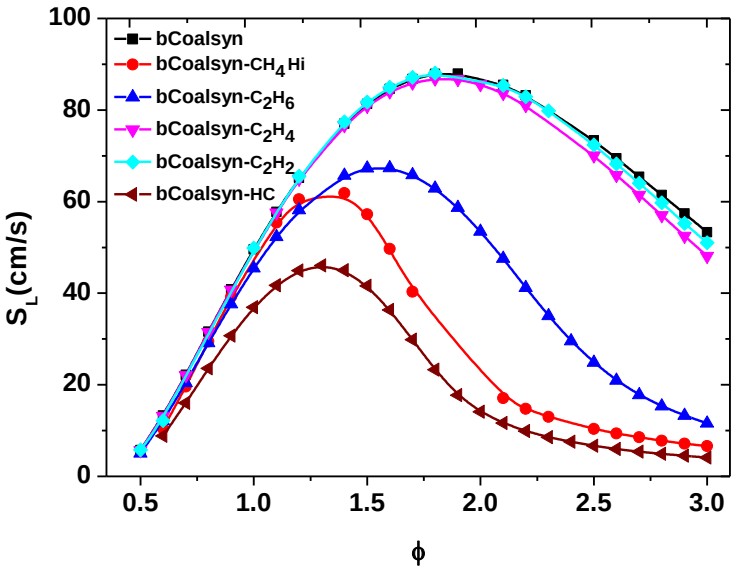

Fig. 98 Laminar flame speed as a function of hydrocarbon addition for the baseline coal-syngas mixture (bCoalsyn) at 15 atm and at an inlet temperature of 300 K.

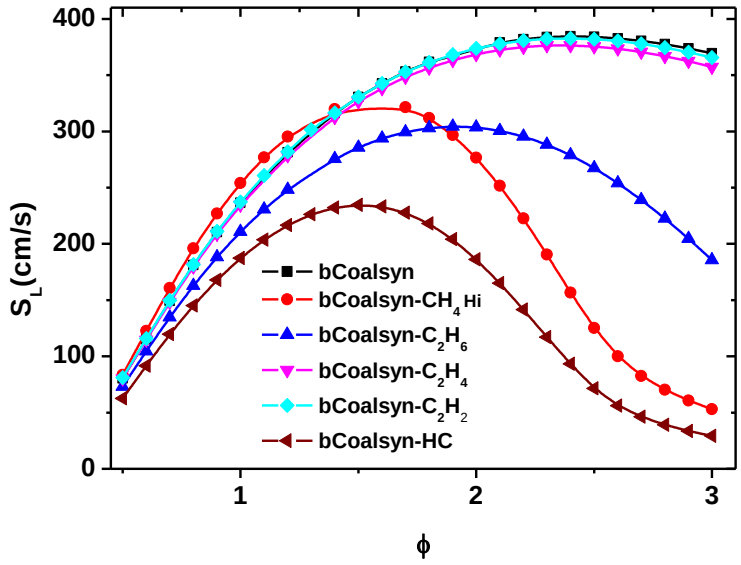

Fig. 99 Laminar flame speed as a function of hydrocarbon addition for the baseline coal-syngas mixture (bCoalsyn) at 1 atm and at an inlet temperature of 500 K.

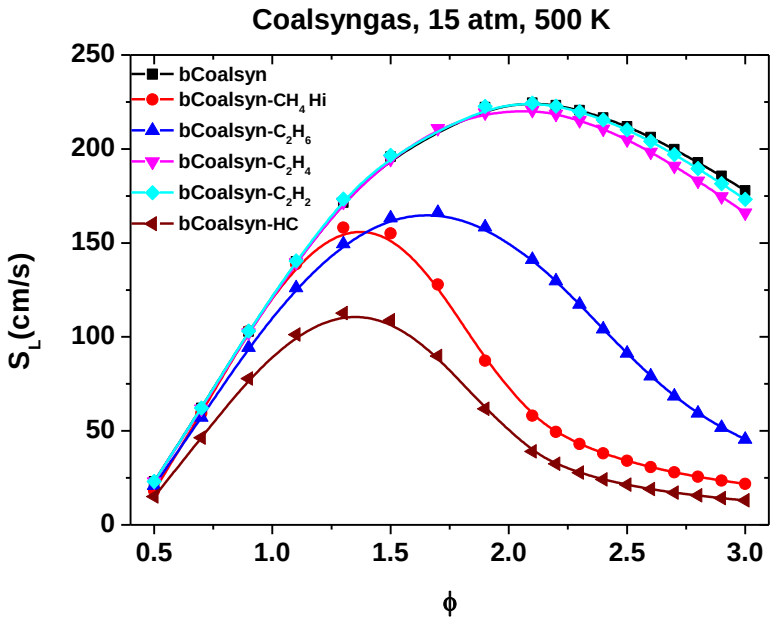

Fig. 100 Laminar flame speed as a function of hydrocarbon addition for the baseline coal-syngas mixture (bCoalsyn) at 15 atm and at an inlet temperature of 500 K.

Averaged Syngas Mixtures

Ignition Delay Time. The comparison at 1, 10, and 35 atm between the ignition delay time of the bBiosyn (H_2/CO as fuel only) and the ignition delay time of the Biosyn (H_2/CO/CH_4 as fuel plus water, CO_2 and N_2) mixture is visible in Fig. 101. As can be seen, there is a large difference between the ignition delay times of these two mixtures, regardless of the pressure investigated (even if differences are mostly seen at high temperatures for the two high-pressure conditions). This figure illustrates the need to take into account components other than CO and H_2 for syngas composition.

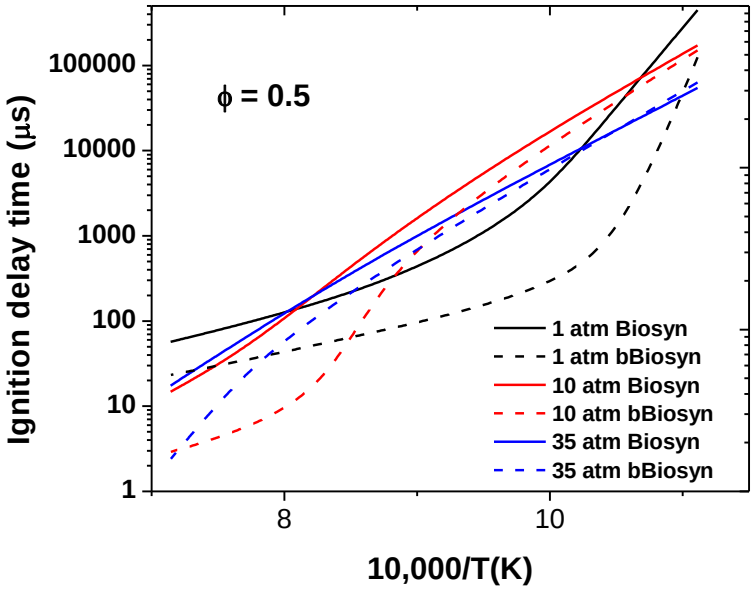

Fig. 101 Comparison between the ignition delay time of a baseline bio-derived syngas (50 H_2/50 CO as fuel), bBiosyn, and the ignition delay time of an averaged bio-derived syngas (H_2/CO/CH_4 as fuel plus water, CO_2 and N_2), Biosyn.

Similarly, Fig. 102 presents the comparison at 1, 10, and 35 atm between the ignition delay times of the bCoalsyn and Coalsyn mixtures. Again, there is a large difference in the ignition delay time of these two mixtures, especially on the low-temperature side of the curve at 1 atm and on the high-temperature side at higher pressure. One can notice however that the differences are not as large as for the bio-derived syngas (Fig. 101).

Figure 103 compares the evolution of the ignition delay time as function of temperature and pressure for the Biosyn and Coalsyn mixtures. As can be seen, the differences in the composition of these mixtures induce some differences in the ignition delay time that cannot be neglected. At 1 atm, the Coalsyn mixture is notably more reactive than the Biosyn mixture, especially for temperatures above 1150 K. At 10 atm, the reactivity of the two mixtures is about the same between 900 and 1100 K. Above this temperature, the ignition delay time for the Biosyn mixture is significantly longer than for the Coalsyn mixture. For the highest pressure investigated, the reactivity of the two mixtures is nearly the same; some small differences are observed however at the extremities of the range of temperature investigated.

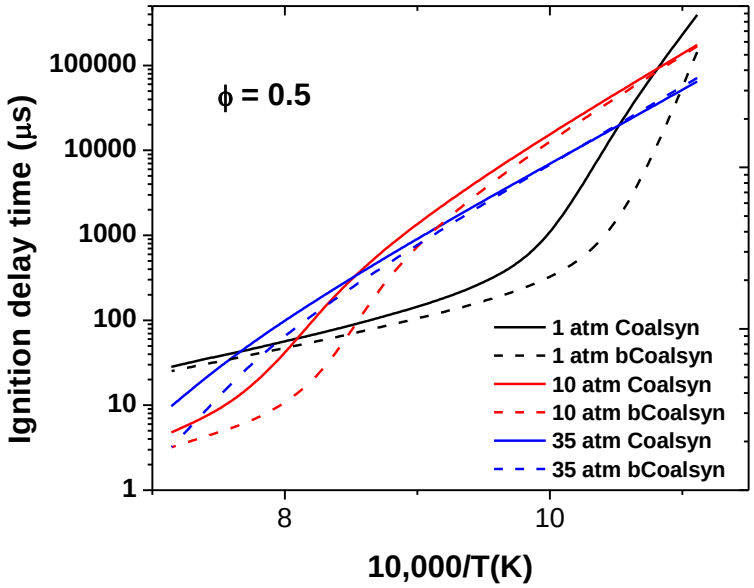

Fig. 102 Comparison between the ignition delay time of a baseline Coal-derived syngas (40 H_2/60 CO as fuel), bCoalsyn, and the ignition delay time of an averaged coal-derived syngas (H_2/CO/CH_4 as fuel plus water, CO_2 and N_2), Coalsyn.

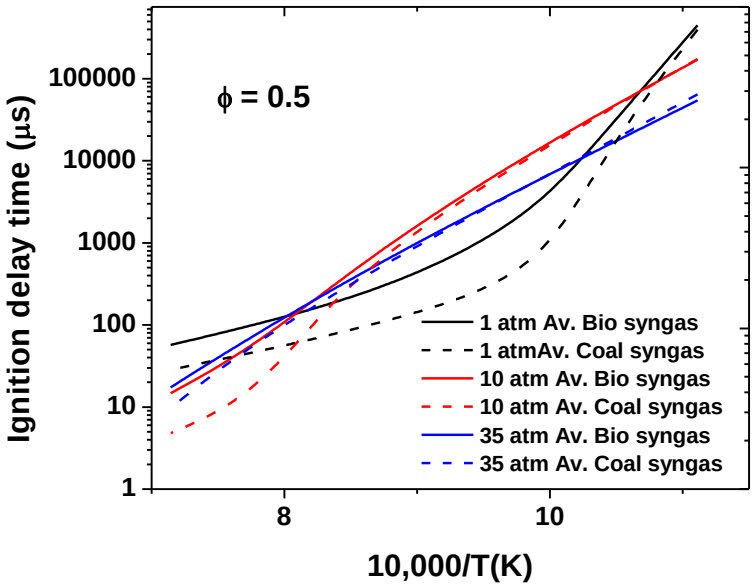

Fig. 103 Comparison between the ignition delay time of the Biosyn and Coalsyn mixtures at 1, 10, and 35 atm.

The effect of the equivalence ratio on the Biosyn mixture can be seen in Fig. 104. At 1 atm, an increase in the equivalence ratio leads to longer ignition delay times over the entire range of

temperature investigated. For a higher pressure, 10 atm, a similar behavior can be observed above 1250 K. Below this temperature the ignition delay time is slightly reduced by the increase in the equivalence ratio. At 35 atm, the ignition delay time is decreased over the entire range of temperature as the equivalence ratio is increased, the difference being more important at low temperatures.

The effect of the equivalence ratio was also investigated for the Coalsyn mixture, as can be seen in Fig. 105. It is visible that the behaviors related to the change in the equivalence ratio are the same as for the Biosyn mixture, Fig. 104.

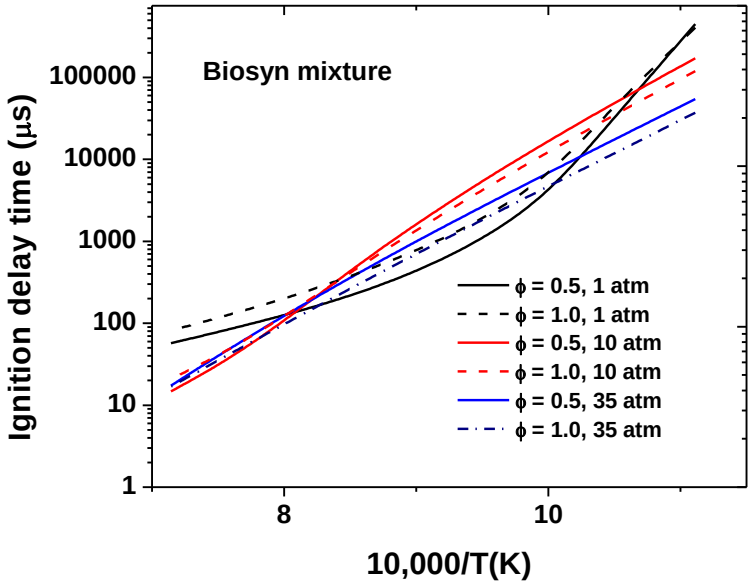

Fig. 104 Pressure and equivalence ratio effect on the ignition delay time of the Biosyn mixture.

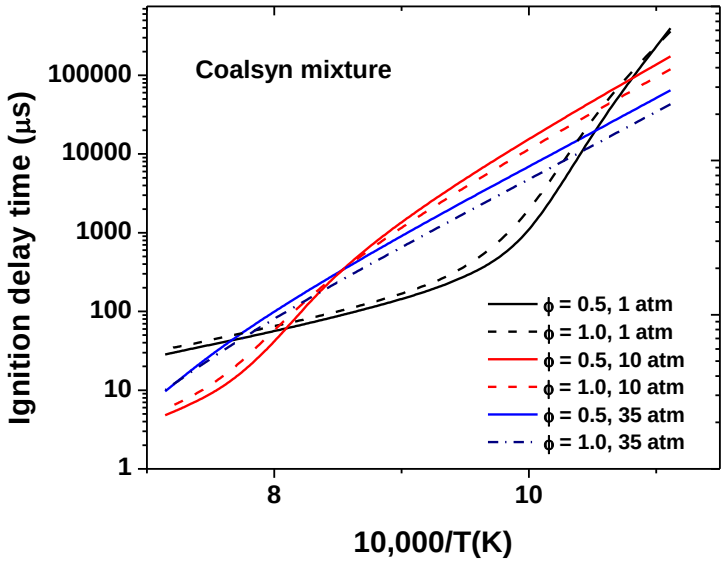

Fig. 105 Pressure and equivalence ratio effect on the ignition delay time of the Coalsyn mixture.

Laminar Flame Speeds. The effects of the initial pressure and temperature conditions on the laminar flame speed of the bBiosyn and Biosyn mixtures are visible in Fig. 106. As can be seen, fuel composition, temperature, and pressure are very important parameters for the flame speed. Between the two extreme conditions (300 K, 15 atm and 500 K, 1 atm), the maximum flame speed varies by a factor 4.5 for the bBiosyn mixture and by a factor 10 for the Biosyn mixture. The flame speed for the Biosyn mixture is significantly lower (factor of 4 or more depending on the intial pressure and temperature condition) than for the bBiosyn mixture, and the maximum flame speed is significantly closer to stoichiometric than the bBiosyn mixture, where the maximum flame speed is around $\phi = 2.0$ regardless of the initial conditions. It is also interesting to note the effects of the fuel composition with regards to the initial conditions. Indeed, the laminar flame speed is higher at 500 K, 15 atm than at 300 K, 1 atm for the bBiosyn mixture, and a reverse order was found for the Biosyn mixture.

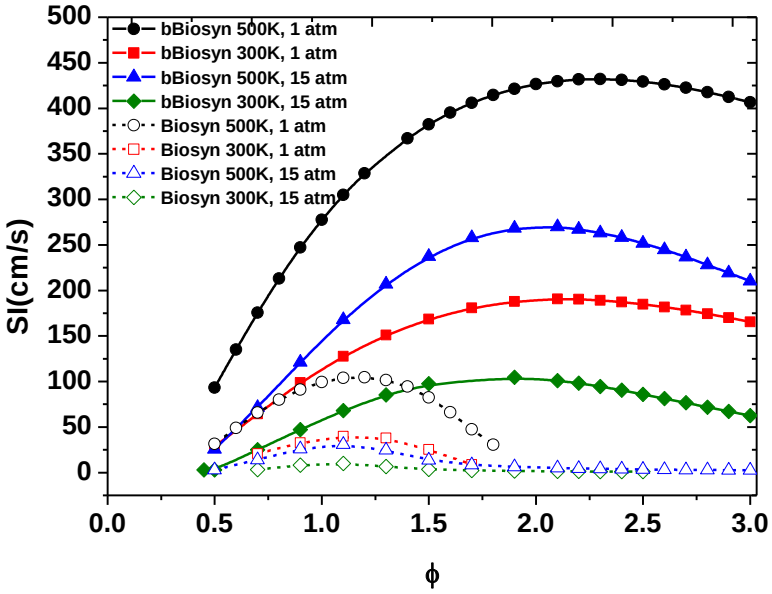

Fig. 106 Laminar flame speeds for the neat CO/H_2 biosyngas mixture (bBiosyn) and for the average biosyngas mixture (Biosyn) at pressures of 1 and 15 atm and inlet temperatures of 300 and 500 K.

Figure 107 shows the effects of the initial pressure and temperature on the laminar flame speed for the bCoalsyn and Coalsyn mixtures. Compared to what was observed for the bio-derived syngas, it is worth noting that the laminar flame speeds of the averaged mixture (Coalsyn) are proportionally not as low compared to the S_L of the bCoalsyn mixtures. Trends related to initial pressure and temperature conditions are however similar between the coal- and bio-derived syngases.

The flame speeds of the Biosyn and Coalsyn mixtures at various pressure and unburned gas temperature conditions (300 K, 1 atm; 500 K, 1 atm; 300K, 15 atm; and 500 K, 15 atm) are compared in Fig. 108. As can be seen, there is a strong influence of both the initial conditions and the syngas composition on S_L. For a given composition, the flame speed follows the next order: 500 K, 1 atm > 300 K, 1 atm > 500 K, 15 atm > 300 K, 15 atm. At 500 K, the calculated

flame speeds are much higher (~ factor 2.4) than those calculated at 300 K, 1 atm, with the peak flame speed for the base mixture being 432 cm/s at ϕ = 2.3, while at 300 K the peak is at 191 cm/s at ϕ = 2.1. The influence of pressure is also observable, and it is seen that increasing the pressure from 1 atm to 15 atm makes flame speeds decrease by approximately a factor of 2.2; but again, the relative effect of each blend component on flame speed prediction for the base mixture and generally the same. At high pressure, increasing the temperature from 300 K to 500 K also leads to flame speeds increasing by approximately a factor of 2.4.

Overall, one can see that the flame speeds are higher and with a larger flammability domain for the Coalsyn mixture than for the Biosyn mixture. This result is certainly due to the lower amounts of methane, N_2, and CO_2 in the coal-derived syngas.

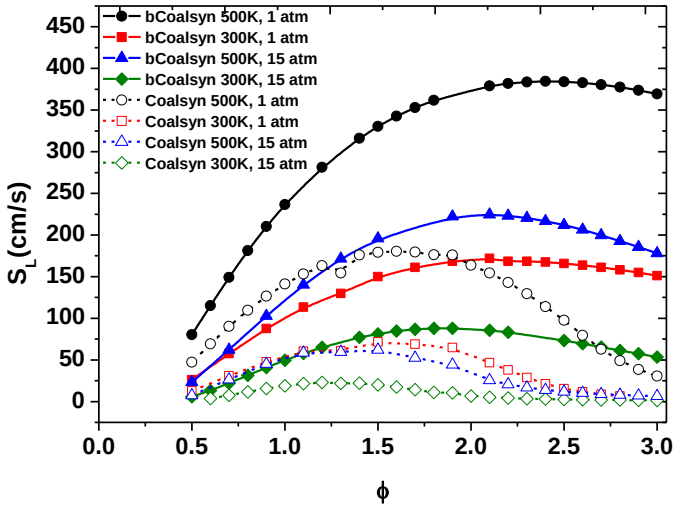

Fig. 107 Laminar flame speeds for the neat CO/H_2 coalsyngas mixture (bCoalsyn) and for the average biosyngas mixture (Coalsyn) at pressures of 1 and 15 atm and inlet temperatures of 300 and 500 K.

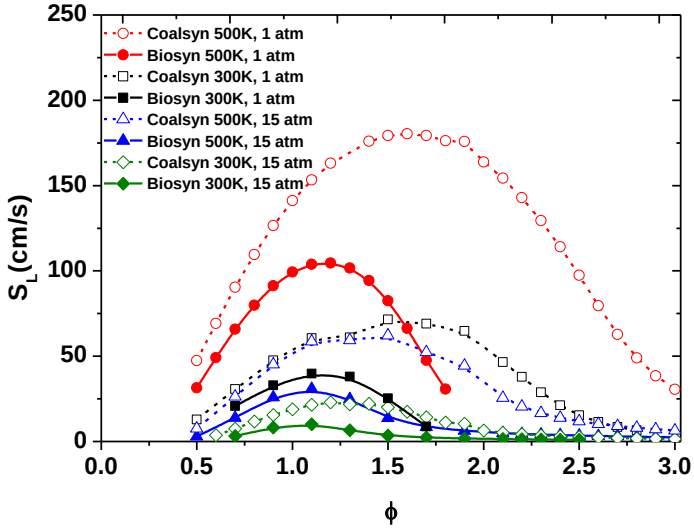

Fig. 108 Laminar flame speed for the averaged bio- and coal-syngas (Biosyn and Coalsyn, respectively) at various pressure and unburned gas temperature conditions.

Comparison with Other Literature Models

As mentioned earlier, several detailed kinetics models (NUIG [Metcalfe et al., 2013], USC [Wang et al., 2007] and SD [Petrova and Williams, 2006]) were compared in this study to estimate the importance of the model on the predictions. Only a selected number of mixtures and conditions are presented for this comparison. Figure 109 shows predictions with the three aforementioned models for the bBiosyn and bBiosyn-HC mixtures at 1 atm, and $\phi = 0.5$. As can be seen, there is nearly no difference amongst models above 1000 K for the bBiosyn mixture. Below this temperature, the NUIG and USC models yield nearly similar results, while the predicted ignition delay time is significantly lower for the SD mechanism at 900 K (19 ms for the SD model against 105 and 125 ms for USC and NUIG, respectively). For the bBiosyn-HC mixture, the SD and NUIG predictions are similar above 1050 K. Below this temperature, the NUIG model predicts ignition delay times that are longer than the SD model. The USC mechanism is the less-reactive model, as predicted ignition delay times are always longer than for the two other models (53 µs at 1400K, against 43-44 µs for the other models), except at 900 K where results are nearly identical to NUIG's mechanism (689 and 674 ms, respectively and 401 ms for SD).

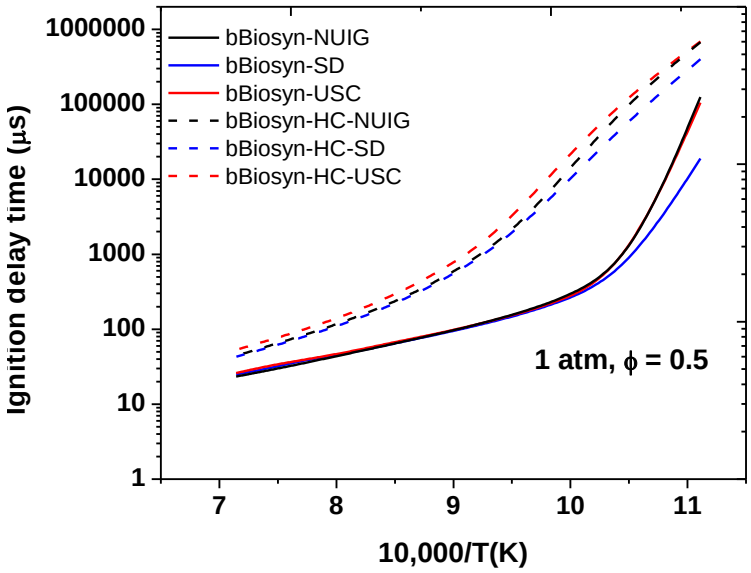

Fig. 109 Comparison of mechanistic predictions for the ignition delay time of the bBiosyn and bBiosyn-HC mixtures at 1 atm and at an equivalence ratio of 0.5.

At 10 atm (Fig. 110), most of the differences amongst the models are seen for the bBiosyn mixture below 1250 K. Between 1250 and 1100K, the NUIG mechanism predicts the longest ignition delay time. In this temperature range, the SD mechanism predicts ignition delay times that are increasing much slowly as the temperature decreases than for the other models. At 900 K, the longest ignition delay time is the one predicted by the USC model (180 ms) followed by the NUIG (151 ms) and SD (98 ms) models. For the bBiosyn-HC mixture, the models have close

predictions at the two extreme temperatures and show some minor differences between these two extremes.

For the highest pressure investigated, 35 atm (Fig. 111), again, differences amongst the models are visible with the bBiosyn mixture (τ_{ign} = 53, 63 and 91 ms at 900 K and 1.5, 2.4 and 1.7 µs at 1400 K for the SD, NUIG and USC mechanisms, respectively). For the bBiosyn-HC mixture, differences between the models are slim. The NUIG and SD mechanisms provide nearly the same predictions while the USD mechanism is slightly less reactive over the range of temperature studied.

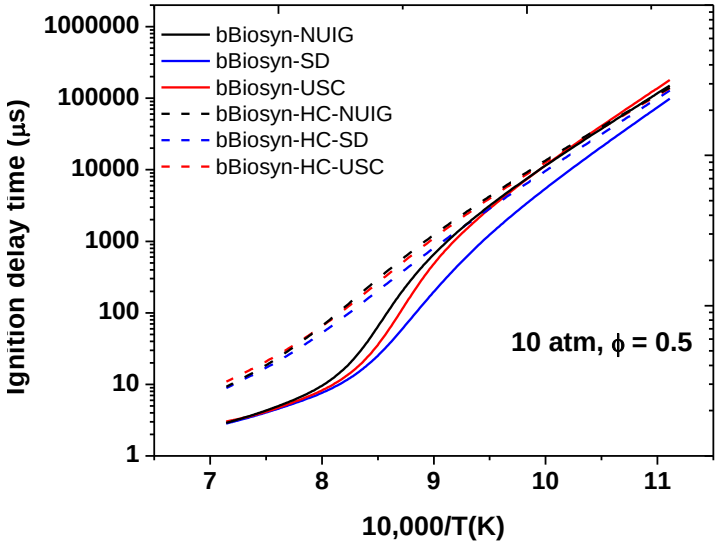

Fig. 110 Comparison of mechanistic predictions for the ignition delay time of the bBiosyn and bBiosyn-HC mixtures at 10 atm and at an equivalence ratio of 0.5.

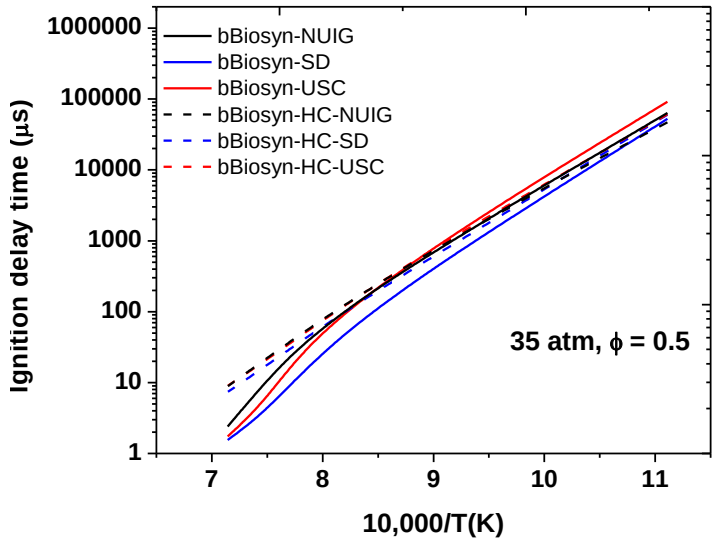

Fig. 111 Comparison of mechanistic predictions for the ignition delay time of the bBiosyn and bBiosyn-HC mixtures at 35 atm and at an equivalence ratio of 0.5.

The flame speed comparison amongst the three models at 300 K and 1 atm as initial conditions is visible in Fig. 112 for the bBiosyn, bBiosyn-C_2H_4 and bBiosyn-HC mixtures. As can be seen, the NUIG mechanism predicts the fastest flame speed in all cases considered, while the USC mechanism always predicts the slowest flame speed. For the bBiosyn mixture, the SD and USC models'predictions are relatively close with a predicted maximum flame speed that is around 10 % slower than for the NUIG mechanism. When hydrocarbons are introduced into the mixture, the NUIG and SD models are now relatively close while the USC mechanism can be significantly slower, such as with the bBiosyn-C_2H_4 mixture.

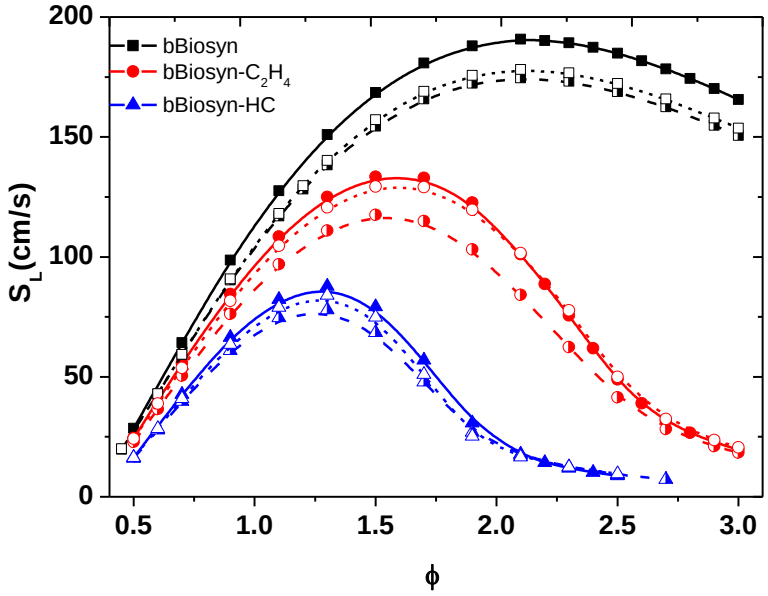

Fig. 112 Comparison of mechanistic predictions for the effect of hydrocarbon addition on laminar flame speed for the baseline bio-syngas mixture (bBiosyn) at 1 atm and at an inlet temperature of 300 K. Solid line and symbol: NUIG mechanism, dashed line and half symbol: USC mechanism, dotted line and open symbol: SD mechanism.

Discussion

During this study, an important effect of pressure has been seen on the ignition delay time of the baseline mixtures, where some important curvatures have been observed for the evolution of τ_{ign} with the temperature, depending on the pressure and temperature. As mentioned before, these pressure/temperature behaviors are due to the competition between a few reactions in the H_2 chemistry. As documented in Keromnes et al. (2013) and in many other places in the literature, these behaviors are in general due to the competition between two reactions: the chain-branching reaction $H+O_2 \rightleftarrows OH+O$ (R1) and the chain-propagating reaction $H+O_2$ (+M) $\rightleftarrows HO_2$ (+M) (R2). The reactivity is indeed controlled by R1 at high temperature and by R2 at low temperature. When the pressure is increased, the transition from R2 to R1 is shifted to higher temperature due to the increased collisional efficiency of R2 which decreases the reactivity. Thus, at the intermediate temperature range, low-pressure experiments show a stronger reactivity than high-pressure experiments, resulting in this unusual cross-over behavior. Note that for the higher

pressure and lower temperatures, R2 can actually act as a chain termination reaction through the formation of H_2O_2 via $HO_2 + HO_2 \rightleftarrows H_2O_2 + O_2$.

To understand better the effects of various additions to the ignition delay times of the baseline CO/H_2 mixtures, sensitivity analyses were performed for some selected conditions. The effect of methane addition was investigated with the bBiosyn-CH_4 Hi mixture. The fact that the effects of methane addition are more important on the higher-temperature side than on the lower-temperature side indicates that methane more or less interferes with the branching reaction $H+O_2 \rightleftarrows OH+H$ (R1). In the conditions where the reaction $H+O_2+M \rightleftarrows HO_2+M$ (R2) is dominant, the effect of methane addition is very small, and no effect can be observed at high pressures/low temperatures. The condition at 1 atm, 1400 K was therefore selected for investigation as this condition corresponds to the region where methane is having the most influence on the ignition delay time compared to the other hydrocarbons. The sensitivity analysis showed several inhibiting reactions involving methane that can explain the decrease in the reactivity. The sensitive reactions with methane are reactions that consume important radicals for the hydrogen chemistry: $CH_4+OH \rightleftarrows CH_3+H_2O$ and $CH_4+H \rightleftarrows CH_3+H_2$. The latest reaction is therefore competing with R1, the dominating reaction in hydrogen chemistry at this condition.

Note that part of the CH_3 will also react via $CH_3 + H (+M) \rightleftarrows CH_4 (+M)$, further decreasing the R1 channel and the overall reactivity of the mixture. The same reactions are also involved at higher pressure on the high-temperature side of the curve, where methane addition showed an effect on the ignition delay time. The effect of a 5.3% C_2H_4 addition was also investigated at 1 atm, 900 K since this condition corresponds to the region where the largest difference with the baseline mixture was observed amongst all the hydrocarbon additions (Fig. 85). Sensitivity analysis showed that the most-sensitive reaction involving C_2H_4 (and third-most-sensitive reaction overall) is the reaction $C_2H_4+H+M \rightleftarrows C_2H_5+M$. This reaction is consuming H radicals and hence competes with the chain branching and promoting reaction R1, therefore reducing the reactivity of the mixture. These conclusions are also valid for the Coal-syngas mixtures, where similar effects were observed but with a lower intensity due to the lower concentration of hydrocarbons.

Concerning the laminar flame speed, it is important to dissociate the effect of the flame temperature from the effect of the chemistry to explain the variations in the laminar flame speed observed during this study. Figure 113 (a) shows a plot of laminar flame speed as a function of equivalence ratio for the series of hydrocarbon additions in the bBiosyn mixture, with the corresponding flame temperatures plotted as a function of equivalence ratio in Fig. 113 (b). It is observed that the order of reactivity is generally reflected in the flame temperatures, in that flames with higher flame temperatures also have higher predicted flame speeds, but this is not always the case. We have chosen to discuss the effect of additive blend on bBiosyn flame speed at 1 atm and 300 K, as this generally represents a standard condition of temperature and pressure and is generally representative of all other cases.

It is observed that the baseline 50/50 H_2/CO mixture (bBiosyn) shows the fastest flame speeds (with the bBiosyn-C_2H_2 mixture), as the reaction $H + O_2 \rightleftarrows O + OH$ dominates reactivity and leads to the fast flame speed predictions. This trend is reflected in the flame temperatures as a function of equivalence ratio, as the bBiosyn mixture has the second highest flame temperature.

The highest flame temperature is actually associated with the base plus acetylene mixture (bBiosyn-C_2H_2, with 0.7% of acetylene), but the values are very similar to those of the base mixture, and this result is also reflected in almost identical flame speed predictions. Across the equivalence ratio range, these two mixtures have flame temperatures of 1688 and 1694 K at ϕ = 0.5 with flame speeds S_L of 28.6 and 28.7 cm/s; flame temperatures of 2395 and 2403 K at ϕ = 1.1, S_L of 127.6 and 129.1 cm/s; and 2124 and 2143 K at ϕ = 2.1, S_L of 190.7 and 189.7 cm/s, respectively.

Thus, in contrast to all other mixtures the higher flame speed of the base mixture is not reduced by acetylene addition since pure acetylene also shows high flame speeds. Jomaas et al. (2005) have shown that acetylene flames have very high flame temperatures with correspondingly high flame speeds that peak at approximately 135 cm/s at an unburned gas temperature Tu = 298 K and at a pressure of 1 atm. In the same study and initial conditions, the peak flame speed for ethylene was found to be approximately 70 cm/s. It is also well known that for atmospheric flames at Tu = 298 K, peak flame speeds for unsaturated hydrocarbons are all approximately 35–40 cm/s [Ranzi et al., 2012].

For the cases of hydrocarbon additions other than acetylene, (namely bBiosyn-CH_4 Hi, bBiosyn-C_2H_4, bBiosyn-C_2H_6) added to the base mixture the situation is very different. For these mixtures, the predicted flame speeds are slower than for the bBiosyn mixture. In the case of ethylene (C_2H_4 = 5.3%) they are considerably slower, peaking at an equivalence ratio of approximately 1.4 and are much slower compared to the base mixture for richer fuel conditions. For the bBiosyn-CH_4 Hi and bBiosyn-C_2H_6 mixtures, flame speeds are much slower, whereas relatively slowest flame speeds are predicted for the cumulative mixture where all hydrocarbons are added at once. These results are true even though the flame temperatures are lower, but not significantly lower, compared to those calculated for the base mixture.

It should be noted that flame speeds are particularly affected for rich mixtures, where hydrocarbon fuel radicals act as hydrogen-atom radical scavengers and inhibit reactivity, particularly at equivalence ratios of approximately 1.3. This scavenger behavior is especially true for the bBiosyn-C_2H_6 mixture, where the reduction in flame speed is remarkable for such a small concentration of ethane added (0.8 %), thus the effect of ethane addition is certainly kinetic and not thermal in this case. The bBiosyn-C_2H_6 mixture has a flame temperature of 2363 K at ϕ = 1.1 compared to 2393 K for the base mixture. The decomposition of ethane leads to the formation of two methyl radicals via the reaction C_2H_6 (+M) ⇄ CH_3 + CH_3 (+M). The subsequent reaction of methyl radicals with hydrogen atoms, CH_3 + H (+M) ⇄ CH_4 (+M), acts as a radical sink for hydrogen atoms, competing with the main chain-branching reaction H + O_2 ⇄ O + OH.

For the bBiosyn-CH_4 Hi mixture too, similar kinetics leads to the same reduction in flame speed, but with the added thermal effect of 15% methane addition reducing the flame temperature (2342 K at ϕ = 1.1) relative to the base mixture (2395 K at ϕ = 1.1) and the bBiosyn-C_2H_6 mixture (2363 K at ϕ = 1.1). For ethylene addition (C_2H_4 = 5.3%), the situation is mainly affected by the chemical kinetics of the system. For example, Fig. 113 (b) shows that the flame temperatures of the ethylene-diluted mixtures (2190 K at ϕ = 1.7) are similar to those of base mixture (2202 K at ϕ = 1.7). Ethylene oxidation leads to the formation of vinyl radicals, which react with hydrogen

atoms in the reaction $C_2H_3 + H \rightleftarrows C_2H_2 + H_2$, a chain termination reaction, consuming two radical species and decreasing flame speeds.

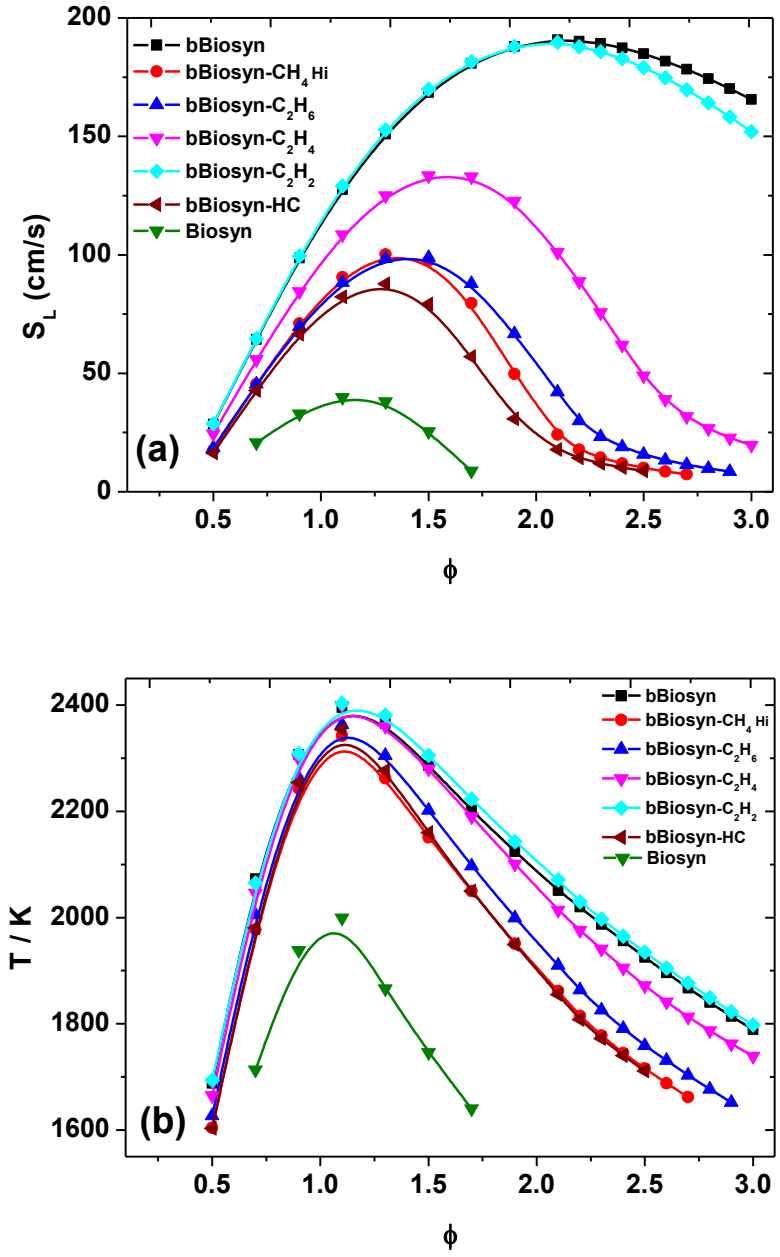

Fig. 113 (a) Laminar flame speed and (b) flame temperature as a function of additive blend for biosyngas at 1 atm and an inlet temperature of 300 K.

The bBiosyn mixture (CH_4 = 8.5%, H_2O = 20%, N_2 = 13%, CO_2 = 15%) has the lowest predicted flame speeds. This result is due to the kinetic effect of methane addition on the rich side, producing methyl radicals which act as radical sinks for hydrogen atoms as discussed before and to some dilution effect of the displacement of the fuel with a large concentration of water, nitrogen, carbon dioxide, and methane. For the case of water and N_2 addition, flame speeds are

reduced by the thermal dilution effect across the entire equivalence ratio range. Das et al. (2011) have shown that, for a 50/50 H_2/CO syngas mixture, laminar flame speed monotonically decreases with water addition, indicating the dominance of the thermal effect of water addition. They also found that by performing a chemical kinetic analysis under these conditions, the chemical effect of water addition was not pronounced.

On the lean side, there is an additional kinetic effect of the addition of CO_2. Indeed, the addition of CO_2 enhances the rate of the reaction $CO_2 + H \rightleftarrows CO + OH$, reducing the concentration of hydrogen atoms in the system, and thus reducing flame speed as any reaction that competes with $H + O_2 \rightleftarrows O + OH$ inhibits reactivity. The CO_2 also reduces the reactivity of the mixture via R2, through a third body effect. Note that these conclusions, drawn from Fig. 113 at 300 K, 1 atm, are also valid at higher pressure and temperature conditions, where the figures for flame speeds and temperatures as functions of ϕ for the bio- and coal-syngas mixtures offers similar behaviors (not shown).

TURBULENT FLAME SPEED VESSEL DESIGN AND CHARACTERIZATION

Combustion processes at engine conditions are highly turbulent, thus making turbulent flame speed an indispensible parameter in the design and development of modern combustors. High-hydrogen-content fuels (such as syngas) are considered as the next generation energy sources for industrial systems such as gas turbines and internal combustion engines. Their extremely high values of laminar flame speeds (S_L) are further augmented by turbulent intensities (u') which can be as high as 14-22% of the axial velocity (V_{ax}) inside a typical gas turbine combustor (Lieuwen et al. 2008). Hence the knowledge of turbulent flame speeds at high-intensity turbulence ($u'>S_L$) is essential to prevent any flashback (propagation of the flame upstream of the burner) or blowout (detachment of the flame from the burner due to excessively high axial core flow) events. The length scale of turbulence is another important parameter that has to be matched to compare the experimental data obtained at the laboratory scale with realistic conditions. The integral length scale of turbulence inside a gas turbine combustor directly correlates with its geometry, and it is usually equal to the dilution-hole size (Barringer 2001) or the inlet jet diameter (Kim et al. 1999). For example, a characteristic integral length scale (L_T) of 10 cm is representative of a high-pressure gas turbine, and this corresponds to a turbulent Reynolds Number range (based on V_{ax} and L_T) between ~ 10^4 at atmospheric conditions and 10^5 at 30 atm (Aldredge 1997). The aim of the present study is to develop an apparatus for the measurement of propagation rates of such candidate fuels in an intensely turbulent environment, and at length scales pertinent to syngas-fired gas turbines.

Speed-controlled impellers are to be installed inside an existing, high-pressure cylindrical flame speed vessel originally designed for measuring the flame speeds of spherically expanding flames under quiescent (laminar) conditions. A symmetrically opposed placement of impellers induces a turbulent flow field without a mean velocity. Furthermore, the stochastic nature of turbulence is greatly simplified by creating a homogeneous and isotropic turbulent field (HIT). These flow constraints entail good repeatability of flow conditions over several experiments as well as precise control and quantification of the levels of turbulence. As a first step in the upgrade of the existing infrastructure, it was necessary to arrive at the best impeller design feasible for establishing near-HIT conditions. To the authors' knowledge, no study exists in the literature that provides guidelines for such impeller designs used to achieve HIT conditions inside a confined volume. So, presented in this report is an experimental study to assess the impact of impeller geometry on the turbulent flow field inside the closed cylinder. Further details are presented in the recent paper by Ravi et al. (2013).

Experimental Setup and Impeller Design Methodology

The existing laminar flame speed vessel is a thick-walled aluminum cylinder (AL 7075-T6) with dimensions 30.5 cm ID × 35.6 cm L (described in detail in de Vries 2009). It is also equipped with a pair of 12.7-cm optical quality quartz viewing windows at the ends of the symmetric axis. The growth of the spherically expanding flame ball under isobaric conditions is optically tracked using high-speed schlieren photography. This vessel will be modified to accommodate mixing fans to induce an HIT-type field at its center. To better understand the control mechanism for u' and L_T, a parametric study to ascertain the effects of impeller geometry on turbulent statistics was conducted. The aim of this impeller study was twofold: (1) to develop an acceptable impeller design capable of generating near-HIT conditions inside the cylinder; and, (2) to check

whether the turbulence parameters can be varied independently by changing the geometrical features of the impeller.

A Plexiglas (clear acrylic) model of the flame speed vessel was fabricated in an attempt to gain a quantitative understanding of the flow fields generated by various impellers without any modification to the existing flame speed vessel. The model had a 33 cm ID × 30.5 cm L making it almost a 1:1 scale with the aluminum bomb. Four impellers were arranged symmetrically along the central circumference, as shown in Fig. 114. The separation distances between two opposing impellers in the vertical and the horizontal directions were kept constant at 20.32 cm. The rotational speeds of all four motors turning the impellers were set to 8300±100 RPM. Two-dimensional digital particle image velocimetry was used to characterize the flow field within a rectangular field-of-view (FOV) in the mid-axial plane of the rig. The intent here was to quantify the turbulence parameters u′ and L_T as well as the flow field characteristics such as homogeneity and isotropy ratios within the measurement area for the different fan designs.

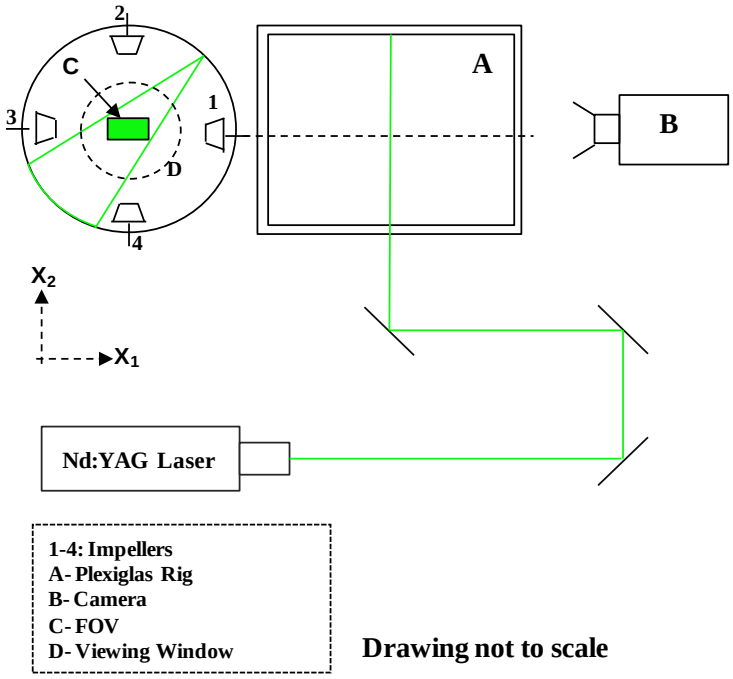

Fig. 114 Schematic of the experimental arrangement. The Plexiglas rig with four impellers mounted circumferentially around the central plane is shown. The laser sheet enters through the top right corner at 45° from the vertical. A CCD camera is mounted on fine adjustment stages to provide a rectangular field-of-view, at the center in the mid-axial plane. The FOV coincides with the center of the viewing window of the existing flame speed vessel.

The impellers used in this study were radial-type fans that directed the flow towards the walls of the vessel instead of directing it towards the center of the vessel, as this configuration was found to yield higher values of turbulence intensities (Fansler and Groff 1990). The effect of the geometric parameters, namely the pitch angle of the fan blade (degrees) and the number of

blades on the impeller, were investigated in the present study (shown in Fig. 115). Prototypes with wide variations of the two parameters were fabricated.

The extreme values for each parameters considered are as follows:

1. Blade Pitch Angle- 20˚, 60˚

2. Number of blades on the impeller- 3, 6

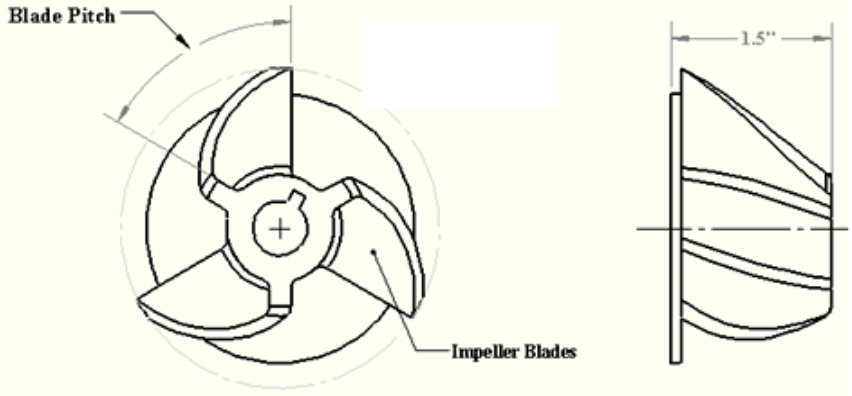

Fig. 115 Geometrical parameters for the impellers used in this study. The axial length of the impeller (3.8 cm) was kept constant, and the remaining parameters were varied.

The axial length of the impellers was kept constant at 3.8 cm (1.5 inches). The rationale behind this fixed axial length is to enable measurement of burning velocity from the pressure trace without any interference from the impellers for flames whose sizes exceed the viewing window diameter. Hence, much variation of the impeller axial length was not possible. The specifications of the prototypes tested are listed in Table 23. Four sets of each prototype were fabricated by laser sintering using Nylon GF.

Table 23 Prototype specifications used in this study. The parameter that was varied for each prototype is italicized.

Prototype	Fan OD (cm)	No of Blades	Blade Pitch (Degrees)	CAD Rendering
#1	7.6	3	20	
#2	7.6	***6***	20	
#3	7.6	3	***60***	

Results of Impeller Characterization

The instantaneous velocity vectors, $u_i(x_1, x_2)$, were ensemble averaged over all 1035 vector maps to yield the mean velocity field, $U_i(x_1, x_2)$, for each prototype. The mean velocities were then subtracted from the instantaneous vectors to obtain the velocity fluctuations $u_i'(x_1, x_2)$ from which the RMS values of the turbulent intensities were computed. Table 23 summarizes the mean and the spatially averaged RMS velocities in the two orthogonal directions for all prototypes. As evident, the mean flow was negligible (at most 0.1u′) for all prototypes. Figs. 116(a) and 116(b) show a sample snapshot of the instantaneous velocity map and the resultant mean velocity field respectively for prototype #1. It should be noted that the reference vector in Fig. 116(b) is scaled up by a factor of five relative to Fig. 116(a) for better visual clarity. A vortex near the center of the vessel was evident from the mean flow field. The streamline topology (not shown here for conciseness) showed spiraling streamlines, thereby suggesting that the flow was three-dimensional.

This observed mean flow could be attributed to the non-symmetric nature of the vessel or due to a slight misalignment of the fans or a slight variability in the fan speeds. Regardless, the fluctuation statistics indicated that this slight mean flow bias was not a significant issue since the mean flow was still negligible when compared to the turbulent intensities. Further, the RMS turbulent intensities showed no appreciable variation with impeller geometry. The prototypes tested had the same fan OD and were turning at approximately the same rotational speeds. Additionally, their moments of inertia were nearly equal. Hence the rotational kinetic energies supplied to the confined volume were the same irrespective of the prototypes, which could explain the near-equal intensity levels that were measured. This result is an indicator that the blade tip velocities (defined as the product of the fan radius and the rotational speed) of the impellers control the intensity levels attained inside the vessel. So, an increase in the fan RPM will effect an increase in the intensity level. This trend is consistent with what is commonly observed in the literature.

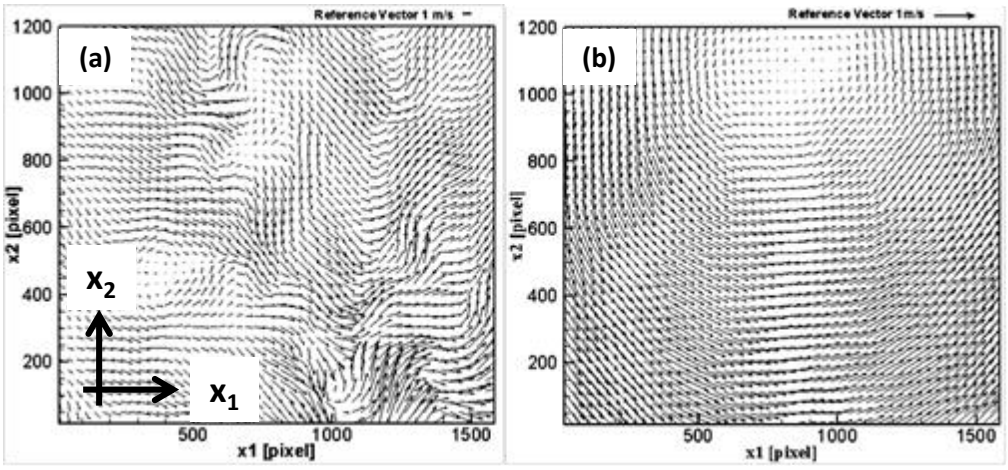

Fig. 116 (a) Instantaneous velocity field (b) Mean velocity field for prototype 1. The reference vector in Fig. 116(b) is scaled up by factor of five to clearly display the negligible mean velocity field in contrast to the fluctuating field. The two orthogonal directions are also shown.

The PDFs were estimated for the normalized fluctuating fields (instantaneous field/local RMS), $u_i'(x_1, x_2)/u_{i,rms}(x_1, x_2)$. To check for the Gaussianity of the PDFs, higher-order standardized moments, namely skewness (Sk) and kurtosis (flatness) (K), were computed for all three prototypes and are shown in Table 24. The skewness factors of all prototypes are near-zero, indicating no biasing of the velocity fields. The velocity PDFs exhibit slightly peaked profiles as evident from the flatness factors. This effect is amplified for prototype #2 (higher number of blades). Such peaked profiles are commonly observed in fan-stirred vessels (Abdel Gayed et al. 1984; Fansler and Groff 1990). This result can be attributed to the lack of an auxiliary device such as a perforated plate in front of the impellers that assists in the introduction of the intermediate scales using the vortex breakdown principle. However, Abdel Gayed et al. (1984) showed that with an increase in the turbulence intensity levels, relaxation of the peaks occurs, and the PDFs assume near-Gaussian-like profiles. This observation is a direct consequence of the widening of the attainable range of velocity scales at higher intensities. It should also be noted that numerical values of higher-order moments can be unreliable due to the sensitivity to noise in the PDF wings (Fansler and Groff 1990).

Table 24 Mean, Spatial RMS and higher order moments- skewness and kurtosis for all prototypes.

	U_i (m/s)	**u'**	**Sk**	**K**
Prototype 1: Baseline Case				
x_1	0.03	1.48	0.04	3.5
x_2	-0.01	1.49	0.03	3.5
Prototype 2: Higher No of Blades				
x_1	0.05	1.17	-0.02	3.9
x_2	0.00	1.39	0.04	3.7
Prototype 3: Higher Pitch Angle				
x_1	0.14	1.57	0.05	3.6
x_2	-0.04	1.67	0.10	3.7

Spatial averages of the quantities leading to length-scale L_T estimates are presented in Table 25. It is evident from Table 25 that the impeller geometry influences the integral length scales. L_T changed with the prototype having the higher number of blades as well as with the greater pitch angle case. However, it was shown earlier that the flow became more anisotropic with a higher number of blades. Hence changing the blade pitch angle will effect a change in L_T while still maintaining HIT conditions. Given the velocity uncertainties and the spatial resolution of these experiments, the Kolmogorov scales shown here are only representative values. Since such finer scales are not of interest to the current application, special arrangements to resolve them were not accommodated.

Table 25 Turbulence statistics for all prototypes.

Prototype	Mod. Kinetic Energy	Dissipation Rate	Integral Scales		Taylor Scales		Kolmogorov Scales	
	$\overline{q^2}$ [m^2/s^2]	$\bar{\varepsilon}$ [m^2/s^3]	τ_ϵ(ms)	L_T(mm)	Re_λ	λ [mm]	τ_k(ms)	η(mm)
#1	6.6	59.7	55	54	277	2.9	0.5	0.1
Higher No of Blades #3	5.1	57.5	44	38	218	2.6	0.5	0.1
Higher Pitch Angle: #4	7.9	109.7	36	39	245	2.4	0.4	0.1

This study provided several important results that aid in the design of the impellers for the final turbulent flame speed vessel. Three-bladed impellers will be installed in the same central-symmetric configuration inside the flame bomb to generate HIT conditions inside the vessel. Changing the blade pitch of the impeller caused a change in the integral length scale of turbulence, though not appreciably. Nevertheless, even such small variations in length scale can significantly impact turbulent flame speeds, as in Venkateshwaran et al. (2011). In their study, two different L_T (12 and 20 mm) were employed, and large differences in the burning velocities were observed keeping all other parameters constant. Hence employing impellers with different pitch angles can provide valuable data that can be used to assess the length scale sensitivity of turbulent flame speed.

The integral length scales attained in the vessel correlates with those typically observed inside a gas turbine combustor, as evident from Table 26. Therefore, two sets of impellers with different pitch angles, namely 20˚ and 60˚, same as the prototypes #1 and #3, will be fabricated to vary L_T. Additionally, S_T will be reported at two radii, one at moderately small flame radius ($r_f \approx L_T$) and one at a larger flame radius ($r_f >> L_T$) to evaluate the contradictory relation between L_T and $S_{T,rf}$ based on the choice of radius used for measurements [Lipatnikov and Chomiak, 2000]. Future work will focus on similar characterization experiments in the modified turbulent flame speed vessel over the entire range of motor speeds (8-15k RPM), and the range of turbulent intensities that can be attained will be measured using LDV (instead of PIV due to lack of a transverse optical port for the laser sheet entry). The FOV will also be expanded to encompass the entire region of optical access of the flame bomb.

Table 26 Integral length scales inside a typical gas turbine.

Gas Turbine Model	**L_T (mm)**	**Reference**
GE - LM6000	34	Kim and Menon (2000)
HiP gas turbine combustor	100	Aldredge (1997)
Simulated combustor	40-60	Ames and Moffat (1990)
Can-type GT combustor	5.6-15.6	Moss (1992)
P&W combustor simulator	60-108	Barringer (2001)

As reviewed in the background literature section of the main paper summarizing this work [Ravi et al., 2013], guidelines for impeller design for fan-stirred vessels are not available. To generalize the results from this study so that they can be directly transferred to vessels with different geometries, the geometrical features of the vessel should be taken into account as well, which adds another level of complexity. The objective of the current investigation was to arrive at an optimal impeller geometry that can produce uniform turbulence conditions with flexibility to change the turbulence parameters inside an existing flame bomb. Hence, variations in vessel geometry were not considered. While this report provides useful flow field information of three different impeller geometries placed in a center-symmetric pattern inside a cylindrical vessel, the applicability of these results to vessels with different geometries cannot be determined from the study conducted here.

TURBULENT FLAME SPEEDS OF A SYNGAS MIXTURE

Gas turbine combustion processes are challenging to model due to the chemistry and fluid dynamic (turbulent flow) interactions. As a result, computational combustion codes use widely validated correlations or combustion models to provide the much needed turbulent flame speed estimates. Damköhler (Peters, 1999) postulated that the increased burning rates under turbulent conditions were due to an increase in the local flame surface area by the turbulent eddies, and he proposed a simple expression for turbulent flame speed. Since then, several experimental investigations have identified different regimes of turbulent flame propagation. However, a universally accepted correlation that can model all these regimes is still under development. Nevertheless, turbulent combustion models have been developed for common fuels of interest such as methane and hydrogen, and they have been validated with experimental measurements over a wide range of conditions.

The primary objective of this study was to assess the most promising burning velocity correlations from the literature with recent measurements from the authors' laboratory. Fuels that are of interest to gas turbine designers, namely, methane (primary constituent of natural gas) and syngas (50:50 H_2:CO by volume) were studied in this work and are organized in the paper as follows. First, the various regimes of turbulent combustion are introduced, followed by a brief background literature review on the existing turbulent combustion models. The experimental apparatus and the post processing procedure are then discussed in detail. Results from flame speed experiments are presented and are compared with the model predictions.

Regimes of Turbulent Combustion

Unlike laminar flames, turbulent flame propagation can be classified into several regimes. The Borghi diagram (Borghi, 1985) demarcates the different regimes based on both flame properties such as the laminar flame speed (S_L) and the flame thickness (δ_L), as well as the turbulent field parameters, namely, the turbulent intensity (u′) and the integral length scale (L). Non-dimensional numbers- Reynolds, Karlovitz, and Damköhler--form the boundaries of each regime (Eqs. (16) - (18)). Two regimes, namely, the thin reaction zone and the corrugated flamelet regime were studied in the present investigation. Flame images corresponding to these regimes are shown in the Borghi diagram in Fig. 117. The sphericity of the growing flame ball decreases as the turbulence intensity is increased due to increased turbulent straining (as a result of moving from corrugated flamelet to thin reaction zone).

$$\text{Turbulent Reynolds Number: } Re_T = \left(\frac{u'}{S_L}\right)\left(\frac{L_T}{\delta_L}\right) \tag{16}$$

$$\text{Damköhler Number: } Da = \left(\frac{u'}{S_L}\right)^{-1}\left(\frac{L_T}{\delta_L}\right) \tag{17}$$

$$\text{Karlovitz Number: } Ka = \left(\frac{u'}{S_L}\right)^{\frac{3}{2}}\left(\frac{L_T}{\delta_L}\right)^{-\frac{1}{2}} \tag{18}$$

Where the laminar flame thickness, δ_L, is given by,

$$\delta_L = \frac{\nu_u}{S_L} = \left(\frac{1}{S_L}\right)\left(\frac{k_u}{\rho_u\, c_{p,u}}\right) \tag{19}$$

and,

$$\text{Mixture-averaged specific heat (unburned): } C_{p,u} = \sum_{i=1}^{N} X_i \, C_{p,i} \tag{20}$$

$$\text{Mixture thermal conductivity (unburned): } k_u = \frac{1}{2}\left(\left(\sum_{i=1}^{N} X_i \, k_i\right) + \frac{1}{\sum_{i=1}^{N} \frac{X_i}{k_i}} \right) \tag{21}$$

Where, X_i is the mole fraction of i^{th} species

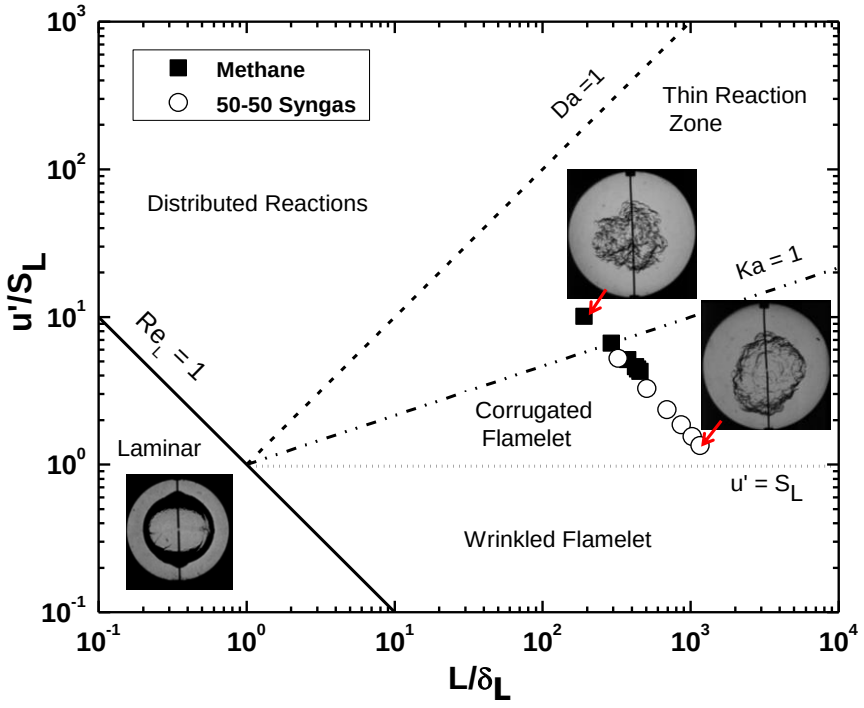

Fig. 117 Turbulent combustion regime diagram (Borghi diagram). The morphologies of the flames (image insets) are distinctly different from one regime to the other. Measurements from the present study are shown as symbols.

Turbulent Combustion Models

Lipatnikov and Chomiak (2002) analyzed experimental data from different facilities and have established six criteria or trends that have to be satisfied by turbulent flame speed models. These criteria are summarized below:

a. Turbulence intensity (u')- Turbulent flame speed (S_T) shows a nonlinear relation with intensity levels. A linear increase in the weak intensity regime ($u' < S_L$) is observed, followed by a power law increase in the moderately turbulent conditions up to maximum, $S_{T,max}$, when $u' = u'_m$. This threshold intensity associated with the maximum S_T is highly dependent on the Lewis number of the mixture. In the high intensity

turbulence regime ($u' > u'_m$), a decrease in the flame speed is observed and is referred to as the bending effect.

b. Integral length scale (L)- There is no consensus on the influence of turbulence length scale on S_T. The ratio of integral length scale and laminar flame thickness (L/δ_L) has a positive exponent ranging between 0.15 and 0.25, as determined by processing the existing spherical flame speed database. However, facilities using grid-generated turbulence mechanisms have reported that with an increase in L, the burning velocities increased or decreased based on the ratio of u'/S_L. As a result, correlations developed using data from a burner-type apparatus may not predict the observed trends of length scale influence as measured in fan-stirred, spherical flame bombs.

c. Laminar flame speed (S_L)- both S_T and dS_T/du' increase with S_L and scale with an exponent q ~ 0.5-0.8 (S_L^q)

d. Molecular heat diffusivity (κ_u)- S_T decreases with κ_u.

e. Pressure- Unlike the laminar flame speed, S_T increases with pressure. But the pressure dependency of S_T is controlled through S_L for most correlations. This trend is contradictory to what is observed experimentally.

f. Damköhler and Karlovitz (Ka) Numbers- (S_T/u') scales as $Da^{0.2\text{-}0.5}$ and $(1/Ka)^{0.2\text{-}0.4}$.

Four numerical models, namely, (1) Zimont burning velocity model (Lipatnikov and Chomiak, 2002) (Eq. (22)); (2) Kerstein pair-exchange model (Kerstein, 1988) (Eq. (23)); (3) coherent flame speed model (Duclos and Veynante, 1993) (Eq. (24)); and (4) Distributed reaction zone (DRZ) model (Ronney, 1995) (Eq. (25)) are evaluated here against experimental measurements. These models were chosen due to better agreement of the model predictions with the experimental data (Lipatnikov and Chomiak, 2002; Liu et al., 2012).

$$\text{Zimont burning velocity model: } S_{t,0.6} = Au'\, Da^{1/4} \tag{22}$$

$$\text{Kerstein pair-exchange model: } S_{t,0.1} = A\sqrt{u'S_L}Re_T^{3/8} \tag{23}$$

$$\text{Coherent flame speed model: } S_{t,0.1} = C\, u'\Gamma_{\bar{k}}^{1/2}\left[1 + C_1\left(1 + C_2\,\frac{u'}{S_L}\right)\right]^{-0.5} \tag{24}$$

$$\text{DRZ Model: } \frac{S_{t,0.5} - S_L}{u'} = A(Da)^{0.5} \tag{25}$$

The model constants are adjusted for a particular fuel.

Definition Dependency of Turbulent Flame Speed

The definition dependency of turbulent flame speed has been discussed extensively in the literature. Global displacement speeds or turbulent flame speeds are commonly measured using schlieren imaging inside a fan-stirred vessel. Global consumption speeds or mass rate of burning can be obtained from pressure transducer measurements. The two definitions differ by the value

of the reaction progress variable, $\bar{c}$, of the measurement surfaces. Recently, Bradley et al. (2011) derived a relationship (Eq. (26)) that can be used to estimate the turbulent burning velocities at different measurement surfaces. The ratios of radii relative to the schlieren radius and the corresponding burning velocities ratios are shown in Table 27.

$$\frac{u_{t\bar{c}_2}}{u_{t\bar{c}_1}} = \left(\frac{r_{\bar{c}_1}}{r_{\bar{c}_2}}\right)^2 \tag{26}$$

Table 27 Radii and burning velocities ratios of different measurement surfaces with respect to the schlieren surface as measured by Bradley et al. (2011).

Measurement Technique	$\bar{c}$	$r_{sch}/r_{\bar{c}}$	$\frac{u_{t\bar{c}_2}}{u_{t,0.1}}$
OH PLIF	0.05	0.9	0.81
Schlieren	0.1	1	1
Equal Volume Method	0.34	1.22	1.49
Equal Area Method	0.4	1.27	1.61
Mean Flame (Cone angle method)	0.5	1.34	1.8
Pressure Trace/ Mass rate of burning	0.6	1.4	1.96

Apparatus and Flame Image Analysis

The turbulent flame speed vessel is made of aircraft-grade aluminum (Al 7075) with an internal diameter of 305 mm and an internal length of 355 mm. Optical-quality quartz windows at the two ends of the vessel enable visual tracking of the expanding flame up to a maximum diameter of 127 mm under constant-pressure conditions. The spark-ignited flame is imaged using a z-type schlieren setup used in combination with a high-speed camera (Photron Fastcam SA 1.1). The temperature inside the vessel is monitored using a k-type thermocouple, and typical initial temperatures are 296 ± 3 K.

Four fans are installed symmetrically around the central circumference of the vessel to generate turbulence during the experiment. The fans are radial impellers with three backward-curved blades which direct the flow towards the vessel wall. They are made of aluminum (Al 6061-T6) with an outer diameter of 76.2 mm and a blade pitch angle of 20°. These fans are fitted on steel shafts (A2 tool steel) that are polished to an extremely fine surface finish. Shaft sealing is provided by means of PTFE lip seals. High-speed bearings for the shafts are stacked inside cartridge housings that are directly mounted onto the vessel. Each fan is turned by a 2.25-HP router motor whose rotational speeds can be varied between 8,000 and 24,000 rpm. The impeller shafts are connected to the motor shafts by means of flexible couplings which can compensate for minor shaft misalignments. Figure 118 shows the actual experimental apparatus along with the 3D computer model.

An average RMS turbulent intensity, u′ = 1.5 m/s with negligible mean flow (< 0.1 u′), was measured at the lowest fan speeds with an integral length scale of 27 mm. Additionally, the turbulent flow field exhibited two features: (1) homogeneity or spatial uniformity; and, (2) isotropy or directional equality of the velocity components in the two orthogonal directions at the center of the vessel. Both the homogeneity and isotropy ratios varied between 0.9 and 1.1 (ideal value being 1), thus providing stationary (no mean flow) and uniform perturbations (also called homogeneous and isotropic turbulence, HIT) during flame growth.

Sample images from a typical turbulent flame speed experiment are shown in Fig. 119. The images are analyzed using a MATLAB code that was developed in house. The program tracks the flame boundary and estimates the area within the turbulent flame kernel for each frame, as shown in Fig. 119d. The enclosed area is then used to compute the radius of a circle with an equivalent area. This radius is defined as the schlieren radius, r_{sch}. To determine the global displacement speed, the instantaneous turbulent flame speed, S_F, is first computed through Eq. (27) using a central difference technique. The global displacement speed ($S_{T,0.1}$) is then estimated by multiplying S_F with the density ratio of the burned to unburnt gases (continuity) following Eq. (28). A polynomial regression-based smoothing filter (Savitzky-Golay) is used when computing the derivative in Eq. (27). This filter has been successfully applied to laminar flame speed measurements using high-frequency dynamic pressure traces without the loss of experimental trend (Dahoe, 2005). For the current application, the derivative errors can be attributed to the unequal flame propagation rates in the different directions. As a result, the flame may become more wrinkled as opposed to growing monotonically in the imaging plane, which results in noisy derivatives

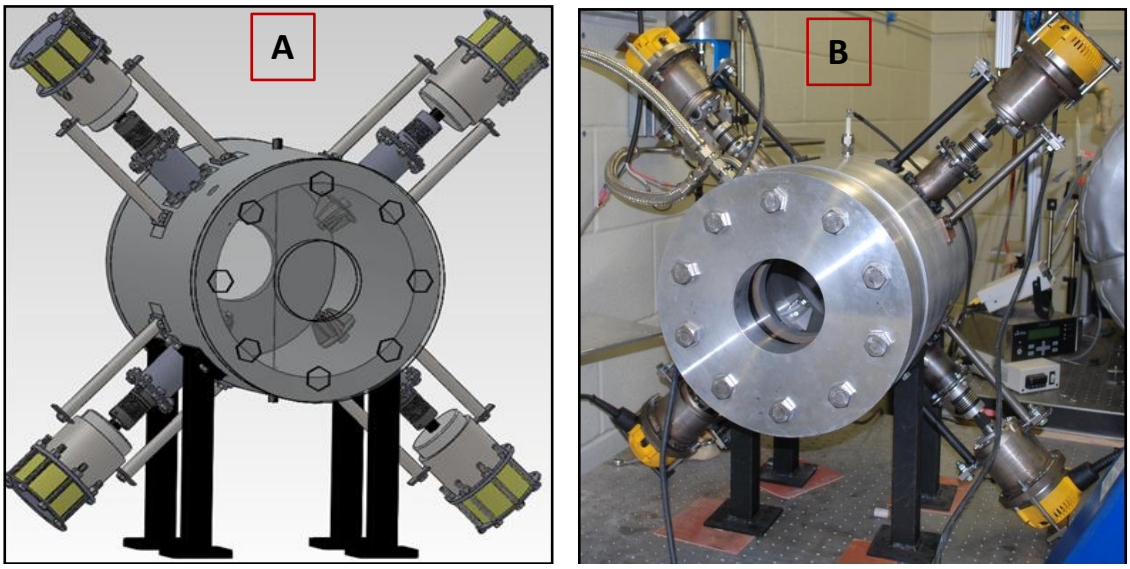

Fig. 118 Fan-stirred flame speed vessel. (a) 3D solid works model (b) photograph of the facility. The four fans at the central circumference generate homogeneous and isotropic turbulence at the vessel center.

.

$$S_F = dr_{sch}/dt = \left(r_{sch}^{t+1} - r_{sch}^{t-1}\right)/(2\Delta t) \quad (27)$$

$$S_{T,0.1} = (S_F)(\rho_b/\rho_u) \quad (28)$$

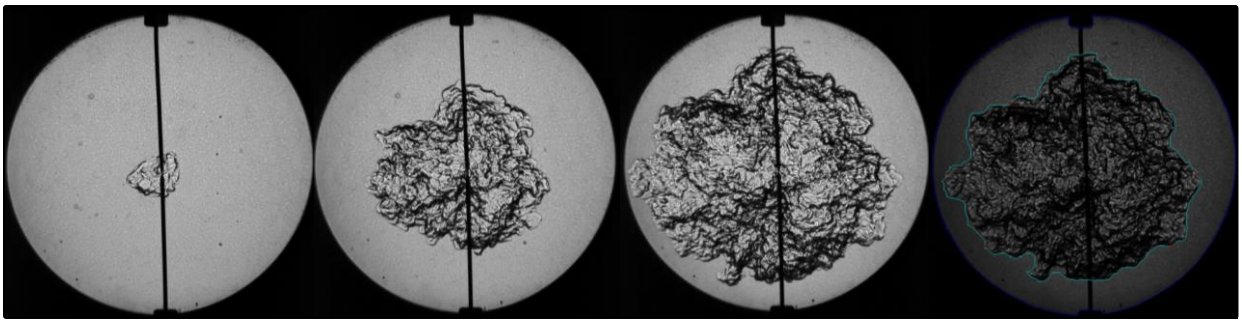

Fig. 119 (a-c) Sample images from a typical turbulent flame speed experiment. (d) Image processing technique used to estimate the flame radius by computing the enclosed area within the kernel boundary (shown in blue).

Results and Discussion

Turbulent flame speeds of methane and syngas mixtures over a wide range of equivalence ratios are shown in Fig. 120. The numerical model predictions at these conditions are also plotted. The flame propagation rates from the various models are converted to global displacement speeds using Eq. (26) to enable comparison with the measured data. The model constants are provided in Table 28. The Kerstein pair-exchange and the Zimont models follow the experimental data closely for both fuels. Additionally, the model constants do not vary significantly for both fuels. The coherent flame speed model, though, is insensitive to changes in equivalence ratio and agrees satisfactorily with the measurements for both fuels. Γ_k in Eq. (24) was computed using the procedure outlined in Duclos and Veynante (1993). The DRZ model under predicts the flame speeds under lean conditions and over predicts for the fuel-rich cases for methane. However, the model fails to capture the flame speeds for syngas.

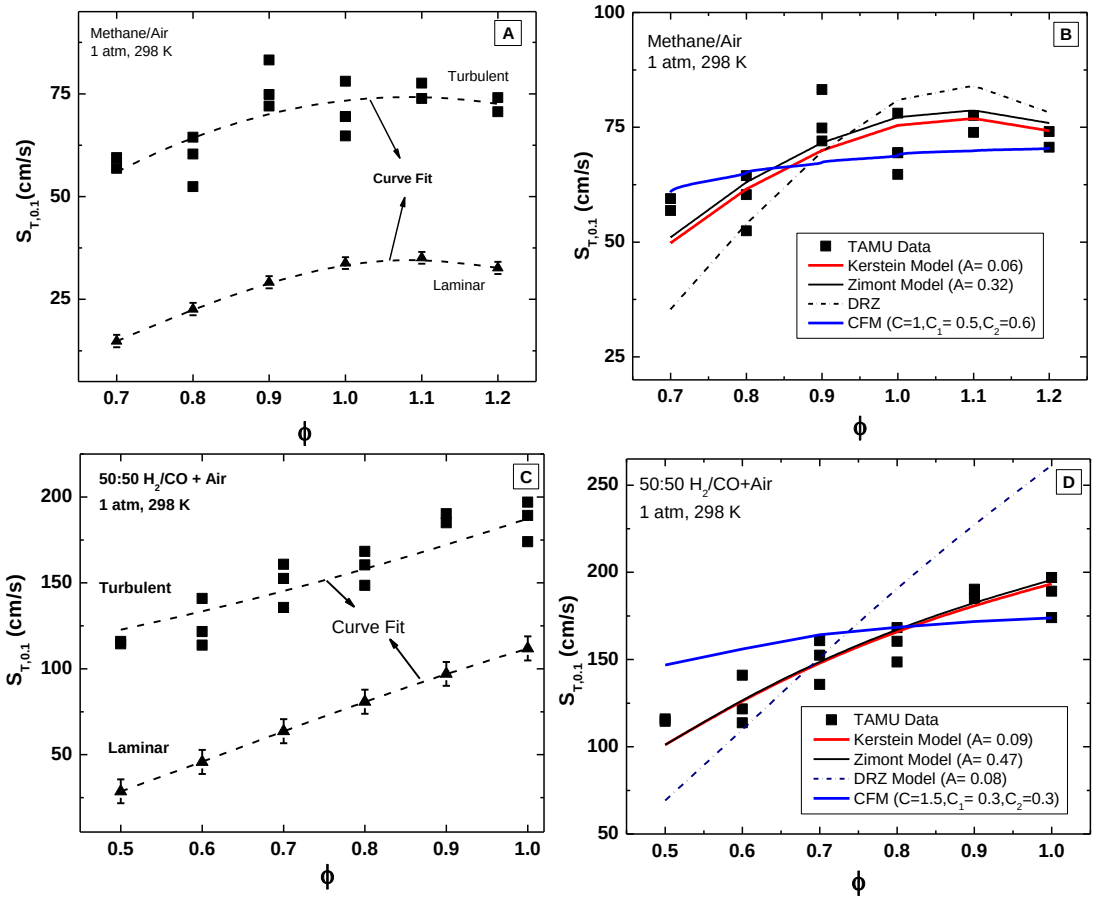

Fig. 120 Global displacement speeds of methane (Ravi et al., 2013) and syngas mixtures at various equivalence ratios. (A, C) Turbulence has increased the flame speeds at all conditions. The corresponding laminar flame speeds are included for reference. (B, D) Turbulent combustion model predictions. Good agreement is seen amongst the experimental data, the Kerstein pair-exchange model and the Zimont burning velocity model for both fuels.

Table 28 Turbulent combustion model constants for the two fuels.

	Kerstein	Zimont	DRZ	CFM		
				C	C_1	C_2
Methane	0.06	0.32	0.08	1	0.5	0.6
Syngas	0.09	0.47	0.08	1.5	0.3	0.3

To assess the effect of u′ on the $S_{T,0.1}$, the turbulent flame speeds are plotted as a function of the intensity levels (both normalized by the laminar flame speed) in Fig. 121. For a given value of u'/S_L, S_T/S_L is higher for syngas than methane. This amplification can be attributed to the increased flame surface distortion due to preferential diffusion of hydrogen (Kwon et al. 1991). Distortion increases the flame surface area, and hence, the burning velocities are higher.

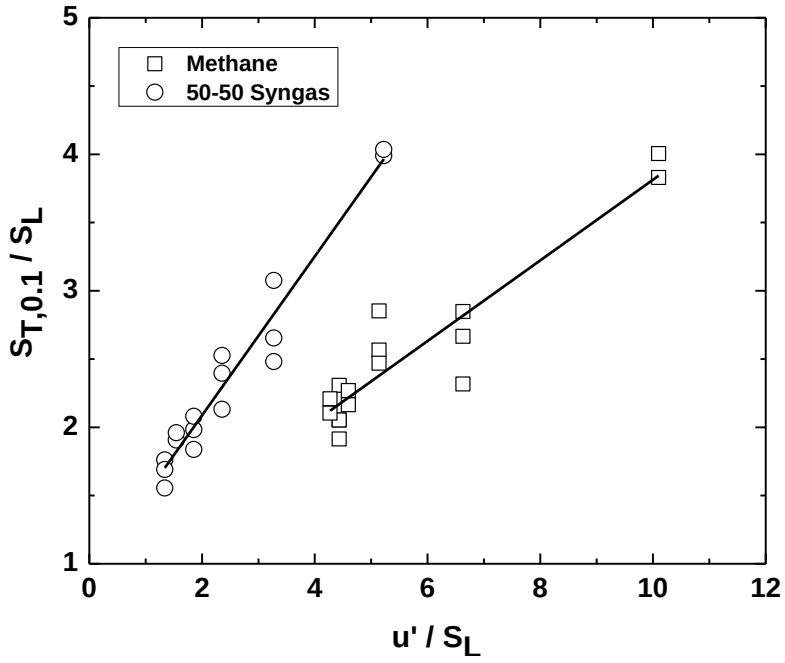

Fig. 121 Normalized global displacement speeds as a function of normalized intensity for methane and syngas. The flame speed increase is higher for syngas than methane due to higher flame surface distortion effected by the preferential diffusion of hydrogen.

OH ABSORPTION DIAGNOSTIC

The importance of the OH molecule in combustion kinetics cannot be understated. AramcoMech 1.1 is a recent detailed chemical kinetics mechanism from the National University of Ireland Galway and is comprised of 1273 reactions including 188 species (Metcalfe et al., 2012). This mechanism was constructed from the ground up and includes some of the base chemistry for C1-C5 hydrocarbons which has been validated by data obtained at the author's laboratory. Of the reactions considered in the AramcoMech 1.1 mechanism, roughly 21% of the mechanism, or 267 reactions, include the OH radical.

Table 29 Sampling of reactions from AramcoMech 1.1 which include the OH radical (Metcalfe et al., 2012).

#	Reaction	A	n	E_a
1	$H+O_2 \rightleftarrows O+OH$	1.04E+14	0	15286
2	$O+H_2 \rightleftarrows H+OH$	5.08E+04	2.67	6292
3	$OH+H_2 \rightleftarrows H+H_2O$	4.38E+13	0	6990
4	$O+H_2O \rightleftarrows 2OH$	2.97E+06	2.02	13400
7	$O+H+M \rightleftarrows OH+M$	2.97E+06	-1	0
	…			
1265	$C_5H_{11a}+HO_2 \rightleftarrows C_5H_{11}O_a+OH$	9.00E+12	0	-1000
1266	$C_5H_{11b}+HO_2 \rightleftarrows C_5H_{11}O_b+OH$	9.00E+12	0	-1000
1267	$C_5H_{11c}+HO_2 \rightleftarrows C_5H_{11}O_c+OH$	9.00E+12	0	-1000

Where: a is first, b is second, and c is third carbon atom location

Several example reactions in AramcoMech 1.1 which include OH are shown in Table 29 where A is the pre-exponential constant, n is the temperature exponent, and E_a is the activation energy for use in the Arrhenius rate equation, which is defined by Eq. 29.

$$k = \mathrm{A}\mathrm{T}^{n}\exp\left(-E_a/\bar{R}T\right) \tag{29}$$

Here, the Arrhenius rate k is defined by A, n, and E_a with T for temperature and $\bar{R}$ being the universal gas constant. In this form, the only variable is the temperature of the system. For pressure-dependent reactions, the Troe fall-off formulation is used (Troe, 1983). Overall, a detailed kinetics mechanism like the AramcoMech 1.1 relies on computing thousands of reactions with hundreds of species at various conditions to predict the combustion behavior of various reactants. The hydroxyl radical is one of the more important intermediate species that has a key role in breaking apart many of the larger chained molecules to drive the global reaction.

The current focus of this task has been the development of an optical diagnostic to measure the concentration of OH in shock-tube experiments using absorption spectroscopy. The results of this effort are described below.

OH Absorption Diagnostic

The diagnostic applied to the shock tube to measure OH time history profiles during an experiment relies on the use of a monochromator tuned to observe the X→A ground vibrational transition. A picture of the overall diagnostic is presented in Fig. 122 as it sits near the endwall of the shock tube. Light from a sidewall port located 1.6 cm from the endwall of the shock tube is focused onto the entrance slit of a Princeton Instruments SpectraPro 500 spectrometer with a focal length of 0.5 meters. This setup is optimized to study either emission (chemiluminescence) or absorption using a collimated light source to study various transitions. The SpectraPro 500 can be configured as a spectrometer in which light can be spread over a Princeton Instruments IRY-700-S/RB linear photodiode array (PDA) or as a monochromator where a slit is used at the exit plane. When using the monochromator to isolate a specific transition, a variety of photoreceivers can be used depending on the nature of light being analyzed.

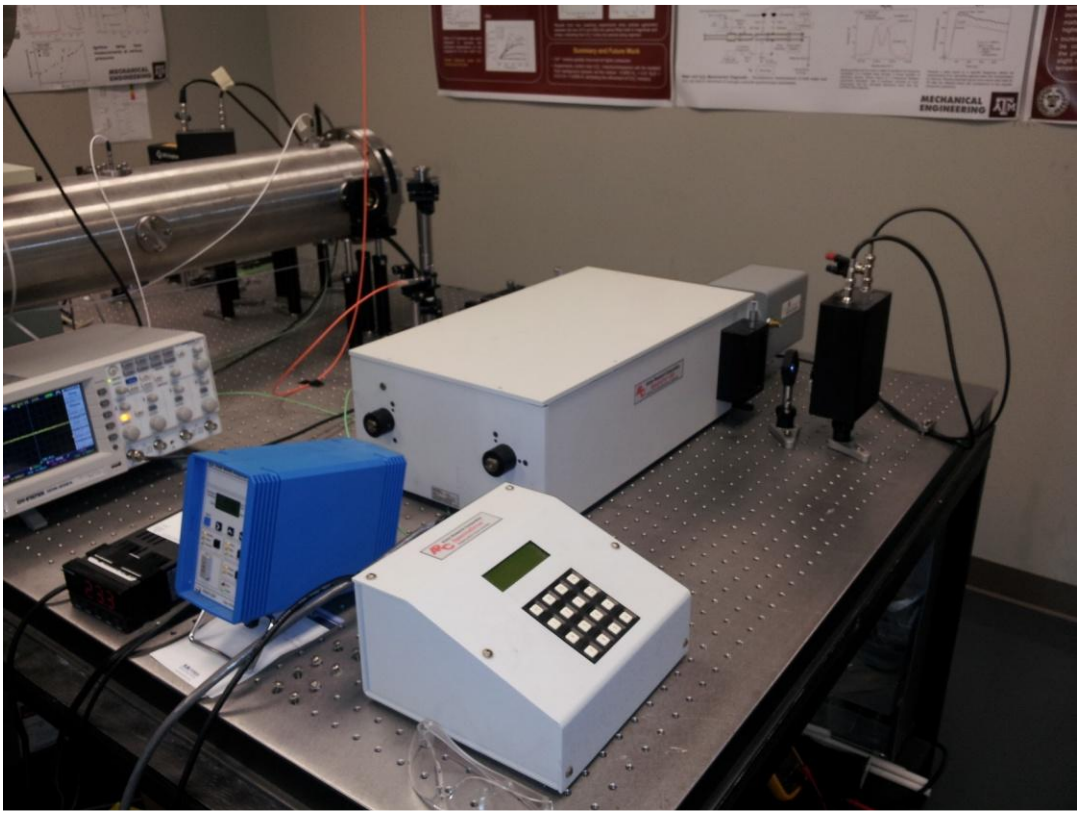

Fig. 122 Picture of the SpectraPro 500 spectrometer in a monochromator configuration with light exiting into a photomultiplier tube (PMT).

For measurements made in this work, the SpectraPro 500 is configured as a monochromator and sends light to a photomultiplier tube (PMT, Hammamatsu R928). It was found that the increased

sensitivity to light that a PMT offers is necessary to accurately measure absorption through the experiment. A diagram of the present configuration of the OH absorption diagnostic is shown in Fig. 123. Illumination of the shock-tube pathlength of 15.24 cm near the endwall of the shock tube is done by a 150-W, UV-enhanced xenon arc lamp source (Oriel Research, Part 66919). The light originating from the lamp source must be sent through a series of optics to collimate the light as best as possible.

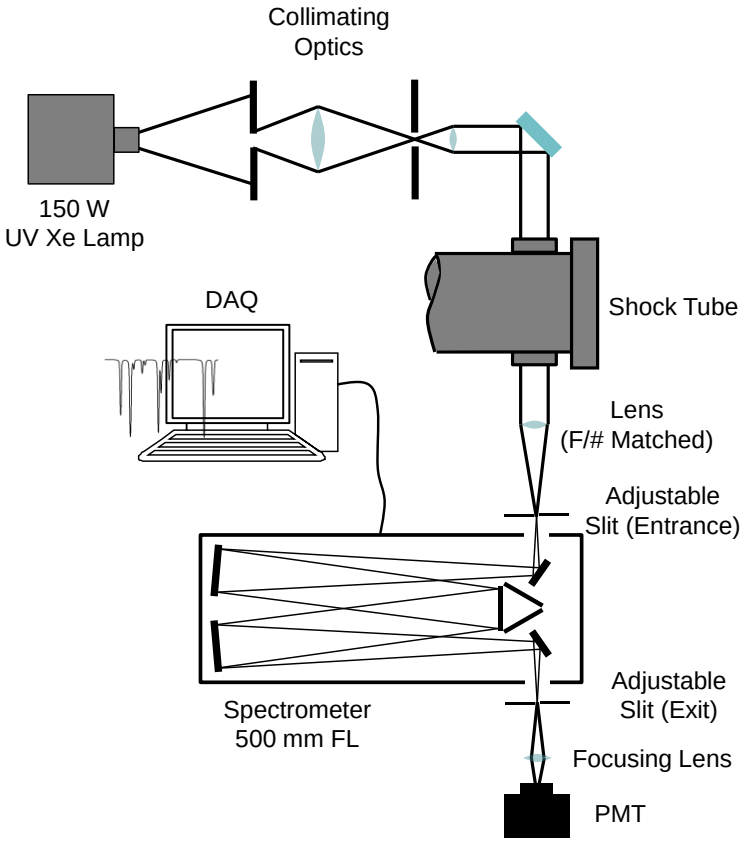

Fig. 123 General schematic of OH measurement diagnostic utilizing a 0.5 m focal length spectrometer configured as a monochromator.

A photograph of the lamp-side of the shock-tube experiment is shown in Fig. 124. Digitally imposed onto the picture is an ideal beam path for the light originating from the UV lamp. Also detailed in Fig. 124 are the optics used to bring down the light to a manageable beam that is near 1.1 cm in diameter. A 5-cm diameter lens with an effective focal length (EFL) of 10 cm is used to focus light down to a point and then converge into a 1.27-cm diameter collimating lens with an EFL of 2.54 cm. Small changes are made with a micrometer adjustment x-y-z opto-mechanic lens holder for the collimating lens as well as an iris placed at the focusing point of the 10-cm EFL lens to block out scattered light. Divergence of the overall beam is still observed due to the nature of the lamp assembly but the core beam is near 1.1 cm in diameter. To block out diverging light, an iris is placed prior to the entrance into the shock-tube port with sapphire window measuring 1.27 cm in optical access diameter.

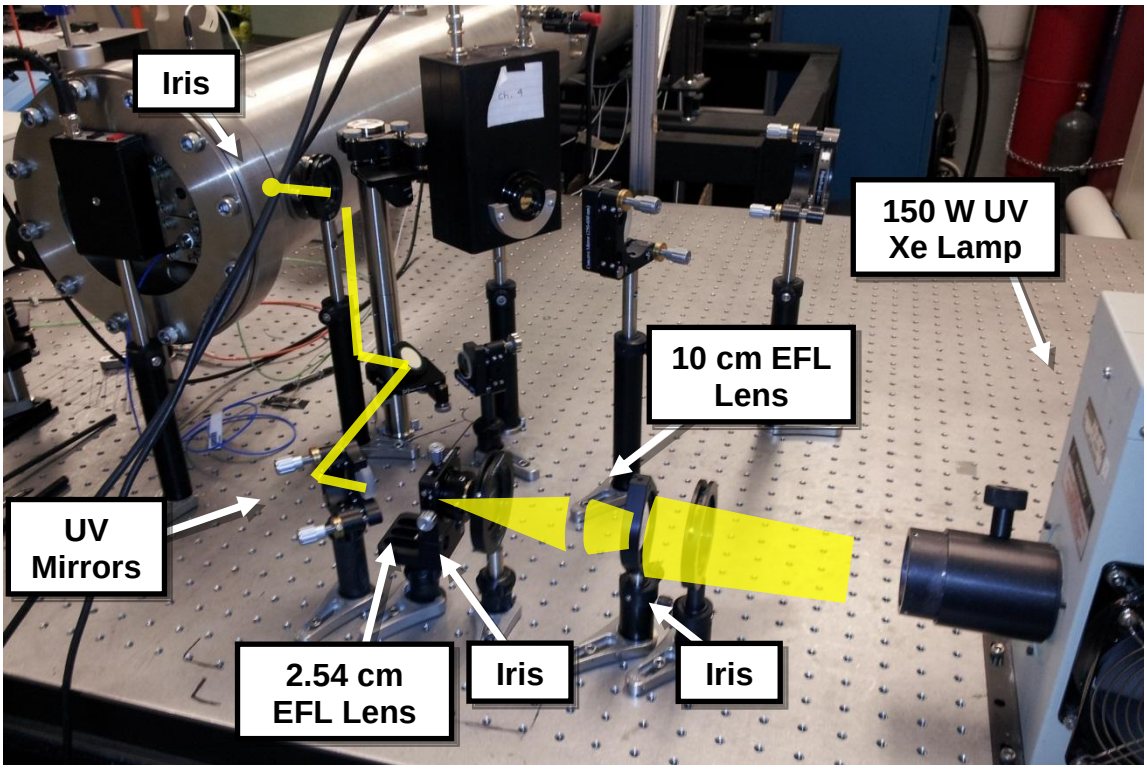

Fig. 124 Picture of UV Xe lamp condensing optics with simulated beam path into shock tube imaged in yellow and appropriate optics detailed.

Figure 125 shows the monochromator-side of the shock-tube area and details the simulated light beam as it comes from the shock tube. The aperture ratio of the monochromator is given as f/6.9 from the manufacturer, and to properly match this f/# by using the paraxial approximation a lens with an EFL of 7.56 cm was used with the 1.1-cm beam. The solid angle output of the focusing lens is matched with the acceptance angle of the monochromator by fine adjustments to the x-y-z position of the lens using the multi-directional opto-mechanic pictured. An optimum entrance slit for the experiments recorded was found to be 45 μm. Another important feature to note is the location of the Hg-Ar calibration pen lamp (Oriel 6035) pictured in Fig. 125. This lamp is used to provide intense UV transitions at 296.73, 302.15, 312.57, and 313.17 nm which are used to calibrate the wavelength control of the monochromator. A calibration of the monochromator shows that the recorded value of wavelength on the monochromator control is nearly 2.5 nm higher than the actual wavelength observed. This calibration was necessary to be able to successfully record time histories of OH by aligning the diffraction grating in such a way to isolate the X→A (0,0) transitions near 309 nm.

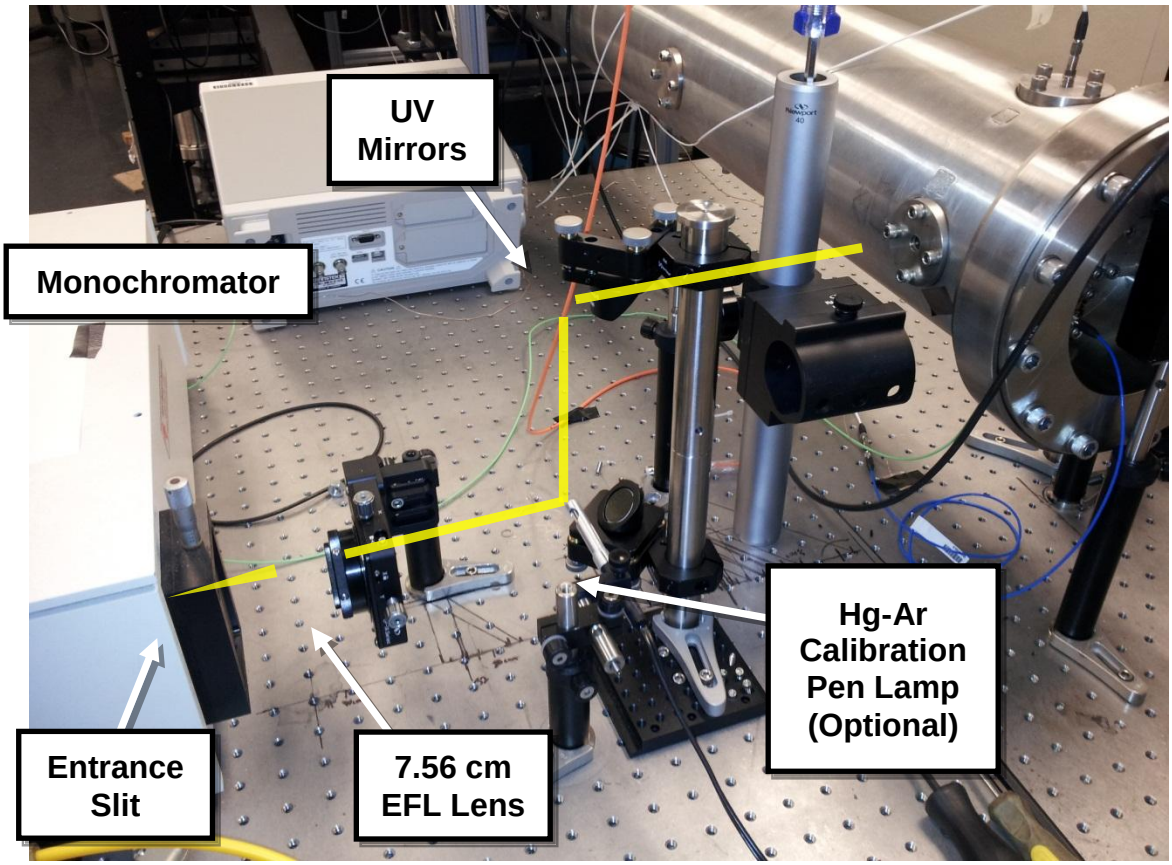

Fig. 125 Photograph of experiment setup collecting light form the shock tube and focusing into the entrance slit of the spectrometer with simulated beam path.

An image of the exit of the monochromator is shown in Fig. 126. Light from the exit of the monochromator is focused down into the PMT by way of a 3.3-cm EFL lens which is placed in a micrometer adjustment x-y-z otpo-mechanical positioner to assure proper focusing. An exit slit of 40 μm was used for all of the experiments recorded. Pictured in Fig. 126 is a cardboard light shroud which has been partially removed to show the position of the focusing lens. This light shroud was used to eliminate any light from the laboratory from entering the unfiltered PMT. Lights in the laboratory space were turned off during experiments, and no interference from the ambient light sources were observed. Similar light shrouds were placed, but not pictured, around the collimating optics in Fig. 124 to block the harmful UV radiation from the lamp from interacting with the experimenter.

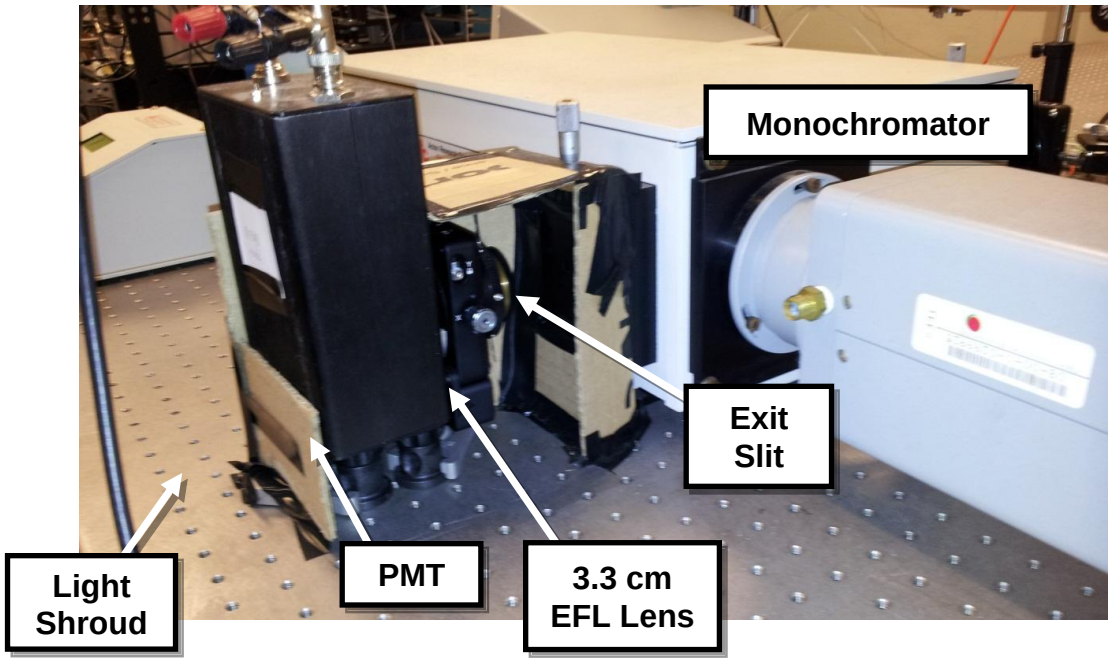

Fig. 126 Picture of PMT applied to the exit of the spectrometer with configured exit slit and focusing lens.

The light originating from the 150-W, UV-enhanced Xe lamp is expected to vary spectrally and must be understood when making measurements with a monochromator. Figure 127 gives the manufacturer's plot of irradiance [mW/m^2nm] versus wavelength [nm] over a broad spectrum for several different lamps. The lamp used in this work was the Oriel 6256, and over the range of wavelength studied in this work the intensity is reasonably constant especially within several nanometers of the 309 nm spectral area utilized.

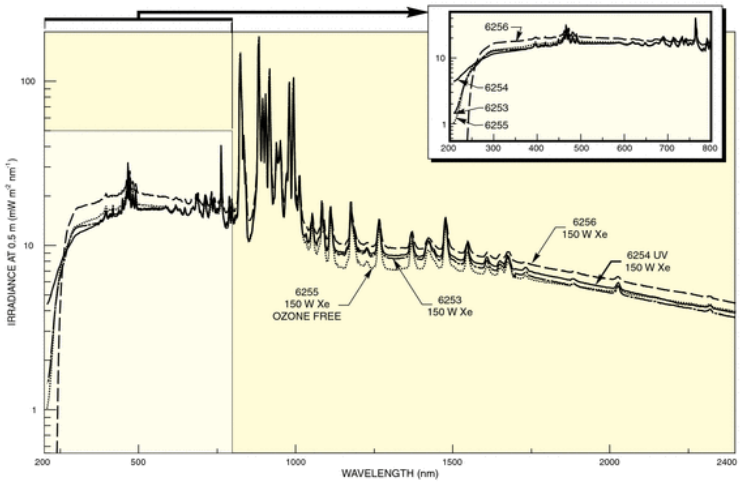

Fig. 127 Plot of irradiance as a function of wavelength (nm) for various lamps available from Oriel (www.newport.com).

The PMT chosen for these experiments was done so because of its excellent sensitivity and quantum efficiency near 309 nm. A plot of spectral sensitivity and quantum efficiency for the Hamamatsu R928 PMT is given in Fig. 128. The response of this particular PMT is excellent hear the 309-nm range and offers the best sensitivity for these experiments. The downside to using a PMT is the relatively large level of noise associated with the high-voltage discharge associated with photon interaction. While the noise is certainly manageable in terms of overall absorption and linearity of the detector, there still exists some areas for improvement in the diagnostic.

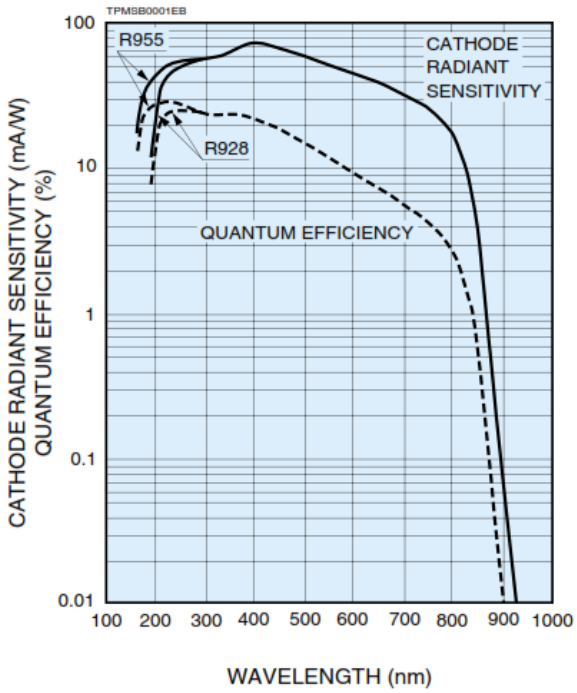

Fig. 128 Plot showing sensitivity and quantum efficiency for the R928 PMT which is used in this work (www.hamamatsu.com).

All mirrors used in the setup were ES #200 UV Mirrors from eSource Optics. These mirrors are specially coated to offer the highest reflectance of light that is known to the author. An experimental plot showing the percent reflectance as a function of wavelength is shown in Fig. 129. The region close to 309 nm gives an average reflectance of near 87.5% when the mirror is angled at 45º. All mirrors were placed in such a way that the light being reflected stayed true to this angle to maximize the light reflected from the source.

Loss of light through the absorption diagnostic was of principal concern when designing the system. For this reason, the UV-enhanced mirrors and UV fused silica lenses were selected to mitigate the inevitable intensity loss occurring from either transmission through mirrors or filtering from the lens material. For a proper absorption diagnostic, it is important to maximize the signal-to-noise prior to the beginning of the experiment. Placing the system closer to the shock tube might help in increasing overall signal, but then an increase in interference emission (i.e., chemiluminescence) from the reaction, which typically occurs at the same wavelength of

light, will interfere with the absorption measurement. For this reason, the monochromator was placed a reasonable distance from the shock tube to virtually eliminate emission from the highly sensitive PMT.

Calibration for OH Concentration

Initial measurements were performed to properly assess that the monochromator was obtaining expected results from a well-studied H_2/O_2 mixture diluted in argon. The procedure began with the appropriate alignment of the light into the spectrometer, a method described in greater detail in the above paragraphs, and running a shock-tube experiment on the hydrogen mixture. A sample OH absorption trace is shown in Fig. 129 with a line signifying the peak absorption at 26.3% representing the attenuation of light when compared with the incident intensity. Also shown in Fig. 129 are the schlieren effects from the passing of the incident and reflected shock waves. This distortion is common with absorption measurements and result from the sharp density change across a shock wave which is much smaller in width than the beam of light passing through the viewing area.

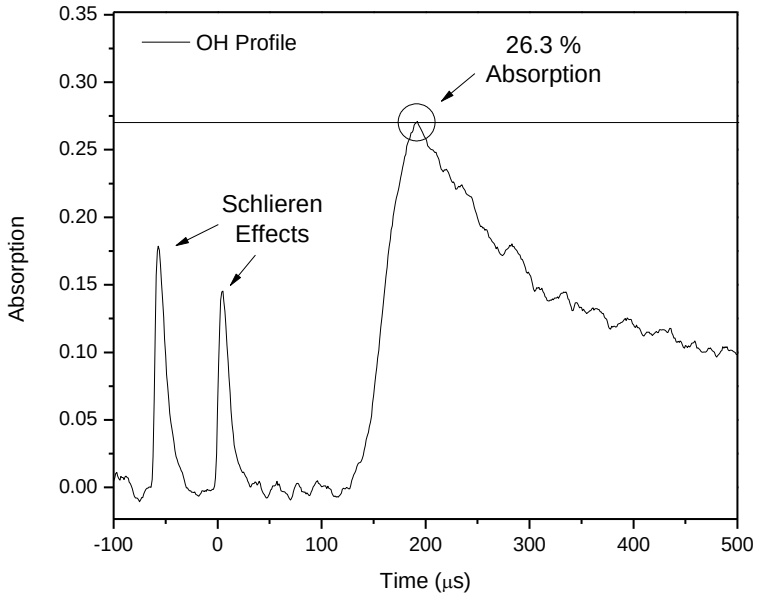

Fig. 129 Sample OH species profile on H_2/O_2 diluted in 98% argon at $\phi = 1$, T = 1185 K, and P = 13.05 atm.

Calculation of overall absorption can be made if the temperature, pressure, and OH mole fraction are known. To assess the mole fraction of the calibration H_2/O_2 data, comparison with the data are made against the predicted results of the Hong et al., 2011, mechanism. The sample data trace from Fig. 129 is compared with the results from the mechanism in Fig. 130 with highlighted OH mole fraction of 0.000176, or 176 ppm.

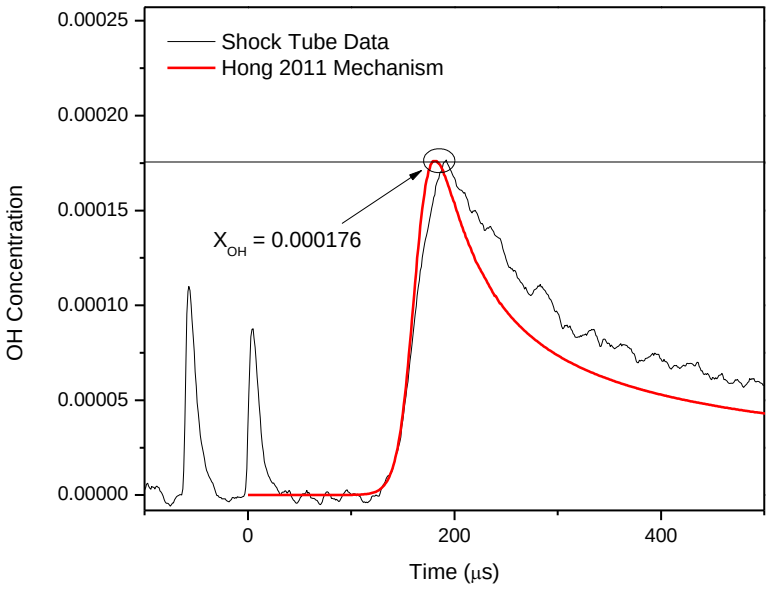

Fig. 130 Comparison of predicted OH profile from the Hong et al., 2011 mechanism and the peak-matched shock tube results from Fig. 129 as derived from the Beer-Lambert relation.

Now that the peak OH has been assessed by the peak-matched experiment, the value can now be used in the OH code developed in-house precisely where the monochromator is situated spectrally. The OH code utilizes the calculated absorption peaks en masse and groups the absorption over an average spectral band defined by the entrance and exit slits of the monochromator. For this example experiment, a slit exit width of 45 μm was used to assess a band of 0.072 nm in which the spectrometer is averaging through to the PMT detector. A Cauchy distribution slit function was assumed over the absorption area with the half-width parameter defined by the 0.072-nm band and is deemed to be accurate in this region (Kostkowski and Bass, 1956).

A comparison of the experimentally measured absorption and the calculated average absorption over the given band of 0.072 nm is shown in Fig. 131. The peak of an absorption feature near 309.55 nm matches up with the experimental value horizontal line and is illustrated in the inset of Fig. 131. This agreement matches well with the calculated spectral calibration using four mercury lines around the 300-nm range. To verify that the OH code is able to recreate this agreement for other experiments more measurements were made on stoichiometric H_2/O_2 at two different pressure ranges around 2 and 12 atm. Good agreement between the calculated and observed absorption through the monochromator at different conditions is found and shown in Fig. 132. Agreement is good between not only temperature variation, but also a large pressure change as shown by the data trace for T = 1270 K and P = 1.92 atm in Fig. 132. Experiments were performed at two pressure ranges of 2 and 13 atm over a wide range of temperatures between 1182 and 2017 K. Peak matching of the experimental data allows for the generation of an absorption coefficient correlation which can be used to analyze the remainder of the data.

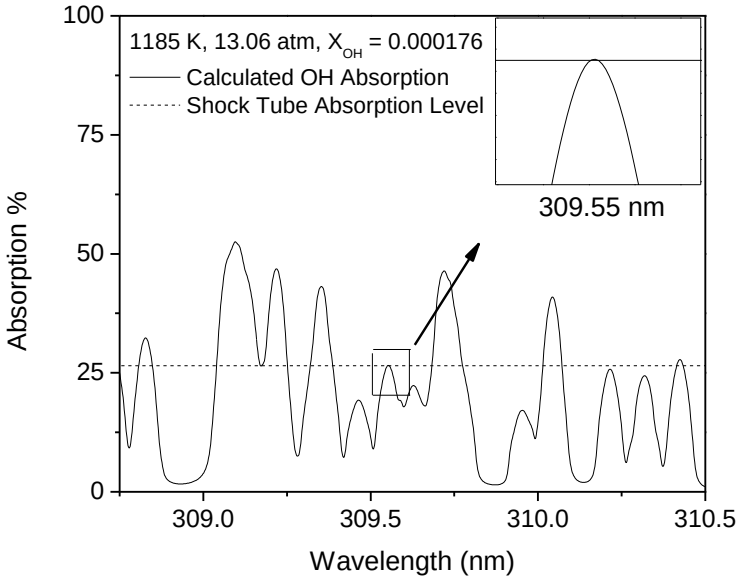

Fig. 131 Calculated average absorption that is expected to be seen through the monochromator exit as a function of wavelength compared with experiment.

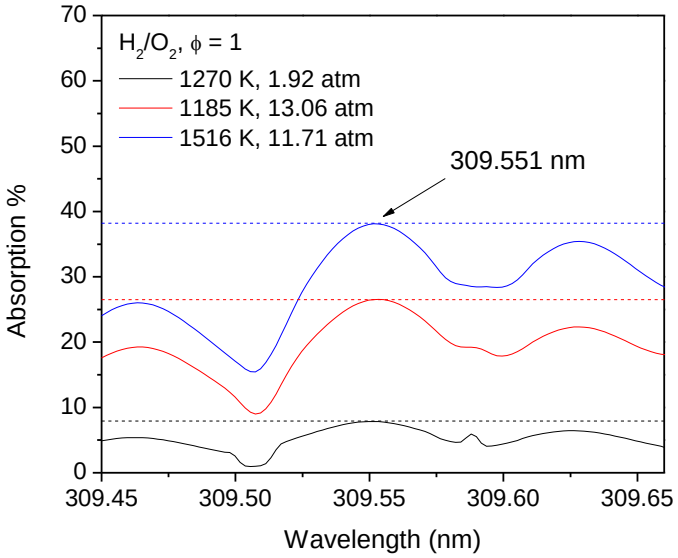

Fig. 132 Four different calibration comparisons with calculated average absorption in the solid lines and the experimentally observed absorption in the dashed lines for H_2/O_2 mixture diluted in 98% argon.

Through a linear regression technique, the absorption coefficient can be correlated to temperature and pressure only. A set of three correlations were generated considering three pressure ranges: Eq. 30 for low pressure (~2 atm) data only, Eq. 31 for high pressure (~12 atm) data only, and Eq. 32 for all data.

$$24981.2 \cdot T^{-1.294} P^{1.682} \tag{30}$$

$$4.7453 \times 10^{7} \cdot T^{-2.381} P^{0.521} \tag{31}$$

$$2.1923 \times 10^{8} \cdot T^{-2.399} P^{-0.041} \tag{32}$$

The three correlations show that there is a weak sensitivity to pressure when considering the high-pressure data as well as an increase in temperature sensitivity. A measure for how accurate a correlation is best illustrated by plotting correlation vs. experimental data to see how close the values match a 1:1 ratio line. For the first correlation, there is very good agreement with the experimental values shown in Fig. 133. A goodness of fit value of R^2 = 0.999 illustrates that there is a high degree of confidence when utilizing this correlation for other data near P_{avg} = 1.82 atm.

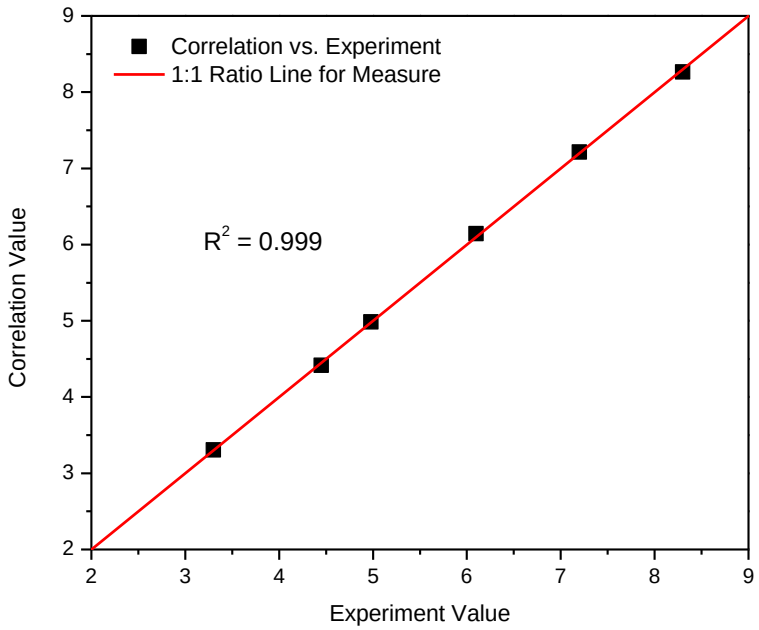

Fig. 133 Comparison for first correlation which considers only low-pressure data with P_{avg} = 1.82 atm, correlation given by Eq. 30.

The second correlation given by Eq. 31 is shown graphically in Fig. 134. The fit for this high-pressure correlation is not as good as with the low pressure case but still holds a respectable R^2 = 0.994 with some slight deviation in the values around absorption coefficient values near 4.5 and 6.5 $atm^{-1}cm^{-1}$.

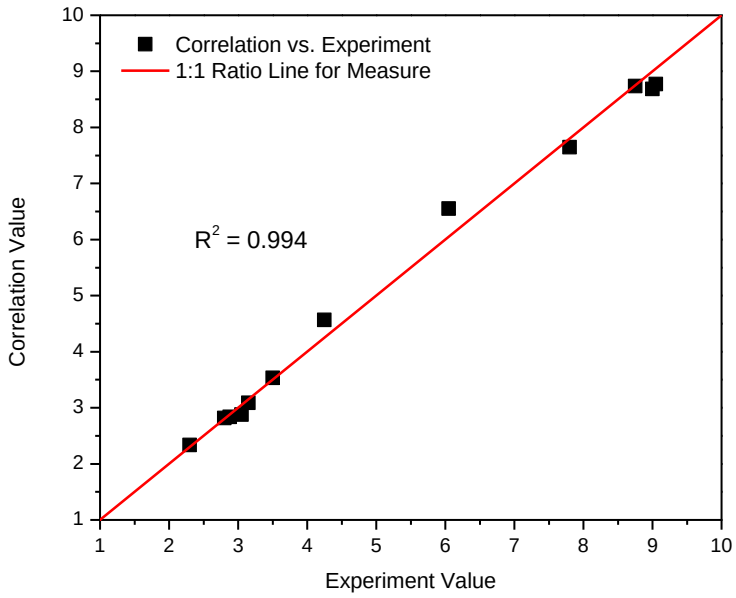

Fig. 134 Correlation predictions vs. experimental data for shock-tube experiments with P_{avg} = 12.1 atm, correlation given by Eq. 31.

The full correlation, as given by Eq. 32, is shown in Fig. 135. The overall correlation does not fit as good as the single-pressure counterparts but still performs quite well across the range of data observed. Different colored markers are used to distinguish between the two pressure ranges.

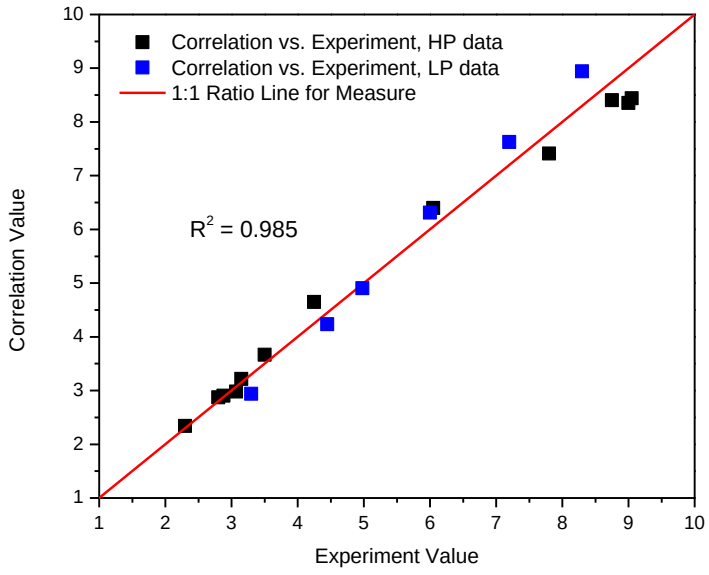

Fig. 135 Correlation predictions vs. experimental data for all H_2/O_2 data, correlation given by Eq. 32.

For the data analyzed herein, the specific-pressure correlations are used for determining the experimental absorption coefficient. The full correlation is shown here for completeness and to illustrate how the data can correlate even over large pressure ranges as seen in the data.

Results for Hydrogen

Experiments were performed on a calibration mixture of stoichiometric H_2/O_2 diluted in 98% argon and are analyzed herein. Conditions were chosen to cover a wide temperature range of 1182 – 2017 K and two pressure ranges at P_{avg} = 1.82 atm and P_{avg} = 12.1 atm. The wide range of temperatures for the H_2/O_2 mixture was studied in expectation that CH_4 is known to react at much higher temperatures and to properly facilitate a proper correlation that could be used for the methane-based tests.

A low-pressure experiment of around 2 atm is shown in Fig. 136. The noise level observed comes from the small level of absorption due to lower collisional broadening averaged through the monochromator. The data agree rather well with both of the mechanisms tested both in terms of profile shape and ignition delay time. There is no observed intensity shift through the incident and reflected shock wave passes as indicated by a constant baseline value through the schlieren effects. The data shown here, as described in the previous section, is purposely peak-matched to the predicted peak value of OH from the Hong et al. 2011 mechanism.

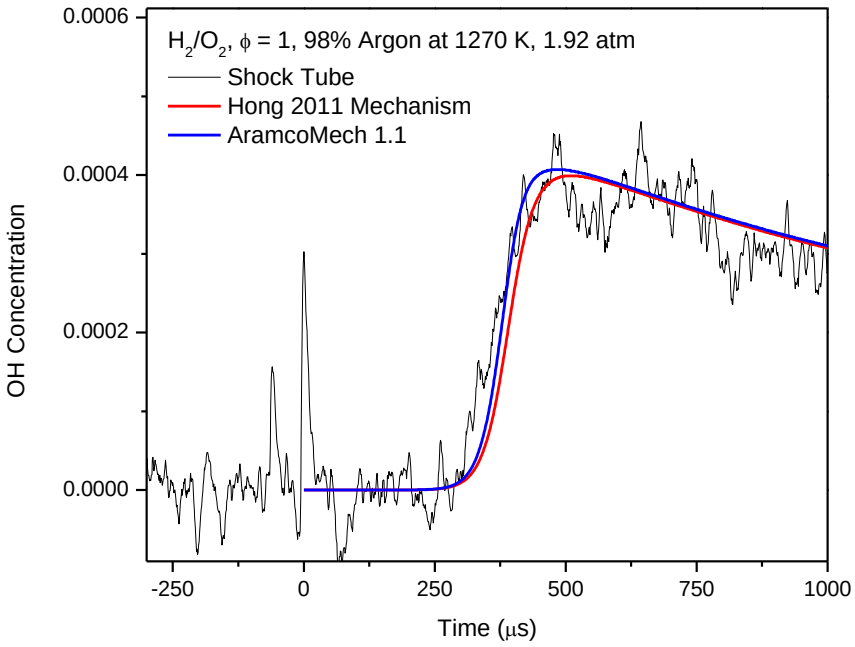

Fig. 136 Shock-tube OH profile of low-pressure experiment compared with two mechanisms, Hong et al. 2011 and AramcoMech 1.1 (Metcalfe et al., 2012).

A low-pressure example of an elevated-temperature shock is shown in Fig. 137. This experiment produces more OH than that of the previous example and shows good agreement through the region after the initial ignition. There is no difference in ignition delay time for both of the models and the experimental data. The profile is well matched between the two mechanisms in both peak and shape, and these also agree with the experiment very well. The higher level of noise is expected at lower pressures.

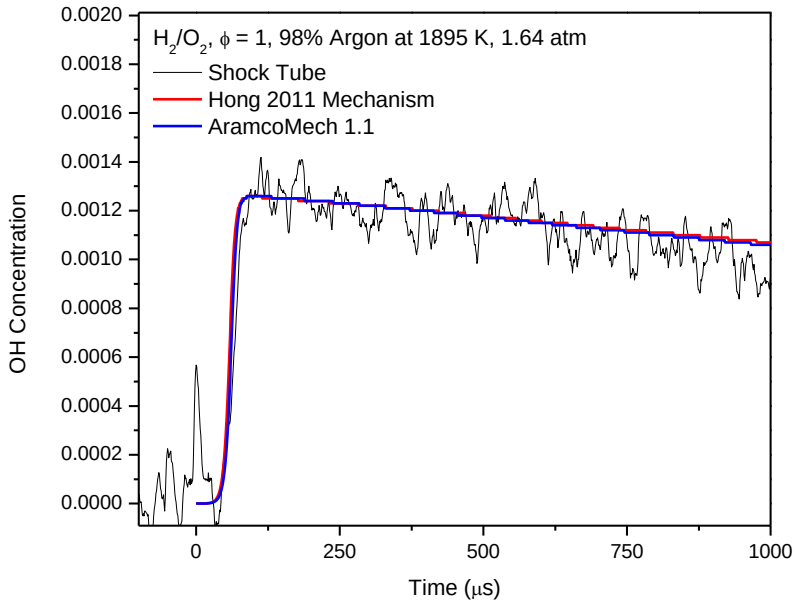

Fig. 137 OH profile at a pressure of 1.64 atm at an elevated temperature of 1895 K, compared with the Hong et al. 2011 and AramcoMech 1.1 (Metcalfe et al., 2012) mechanisms.

Experiments from another study in the author's laboratory on the light emission of OH* chemiluminescence were used to compare with conditions which align in this dissertation (Keromnes et al., 2013). In this study, light was captured using a photomultiplier tube which was filtered around 307 nm and placed at the same sidewall location as the present ground-state OH diagnostic. An example comparison is shown in Fig. 138 for a low-pressure case near 1.8 atm. The signals were normalized to the peak value from the OH* chemiluminescence signal and the average peak of the ground-state OH measurement peak. There is good agreement between the two signals for the initial formation of both species. The decay of OH* is expected to be much faster as the population of the ground state increases.

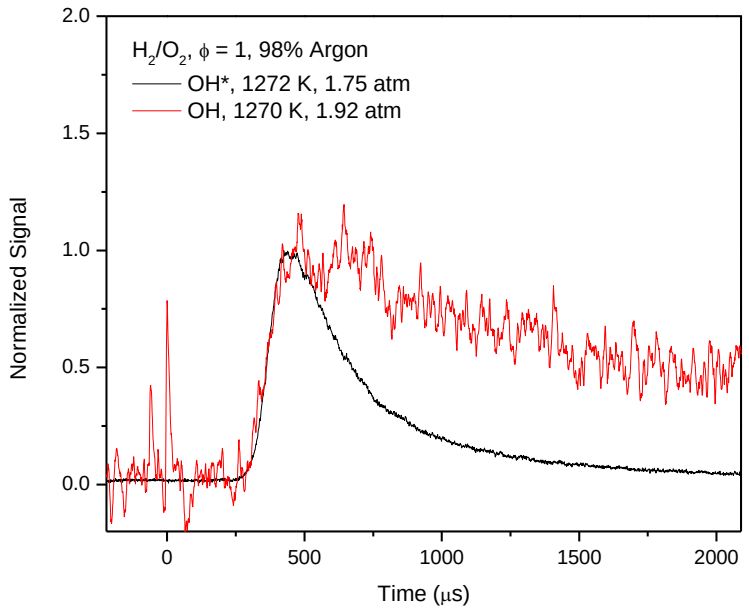

Fig. 138 Ground-state OH measurement compared with OH* chemiluminescence at similar conditions at low pressure.

When looking at high-pressure shock tube OH profiles there is a marked increase in signal-to-noise ratio due to the much broader transitions which are being seen by the monochromator. Figure 139 shows a representative plot of OH from experiment and the two mechanism predictions at high pressure. This experiment was at a relatively low temperature when compared with the rest of the data set and has an ignition delay time of 138 μs. Lower temperatures could be obtained but were not relevant to the higher temperatures necessary for oxidizing the hydrocarbon fuels in this work. A distinct discrepancy is apparent between the peak OH predicted from the two mechanisms at this low-temperature condition. These data were peak matched with the Hong et al. 2011 mechanism to generate the previously described absorption coefficient correlation. Good agreement was found in both ignition delay time and throughout the profile shape.

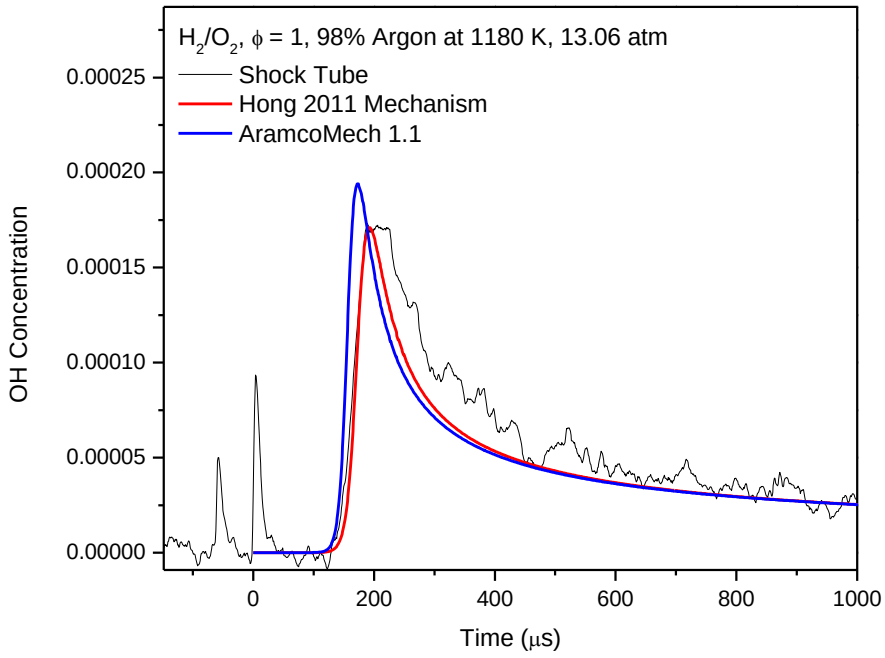

Fig. 139 Shock-tube data comparison with two mechanisms for a high pressure H_2/O_2 mixture diluted in argon.

Figure 140 shows a comparison of a higher-temperature OH profile at an elevated pressure. There is very little difference in ignition delay time between the three sets of data and the predicted profiles of the two mechanisms match closely in peak value and overall shape. There is, however, a distinct departure from the mechanism results and the experiment data. This trend is apparent at higher temperatures as can be seen in the differences between Fig. 139 and Fig. 140. This discrepancy comes from the secondary chemistry involved past the dominant chain branching reaction $H + O_2 \rightleftarrows OH + O$. A full recording of all the H_2/O_2 OH profiles are cataloged in the appendix for reference.

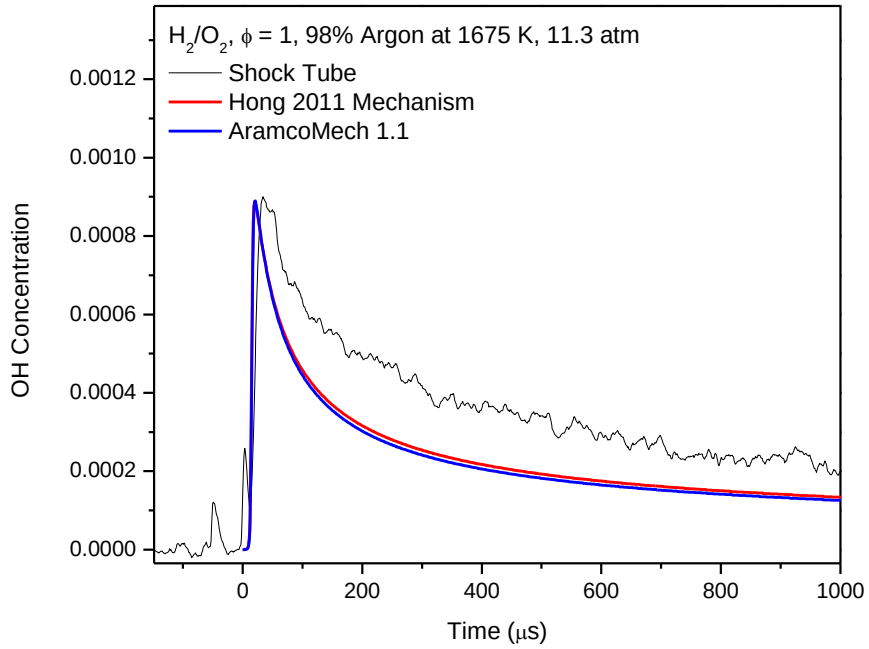

Fig. 140 A representative high-temperature experiment at high pressure and compared with two mechanism predictions.

A chemiluminescence signal of OH* was measured through filtered light near 307 nm emitted from a shock-tube experiment in a previous study (Keromnes et al., 2013). This diagnostic was placed at the same location as the OH absorption diagnostic and a representative comparison near 12 atm is shown in Fig. 141. Both the OH and OH* signals are normalized in an effort to compare the kinetic shape throughout the experiment. The chemiluminescence signal is peak shifted by 20 μs to show similarity as there exists a considerable pressure difference between the two experiments. It can be seen that the formation of both OH and OH* occurs in the same manner, with the decay of OH* being much faster due to the population returning to ground state.

Ignition delay time is defined from the time of the reflected shock passing over the sidewall location to the intersection of the baseline from an intersecting parallel of the steepest slope on the profile curve. A graphical representation of the determination of ignition delay from the experiment is shown in Fig. 142. Ignition delay data are invaluable on their own accord in the development of detailed mechanisms and add to the utility of measuring OH profiles within the shock tube. The sharp rise of OH during the ignition event is prominent in most cases when determining ignition delay from light emission or, for more exothermic conditions, the pressure rise. A grouping of the ignition delay data are presented in Fig. 143 for H_2/O_2.

The ignition delay time data are compared with the two mechanisms used in this study and show excellent agreement throughout in Fig. 143. Ignition delay time data are traditionally represented in an Arrhenius fashion with logarithmic time on the vertical axis and inverse temperature along

the horizontal axis. In this plot high-temperature data are located toward the left of the plot and temperature decreases toward the right. The logarithmic plot shows small changes at high temperature very well and in the case for these experiments there is very good agreement between the mechanism and the experiment. A typical error in ignition delay time determination comes from the appropriate placement of the intersection of the steepest slope and baseline. For this work ignition delay time error was found to be ±7 μs for the low pressure data and ±3 μs for the high-pressure data and are shown as error bars in Fig. 143.

The high-temperature predictions in Fig. 143 for both mechanisms are near identical with some very slight deviation at lower temperatures. This agreement is to be expected as H_2/O_2 chemistry has been verified for both of these mechanisms.

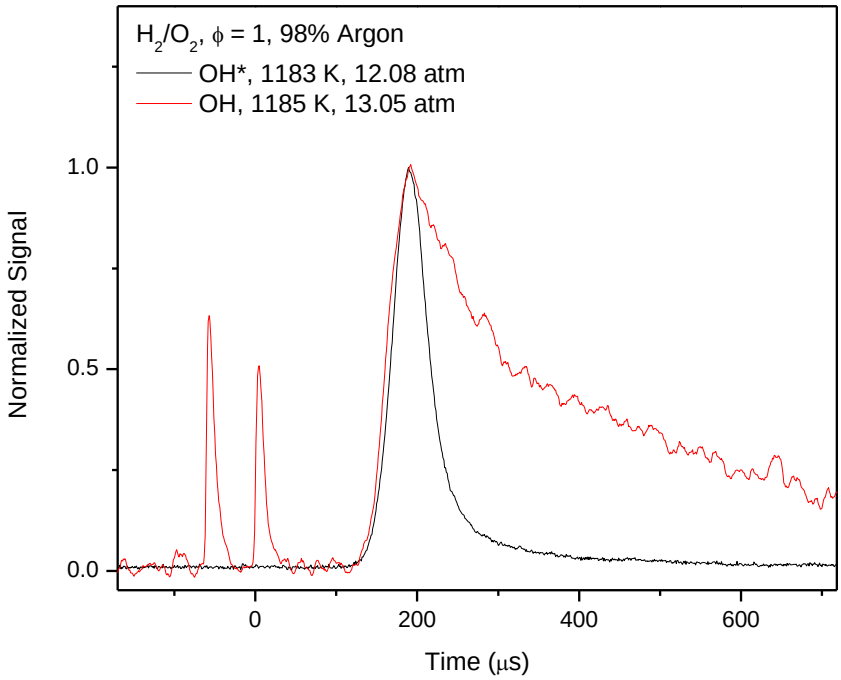

Fig. 141 Comparison of ground-state OH with OH* from chemiluminescence measurement within the shock tube at similar conditions at elevated pressure.

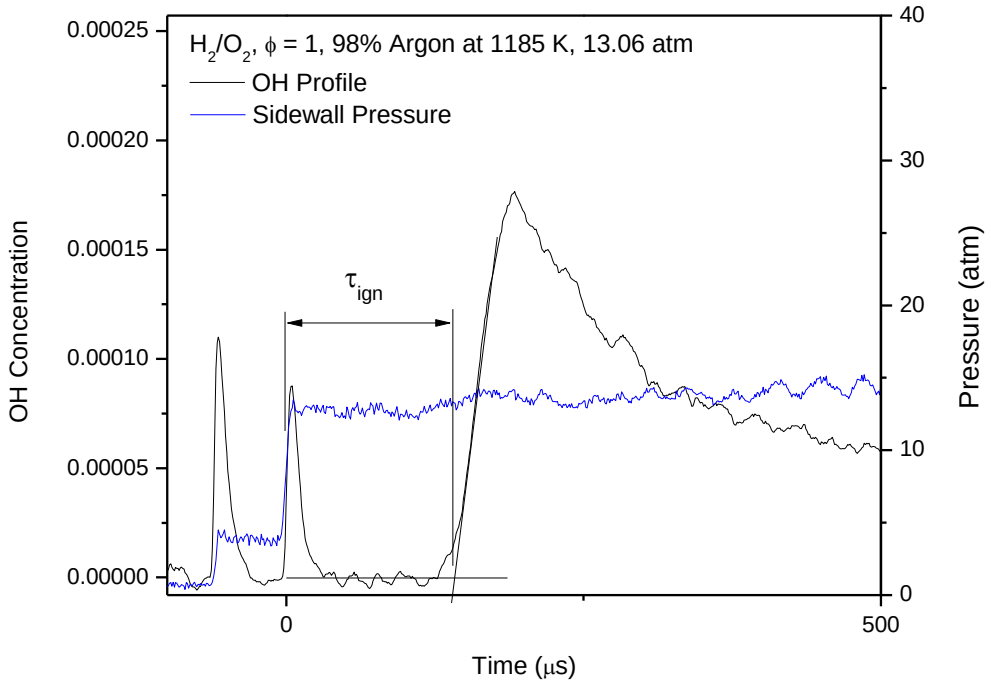

Fig. 142 Ignition delay time determination for an example experiment.

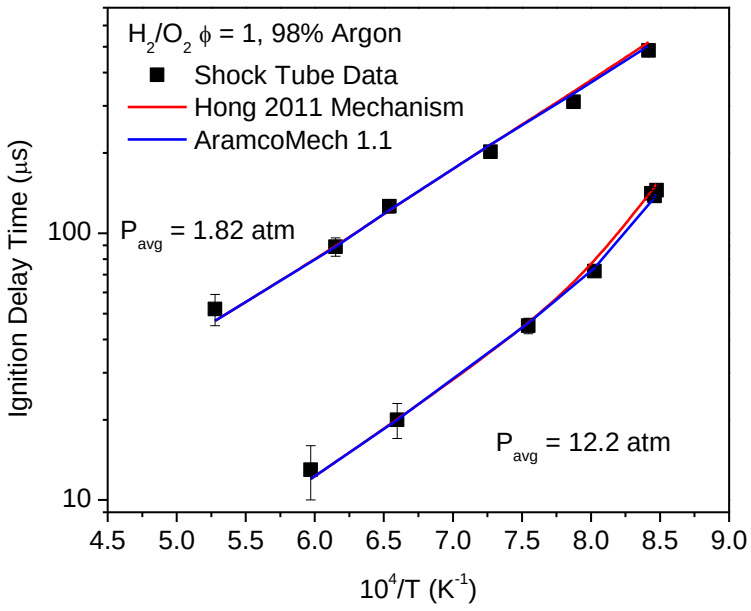

Fig. 143 Ignition delay time plot from OH profiles of H_2/O_2 diluted in argon.

SUMMARY AND CONCLUSIONS

Laminar Flame Speeds

Correlations for the stable laminar flame speeds of hydrogen and oxygen with different diluents, namely nitrogen and helium, were developed. The recently updated kinetic mechanism employed in this study was sufficiently validated using recent, experimentally measured laminar flame speeds and ignition delay times. A wide range of equivalence ratios, temperatures, and pressures which are relevant to industrial combustion systems such as gas turbines were simulated. Contrary to the conventional global pressure correlations, a different approach was adopted in this study, and the correlations were developed at constant pressures. This method resulted in better agreement between the kinetic model predictions and the correlation estimates than seen in the literature, and it provided flame speed estimates that are within ±13 cm/s of the model predictions even at extreme conditions.

Due to the growing interest in hydrogen-based fuels for gas turbine applications, a correlation for lean syngas blends (H_2/CO) was also developed solely using the pure-hydrogen correlations. In addition to the variation in pressure and temperature, the hydrogen content in the blend and the steam contaminant levels were also varied. To reduce the number of numerical simulations required to develop the correlation, a design of experiments approach was adopted, which resulted in a wide excursion of the parameter space. The strong influence of hydrogen on the properties of the blend was evident even for a blend containing only 15% hydrogen by volume. This simplified approach yielded flame speed estimates that were within ±12% of the corresponding model predictions. Future work will focus on development of correlations for natural gas blends of common hydrocarbon fuels with varying amounts of hydrogen.

Two high-precision experimental gas dynamic apparatuses were used to validate and produce new information on the combustion kinetics of hydrogen and syngas. The first device used was a constant-volume cylindrical bomb to measure laminar flame speeds. The current facility has two constant-volume cylindrical bombs: one capable of initial conditions only at room temperature and up to 15 atm and the other capable of initial temperatures and pressures up to 600 K and 30 atm, respectively. Laminar flame speed measurements were made at various conditions of hydrogen and syngas and compared to available literature information with generally good agreement, although variations as high as 34 cm/s are seen amongst the literature data at lean conditions. Additionally, a recently improved chemical kinetics model was shown to have overall very good agreement at the conditions presented herein. The second device used was a high-pressure shock tube. Several compositions of syngas were performed at a single equivalence ratio and 98% dilution at three pressures and compared to previously published hydrogen-oxygen data from our laboratory. The results showed that an increase in carbon monoxide in the fuel will increase the ignition delay time, but pressure appears to play a role on this result. Also, it was seen that the activation energy will decrease with increasing amounts of carbon monoxide. Both of these phenomena are accurately reproduced by the model.

This report presented new experimental data for three syngas fuels with varying steam dilution at several initial temperatures and pressures using a well-known method of analysis. A Design of Experiments methodology allowed us to explore the combination of four different factors with three levels. The three syngas blends studied were 100:0 H_2:CO, 50:50 H_2:CO, 5:95 H_2:CO at

initial pressures of 1, 5, and 10 atm. The other factors included initial temperatures of 323, 373, and 473 K and steam dilutions of 0, 7.5, and 15% on a molar basis of the fuel blend. Some experimental data are compared to published data demonstrating good agreement, while all new data are compared to the most-recently improved chemical kinetics model from NUIG authors. A performance sensitivity analysis revealed that the syngas composition is the most important factor over initial temperature, initial pressure, and water dilution that affects the laminar flame speed. However, the same type of analysis could not provide conclusive results for the mass burning rate and the Markstein length, i.e., there was no dominant variable affecting these parameters. The syngas composition still plays an important role in these two global flame parameters, but several other factors had competing effects from fuel lean to fuel rich. Although it was shown that water dilution plays a relatively insignificant role in affecting global flame parameters in comparison to syngas composition, pressure, or temperature, water dilution demonstrated the potential to promote chemical kinetic reactions in highly CO-diluted syngas mixtures at low pressures instead of acting as purely a diluent in most situations, retarding the chemical kinetic reactions. The overall agreement with the model is excellent in most cases with some discrepancies seen around the peak flame speed for particular mixtures, which identifies potential areas where improvements can be made.

Nitrogen Oxide and Ammonia Chemical Kinetics

Ignition delay times of H_2/O_2 mixtures highly diluted in Ar with various amounts of N_2O were measured behind reflected shock waves in the 940-1675 K temperature range and for pressures up to 32 atm with an equivalence ratio for the H_2/O_2 mixture set at 0.5. Under some conditions and concentrations, nitrous oxide addition either had no observable effect or decreased the ignition delay time; this decrease when observed was proportional to the N_2O concentration and was dependent on the pressure and temperature. For example, the decrease in the ignition delay time is noticeable only for high temperatures and for N_2O additions of 1600 ppm and above at the lowest pressure investigated. At around 13 atm, a very small decrease in the ignition delay time was observed over the whole range of temperatures investigated, whereas a more-noticeable decrease was observed for the high-pressure conditions. A detailed chemical kinetics model was developed based on mechanisms and reaction rate measurements from the literature. Compared to the other mechanisms from the literature, the model showed improvements on the predictions for the results of this study and for results from the literature. Finally, the model was used to explain the results of the present study, and this analysis showed that, under the conditions herein, the decrease in the ignition delay time when there was one was essentially due to the reaction $N_2O + M \rightleftarrows N_2 + O + M$. The released of O radicals by this reaction will then strengthen the channel $O + H_2 \rightleftarrows OH + H$ and promote the ignition delay time.

New ignition delay time measurements were obtained in a shock tube for diluted H_2/O_2 mixtures doped with various amount of NO_2. Results showed a strong dependence on pressure and on NO_2 concentration. Several NOx mechanisms from the literature were tested, and good agreement with the data over the range of conditions investigated was found for a model that combines the H_2/O_2 chemistry from Healy et al. (2010) and the NOx chemistry from Sivaramakrishnan et al. (2007) and Dayma and Dagaut (2007) with the reaction rate for $H_2+NO_2 \rightleftarrows HONO+H$ from Parks et al. (1998). This study confirmed the assessment made in Mueller et al. (2007) and Dayma and Dagaut (2007) on the validity for the rate of the reaction (R3) determined in Slack and Grillo (1978). Chemical analyses showed, for pressures above 1.5 atm, that additions of NO_2 up to 400

ppm were promoting τ_{ign} *via* $NO+HO_2 \rightleftarrows NO_2+OH$ (NO_2 being mostly converted to NO by the reaction $NO_2+H \rightleftarrows NO+OH$ under these conditions). The OH radicals produced then oxidize the hydrogen *via* $OH+H_2 \rightleftarrows H_2O+H$, and this reaction then allows recycling NO *via* $NO_2+H \rightleftarrows NO+OH$. For the 1600-ppm NO_2 addition cases, τ_{ign} was longer at low temperatures than for the 400-ppm NO_2 concentrations cases for the three pressure ranges investigated. The analyses showed that this large concentration of NO_2 favored the propagating channel $OH+H_2 \rightleftarrows H+H_2O$ rather than the branching channel $H+O_2 \rightleftarrows OH+H$.

It is important to understand the details of NH_3 combustion chemistry for practical reasons such as the control of NOx formation or NOx removal processes. To date, several shock-tube studies have been performed several decades ago, and several detailed kinetics mechanisms are available from the literature. Unfortunately, the experimental conditions are not accurately reported in the experimental studies and a large discrepancy is observed amongst models, making the selection of a good model to predict NH_3 combustion difficult. Thus, new ignition delay time measurements have been performed over a wide range of conditions (around 1.4, 11.0, and 30 atm, between 1560 and 2490 K, and for equivalence ratios 0.5, 1.0, and 2.0). Results showed that both the equivalence ratio and the pressure had an important effect on the ignition delay time. To model the data, it was found necessary to add the reaction $N_2O + H = N_2 + OH^*$ from Hidaka et al. (1985) to the OH* mechanism from Hall and Petersen (2006). Modeling results showed that only the mechanism from Dagaut et al. (2008) was capable of reproducing satisfactorily the experimental results. However, further analysis showed that this mechanism needs to be improved at the H_2/O_2 and NOx sub-mechanisms levels.

Impurity Chemical Kinetics

New ignition delay time measurements in a high-pressure shock tube were performed between 1.6 and 33 atm for mixtures of 1% H_2 / 1% O_2 diluted in Ar and seeded with various concentrations of H_2S (100, 400 and 1600 ppm). Results, when compared to ignition delay time measurements recently obtained for a neat H_2 / O_2 mixture studied at similar conditions, showed that the addition of hydrogen sulfide can significantly decrease the reactivity of the H_2/O_2 mixture. At around 1.6 atm, the ignition delay time is increased on the low-temperature side of the range investigated, whereas the effect is more prominent on the high-temperature side for pressures above 10 atm. At the highest pressure investigated, however, an increase in the reactivity was observed for the lowest temperature and the highest H_2S concentration investigated.

Several kinetics mechanisms from the literature were tested against these data. Although the data at around 1.6 atm are generally well predicted by these mechanisms, it was shown that the data at around 33 atm as well as the data at 13 atm, 1600 ppm H_2S were poorly predicted by these models. The most recent and complete H_2S mechanism from Zhou et al. (2013) was then merged with the recent H_2/O_2 mechanism from Kéromnès et al. (2013). Based on sensitivity analyses, several important reactions were then identified and modified within their reported error factor to better match the data. These modifications also improved the predictions on the few shock-tube data available from the literature. Several flow reactor data were also modeled. If the data with the pyrolysis of a H_2/S_2 mixture were modeled with some success, it is worth mentioning that the data when H_2S is a reactant were very poorly reproduced by all the recent H_2S models available. It is however not clear whether this discrepancy is due to catalytic surface reactions with H_2S

with the silica walls of the flow reactors or to some deficiencies into the detailed kinetics model. To remove the ambiguity, at least two reactions would need to be better estimated over a large range of pressure and temperature: $H_2S+S \rightleftarrows 2\ SH$ and $SH + SH\ (+M) \rightleftarrows HSSH\ (+M)$. Note that better estimation on the other sensitive reactions involving SH would also certainly allow for better model optimization and predictions. Using sensitivity and reaction path analyses, the model proposed in the present study was used to explain the results obtained with the H_2 / O_2 / H_2S mixtures diluted in Ar. It was found that H_2S starts reacting before H_2, mostly through $H_2S + H \rightleftarrows SH + H_2$, and inhibits the branching reaction $H + O_2 \rightleftarrows O + OH$ and hence leads to an increase in the ignition delay time.

To assess the effect of the mixture composition and ammonia impurities on the ignition delay times of syngas, compounds that are found in a real syngas (H_2O, CO_2 and CH_4) were added separately to a baseline $H_2/CO/O_2$ mixture highly diluted in Ar, and a mixture representative of a syngas produced from biomass combining all of the aforementioned compounds was also studied. The effect of impurities was studied with an additional 200 ppm of NH_3 on the baseline and bio-type syngas mixtures. Results showed that the CO_2 addition did not have any effect on τ_{ign}, whereas a small promoting effect was observed with the water addition. The CH_4 addition showed a noticeable increase in τ_{ign} for the lower temperatures investigated at around 1.6 atm and for higher temperatures at a pressure around 32 atm. At a pressure around 12.5 atm, an important increase in τ_{ign} was observed, mostly for the lower temperatures. Similar but amplified trends were observed below 32 atm for the biosyn mixture. For most of the conditions, no effect of the NH_3 impurities was observed, and only a limited promoting effect was observed with the baseline mixture for pressures below 32 atm. These experimental trends were captured by models from the literature, except for the water addition where models predicted a small increase in the ignition delay time. A sensitivity analysis performed at 1150 K and 12.5 atm for the BS and Biosyn mixtures showed that the difference in τ_{ign} was mainly due to methane through the reaction $CH_4+OH \rightleftarrows CH_3+H_2O$. Experimental results from this study showed that a simple H_2/CO mixture is not fully adequate to represent a real syngas. This observation was confirmed by modeling τ_{ign} for BS and Biosyn mixtures in air at high pressures and intermediate temperatures using the chemical kinetics model.

To help in model validation and in designing efficient gas turbines, ignition delay times of a realistic coal-derived syngas mixture (containing $CO/H_2/CH_4/CO_2/H_2O$ and O_2) diluted in Ar were measured between 1.7 and 32 atm in a shock tube. Results showed a significant effect of pressure on the ignition delay time due to the hydrogen chemistry that dominates the ignition kinetics over these conditions. Compared to a baseline mixture with the same CO/H_2 ratio, small variations in τ_{ign} were observed with the realistic syngas mixture, but only for certain conditions. A small decrease in the ignition delay time was observed at around 1.7 atm over the range of temperature investigated. This decrease was relatively important above 1200 K at around 13 atm. For the highest pressure investigated, a small increase in τ_{ign} was observed between the Csyn and the BS mixtures above 1200 K. This increase in τ_{ign} was predicted by recent models from the literature, whereas the decrease in τ_{ign} above 1200 K at 13 atm for the Csyn mixture was not well predicted by the models. Overall, the models from Metcalfe et al. (2013) and Li et al. (2007) were able to predict the experimental trends and the ignition delay times with the greatest accuracy over the whole range of conditions. The comparison between the results of the present study and measurements for a biomass-derived syngas [Mathieu et al., 2013], which contains a

higher concentration of methane, showed an important difference in τ_{ign}, where ignition delay times are notably longer for the bio-derived syngas. This study exhibited the importance of the mixture composition on the ignition delay time, especially for pressures of interest for gas turbines, around 13 atm. Hydrocarbons larger than methane were not considered in this study, due to their low reported concentrations in the literature. However, recent computations showed the importance of these hydrocarbons on fundamental combustion properties at gas turbine conditions. Experiments with hydrocarbons larger than methane would therefore be necessary to further validate detailed kinetics models.

Due to the large variety of feedstock and production methods, the nature (beside H_2 and CO) and proportion of components entering into the composition of syngas can vary significantly. To investigate how the variation in the hydrocarbon concentration can induce changes in the combustion properties (and introduce design and operation issues for gas turbines), the ignition delay time and laminar flame speed of various mixtures containing hydrocarbons, at various temperature, pressure, and equivalence ratio conditions, were computed. Results showed some important effects from hydrocarbon addition on the ignition delay time, where the ratio between CO and H_2 was found to be of relatively small significance. Except for C_2H_2, the addition of hydrocarbons increased the ignition delay time under the conditions investigated. This increase in the ignition delay time varies with the nature of the hydrocarbon, its concentration, and the pressure and temperature range. At 10 and 35 atm, the ignition delay time is increased only on the high-temperature side of the curve, whereas the ignition delay time is increased on the entire range of temperature at 1 atm, even though a stronger decrease in the reactivity is observed below 1000 K. If methane and ethylene have demonstrated a greater inhibiting effect on the ignition delay time, ethane was found to be of larger importance for the flame speed with regards to its concentration. These effects of hydrocarbon addition are due to reactions of these hydrocarbons and/or their radicals with the radical H, hence competing with the most important promoting reaction $H + O_2 \rightleftarrows OH + O$ in these conditions.

The baseline coal- and bio-derived syngases, both neat and doped with hydrocarbons, have been compared to averaged syngases. For each type of these averaged syngases, a relatively important difference in the ignition delay time was observed when put side by side with the corresponding baseline mixtures (bBiosyn and bCoalsyn). Great variations in the flame speeds were also observed, due to both chemical and flame temperature effects. These results indicate that the baseline CO/H_2 mixtures generally studied are not in many cases good candidates to study syngas combustion at actual gas turbine conditions (mostly in terms of fuel-air concentration and pressure). Experimental results are still needed to confirm and possibly improve the model predictions for realistic syngas combustion under these gas turbine conditions.

Comparisons amongst models from the literature exhibit some noticeable differences in the flame speed and ignition delay time. It is however worth mentioning that these differences are more important for the neat H_2/CO mixture than for more complex and realistic mixtures, such as with hydrocarbons for example. For the latter case, ignition delay times are relatively close between any two mechanisms tested whereas larger differences can be observed for the maximum flame speed.

Turbulent Flame Speed Measurements

A parametric study was conducted to determine the optimum impeller design capable of generating homogeneous and isotropic turbulence inside a closed, fan-stirred, cylindrical flame speed vessel. Additionally, the ability to control the turbulence parameters, u′ and L_T, through geometric modification of the impeller was also evaluated. A 1:1 scale Plexiglas model of the flame bomb was fabricated to allow non-intrusive optical flow field characterization. Four impellers were arranged symmetrically along the central circumference of the cylinder. The impact of blade pitch angle and the number of blades on the impeller were assessed. Digital PIV was used to accurately measure the turbulence statistics, and turbulent intensity levels between 1.2 and 1.7 m/s with negligible mean flow (<10% u′) were attained. Much variation in the intensity levels was not observed for the different impellers. The velocity PDFs of the 3-bladed impellers closely followed a Gaussian profile. The acceptable ranges for homogeneity and isotropy ratios were set in a narrow range between 0.9 and 1.1 (±10% ideal case). The homogeneity of the flow field showed only a slight dependency on the impeller geometry with the fans arranged in a central-symmetric configuration. However, the isotropy ratio was sensitive to the geometry, and a clear deviation from isotropic turbulence was observed for the prototype with higher number of blades (6-bladed fans). Two-point velocity correlations in the longitudinal and lateral directions were also computed to further validate the isotropic nature of the flow fields. The inertial subrange with a -5/3 slope was observed in the energy spectra. The turbulent kinetic energy dissipation rates as estimated from the energy spectra were used to determine the integral length scales. The integral length scales computed from the scaling law agreed well with those obtained by integrating 2-point velocity correlation curves. It was concluded that L_T can be changed by varying the blade pitch angle while still maintaining near-HIT conditions. Hence, two sets of three-bladed impellers with different blade pitch angles (20˚, 60˚) will be used interchangeably inside the final turbulent flame bomb. LDV validation and extension of these results to higher fan speeds are proposed as a part of the future work.

Global displacement speeds of methane and a 50:50 blend (by volume) of H_2:CO were measured in the recently developed, fan-stirred, constant-volume flame speed vessel. A wide range of equivalence ratios that are relevant to practical applications such as gas turbine combustion were studied. The turbulent flame propagation rates were estimated using high-speed schlieren photography whose flame surfaces are characterized with a reaction progress variable, $\bar{c}$ = 0.1. Four widely used numerical combustion models were validated with measurements from this study. The Kerstein pair exchange model and the Zimont burning velocity model agreed well with the experimental data. Additionally, it was shown that S_T/S_L was higher for syngas than methane for the same value of u'/S_L, which is indicative of the strong preferential diffusion effect of hydrogen in distorting the flame surface thereby increasing the turbulent propagation rates. Extension of these results to higher intensity levels and to higher-hydrogen-content fuels is proposed as a part of future work.

OH Absorption Diagnostic for Chemical Kinetics

The hydroxyl (OH) radical is a common intermediate species in any hydrogen- or hydrocarbon-based flame. Investigating OH at elevated temperatures and pressures is not a trivial task, and many considerations must be made to fully study the molecule. Shock tubes can provide the experimenter with a wide range of temperatures and pressures to investigate a variety of

combustion characteristics including, but not limited to, OH kinetic profiles. Described in this dissertation is the diagnostic used to measure OH within a shock tube using UV absorption spectroscopy from an enhanced UV Xenon lamp passed through a spectrometer. OH absorption was made over a narrow range of wavelengths around 309.551 nm within the widely studied OH X→A ground vibrational transition region. Experiments have been performed in the shock-tube facility at Texas A&M University using this OH absorption diagnostic. A calibration mixture of stoichiometric H_2/O_2 diluted in 98% argon by volume was tested initially and compared with a well-known hydrogen-based kinetics mechanism to generate an absorption coefficient correlation. This correlation is valid over the range of conditions observed in the experiments at two pressures near 2 and 13 atm and temperatures from 1182 to 2017 K. In general, the agreement between the hydrogen kinetics model and the measured OH time histories is quite good, although some improvement can be made for times longer than the main ignition event.

REFERENCES

Abdel-Gayed R. G., Al-Khishali K. J., and Bradley, D. (1984) Turbulent burning velocities and flame straining in explosions. *Proc R. Soc. Lond. Ser-A* 391, pp. 393-414.

Aldredge, R. C. (1997) On the structure of turbulent premixed flame in high-pressure combustors. *Int Comm Heat Mass Transfer* 24:565-568.

Alzueta, M. U., Bilbao, R., and Glarborg, P. (2001) *Combust. Flame*, Vol. 127, pp. 2234–2251.

Atkinson, R., D. L. Baulch, R. A. Cox, R. F. Hampson Jr., J. A. Kerr, M. J. Rossi, J. Troe (1997) *J. Phys. Chem. Ref. Data*, Vol. 26, pp. 1329–1499.

Aul, C. J., Metcalfe, W. K., Burke, S. M., Curran, H. J., and Petersen, E. L. (2013) *Combustion and Flame*, Vol. 160, pp. 1153–1167.

Aung K. T., Hassan M. I., and Faeth G. M. (1997) "Flame Stretch Interactions of Laminar Premixed Hydrogen/Air Flames at Normal Temperature and Pressure," *Combustion and Flame*, Vol. 109, pp.1-24.

Barrett, A. B. (2009) "Measurement of Water Vapor Concentration Using Tunable Diode Laser Absorption Spectroscopy," M.S. thesis, Texas A&M University, College Station, Texas, USA.

Barringer M. (2001) Design and benchmarking of a combustor simulator relevant to gas turbine engines. MS Thesis, Virginia Polytechnic Institute and State University, USA.

Baulch, D. L., Bowman, C. T., Cobos, C. J. *et al*. (2005) *J. Phys. Chem. Ref. Data* 34, pp. 757-1397.

Binoist, M., B. Labegorre, F. Monnet, P. D. Clark, N. I. Dowling, M. Huang, D. Archambault, E. Plasari, and P.-M. Marquaire (2003) *Ind. Eng. Chem. Res*., Vol. 42, pp. 3943-3951.

Borghi, R. (1985) *On the Structure and Morphology of Turbulent Premixed Flames, Recent Advances in the Aerospace Science*, Plenum, New York, 1985, p. 117-138.

Bouvet N., Chauveau C., Gokalp I., and Halter F. (2011) "Experimental studies of the fundamental flame speeds of syngas (H_2/CO)/air mixtures," *Proceedings of the Combustion Institute*, Vol. 33, pp. 913-920.

Bowman, C. T. and Dodge, L. G. (1977) *Proceed. Combust. Instit*., Vol. 16, pp. 971–982.

Bozzelli, J. W., Chang, A., and Dean, A. M. (1994) *Proceed. Combust. Inst*. 25, pp. 965-974.

Bradley, J. N. and Dobson, D. C. (1967) *J. Chem. Phys.*, Vol. 46, pp. 2872-2875.

Bradley, J. N. and Dobson, D. C. (1967) *J. Chem. Phys*., Vol. 46, pp. 2865-2871.

Bradley J. N., Butlin R. N., and Lewis D. (1968). *Trans. Faraday Soc*. 64, 71-78.

Bradley, D., Lawes, M., and Mansour, M. S. (2011) *Combust. Sci*., Vol. 158, pp. 123-138.

Brown J.M., McLean I.C., Smith D. B., and Taylor S. C. (1996) "Markstein Lengths of CO/H_2/Air Flames, Using Expanding Spherical Flames," *Proceedings of the Combustion Institute*, Vol. 26, pp. 875-881.

Bull D. C. (1968) *Combust Flame* 12, 603-610.

Burke M. P., Qin X., Ju Y., and Dryer F. L. (2007) "Measurements of hydrogen syngas flame speeds at elevated pressures," 5th U.S. Combustion Meeting.

Burke M. P., Chen Z., Ju Y., and Dryer F. L. (2009) "Effect of Cylindrical Confinement on the Determination of Laminar Flame Speeds using Outwardly Propagating Flames," *Combust Flame*, Vol. 156:771-779.

Burke, M. P., Chaos, M., Ju, Y., Dryer, F. L., and Klippenstein, S. J. (2012) *Int. J. Chem. Kinet*., Vol. 44, pp. 444–474.

Campbell A, Goldmeer J, Healy T, Washam R, Moliere M, and Citeno J. (2008) "Heavy Duty Gas Turbine Fuel Flexibility," ASME Conf. Proc. GT2008-51368.

Cerru, F. G., Kronenburg, A., and Lindstedt, R. P. (2005) *Proc. Combust. Inst*., Vol. 30, pp. 1227-1235.

Cerru, F. G., Kronenburg, A., and Lindstedt, R. P. (2006) *Combust. Flame*, Vol. 146, pp. 437-455.

Chacartegui, R., Torres, M., Sánchez, D., Jiménez, F., Muñoz, A., and Sánchez, T. (2011) *Fuel Processing Technology* 92, pp. 213–220.

CHEMKIN-PRO 15101 (2010) Reaction Design: San Diego.

Cullis, C. F. and Mulcahy, M. F. R. (1972) *Combust. Flame*, Vol. 18, pp. 225-292.

Dagaut, P., Lecomte, F., Mieritz, J., and Glarborg, P. (2003) *Int. J. Chem. Kinet*., Vol. 35, pp. 564–575.

Dagaut, P., Mathieu, O., Nicolle, A., and Dayma, G. (2005) *Combust. Sci. and Tech*. 177, pp. 1767-1791.

Dagaut P. and Nicolle A. (2005) *Proc. Combust. Inst*., Vol. 30, pp. 1211-1218.

Dagaut P., Glarborg P., and Alzueta M. U. (2008) *Prog. Energy Combust. Sci*., Vol. 3, 1-46.

Dahoe A. E. (2005) “Laminar Burning Velocities of Hydrogen-Air Mixtures from Closed Vessel Gas Explosions,” *J Loss Prevent Proc*., Vol. 18:152-166.

Das, A. K., Kumar, K., and Sung, C.-J. (2011) *Combust. Flame*, Vol. 158, pp. 345-353.

Davidson, D. F., Kohse-Hoinghaus, K., Chang, A. Y., and Hanson, R. K. (1990) *Int. J. Chem. Kinet.* 22, pp. 513-535.

Dayma, G. and Dagaut, P. (2006) *Combust. Sci. and Tech*., Vol. 178, pp. 1999-2024.

D’Errico G, Onorati A, and Ellgas S. (2008) “1D Thermo-Fluid Dynamic Modelling of an SI Single-Cylinder H_2-Engine with Cryogenic Port Injection,” *Int J Hydrogen Energy*, Vol. 33:5829-41.

de Vries, J. D. (2009) A study on spherical expanding flame speeds of methane, ethane and methane/ethane mixtures at elevated pressures. PhD Dissertation, Texas A&M University, USA.

de Vries J., Lowry W., Serinyel Z., Curran H., and Petersen E. (2011) “Laminar flame speed measurements of dimethyl ether in air at pressures up to 10 atm,” *Fuel*, 90(1), pp. 331-338.

Dong C., Zhou Q., Zhao Q., Zhang Y., Xu T., and Hui S. (2009) “Experimental study on the laminar flame speed of hydrogen/carbon monoxide/air mixtures,” *Fuel*, Vol. 88, pp. 1858-1863.

Dowdy D. R., Smith D. B., Taylor S. C., and Williams A. (1990) “The use of expanding spherical flames to determine burning velocities and stretch effects in hydrogen/air mixtures,” *Proceedings of the Combustion Institute*, Vol. 23, pp. 325-332.

Drummond L. J. (1972) *Combust. Sci. Technol*., Vol. 5, pp. 175-182.

Duclos, J. M. and Veynante, D. (1993) *Combust. Flame*, Vol. 95, pp. 101- 117.

Duynslaegher C., Contino F., Vandooren J., and Jeanmart H. (2012) *Combust. Flame*, Vol. 159, pp. 2799-2805.

Egolfopoulos F. N. and Law C. K. (1990) “An experimental and computational study of the burning rates of ultra-lean to moderately-rich $H_2/O_2/N_2$ laminar flames with pressure variations,” *Proceedings of the Combustion Institute*, Vol. 23, pp. 333-340.

Fansler, T. D. and Groff, E. G. (1990) Turbulence characteristics of a fan-stirred combustion vessel. *Combust Flame* 80:350-354.

Faravelli, T., Frassoldati, A., and Ranzi, E. (2003) *Combust. Flame* 132, pp. 188-207.

Frenklach, M., Lee, J. H., White, J. N., and Gardiner, W. C. (1981) *Combust. Flame*, Vol. 41, pp. 1–16.

Friedl, R. R., Brune, W. H., and Anderson, J. G. (1985) *J. Phys. Chem*., Vol. 89, pp. 5505-5510.

Fujii N., Miyama H., Koshii M., and Asaba T. (1981). *Proceed Combust. Instit*., Vol. 18, pp. 873-883.

Garland, N. L. (1998) *Chem. Phys. Letters*, Vol. 290, pp. 385-390.

Gerke U, Steurs K, Rebecchi P, and Boulouchos K. (2010) "Derivation of Burning Velocities of Premixed Hydrogen/Air Flames at Engine Relevant Conditions using Single-Cylinder Compression Machine with Optical Access," *Int J Hydrogen Energy*, Vol. 35:2566-77.

Glarborg, P., Kubel, D., Dam-Johansen, K., Chiang, H.-M., and Bozzelli, J. W. (1996) *Int. J. Chem. Kinet*., Vol. 28, pp. 773–790.

Glarborg, P. (2007) *Proceed. of the Combust. Instit*., Vol. 31, pp. 77–98.

Glarborg, P. and Marshall, P. (2013) *Int. J. Chem. Kinet*., Vol. 45, pp. 429–439.

Göransson, K., Söderlind, U., He, J., and Zhang, W. (2011) *Renewable and Sustainable Energy Reviews* 15, pp. 482-492.

Hall, J. M. and Petersen, E. L. (2004) AIAA Paper No 2004-4164.

Hall, J. M. and Petersen, E. L. (2006) *Int. J. Chem. Kinet*. 38, pp. 714–724.

Hassan M. I., Aung K. T., and Faeth G. M. (1997) "Properties of laminar premixed CO/H_2/Air flames at various pressures," *Journal of Propulsion and Power*, Vol. 13, pp. 239-245.

Hawboldt, K. A. (1998) "Kinetic modelling of key reactions in the modified Claus plant front end furnace," Ph.D. thesis, University of Calgary, Calgary, Alberta, Canada.

Hawboldt, K. A., Monnery, W. D., and Svrcek, W. Y. (2000) *Chem. Engineer. Sci*., Vol. 55, pp. 957-966.

Healy, D., Donato, N. S., Aul, C. J., Petersen, E. L., Zinner, C. M., Bourque, G., and Curran, H. J. (2010) *Combust. Flame*, Vol. 157, pp. 1540-1551.

Herzler, J. and Naumann, C. (2008) "Shock Tube Study of the Ignition of Lean CO/H_2 Fuel Blends at Intermediate Temperatures and High Pressure," *Combust. Sci. and Tech*., 180, pp. 2015-2028.

Herzler, J., Herbst, J., Kick, T., Naumann, C., Braun-Unkhoff, M., and Riedel, U. (2012) "Alternative Fuels Based on Biomass: an Investigation of Combustion Properties of Product Gases," Proceedings of ASME Turbo Expo 2012, GT2012, June 11-15, Copenhagen, Denmark, paper GT2012-69282.

Hidaka, Y., Takuma, H., and Suga, M. (1985a) *J. Phys. Chem*. 89, pp. 4903–4905.

Hidaka, Y., Takuma, H., and Suga, M. (1985b) *Bull. Chem. Soc. Jpn*. 58, pp. 2911–2916.

Higman, C. and Van der Burt, M. (2008) *Gasification*, Gulf Professional Publishing Title, 2nd edition, p 170.

Hong, Z., Davidson, D. F., and Hanson, R. K. (2011) 158, pp. 633-644.

Hu E., Huang Z., He J., Miao H. (2009) "Experimental and numerical study on laminar burning velocities and flame instabilities of hydrogen-air mixtures at elevated pressures and temperatures," *International Journal of Hydrogen Energy*, Vol. 34, pp. 8741-8755.

Hughes K. J., Tomlin A. S., Hampartsoumian E., Nimmo W., Zsély I. G., Ujvári M., Turányi T., Clague A. R., and Pilling M. J. (2001) *Combust. Flame*, Vol. 124, pp. 573-589.

Hughes, K. J., Turányi, T., Clague, A., and Pilling, M. J. (2001) *Int. J. Chem. Kinet*., Vol. 33, pp. 513-538, associated with the SOx chemistry update (v.5.2) available on http://garfield.chem.elte.hu/Combustion/sox.htm.

Javoy, S., Mevel, R., and Paillard, C. E. (2009) *Int. J. Chem. Kinet*. 41, pp. 357-375.

Kéromnès, A., Metcalfe, W. K., Donohoe, N., Curran, H. J., and Pitz, W. J. (2011) "Detailed Chemical Kinetic Model for H_2 and H_2/CO (Syngas) Mixtures at Elevated Pressure," 7th US National Meeting of the Combustion Institute, March 21-23, Atlanta.

Kéromnès A., Metcalfe W. K., Heufer K.A., Donohoe N., Das A.K., Sung C.J., Herzler J., Naumann C., Griebel P., Mathieu O., Krejci M.C., Petersen E.L., Pitz W.J., and Curran H. J. (2013) "An Experimental and Detailed Chemical Kinetic Modeling Study of Hydrogen and Syngas Mixtures at Elevated Pressures," *Combust Flame*.

Kerstein, A. R. (1988) *Proc. Combust. Inst*., Vol. 21, pp. 1281-1289.

Kim W. W., Menon S., and Mongia H. C. (1999) Large eddy simulation of a gas turbine combustor flow. *Combust Sci Tech* 143:25-62.

Kohse-Höinhaust K., Davidson D. F., Chang A. Y., and Hanson R. K. (1989) *J. Quantitative Spectroscopy and Radiative Transfer*, Vol. 42, pp. 1 - 17.

Konnov, A. A. (2009) *Combust. Flame* 156, pp. 2093-2105.

Kosarev, I. N., Starikovskaia, S. M., and Starikovskii, A., Yu. (2007) *Combust. Flame* 151, pp. 61–73.

Kostkowski, H.J., and Bass, A.M. (1956) "Slit function effects in the direct measurement of absorption line half-widths and intensities," *Journal of the Optical Society of America*, Vol. 46, 1060-1064.

Krejci M., Vissotski A., Lowry W., Ravi S., and Petersen E. (2011) "Development of a High-Temperature and High-Pressure Vessel for Laminar Flame Speed Measurements," 7th U.S. National Technical Meeting.

Krejci M. C, Vissotski A. J, Ravi S, Metcalfe W. J, Keromnes A, Curran H. J, and Petersen E. L. (2012) "Laminar Flame Speeds of Moist Syngas Fuel Blends at Elevated Pressures and Temperatures," Spring Technical Meeting of the Central States Section of the Combustion Institute, Paper 12S-02, Ohio, USA.

Krejci, M., Mathieu, O., Vissotski, A. J., Ravi, S., Sikes, T. G., Petersen, E. L., Kéromnès, A., Metcalfe, W., and Curran, H. J. (2012) "Laminar Flame Speed and Ignition Delay Time Data for the Kinetic Modeling of Hydrogen and Syngas Fuel Blends," Proceedings of ASME Turbo Expo 2012, GT2012, June 11-15, Copenhagen, Denmark.

Krejci M.C, Mathieu O, Vissotski A.J, Ravi S, Sikes T.G, Petersen E.L, et al. (2013) "Laminar Flame Speed and Ignition Delay Time Data for the Kinetic Modeling of Hydrogen and Syngas Fuel Blends," *J Eng Gas Turb Power* (2013); also: ASME Paper GT 2012-69290.

Kwon O. C. and Faeth G. M. (2001) "Flame/stretch interactions of premixed hydrogen-fueled flames: measurements and predictions," *Combustion and Flame*, Vol. 124, pp. 590-610.

Lacy B, Ziminisky W, Lipinski J, Varatharajan B, Yilmaz E, and Brumberg J. (2008) "Low Emission Combustion System Development for the GE Energy High Hydrogen Turbine Program," ASME Conf. Proc., GT2008-50823.

Lamoureux N., Djebaili-Chaumeix N., and Paillard C. E. (2003) "Laminar flame velocity determination for H_2-air-He-CO_2 mixtures using the spherical bomb method," *Experimental Thermal and Fluid Science*, Vol. 27, pp.385-393.

Li, J., Zhao, Z. W., Kazakov, A. and Dryer, F. L. (2004) *Int. J. Chem. Kinet.*, Vol. 36, pp. 566-575.

Lieuwen T., McDonell V., Santavicca D., and Sattelmayer T. (2008) Burner development and operability issues associated with steady flowing syngas fired combustors. *Combust Sci Tech* 180:1167-1190.

Lieuwen T, McDonnell V, Petersen E, and Santavicca D. (2008) "Fuel Flexibility Influences on the Premixed Combustor Blowout, Flashback, Autoignition, and Stability," *J Eng Gas Turb Power*, Vol. 130:011506.

Lipatnikov, A. N. and Chomiak, J. (2000) Transient and geometrical effects in expanding turbulent flames. *Combust Sci Technol* 154:75-117.

Lipatnikov, A. N. and Chomiak, J. (2002) *Prog. Energy Combust. Sci*., Vol. 28, pp. 1-74.

Liu, C. C., Shy, S. S., Peng, M. W., Chiu, C. C., and Dong, Y. C. (2012) *Combust. Flame*, Vol. 159, pp. 2608-2619.

Lowry W., de Vries J., Krejci M., Serinyel Z., Metcalfe W., Curran H., Petersen E., and Bourque G. (2011) "Laminar Flame Speed Measurements and Modeling of Pure Alkanes and Alkane Blends at Elevated Pressures," *Journal of Engineering for Gas Turbines and Power*, 133 (9).

Lu, C. W., Wu, Y. J., Lee, Y. P., Zhu, R. S., and Lin, M. C. (2004) *J. Chem. Phys*., Vol. 121, pp. 8271-8278.

Markstein G. H. (1964) *Non-Steady Flame Propagation*, Pergamon, New York.

Mathieu, O., Levacque, A., and Petersen, E. L. (2012) "Effects of N_2O Addition on the Ignition of H_2-O_2 Mixtures: Experimental and Detailed Kinetic Modeling Study," *International Journal of Hydrogen Energy*, Vol. 37, pp. 15393-15405.

Mathieu O., Levacque A., and Petersen E. L. (2013) *Proceed. Combust. Instit*., Vol. 34, pp. 633-640.

Mathieu, O., Petersen, E. L., Heufer, A., Donohoe, N., Metcalfe, W., Curran, H. J., Güthe, F., and Bourque, G. (2013a) *J. Engineer. for Gas Turbines and Power*, Vol. 136, pp. 011502.

Mathieu, O., Kopp, M. M., and Petersen, E. L. (2013b) *Proceed. Combust. Instit*., Vol. 34, pp. 3211-3218.

Mathieu, O., Deguillaume, F., and Petersen, E. L. (2014) *Combustion and Flame*, Vol. 161, pp. 23-36.

McLean I. C., Smith D. B., and Taylor S.C. (1994) "The use of carbon monoxide/hydrogen burning velocities to examine the rate of the CO + OH reaction," *Proceedings of the Combustion Institute*, Vol. 25, pp. 749-757.

Mendiara T. and Glarborg P. (2009) *Combust. Flame*, Vol. 156, pp. 1937-1949.

Metcalfe, W. K., Burke, S. M., Ahmed, S. S., and Curran, H. J. (2013) *Int. J. of Chem. Kinetics*, Vol. 45, pp. 638-675.

Mével, R., Javoy, S., Lafosse, F., Chaumeix, N., Dupré, G., and Paillard, C. E. (2009) *Proceed. Combust. Inst.* 32, pp. 359–366.

Mihelcic, D. and Schindle, R. N. (1970) *Berichte der Bunsen-Gesellschaft für Physikalische Chemie*, Vol. 74, pp. 1280-1288.

Miller J. and Bowman C. (1989) *Prog. Energy Combust*. Sci., Vol. 15, pp. 287-338.

Miller, J. A., Pilling, M. J., and Troe, J. (2005) *Proceed. Combust. Inst*., Vol. 30, pp. 43–88.

Miyama H. and Endoh R. (1967a) *Combust. Flame*, Vol. 11, pp. 359-360.

Miyama H. and Endoh R. (1967b) *J. Chem. Phys*., Vol. 46, pp. 2011-2012.

Miyama H. (1968a) *Bull. Chemical Society Japan*, Vol. 41, pp. 1761-1765.

Miyama H. (1968b) *J. Chem. Phys*., Vol. 48, pp. 1421-1422.

Moffat R. J. (1988) "Describing uncertainties in experimental results," *Experimental Thermal and Fluid Science*, Vol. 1, pp. 3-17.

Molière M. (2000) "Stationary Gas Turbines and Primary Energies: A Review of Fuel Influence on Energy and Combustion Performances," *Int J Therm. Sci*., Vol. 39:141-172.

Montoya, A., Sendt, K., and Haynes, B. S. (2005) *J. Phys. Chem. A*, Vol. 109, pp. 1057-1062.

Mueller, M. A., Yetter, R. A., and Dryer, F. L. (2000) *Int. J.Chem. Kinet.* 32, pp. 317-339.

Nagali, V., Davidson, D. F., and Hanson, R. K. (2000) *J. Quant. Spectrosc. Radiat. Transfer*, Vol. 64, pp. 651-655.

Natarajan J., Nandula S., Lieuwen T., and Seitzman J. (2005) "Laminar flame speeds of synthetic gas fuel mixtures," ASME Paper GT2005-68917.

Ó Conaire M, Curran H, Simmie J, Pitz W, and Westbrook C. (2004) "A Comprehensive Modeling Study of Hydrogen Oxidation," *Int J Chem Kinet*., Vol. 36:603–22.

Pang, G. A., Davidson, D. F., and Hanson, R. K. (2009) *Proceed. Combust. Instit*., Vol. 32, pp. 181–188.

Pareja J., Burbano H. J., and Ogami Y. (2010) "Measurements of the Laminar Burning Velocity of Hydrogen-Air Premixed Flames," *Int J Hydrogen Energy*, Vol. 35: 1812-1818.

Parks, J., Giles, N. D., Moore, J., and Lin, M. C. (1998) *J. Phys. Chem. A*, Vol. 102, pp. 10099-10105.

Peng, J. P., Hu, X. H., and Marshall, P. (1999) *J. Phys. Chem. A*, Vol. 103, pp. 5307-5311.

Peschke, W. T. and Spadaccini, L. J. (1985) Determination of Autoignition and Flame Speed Characteristics of Coal Gases Having Medium Heating Values, Report No. EPRI AP-4291, Electric Power Institute.

Peters, N., J. (1999) *Fluid Mech.*, Vol. 384, pp. 107-132.

Petersen E. L., Rickard M. J. A., Crofton M. W., Abbey E. D., Traum M. J., and Kalitan D. M. (2005) *Meas. Sci. Technol*., Vol. 16, pp. 1716-1729.

Petersen, E. L., Kalitan, D, M., Barrett, A. B. et al. (2007) *Combust. Flame*, Vol. 149, pp. 244–247.

Prathap C., Ray A., and Ravi M. R. (2008) "Investigation of nitrogen dilution effects on the laminar burning velocities and flame stability of syngas fuel at atmospheric condition," *Combustion and Flame*, Vol. 155, pp. 145-160.

Pratt D. T. and Starkman E. S. (1969) *Proceed. Combust. Instit*., Vol. 12, pp. 891-899.

Rasmussen, C. L., Rasmussen, A. E., and Glarborg, P. (2008) *Combust. Flame*, Vol. 154, pp. 529–545.

Ravi, S., Peltier, S. J., and Petersen, E. L. (2013) "Analysis of the Impact of Impeller Geometry on the Turbulent Statistics inside a Fan-Swirled, Cylindrical Flame Speed Vessel using PIV," *Experiments in Fluids*, Vol. 54, pp. 1424.

Ravi, S., Morones, A., and Petersen, E. L. (2013) AIAA Paper 2013-1184.

Reynolds W. C. (1986) "The Element Potential Method for Chemical Equilibrium Analysis: Implementation in the Interactive Program STANJAN," Department of Mechanical Engineering, Stanford University.

Richards, G. A., McMillian, M. M., Gemmen, R. S., Rogers, W. A., and Cully, S. R. (2001) *Progress in Energy and Combust. Science* 27, pp. 141–169.

Ronney, P. D. (1995) in: Buckmaster, J. D., Takeno, T., (Eds.), *Modeling in Combustion Science, Lecture Notes in Physics*, Springer-Verlag, Berlin, p. 3-20.

Roose T. R., Hanson R. K., and Kruger C. H. (1981) *Proceed. Combust. Instit*., Vol. 18, pp. 854-862.

Ross, P. J. (1996) *Taguchi Techniques for Quality Engineering*, McGraw-Hill, New York, N.Y.

Roth, P., Löhr, R., and Barner, U. (1982) *Combust. Flame*, Vol. 45, pp. 273-285.

Salimian S., Hanson R. K., and Kruger C. H. (1984) *Combust. Flame*, Vol. 56, pp. 83-95.

Sendt, K., Jazbec, M. and Haynes, B. S. (2002) *Proceed. Combust. Instit*., Vol. 29, pp. 2439-2446.

Settles G. S. (2006) *Schlieren and Shadowgraph Techniques*, Springer, Heidelberg, Germany.

Shiina, H., Oya, M., Yamashita, K., Miyoshi, A. and Matsui, H. (1996) *J. Phys. Chem*., Vol. 100, pp. 2136-2140.

Sivaramakrishnan, R., Brezinsky, K., Dayma, G., and Dagaut, P. (2007) *Phys. Chem. Chem. Phys.* 9, pp. 4230-4244.

Slack, M. W. and Grillo, A. R. (1977) "Investigation of hydrogen-air ignition sensitized by nitric oxide and by nitrogen dioxide," NASA Contract report No. NASA CR-2896, Grumman Aerospace Corp.

Slack, M. and Grillo, A. (1978) *Combust. Flame*, Vol. 31, pp. 275-283.

Slack, M. W. and Grillo, A. R. (1981) *Combust. Flame*, Vol. 40, pp. 155-172.

Smith G. P., Golden D. M., Frenklach M., Moriarty N. W., Eiteneer B., Goldenberg M., C. Bowman T., Hanson R. K., Song S., Gardiner W. C., Jr., Lissianski V. V., and Qin Z. (1999) http://www.me.berkeley.edu/gri_mech/.

Sun H., Yang S. I., Jomaas G., and Law C. K. (2007) "High-pressures laminar flame speeds and kinetic modeling of carbon monoxide/hydrogen combustion," *Proceedings of the Combustion Institute*, Vol. 31, pp. 439-446.

Takeyama T. and Miyama H. (1965a) *J. Chem. Phys*., Vol. 42, pp. 3737-3738.

Takeyama T. and Miyama H. (1965b) *Bull. Chemical Society Japan*, Vol. 38, pp. 1670-1674.

Takeyama T. and Miyama H. (1966a) *Bull. Chemical Society Japan*, Vol. 39, pp. 2352-2355.

Takeyama T. and Miyama H. (1966b) *Bull. Chemical Society Japan*, Vol. 39, pp. 2609-2612.

Takeyama T. and Miyama H. (1967) *Proced. Combust. Instit*., Vol. 11, pp. 845-852.

Troe, J. (1983) "Theory of the thermal unimolecular reactions in the fall-off range. I. Strong collision rate constants," *Berichte der Bunsengesellschaft für physikalische Chemie*, Vol. 87, pp. 161-169.

Tsang, K. W. and Lifshitz, A. (2001) "Single pulse shock tube," in: *Handbook of Shock waves, Part III - Chemical Reactions in Shock Waves and Detonations*, Academic Press, New York, pp. 107–210.

Tse S.D, Zhu D.L, and Law C. K. (2000) "Morphology and Burning Rates of Expanding Spherical Flames in H_2/O_2/Inert Mixtures up to 60 Atmospheres," *Proc. Combust Inst*., Vol. 28: 1793-00.

Vagelopoulos C. M., Egolfopoulos F. N., and Law C. K. (1994) "Further considerations on the determination of laminar flame speeds with the counterflow twin-flame technique," *Proceedings of the Combustion Institute,* Vol. 25, pp. 1341-1347.

Venkateswaran, P., Marshall, A., Shin, D. H., Noble, D., Seitzman, J., and Lieuwen, T. (2011) Measurements and analysis of turbulent consumption speeds of H_2/CO mixtures. *Combust Flame* 158:1602-1614.

Verhelst S. and Sierens R. (2003) "A Laminar Burning Velocity Correlation for Hydrogen/Air Mixtures Valid at Spark-Ignition Engine Conditions," ASME Conf. Proc.; ICES2003-555: 35-43.

Verhelst S., Woolley R., Lawes M., and Sierens R. (2005) "Laminar and Unstable Burning Velocities and Markstein Lengths of Hydrogen-Air Mixtures at Engine-Like Conditions," *Proc. Combust Inst*., Vol. 30: 209-216.

Verhelst S. and Wallner T. (2009) "Hydrogen-Fueled Internal Combustion Engines," *Prog Energy Combust Sci.,* Vol. 35:490-527.

Verhelst S, T'Joen C, Vancoillie J, and Demuynck J. (2011) "A Correlation for the Laminar Burning Velocity for Use in Hydrogen Spark Ignition Engine Simulation," *Int J Hydrogen Energy*, Vol. 36:957-74.

Walton, S. M., He, X., Zigler, B. Z., and Wooldridge, M. S. (2007) "An Experimental Investigation of the Ignition Properties of Hydrogen and Carbon Monoxide Mixtures for Syngas Turbine Applications," *Proc. Combust. Inst*. 31, pp. 3147-3154.

Wang, H., You, X., Joshi, A. V. et al. (2007) USC Mech Version II. High-Temperature Combustion Reaction Model of H2/CO/C1-C4 Compounds, May, available at http://ignis.usc.edu/USC_Mech_II.htm.

Wang, J., Zhang, M., Huang, Z., Kudo, T., and Kobayashi, H. (2013) *Combust. Flame*, Vol. 160, pp. 2434-2441.

White C. M, Steeper R. R, Lutz A. E. (2006) "The Hydrogen Fueled Internal Combustion Engine: A Technical Review," *Int. J Hydrogen Energy*, Vol. 31:1292-05.

Woiki, D. and Roth, P. (1994) *J. Phys. Chem*., Vol. 98, pp. 12958-12963.

Wu, M. S., Kwon, S., Driscoll, J. F., and Faeth, G. M. (1991) *Combust. Sci. Tech*., Vol. 78, pp. 69-96.

Wu F, Kelley A. P, Tang C, Zhu D, and Law C. K. (2011) "Measurement and Correlation of Laminar Flame Speeds of CO and C2 Hydrocarbons with Hydrogen Addition at Atmospheric and Elevated Pressures," *Int J Hydrogen Energy*, Vol. 36:13171-80.

Xu D., Tree D. R., and Lewis R. S. (2011) *Biomass and Bioenergy*, Vol. 35, pp. 2690-2696.

Zhou, C. (2009) "Kinetic study of the oxidation of Hydrogen Sulfide," Ph.D. thesis, The University of Sydney, Sydney, Australia.

Zhou, C. R., Sendt, K., and Haynes, B. S. (2013) *Proceed. Combust. Instit*., Vol. 34, pp. 625-632.

Zimont V. and Lipatnikov A. (1995) "A Numerical Model of Premixed Turbulent Combustion of Gases," *Chem Phys Rep*., Vol. 14: 993–1025.

Zuev, A. P. and Starikovskii, A. Y. (1991) *Khim. Fiz.* 10, pp. 52-63.